

THEORETICAL STUDIES OF MOLECULAR
DYNAMICAL PROCESSES ON SOLID
SURFACES AND IN THE
GAS PHASE

By

DAN CONSTANTIN SORESCU

Bachelor of Science
University of Bucharest
Bucharest, Romania
1986

Master of Science
University of Bucharest
Bucharest, Romania
1987

Submitted to the Faculty of the
Graduate College of the
Oklahoma State University
in partial fulfillment of
the requirements for
the Degree of
DOCTOR OF PHILOSOPHY
December, 1994

THEORETICAL STUDIES OF MOLECULAR
DYNAMICAL PROCESSES ON SOLID
SURFACES AND IN THE
GAS PHASE

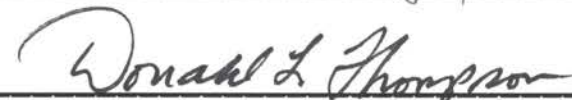
Thesis Approved:




Thesis Adviser









Dean of the Graduate College

PREFACE

The studies contained in this Dissertation are designated to make a contribution to the understanding of different fundamental processes involved in the dynamics of molecular systems in the gas-phase and on solids surfaces. The central idea is to develop detailed models for the real systems and then, using computer experiments within the range of different theories, to investigate the response of these model systems to different perturbations. Our ultimate objective is to give a more precise description of the types of interactions operating in the studied molecular systems and to predict certain physical quantities which are difficult or impossible to determine experimentally. It is my privilege to present the following pages to the critical reader with the open intention to debate some of the topics presented in this work.

The present work is the result of continuous intellectual development in a climate of high scientific level, guided by my professors Dr. Lionel M. Raff and Dr. Donald L. Thompson. I would like to thank both of them for the chance to be a part of their scientific group and for the inspired passion in understanding the complex subjects.

I would like to thank Drs. Larry Scott and Paul A. Westhaus for serving on my committee and for continuous guidance during my research work.

A continuous inspiration for me was my wife Monica. The words are too poor to describe her love, encouragement and brilliant ideas in every day life. My thoughts are also with our families, which have created a strong climate of love and support throughout our lives.

I am also pleased to acknowledge financial support from the Air Force Office of Scientific Research.

TABLE OF CONTENTS

| Chapter | Page |
|--|------|
| I. INTRODUCTION | 1 |
| Structure of the Thesis | 3 |
| II. THEORETICAL METHODS USED IN MOLECULAR DYNAMICS SIMULATIONS..... | 5 |
| General Aspects of Potential-Energy Surfaces | 5 |
| The Concept of a Potential-Energy Surface..... | 5 |
| Important Topological Regions of the Potential-Energy Surface..... | 6 |
| Types of Data Used in Potential-Energy Surface Construction..... | 7 |
| Information Obtained Using <i>Ab Initio</i> Calculations for Potential-Energy Construction..... | 8 |
| Equilibrium and Transition States Geometries..... | 9 |
| Calculation of Fundamental Vibrational Frequencies..... | 10 |
| Calculation of Bond Dissociation Energies..... | 12 |
| Calculation of Enthalpies of Formation..... | 13 |
| Procedures for Potential-Energy Surface Fitting | 15 |
| Analytical Functional Forms Used in Description of Potential Interactions..... | 15 |
| Connection of the Important Regions on the Potential Surface | 18 |
| Force Constant Fitting Procedure..... | 19 |
| Classical Trajectory Methods..... | 21 |
| Selection of Initial Condition. The Projection Method..... | 21 |
| Integration of Trajectories..... | 23 |
| Analysis of Trajectories..... | 26 |
| RRKM Theory..... | 26 |
| Non-Statistical Behavior..... | 30 |
| Mode Energies..... | 32 |
| Power Spectra..... | 33 |
| Variational Phase-Space Theory Methods | 35 |
| Monte Carlo Methods..... | 38 |
| Importance Sampling..... | 38 |
| III. DIFFUSION OF HYDROGEN ATOMS ON A SI(111)-(7X7) RECONSTRUCTED SURFACE..... | 43 |

| Chapter | Page |
|---|---------|
| Introduction..... | 43 |
| DAS Lattice Model..... | 45 |
| Selected Data on Elementary Chemical Processes of Hydrogen on Si(111)-(7x7) Surfaces | 47 |
| General Computational Model..... | 52 |
| Potential-Energy Surface | 53 |
| Computational Methods | 56 |
| A. Monte Carlo Variational Phas-Space Theory..... | 56 |
| B. Thermal Diffusion Equations..... | 60 |
| Results | 61 |
| A. Classical Jump Frequencies..... | 61 |
| B. Diffusion Coefficients..... | 63 |
| C. Tunneling Contributions | 66 |
| Conclusions..... | 68 |
| IV. STATISTICAL EFFECTS IN THE SKELETAL INVERSION OF BICYCLO(2.1.0) PENTANE | 90 |
| Introduction | 90 |
| Selected Data Related to Thermal Skeletal Inversion of Bicyclo(2.1.0)pentane..... | 92 |
| General Calculation Method | 94 |
| Potential-Energy Surface..... | 96 |
| A. Evaluation of Bond-Dissociation Energies in Bicyclo(2.1.0)pentane..... | 96 |
| B. General Requirements on the Potential-Energy Surface | 99 |
| C. Technical Aspects of the Potential-Energy Surface..... | 101 |
| D. Properties of the Potential-Energy Surface | 104 |
| Computational Procedures..... | 105 |
| A. Trajectory Calculations | 105 |
| B. Power Spectra | 107 |
| Results and Discussions..... | 110 |
| Summary | 114 |
| V. MOLECULAR DYNAMICS STUDIES OF THE THERMAL DECOMPOSITION OF 2,3-DIAZABICYCLO(2.2.1) HEPT-2-ENE..... | 139 |
| Introduction | 139 |
| Selected Experimental and Theoretical Data Related to Thermal Decomposition of 2,3-Diazabicyclo(2.2.1) hept-2-ene | 140 |
| General Calculation Method..... | 143 |
| Potential-Energy Surface | 144 |
| A. Determination of the Equilibrium Geometries | 144 |
| B. Vibrational Spectra..... | 147 |

| Chapter | Page |
|---|---------|
| C. Bond Dissociation Energies | 147 |
| D. Technical Aspects of the Potential-Energy Surface | 151 |
| E. Properties of the Potential-Energy Surface | 156 |
| Computational Procedures | 159 |
| Results of Trajectory Calculations and Discussions | 160 |
| Summary | 166 |
| VI. CONCLUSIONS | 210 |
| Diffusion of Hydrogen Atoms on a Si(111)-(7x7) Reconstructed Surface | 211 |
| Statistical Effects in the Skeletal Inversion of Bicyclo(2.1.0)pentane | 213 |
| Molecular Dynamics Studies of the Thermal Decomposition of 2,3-Diazabicyclo(2.2.1)hept-2-ene | 214 |
| BIBLIOGRAPHY | 217 |

LIST OF TABLES

| Table | Page |
|--|------|
| I. The Equilibrium Length and Binding Energies of the Si-H Bond and the Fundamental Vibrational Frequencies for SiH Species on the Si(111)-(7x7) Surface. The Corresponding Results Obtained in Our Calculations Are also Indicated | 70 |
| II. Hydrogen-Lattice Potential Parameters | 72 |
| III. Classical Jump Frequencies K_{AB} and Diffusion Coefficients D as a Function of the Surface Temperature | 73 |
| IV. Tunneling Jump Frequencies K_t and Diffusion Coefficients D as a Function of the Surface Temperature | 74 |
| V. <i>Ab initio</i> Calculated and Experimental Observed Geometries for Cyclopropane, Cyclobutane and Bicyclo(2.1.0)pentane | 116 |
| VI. Total Energies (Hartrees) for Bicyclo(2.1.0)pentane, Cyclopropane, Cyclobutane and Related Radicals. Radicals (6), (9) and (13) Correspond to Elimination of Hydrogen Atoms H ₆ , H ₉ and H ₁₃ from BCP | 118 |
| VII. Calculated and Experimental Bond Dissociation Energies (kcal/mol) | 119 |
| VIII. Thermodynamic Data for Cyclopropane, Cyclobutane and Bicyclo(2.1.0)pentane | 120 |
| IX. Bond and Angle Assignments for Bicyclo(2.1.0)pentane | 121 |
| X. Equilibrium Morse Parameters | 122 |
| XI. Bending Potential Parameters | 123 |
| XII. Flap and Dihedral Potential Parameters | 124 |
| XIII. Predicted and <i>Ab Initio</i> Calculated Geometries for Planar Configuration. The Distances Are Given in Å and the Angles in Degrees | 125 |

| Table | Page |
|--|------|
| XIV. Experimental and Calculated Frequencies for Bicyclo(2.1.0)-pentane | 126 |
| XV. Microcanonical Rate Constants for Flap Motion in Bicyclo(2.1.0)-pentane for Initial Random Energization. The Correlation Coefficients for the Fitting Are also Indicated | 128 |
| XVI. Total IVR Rates and other Parameters for Relaxation Out of the Flap Mode. The Parameters Were Obtained from Least-Squares Fits of the Average Normal-Mode Decay | 129 |
| XVII. <i>Ab initio</i> Calculated and Experimentally Observed Geometry for DBH | 169 |
| XVIII. Calculated Geometries of the Diazenyl Biradical and its Transition State for Nitrogen Loss | 170 |
| XIX. The <i>Ab Initio</i> Scaled Vibrational Frequencies for DBH and Diazenyl Biradical. The Scaling Factors Are 0.8929 for HF/6-31G* Values and 0.94 for MP2/6-31G* Data. Zero-Point Energies (ZPE) Are Given in kcal/mol | 172 |
| XX. Thermochemical and <i>Ab Initio</i> Calculated Data for the Compounds of Interest. The Enthalpies of Formation and the Thermal Corrections (TC) Are Given in kcal/mol. The Total G1 Energies and Zero-Point Energies Are in Hartrees and Milihartrees Respectively | 174 |
| XXI. <i>Ab initio</i> Calculated Geometries (C_{2v} Symmetry) and Energies (in Hartrees) of Dimethylenediazene (Diazetine) | 175 |
| XXII. Optimized Parameters (Bond Distances in Å, Angles in Degrees), Total Energies (in Hartrees) and Zero-Point Energies (ZPE) (in kcal/mol) for Conformations gGg' (1), tGg' (2) and tTt (3) of Ethylenediamine | 176 |
| XXIII. Total Energies (in Hartrees) and G1 Corrections (in Mhartrees) for Dimethylenediazene | 178 |
| XXIV. Bond and Angle Assignments for DBH and the Diazenyl Biradical | 179 |
| XXV. Morse Parameters for: (a) DBH; (b) Diazenyl Biradical; and (c) Nitrogen | 181 |
| XXVI. Bending Potential Parameters for: (1) DBH and (2) Diazenyl Biradical | 182 |

| Table | Page |
|---|------|
| XXVII. Dihedral Potential Parameters for: (1) DBH and (2) Diazenyl Biradical | 184 |
| XXVIII. Switching Functions Parameters Used in Eqs. (V.4)-(V.20) | 185 |
| XXIX. Equilibrium Energies (Not Including Zero-Point Energies) on the Analytic Surface. The Separated Atoms Are Taken as the Potential Zero | 186 |
| XXX. Calculated Frequencies (cm^{-1}) for DBH and Diazenyl Biradical | 187 |
| XXXI. Microcanonical Rates Constants for Diazetization of DBHD and the Corresponding Branching Ratios for Random Initial Energization. The Correlation Coefficients r of the Fitting Are Also Indicated | 189 |
| XXXII. Distribution of Available Energy Among Different Products of Dissociation of DBHD as a Function of Total Excitation Energy, in Excess to Zero-Point Energy. $\langle F_T \rangle$, $\langle F_R \rangle$, and $\langle F_V \rangle$ Denote the Fractions of Available Energy Partitioned into Translation, Rotation, and Vibration, Respectively | 190 |

LIST OF FIGURES

| Figure | Page |
|---|------|
| <p>1. Top View of the Atomic Structure of the DAS Model of the Si(111)-(7x7) Reconstruction. Atoms at Increasing Depth Are Represented by Circles of Decreasing Diameters. The Larger Black and Open Circles Represent the Adatoms and the Atoms in the Stacking Fault Layer, Respectively. Smaller Open Circles Represent the Atoms in the Unreconstructed Layers Beneath the Reconstructed Surface. The Left Half of the Unit Cell Contains the Stacking Fault. The Parallelogram Defines the Unit Cell</p> | 75 |
| <p>2. Detail of the DAS Surface Containing the Stacking Fault Layer (Open Circles) and the 12 Adatoms (Dark Circles) at A Sites with Local 2 x 2 Structure. Two of the 6 Rest Atoms of the Stacking Fault Layer Are also Indicated</p> | 76 |
| <p>3. Detail of the DAS Surface Containing the Layer with Dimers Along the Sides of the Triangular Subunits (Open Circles) and the Atoms in the Next Unreconstructed Layer (Solid Circles). Most of the Atoms in the Unreconstructed Layer Are Directly Beneath Second-Layer Atoms and Are Hidden from View</p> | 77 |
| <p>4. The Relative Positions of the Atoms with Dangling Bonds in the First (Dark Circles) and in the Second (Open Circles) Layers for Nine Adjacent Unit Cells on the (7x7) DAS Surface</p> | 78 |
| <p>5. Potential Energy Variation for the Symmetric Stretch of the Si-H Bond with the H Atom Positioned Directly Above the Adatom A in Fig. 4</p> | 79 |
| <p>6. A Perspective Plot of the Interaction Potential V_{gL} between the H Atom and the Relaxed (7x7) Lattice as Function of x and y Coordinates in a Plane Parallel to, and 3.0 a.u. Above Atom A, of the Top Layer of the Si(111)-(7x7) Lattice as Shown in Fig. 4</p> | 80 |
| <p>7. Contour Plot for the Interaction Potential V_{gL} between the H Atom and the Relaxed (7x7) Lattice as a Function of x and y Coordinates in Atomic Units in a Plane Parallel to, and 3.0 a.u. Above Atom A, of the Top Layer of the Si(111)-</p> | |

| Figure | Page |
|---|------|
| (7x7) Lattice. Contour Levels Are Given in Electron Volts Relative to the Hydrogen Atom at Infinity | 81 |
| 8. Details of the Cross Section of the Dividing Surfaces Used in the Variational Calculation. Dark and Open Circles Represent the Atoms with Dangling Bonds in the First and Second Layers, Respectively | 82 |
| 9. Minimum-Energy Diffusion Path for A→B Jumps. The Triangles Denote the Values Obtained in the Variational Calculations. The Circles Represented Extrapolated Results Based on Symmetry Considerations | 83 |
| 10. (x,z) Coordinates of the Points Corresponding to the Minimum-Energy Diffusion Path Given in Fig. 9. The Triangles Denote the Values Obtained in the Variational Calculations. The Circles Represent Extrapolated Results Based on Symmetry Considerations | 84 |
| 11. Arrhenius Plot of the A→ B Jump Frequencies Given in Table III | 85 |
| 12. The Simplified Diffusion Model for 49 Unit Cells on the DAS Surface. Each Triangle Corresponds to the Triangular Region Shown in Fig. 4 and Contains Nine Atoms with Dangling Bonds | 86 |
| 13. A Plot of the Mean-Square Displacement $\langle r^2(t) \rangle$ as a Function of Time in Units of 1.0×10^{-6} s. The Triangles Are the Computed Points and the Straight Line is the Least-Squares Fit | 87 |
| 14. Arrhenius Plot of the Diffusion Coefficients Given in Table III | 88 |
| 15. The Frequency of Surface-Plane Vibration of the Hydrogen Atom in the Well of the Minimum-Energy Diffusion Potential Given in Fig. 7 as a Function of Energy | 89 |
| 16. The General Reaction Scheme for Skeletal Inversion of Bicyclo(2.1.0)pentane Obtained in Thermal Decomposition of 2,3-Diazabicyclo(2.2.1)hept-2-ene-exo-,exo-5,6-d ₂ (1). (2x) and (2n) Represent the Exo- and Endo-Deuterium Labeled Bicyclo(2.1.0)pentane and (3) is the 1,3-CyclopentanediyI Radical | 130 |
| 17. Atom Designation and Numbering for Bicyclo(2.1.0)pentane | 131 |

| Figure | Page |
|---|------|
| 18. The Variation of the Total Potential as Function of the Flap Angle. The Dashed Line Is a Guide for the Eye | 132 |
| 19. Temporal Variation of the Flap Angle Extracted from a Trajectory for which Ring Inversion Takes Place. The Abscissa Unit Is 1 t.u. = 1.018×10^{-14} s | 133 |
| 20. Decay Plots for Random Excitation of the Vibrational Modes at the Energies (a) $E=120$ kcal/mol, (b) 150 kcal/mol, (c) 180 kcal/mol and (d) 210 kcal/mol in Excess to Zero-Point Energy. In Each Case, the Line Is a Linear Least-Squares Fit to the Calculated Points | 134 |
| 21. Total Microcanonical Rate Constants for the Ring Inversion of BCP as Function of the Excitation Energy in Excess to Zero-Point Energy. Calculated Points Are Denoted by Symbols and the Corresponding RRK Fit by Smooth Curve | 135 |
| 22. Power Spectra for BCP in Arbitrary Units (a.u.) at: (a, b) Zero-Point Energy, (c, d) 120 kcal/mol, (e, f) 225 kcal/mol. The Excitation Energies Are Initially Distributed at Random Over the Normal-Modes in Excess to Zero-Point Energy. Plots (a), (c) and (e) Represent the Composite Spectrum. The Power Spectrum of the Flap Angle is Given in Plots (b), (d) and (f) | 136 |
| 23. Instantaneous Mode Kinetic Energies for the Modes with the Highest Increase in Energy Subsequent to the Initial Excitation of the Flap Mode ν_2 . Initial State Corresponds to Excitation of the Flap Mode with 30 kcal/mol Above Zero-Point Energy. Each Successive Curve Is Displaced Upward by 0.75 eV To Provide Clarity. The Abscissa Unit Is 1 t.u. = 1.018×10^{-14} s | 137 |
| 24. Decay Curve for the Average Mode Energy of the Flap Mode Initially Excited with 30 kcal/mol in Excess of Zero-Point Energy. The Solid Curve Is a Nonlinear Least-Squares Fit of the Points with the Equation (IV.10) | 138 |
| 25. The General Reaction Scheme for Thermal Decomposition of 2,3-Diazabicyclo(2.2.1)hept-2-ene-exo, exo-5,6-d ₂ | 191 |
| 26. Atom Designation and Numbering for: a) 2,3-Diazabicyclo(2.2.1)hept-2-ene and b) Diazenyl Biradical | 192 |
| 27. Calculated (MP2/6-31G*) Infrared Spectra of DBH | 193 |

| Figure | Page |
|--|------|
| 28. Pictorial View of Dimethylenediazene (a) and Ethylenediamine Configurations: gGg' (b); tGg' (c) and tTt (d) | 194 |
| 29. The Variation of the Total Potential as a Function of the C-N Bond Distances: a) $r(\text{C}_1\text{-N}_{14})$; b) $r(\text{C}_4\text{-N}_{15})$ for the Successive Cleavage Reaction Mechanism | 195 |
| 30. The Variation of the Flap Angle as a Function of the C-N Bond Distances: a) $r(\text{C}_1\text{-N}_{14})$; b) $r(\text{C}_4\text{-N}_{15})$ Corresponding to the Potential Profile Given in Figs. 29 a) and 29 b) | 196 |
| 31. Panel Showing Different Molecular Structures Corresponding to the Potential Profile Given in Figs.29 a) and 29 b). The Configurations (a-d) Correspond to r_5 Values of 1.503 Å, 2.5 Å, 3.5 Å, and 4.45 Å. The Configurations (e) and (f) Correspond to r_6 Values of 1.73 Å and 3.5 Å | 197 |
| 32. The Variation of the Total Potential as a Function of the C-N Bond Distance for Simultaneous Stretching of Both C-N Bonds | 198 |
| 33. Temporal Variation of (a) the C-N Bond Lengths $r(\text{C}_1\text{-N}_{14})$ and $r(\text{C}_4\text{-N}_{15})+2.5$ Å and (b) Flap Angle, for a Trajectory Leading to (5x). $r(\text{C}_4\text{-N}_{15})$ Has Been Displaced Upwards by 2.5 Å to Enhance the Visual Clarity. Time Is Given in Units of 1.018×10^{-14} sec | 199 |
| 34. Temporal Variation of (a) the C-N Bond Lengths $r(\text{C}_1\text{-N}_{14})$ and $r(\text{C}_4\text{-N}_{15})+2.5$ Å and (b) Flap Angle, for a Trajectory Leading to (5n). $r(\text{C}_4\text{-N}_{15})$ Has Been Displaced Upwards by 2.5 Å to Enhance the Visual Clarity. Time Is Given in Units of 1.018×10^{-14} sec | 200 |
| 35. Temporal Variation of (a) the C-N Bond Lengths $r(\text{C}_1\text{-N}_{14})$ and $r(\text{C}_4\text{-N}_{15})+2.5$ Å and (b) Flap Angle, for a Trajectory Leading to (5x) without Passing Through the Well Corresponding to the 1,3-cyclopentadiyl Radical. $r(\text{C}_4\text{-N}_{15})$ Has Been Displaced Upwards by 2.5 Å to Enhance the Visual Clarity. Time Is Given in Units of 1.018×10^{-14} sec | 201 |
| 36. Decay Plots for Random Excitation of the Vibrational Modes of DBHD at the Energies (a) 60 kcal/mol; (b) 100 kcal/mol; (c) 125 kcal/mol; (d) 175 kcal/mol in Excess of Zero-Point Energy. In Each Case, the Line Is the Result of Linear Least-Squares Fit to the Calculated Points | 202 |
| 37. Microcanonical Rate Coefficients for the Decomposition of DBHD as a Function of Excitation Energy in Excess of Zero-Point | |

| Figure | Page |
|---|------|
| Energy. The Points Are the Calculated Values. The Line Is a Least-Square Fit of Eq. (V.23) | 203 |
| 38. Normalized Distribution of the Total Translational Energy Released in Deazetization Reaction of DBHD. Total Energies Are (a) 60 kcal/mol; (b) 175 kcal/mol | 204 |
| 39. Normalized Distribution of the Rotational Energy of N ₂ Molecules Formed in Deazetization Reaction of DBHD. Total Energies Are (a) 60 kcal/mol; (b) 175 kcal/mol | 205 |
| 40. Normalized Distribution of the Vibrational Energy of N ₂ Molecules Formed in Deazetization Reaction of DBHD. Total Energies Are (a) 60 kcal/mol; (b) 175 kcal/mol | 206 |
| 41. Normalized Distribution of the Vibrational Energy of BCP Molecules Formed in Deazetization Reaction of DBHD. Total Energies Are (a) 60 kcal/mol; (b) 175 kcal/mol | 207 |
| 42. Time Variation of the Root-Mean-Square of the Average Normal-Mode Energies for an Ensemble of Trajectories Initial Excited with 60 kcal/mol | 208 |
| 43. Composite Power Spectra for DBHD in Arbitrary Units at: (a) Zero-Point Energy; (b) 40 kcal/mol; (c) 70 kcal/mol; and (d) 100 kcal/mol. The Excitation Energies, in Excess to Zero-Point Energy, Are Initially Distributed at Random Over the Normal-Modes | 209 |

CHAPTER I

INTRODUCTION

The methodology adopted in this work to investigate molecular systems on solid surfaces and in the gas phase is that of classical molecular simulations.^{1,2} Numerous studies published in the last three decades show that this method can be successfully used for many types of systems, such as simple molecular systems,¹ liquids,³ macromolecules,⁴ or crystals.⁵⁻⁶ However, limitations of the method occur for those processes which are quantumly allowed but classically closed. Tunneling effects, scattering into classically forbidden states, and potential surface crossing are examples of processes which require investigations based on quantum mechanics or semiclassical methods.⁷⁻⁹

Three main stages are generally involved in classical molecular simulations. In the first stage, a model for the molecular system subject to analysis is created. This model, given in the form of a potential-energy surface, contains the information related to molecular configurations, inter particle interactions and interactions between the molecular system and the environment. Obtaining an accurate potential-energy surface is a central goal of the theoretical and experimental efforts. In the construction of such a potential surface, the information available from dynamical and non-dynamical studies, from semiempirical and *ab initio* theories is included. This information is continuously updated as a result of newly refined data generated both experimentally and theoretically. This means that a potential-energy surface used in the elucidation of the characteristics of a given molecular system is

evolutionary in concept.

The second step of the methodology involves the execution of molecular trajectories on the given potential-energy surface and for a given selection of the initial conditions. For this purpose, two main directions can be considered.

In a deterministic situation, the interaction potential for the system will generate the forces between particles and correspondingly, the equations of motion which describe the dynamics of the system. In other words, the execution of molecular trajectories means the numerical integration of the classical equations of motion for the system of interacting particles. To do so, the equations of motion are approximated by adequate schemes, suited for numerical evaluation on a computer. Due to the transition from a description in terms of continuous variables with differential operators to a description with discrete variables and finite difference operators, the numerical analysis will be affected by errors. Depending upon the specific approximations, the level of errors will be different, but in principle, the error can be made as small as desired, restricted only by the speed and computing resources available. The end point of a trajectory is considered to occur when the moving particle enters in a region of phase space designated as product space.² The boundaries of a such region are generally described in terms of different internal coordinates of the atoms, such as the separation of groups of atoms, or dihedral angles. Criteria to test whether the product molecules are in bound, quasi-bound or dissociative states can be found in Ref. 2.

In stochastic cases, such as Monte Carlo simulations¹⁰, the deterministic trajectory is replaced by a Markov chain, in which case the set of molecular coordinates at a given moment depends only on the molecular configuration at the previous moment.

The final part of molecular dynamics methodology refers to the analysis

of trajectories. This step includes extraction of information with relevance to the phenomenon of interest. The calculations of the reaction rates and cross sections, intramolecular and intermolecular energy transfer rates, or distribution of energy over the available degrees of freedom are typical examples of quantities determined at this step.

It can be seen that a significant advantage of deterministic molecular dynamics simulations is related to the possibility of providing a detailed description of the individual particle motions and of the internal modes as a function of time, such that they can be used for a detailed characterization of the system's properties. In addition, due to the fact that different elements of the potential used in calculations are under the users' control, their role in determining a given property can be examined by changing specific contributions.

It should be mentioned that deterministic molecular dynamics techniques are not appropriate for the investigation of infrequent motions or processes which have characteristic times longer than 100 ps, because these events are unlikely to occur spontaneously during the short time involved in the simulation. In these cases, the use of stochastic methods, such as Monte Carlo in combination with the Metropolis sampling procedure,¹¹ constitutes an alternative approach for description of these systems.

We shall exemplify the application of the above presented methodology for particular cases in the next chapters.

Structure of the Thesis

Following the Introduction, we present in Chapter II the main theoretical methods that we have used in performing the molecular dynamics simulations. The essential elements for construction of potential-energy surfaces, selection

of initial conditions, analysis of the reaction products, as well as the Monte Carlo methodology are discussed.

Chapter III describes the investigation of hydrogen-atom diffusion on a Si(111)-(7x7) reconstructed surface. Following a review of the literature in this field, the potential-energy surface for hydrogen-lattice interactions is described. Next, the results of hydrogen diffusion obtained using Monte Carlo variational phase space theory are presented.

Chapter IV reports studies of statistical effects in the skeletal inversion of bicyclo(2.1.0)pentane. The detailed procedure of construction of potential-energy surface for this molecule together with the results of classical trajectory calculations performed on this surface are discussed.

In Chapter V, we extend the development of the potential-energy surface for bicyclo(2.1.0)pentane to a much more complex reaction, i.e. thermal deazetization of 2,3-diazabicyclo(2.2.1)hept-2-ene. The results of classical trajectory calculations on this potential are also presented.

Conclusions emerging from the analysis of these three systems are summarized in Chapter VI.

CHAPTER II

THEORETICAL METHODS USED IN MOLECULAR DYNAMICS SIMULATIONS

The goal of this chapter is to give a brief description of the essential elements used by us in construction of the potential-energy surfaces, integration of classical trajectories, Monte Carlo simulations, and in analysis of trajectories. In every particular case, the numerical analysis was performed using specific computer codes written by us, excepting the *ab initio* calculations which were done using the standard Gaussian 92 package of programs.¹²

General Aspects of Potential-Energy Surfaces

The Concept of Potential-Energy Surface

The molecular dynamics simulations are performed assuming the validity of the Born-Oppenheimer approximation,¹³ which states that the Schrödinger equation for a molecule can be separated into a part describing the motions of the electrons and a part describing the motions of the nuclei. Moreover, these two sets of motions can be independently studied. In addition, it is assumed that the motion of the electrons is very fast relative to the nuclear motion, such that the energy of electrons may be computed in the field of stationary nuclei by solution of the time-independent Schrödinger equation. In molecular dynamics, the motions of the nuclei are studied without explicit examination of the electrons. In this case, the ground electronic state of the molecule will be a

function of the nuclear positions. For a system of N nuclei, the hypersurface which describes the potential energy in terms of the nuclear positions is called the Born-Oppenheimer surface. In the particular case of molecular dynamics, this surface is termed potential-energy surface.¹⁴ The investigation of the motion of nuclei on this potential surface is the objective of molecular dynamics simulations.

Important Topological Regions of the Potential-Energy Surface

As defined above, the potential-energy surface for a molecular system can be described in terms of the positions of the nuclei. This can be done using a set of orthogonal coordinates, usually Cartesian coordinates, or a set of internal coordinates such as bond lengths, bond angles or dihedral angles. Generally, a potential-energy surface presents a number of local minima which correspond to different equilibrium structures. These structures can represent different molecular conformations, different isomers, or the reactant and product molecules.

These local minima are connected by an infinite number of different energy paths, but under most circumstances, configuration points close to the minimum-energy pathway will be followed in a given reaction. In the case of a potential-energy surface which describes a chemical reaction, it is therefore important to determine the minimum-energy path between the reactants and products. Particularly, the characterization of transition-states or first-order saddle points is of prime interest. On a multidimensional potential-energy surface, a first-order saddle point is defined as a point which is a maximum in one and only one direction, and minimum in all of the remaining independent directions.¹⁵

In conclusion, a main goal in describing the potential-energy surface for

a given molecular system is the accurate location of the stationary points corresponding to reactants and products, and of the transition states along different reaction coordinates.

Types of Data Used in Potential-Energy Surface Construction

In the case of molecular dynamics, the Born-Oppenheimer surface for the nuclei is approximated by a set of parametrized potential functions to obtain the best fit of calculated and experimental properties of the molecules. These properties generally include the geometrical configurations and fundamental vibrational frequencies for reactants and products, thermochemical data (such as heats of formation, reaction endo- or exothermicities) and kinetic data (such as reaction rate constants, relative and absolute yields, or activation energies).

A simplified way to describe the potential-energy surface for molecular systems is the use of molecular mechanics force fields.^{14,16-18} In this case, it is assumed that the force constants and the set of adjustable parameters optimized for a limited set of molecules can be transferred to other molecules. Currently, the available force fields for aliphatic hydrocarbons, such as MM2¹⁶ or MM3^{17,18} are adequate to describe with reasonable agreement the structures, heats of formation, conformational energies and rotational barriers. However, the assumption of transferability of the set of molecular parameters between different molecules should be analyzed in each case. Another disadvantage of these potentials is related to the fact that they can be used only for the study of equilibrium states since their accuracy for configurations far removed from the stationary points is low. Consequently, they are not useful in the study of molecular dynamics.

The approach adopted by us is to construct specific potential-energy surfaces for individual molecular systems which are able to reproduce not only

equilibrium state properties, such as geometrical structure, enthalpy of formation or fundamental vibrational frequencies, but at the same time, data related to transition-state geometries, experimental activation energies or reaction profiles. Even though this procedure is more laborious than that used in molecular mechanics force fields, the complexity of the systems under investigation requires this approach to the problem.

Information Obtained Using *Ab Initio* Calculations for Potential-Energy Construction

A significant part of the work performed in the construction of potential-energy surfaces for different molecular systems is related to *ab initio* calculations. The purpose of these calculations is to extract the necessary information for a more comprehensive description of different points on the molecular potential surface. Consequently *ab initio* calculations constitute an important additional tool in molecular dynamics methodology.

A significant difficulty in the construction of a realistic potential-energy surface is encountered in those cases when different experimental studies present results with significant differences or when the necessary data to construct such potentials are not available. In particular, this is the case for the majority of reaction transition states or biradical states, which are difficult to probe experimentally.

We have used *ab initio* molecular orbital calculations for four main types of computations: a) geometry optimization for equilibrium and transition states; b) fundamental vibrational frequencies; c) bond dissociation energies; and d) determination of the enthalpy of formation. In all these cases, standard *ab initio* calculations have been performed using the Gaussian 92 package of programs.¹²

Equilibrium and Transition States Geometries

In the case of equilibrium states, the general methodology is to obtain the optimized geometries at the Hartree-Fock (HF)¹⁹ level using the internal basis sets 6-31G* or 6-31G**. ^{20,21} In this case, the term "optimization" refers to finding the minimum on an energy surface using a series of grid-points that explore the surface and converge to a local minimum. A geometry optimization begins at the initial molecular structure given as input, it computes the energy and the gradient at that point, and then determines the direction and the maximum size for the next step. A list of energy or gradient algorithms used in these calculations can be found in Ref. 22. The calculation is complete when the forces and the root-mean-square of forces are zero (within a given tolerance), and when the calculated displacements and their root-mean-square for the next step are below a cutoff value.

In the HF approximation, each electron moves in a field which is the average over all other electrons. However, in the real situation, the motion of electrons is correlated such that the movement of every electron is influenced by the instantaneous positions of all other electrons. These limitations cause calculated HF energies to be above the exact values. In order to consider electron correlation, specific methods, such as limited configuration interaction¹⁹ or Möller-Plesset (MP) perturbation theory²⁰ should be used.

Extensive application of the above methodology for molecules having two to five heavy-atoms has been shown to give results in very close agreement with experimental data. For example, it has been shown that at the MP2/6-31G* level, the mean absolute deviation between the calculated and experimental bond distances for a series of 16 two-heavy-atom hydrides is only 0.019 Å for

multiple bonds.¹⁹ Moreover, while the MP2/6-31G* bond lengths are greater than the corresponding experimental results, the magnitude of the differences is smaller than that corresponding to HF/6-31G* values.¹⁹

In most *ab initio* calculations performed to obtain the structures and energies of different molecules at a local minimum or at a transition state, we have followed this two-step procedure, i.e. the geometry is first optimized at the HF/6-31G* level and then refined at the MP2/6-31G* level. Our results for a number of intermediate-size molecules such as cyclopropane, cyclobutane, diazetine, ethylenediamine, bicyclo(2.1.0)pentane and 2,3-diazabicyclo(2.2.1)hept-2-ene show close agreement between the calculated and accurate experimental geometrical parameters. In addition, we have determined the optimized geometry of diazenyl biradical involved in thermal decomposition of 2,3-diazabicyclo(2.2.1)hept-2-ene for which no experimental data are available.

Calculation of Fundamental Vibrational Frequencies

The second type of information obtained from *ab initio* calculations are the surface curvatures which are related to the vibrational frequencies of the corresponding normal-modes. It is well known that in vicinity of a critical point, where all first derivatives are zero, the energy surface can be approximated as

$$E(\mathbf{q}) = E_0 + (1/2) \sum_{i,j} f_{ij} (q_i - q_i^0)(q_j - q_j^0) \quad (\text{II.1})$$

where

$$f_{ij} = \frac{\partial^2 E}{\partial q_i \partial q_j} \quad (\text{II.2})$$

Here q_i^0 and q_i refer to the coordinates of the stationary point and of the geometry of interest, respectively. The force constant matrix, \mathbf{F} , also called Hessian matrix, can be calculated either directly, using analytical second differentiation, or by numerical first differentiation of analytical first derivatives.¹⁵ For a given molecule, the harmonic vibrational frequencies can then be determined as a solution of the secular $\mathbf{F-G}$ matrix equation,²³

$$\det(\mathbf{FG} - \lambda\mathbf{I}) = 0 \quad (\text{II.3})$$

where \mathbf{G}^{-1} is the kinetic energy matrix and \mathbf{I} is the unit matrix. The vibrational frequencies are related to the eigenvalues λ of Eq. (II.3) by the relation $\lambda = (2\pi\nu)^2$. In mass-weighted coordinates, the \mathbf{G} matrix is proportional to the unit matrix and the normal coordinates are the eigenvectors of the \mathbf{F} matrix.

Several important points are related to the calculation of fundamental frequencies. First, these frequencies are used to give a better characterization of the stationary points on the potential surface. This means that at local minimum, all vibrational frequencies should be real, while at first-order saddle points a single imaginary frequency should be found. In addition, the vibrational frequencies can be used to evaluate thermodynamical properties, such as reaction entropy or equilibrium isotope effects, or to determine temperature corrections of thermochemical data evaluated at 0 K and zero-point energy.¹⁹ Analysis of the corresponding normal-eigenvectors offers the possibility of identifying the types of motion associated with a given vibrational mode and further, the assignment of spectra.

Extensive computations of vibrational frequencies for polyatomic molecules^{19,24-30} using *ab initio* calculations have shown that the results consistently larger by 10-15 % than the measured values. In order to correct

this overestimation of the calculated vibrational frequencies, different scaling factors have been proposed. It is generally accepted that at the HF/6-31G* level, the fundamental frequencies should be uniformly scaled by a factor of 0.8929,^{27,29,30} while at the MP2/6-31G* level, the corresponding correction factor is 0.94.²⁶ However, schemes which differentiate the scaling factors for the stretching modes relative to all the other modes have also been proposed.^{24,25}

We found good agreement between the scaled *ab initio* frequencies and the experimental data in the case of bicyclo(2.1.0)pentane. In addition, in the case of 2,3-diazabicyclo(2.2.1)hept-2-ene molecule and the corresponding diazenyl biradical, the use of *ab initio* calculations is the only reliable source for the vibrational frequencies. The detailed results of these calculations are presented in Chapters IV and V.

Calculation of Bond Dissociation Energies

The third category of data extracted using *ab initio* calculations is related to bond dissociation energies. It has been shown¹⁹ that the use of Hartree-Fock theory for direct calculation of the energy of a homolytic dissociation process $A-B \longrightarrow A + B$ gives poor results relative to the experimental values. This fact can be easily understood since the correlation energy correction for the electrons forming a bond is a significant fraction of the total bond dissociation energy. Due to the fact that the correlation energy is omitted in Hartree-Fock calculations, it is expected that smaller dissociation energies will be obtained. This is due to the different error levels for the bonded A-B system and for the separated A and B system.

A first method to improve the accuracy of the calculated bond-dissociation energies is the treatment of the correlation effects using a second-order Möller-Plesset (MP2) expansion or the successively higher order MP3 and

MP4 calculations. For one-heavy-atom hydrides comprising first-row elements, the general difference between the calculated and experimental data is within 10 kcal/mol.¹⁹ The quality of these results can be further improved by using larger basis sets and levels of correction. For example, in the case of methane, the bond dissociation energy calculated at the MP4/6-311G** theoretical level differs by only 1.4 kcal/mol from the experimental value.¹⁹ However, calculations of bond-dissociation energies beyond fourth order in Möller-Plesset perturbation theory are not practical for large molecules.

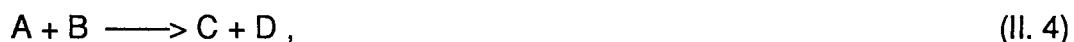
In our calculations, we have determined the cyclopropyl-H, cyclobutyl-H bicyclo(2.1.0.)propyl-H, bicyclo(2.1.0)butyl-H and bridgehead bicyclo(2.1.0)-pentane-H bond dissociation energies using the calculated energetical values at the MP4/6-31G* level. The corresponding results will be presented in Chapter IV.

More precise procedures developed for computation of the total energies of molecules at their equilibrium geometries are represented by Gaussian-1 (G1)³⁰ and Gaussian-2 (G2)³¹ procedures. The main idea of these methods is to replace very large calculations at the QCISD(T)/6-311+G(2df) and QCISD(T)/6-311+G(3df,2p) levels with a succession of much smaller and correspondingly much faster calculations. The individual steps involved in these calculations are described elsewhere.^{30,31} For a set of 31 molecules, it has been found that the total atomization energies agree with experimental thermochemical data to an accuracy greater than 2 kcal/mol in case of G1 theory, and 1.21 kcal/mol for G2 theory.^{30,31} However, the use of these methods for large molecules is still impractical.

Calculation of Enthalpies of Formation

The molecular energies and vibrational frequencies calculated using the

methods presented above can be further used to evaluate theoretically thermochemical data. In those cases where such experimental data are not available, theoretical methods constitute a reliable alternative to a speculative guess. As an illustration, we consider the case when the enthalpy of formation needs to be determined. In this case, a convenient method of calculation is the use of thermochemical cycles where all the enthalpies of formation except one are known.³² For a reaction of the general form



it follows that

$$\Delta H_f(A) = \Delta H_f(C) + \Delta H_f(D) - \Delta H_f(B) - \Delta E_R, \quad (\text{II. 5})$$

where

$$\Delta E_R = (E_C + E_D - E_A - E_B) + (TC_C + TC_D - TC_A - TC_B). \quad (\text{II. 6})$$

Here E_α is the total electronic energy and TC_α is the corresponding thermal correction. For a polyatomic molecule, with the assumption of ideal gas behavior, the thermal corrections at temperature T from 0 K can be evaluated as

$$TC = 4RT + N_A \sum_i^{\text{normal modes}} \frac{hv_i}{e^{hv_i/kT} - 1} \quad (\text{II.7})$$

where R is the ideal gas constant, k is the Boltzmann constant, h is the Planck constant and N_A is Avogadro's number. For a linear molecule, the $4RT$ term in

(II.7), which includes translational, rotational and work term contributions, should be replaced with $(7/2)RT$.

Two general rules are considered in this type of calculation. The first is related to the selection of working reactions which present the greatest degree of similarity between reactant and product sides. A good choice will minimize correlation effects by their mutual cancellation. The second rule states that as large as possible basis sets should be used, along with high-level correlated methods. Accuracy within few kcal/mol has been reported using the above methods.^{33,34}

We employed this method, with energy determined at the G1 level, for the case of the diazetine molecule (see Chapter IV), for which the experimental enthalpy of formation is not available.

Procedures for Potential-Energy Surface Fitting

Analytical Functional Forms Used in Description of Potential Interactions

The use of theoretical dynamics methods in the study of a given molecular system assumes knowledge of the energy and its gradient for each point on the potential-energy surface. This means that, in principle, every method able to generate these two essential quantities for each molecular configuration can be a valid candidate for dynamical studies.

From this point of view, the first choice would be the use of *ab initio* molecular orbital calculations. To the best of our knowledge, full trajectories calculations on *ab initio* potential-energy surface have not yet been reported for systems with more than 4 atoms. Instead, *ab initio* methods have been employed to evaluate the molecular energy and the energy derivatives only at a limited number of points. The potential surface is then generated by different

fitting procedures³⁵⁻³⁸ or by the moving interpolant technique.³⁹

The second alternative in obtaining the energy and its gradient is the development of a set of analytical potential functions able to fit the main features of the potential-energy surface.⁴⁰ In this case, the molecular potential is written as a superposition of empirical functions for each of the valence internal coordinates, such as bond lengths, bond angles and dihedral angles. This is the procedure used in the present work to describe polyatomic systems such as bicyclo(2.1.0)pentane, 2,3-diazabicyclo(2.2.1)hept-2-ene or the diazenyl biradical. In these cases, the total molecular potential for states close to the equilibrium configuration is taken to be

$$V = \sum_{\text{bonds}} V(r_i) + \sum_{\text{angles}} V(\theta_i) + \sum_{\text{torsions}} V(\tau_i). \quad (\text{II.8})$$

Here, the $V(r_i)$ term is the bond stretching potential for a bond with distance (r_i), $V(\theta_i)$ represents the bending potential corresponding to the bond angle θ_i and $V(\tau_i)$ is the dihedral potential associated with the torsional angle (τ_i).

For bond stretching potentials, Morse-type functions have been employed

$$V(r) = D\{\exp[-2\beta (r-r^0)] - 2\exp[-\beta (r-r^0)]\}, \quad (\text{II.9})$$

where D is the potential well depth, β is the curvature parameter and r^0 is the equilibrium distance. The parameters D and β are related to the harmonic force constant k_r by the relation

$$k_r = 2 D \beta^2. \quad (\text{II.10})$$

The bending potentials in Eq. (II.8) have the quadratic form

$$V(\theta) = 0.5 k_{\theta} (\theta - \theta^0)^2, \quad (\text{II.11})$$

where k_{θ} is the force constant associated with the bond angle θ , which has the value θ^0 at equilibrium.

For the torsional potential terms, different types of representations have been used, depending on the particular torsional configuration. In the cases when the dihedral angles are zero at equilibrium, the following functional forms have been employed^{41,42}

$$V(\tau) = 0.5 k_{\tau} \tau^2 \quad (\text{II.12})$$

and

$$V(\tau) = V_0 \sin^3\theta_1 \sin^3\theta_2 \sin^2\tau. \quad (\text{II.13})$$

In Eq. (II.12) k_{τ} is the torsional force constant corresponding to the dihedral angle τ . For a dihedral angle determined by a set of four atoms α - ψ - γ - δ , the angles θ_1 and θ_2 in Eq. (II.13) represent the bond-angles α - ψ - γ and ψ - γ - δ , respectively. The advantage of the functional form given in Eq. (II.13) is that the torsional potential decreases to zero when either of the two angles θ_1 and θ_2 is equal to 180° and the dihedral angle is no longer defined.

In the cases when the equilibrium dihedral angle is different from zero, the analytical form (II.13) was replaced by

$$V(\tau) = V_0 \sin^3\theta_1 \sin^3\theta_2 [\cos\tau - \cos\tau^0]^2, \quad (\text{II.14})$$

where τ^0 represents the equilibrium value of the dihedral angle.

In those cases when the torsional potential shape is a symmetric double-well, a convenient analytical representation can be obtained using a truncated cosine series.⁴³ The use of this method is dependent on knowledge of the torsional barrier values and torsional frequencies. We have used a cosine series expansion for the potential term describing the flap motion in the skeletal inversion of bicyclo(2.1.0)pentane molecule. In this case, the flap potential shape as function of the flap angle contains two symmetric wells corresponding to equilibrium angles $\pm\tau_{\text{equil}}$ and an additional well centered at $\tau=0$. Details of this calculation are presented in Chapter IV.

Connecting Important Regions on the Potential Surface

The analytical forms given in Eqs. (II.8-II.14) can be successfully used to fit the potential surface for regions around different equilibrium states. However, in the practical cases involving reactions, the general form of the potential should be able to describe not only these local minima, but, at the same time, the intermediate regions which connect these minima. In particular, as it has been noted in the previous sections, the correct description of the region around the saddle points is of prime interest.

A general procedure used to perform such connections on the potential-energy surface is the use of switching functions. These functions, which depend on the variables associated with the motion of the system along the reaction coordinate, should be continuous and have continuous first derivatives. In addition, their asymptotic limits should lead to the proper description of the critical points on the potential-energy surface. In addition, it is highly desirable that the switching function be sufficiently flexible to permit adjustment of the rate of variation between the asymptotic limits.

Generally, the switching functions can operate upon the global potentials describing different reaction channels or alternatively, on the individual terms of a given potential.

In the former case, for a total potential described as

$$V = V^R + (V^P - V^R) S(\gamma) , \quad (II.15)$$

a continuous monotonical variation of the switching function $S(\gamma)$ between the limits 0 and 1 will determine a corresponding variation of the total potential between V^R (reactants) and V^P (products). Here, γ represents the set of variables associated with motion along the reaction coordinate.

When modifications of the geometrical parameters, force constants or bond dissociation energies are needed along the reaction coordinate, the action of the switching functions can be limited to these parameters. In these cases, a form similar to that in (II.15) should be used with the parameter of interest instead of the potential values V .

The particular functional forms of the switching functions used in our studies were either hyperbolic tangent or exponential. The specific forms will be described in the appropriate sections of Chapters IV and V.

Force Constant Fitting Procedures

After the analytical potential terms have been chosen, the next step is to fit the potential parameters to the totality of geometrical, thermochemical, spectroscopic and kinetic data available for a given system.

In the first step of this procedure, the equilibrium coordinates are set equal to the corresponding experimental or *ab initio* calculated data. In addition, the experimental or *ab initio* calculated bond dissociation energies are

assigned to the corresponding terms in the Morse potential. The second step of the procedure consists in iterative adjustment of a trial set of force constants, such that the normal-mode frequencies fit the experimental or *ab initio* values. This step is generally achieved by direct normal-mode analysis^{23,44} or by power spectra calculations. When the frequency assignments are known, the simplest choice is to adjust the stretching frequencies first (by using only the curvature parameters in Morse potentials) and to proceed to the adjustment of the other modes. The final step of the fitting procedure is related to adjustment of the switching function parameters. Depending on the type of modification needed (geometrical or energetic), these parameters are iteratively adjusted to reproduce either specific geometries, as in the case of transition states or products of reaction, or different barrier heights or reaction profiles. At the end of this step, it is often necessary to refine again the set of force constants.

The initial stage of the fitting procedure is terminated when the following four types of tests are passed:

The first test is related to verification of equality of the numerical and analytical derivatives of the potential for different molecular configurations. In addition, the initial reference states should be obtained upon back-integration of a trajectory.

Second, the equilibrium geometries predicted by the potential should be determined using the damped trajectory method.⁴⁵ In this procedure, the atoms are initially placed in a configuration near the local minimum being sought, with all initial momenta set to zero. The Hamiltonian equations of motion are then integrated until the total kinetic energy attains a maximum value. At this instant, the integration is halted and the momenta of all atoms are again set equal to zero. This procedure is repeated until the system converges to a local potential minimum.

At the equilibrium state, the set of fundamental frequencies and the corresponding zero-point energy are determined, using normal-mode analysis. The calculated values need to be in close agreement with experimental or *ab initio* determined data.

Knowledge of the potential values at the equilibrium geometries for reactants and products, together with the corresponding zero-point energies can be further used to determine the heats of reaction. The necessity of close agreement of the calculated data with theoretical or experimental values represents the fourth test of the potential.

After the results of trajectory calculations on a given potential-energy surface are available, other small modifications of the potential parameters, especially those related to potential barrier, may be necessary in order to adjust the calculated reaction rates to experimental values. However, in these cases, the consequences of energetic parameter modification on the other potential characteristics (see steps 2-4 of the testing procedure) should be reanalyzed.

Classical Trajectory Method

Selection of Initial Conditions. The Projection Method

The first step of classical trajectory calculations is related to the choice of initial conditions. In our studies, we were interested in the investigation of isolated molecular systems with a given total excitation energy, initially distributed over the vibrational degrees of freedom. For this purpose, we have used the projection method proposed by Raff.^{46,47}

The starting point of this method takes into account the fact that the instantaneous Cartesian velocities can be related to the normal mode velocity vectors by a set of normalized projection vectors. In matrix form, this can be

written as

$$\dot{\mathbf{q}}(t) = \mathbf{L} \dot{\mathbf{Q}}(t), \quad (\text{II.16})$$

where \mathbf{L} is the $(3N \times 3N)$ square matrix of the normalized projection vectors, $\dot{\mathbf{q}}(t)$ is a $(3N \times 1)$ column vector whose elements are the Cartesian velocities, and $\dot{\mathbf{Q}}(t)$ is a $(3N \times 1)$ column vector whose elements are the vibrational normal mode, center-of-mass, and rotation velocities. Considering Eq. (II.16), the normal-mode velocities are given by

$$\dot{\mathbf{Q}}(t) = \mathbf{L}^{-1} \dot{\mathbf{q}}(t) . \quad (\text{II.17})$$

The corresponding total kinetic energy $T(t)$ may be written as a superposition of individual mode kinetic energies (T_j):

$$T(t) = \sum_{j=1}^{3N} T_j(t) = \sum_{j=1}^{3N} a_j \dot{Q}_j^2(t) . \quad (\text{II.18})$$

Here the mode constant a_j is defined as

$$a_j = 0.5 \sum_{i=1}^{3N} m_i L_{ij}^2 . \quad (\text{II.19})$$

For the purpose of trajectory calculations, zero-point energy is first inserted into the molecule. This determines the initial normal-mode velocities, from which the initial Cartesian velocities are then computed using Eq. (II.16). The trajectory is then integrated for a random period of time t^* . At this moment,

the trajectory is halted and the instantaneous normal-mode velocities are determined using Eq. (II.17). The system excitation can now be done by pumping a given vibrational mode j with energy E_p , such that its total kinetic energy becomes

$$T_j(t^*) = a_j \dot{Q}_j^2(t^*) + E_p . \quad (\text{II.20})$$

The new normal-mode velocity $\dot{Q}_j'(t^*)$ is then calculated as

$$\dot{Q}_j'(t^*) = \{ [a_j \dot{Q}_j^2(t^*) + E_p] / a_j \}^{1/2} , \quad (\text{II.21})$$

and the corresponding Cartesian velocities are obtained from Eq. (II.16). From this point, taken as the time origin, the dynamics are followed using trajectory integration.

A first advantage of this procedure is that the energy can be initially inserted either at random over vibrational modes, or into a given mode. In addition, this method is very useful for studies related to intramolecular energy transfer rates, which can be determined by monitoring the time variation of the projected normal mode velocities.^{46,47}

Integration of Trajectories

After the selection of initial conditions, the trajectories for a system of N atoms are obtained by integration of the Hamiltonian equations of motion^{1,44}

$$\frac{\partial H(\mathbf{p}, \mathbf{q})}{\partial p_i} = \dot{q}_i \quad (i=1,2,\dots,3N) \quad (\text{II.22})$$

and

$$\frac{\partial H(\mathbf{p},\mathbf{q})}{\partial q_i} = -\dot{p}_i \quad (i=1,2,\dots,3N), \quad (\text{II.23})$$

where $H(\mathbf{p},\mathbf{q})$ is the Hamiltonian of the system, and \mathbf{p} and \mathbf{q} are the set of $6N$ generalized coordinates. Integration can be done using a variety of numerical methods.^{1,2} In our calculations, we have used the fourth-order Runge-Kutta method,¹ in a space-fixed Cartesian coordinate system. The trajectory is integrated until it reaches a region of phase space identified with the product states, or until a maximum time limit is reached.

The equations of motion (II.22) and (II.23) are valid for those cases when the motion of the molecular system is governed only by the interatomic forces derived from the potential-energy surface. However, in some cases it is necessary to impose constraints on some of the internal variables of the system. These constraints require the modification of Hamilton's equations of motion to include the effect of appropriate virtual forces upon the system. This can be conveniently done using Lagrangian multipliers.^{1,44}

For a N -atom system with m constraints written in the form

$$\sum_{i=1}^{3N} a_{ji} \partial q_i = 0, \quad (j=1,2,\dots,m) \quad (\text{II.24})$$

the modified Hamiltonian equations of motion become

$$\frac{\partial H}{\partial p_i} = \dot{q}_i \quad (\text{II.25})$$

and

$$-\frac{\partial V}{\partial q_i} + \sum_{j=1}^m \lambda_j a_{ji} = \dot{p}_i \quad (\text{II.26})$$

where the λ_i ($i=1,2,\dots,m$) are the Lagrangian multipliers. It can be shown¹ that in this case, the general solution of the system (II.25) and (II.26) can be obtained iteratively by determining at each step the values a_{ji} and \dot{a}_{ji} , computing the values of λ_i by solving a set of m linear algebraic equations, and then executing a numerical integration step. The detailed procedure can be found in Refs.1 and 48.

We have used this method to execute damped trajectories with constraints on the bond lengths. If the bond to be constrained connects two atoms (k and l), characterized by the set of coordinates $\{q_{3k+m}\}_{m=1,2,3}$ and $\{q_{3l+m}\}_{m=1,2,3}$, then the coefficients a_{ji} in (II.24) corresponding to this constraint are

$$a_{j,3k+m} = (q_{3k+m} - q_{3l+m})/R \quad (m=1,2,3) \quad (\text{II.27})$$

and

$$a_{j,3l+m} = -a_{j,3k+m} \quad (\text{II.28})$$

with all other $a_{ji}=0$, $i \neq \{3k+m, 3l+m\}_{m=1,2,3}$.

Analysis of Trajectories

In our studies, the analysis of trajectories was primarily related to calculation of first-order rate coefficients, intramolecular energy transfer

analysis, investigation of the reaction mechanism, and final energy distribution over the reaction products. In addition, power spectra calculations of the internal coordinates have been used to qualitatively test the statistical/nonstatistical character of the reactions. We begin this section with a brief presentation of the theoretical environment in which we analyzed the reactions of interest.

RRKM theory

To date, much evidence⁴⁹ shows that the results of classical trajectory calculations of the intramolecular dynamics of vibrationally excited molecules agree with similar data obtained using both quantum mechanics and semiclassical theories. This indicates that when an accurate potential-energy surface is available, classical trajectories can be used to provide accurate information about the type of dynamics obeyed by the system. A particular role is played by classical trajectory calculations in investigation of the unimolecular reaction dynamics.^{1,49,50}

For an ensemble of molecules, each vibrationally excited with energy E , unimolecular decomposition has a random probability⁵¹, such that the number of undissociated molecules $N(t)$ and the probability of decomposition $P(E,t)$ at time t are

$$N(t) = N(0) \exp[-k(E)t] \quad (\text{II.29})$$

and

$$P(E,t) = k(E) \exp[-k(E)t] \quad (\text{II.30})$$

In practical calculations, the rate coefficients $k(E)$ can be extracted by fitting the distribution of lifetimes to equation (II.29), where the number of particles $N(0)$ and $N(t)$ are replaced by the total number of trajectories in the ensemble and the number of undissociated trajectories at time t .

The main theory used to describe the statistical decomposition of unimolecular reactions is that developed by Rice, Ramsperger, Kassel and Marcus (RRKM).⁵²

The reaction scheme used in RRKM theory consists of the following steps:



The mechanisms (II.31) and (II.32) correspond to the activation and deactivation processes of the molecule A . Here $A_{E,dE}^*$ is the concentration of A molecules in the system with energy between $(E, E+dE)$ and M can represent a product molecule or a second molecule of reactant. The process (II.33) shows that from an energized state A^* to products, the molecule should pass through a critical configuration A^+ .

In RRKM theory, the determination of the microscopic unimolecular rate constant $k_a(E^*)$ is based on several assumptions.^{49,52} In contradistinction to RRK theory,⁵² which considers the molecule as an ensemble of classical oscillators, RRKM theory uses the quantum-statistical-mechanic treatment for the normal modes of vibration. It is also assumed that for the molecular

energetical range ($E, E+dE$) there is an equilibrium between the molecules which are and are not in the critical configuration. This implies that the flux from A^+ towards products is equal to the flux from A^+ toward A^* and consequently, the intrinsic rate constant for decomposition of A^* is given by

$$k_a(E) = \frac{v [A^+]}{2 [A^*]} , \quad (II.34)$$

where v is the frequency of passage from A^+ and $[A^+]/[A^*]$ is the concentration ratio of critical configurations to energized molecules. The relation (II.34) is valid in the hypothesis that vibrational energy redistribution within the energized molecule is much faster than the unimolecular reaction. This means that all vibrational quantum states of A^* have equal probabilities per unit time of proceeding to products.

In order to evaluate the k^+ rate, the reaction is considered to take place along a critical coordinate. In this case, the motion along this critical coordinate can be described as a translational motion.

Based on these assumptions, it is shown⁴⁹⁻⁵³ that the general expression for the microscopic unimolecular rate constant has the form

$$k_a(E) = \frac{G^+(E-E_0)}{h N(E)} \quad (E \geq E_0) \quad (II.35)$$

where E_0 is the critical energy for reaction. In Eq. (II.35), $G^+(E-E_0)$ represents the sum of states for the activated complex with energy equal to E and $N(E)$ is the density of states for reactants at total energy E .

In principle, the evaluation of the quantities in (II.35) can be done by exact counting procedures.^{52,53} However, for large values of E , approximate

procedures, such as Laplace inversion of the partition function or empirically fitted functions (for example the Whitten-Rabinovitch approximation) to approximate the results of exact counting, have been developed.^{52,53}

In the study of unimolecular reactions, the RRK expression for the microcanonical rate constant⁵² it is often used:

$$k(E) = \nu [(E-E_0)/E]^{s-1} \quad (\text{II.36})$$

where E_0 is the critical, minimum energy required for dissociation and s is the number of oscillators in the system. In the RRK theory, the molecule is considered to contain s independent oscillators and the unimolecular reaction takes place only if a given oscillator has an energy E larger than the critical amount of energy E_0 .

For unimolecular reactions, the rate coefficients at internal energy E obtained from trajectory calculations can be fitted with an equation of the type (II.36). In this case, the parameter s is the number of "effective" degrees of freedom participating in the reaction, and ν is the frequency factor or high-energy limit of the rate coefficient. The value of the s parameter is related to entropy effects.⁵⁴ For large s values, the internal energy of the system available for motion along the reaction coordinate will tend to spread over more internal degrees of freedom, reducing the probability that a particular coordinate attains the necessary energy E_0 for decomposition.

Non-Statistical Behavior

The basic assumption of RRKM theory is that a complete randomization of the internal energy takes place prior to reaction. This means that the energetically accessible phase space of the system is fully explored on a time

scale that is short relative to the reaction time.

It is clear that when transitions between vibrational states of a molecule are slower than transitions leading to products, an "intrinsic" nonstatistical behavior occurs.^{49,50} This is equivalent to the fact that the molecular phase space presents at least one additional bottleneck other than the one defining the critical configuration. Examples of such systems are low-barrier processes in conformer transformations.^{55,56}

Nonstatistical behavior can also be found for nonrandom excitation of the molecular vibrational states. This case was called "apparent" non-RRKM behavior by Hase and Bunker.⁵⁷ If the RRKM model were valid for these cases, the randomization of the initial vibrational excitation energy would take place in a negligibly short time period. However, in practical cases it was found that the probability of a short lifetime with respect to reaction can be enhanced or reduced, depending on the initial location of the excitation energy within the molecule. Examples of both intrinsic and apparent non-RRKM unimolecular reactions can be found in Refs. 49,50,57.

It is important to point out that the existence of an energy-decay rate out of a given bond that is fast relative to the unimolecular reaction rate is not a sufficient condition to guarantee that the statistical dynamics assumption will hold. That is for a particular molecular system, it might be found that the intramolecular vibrational rate out of a given set of modes is fast relative to the unimolecular reaction rate but that the energy remains confined within a small subset of modes rather than becoming completely randomized over all internal degrees of freedom. In such a case, non-statistical dynamics will be the results. For example, it was found^{47,54,58-61} that the unimolecular bond cleavage processes in disilane and 1,2-difluoroethane are nonstatistical even though the reaction rates were much smaller than the intramolecular energy transfer rate

out of Si-H, C-F, or C-H vibrational modes.

In a comparative study of statistical and nonstatistical behavior for bond fission reactions in 1,2-difluoroethane, disilane and the 2-chloroethyl radical, Sewell *et al.*⁶² presented some general factors favoring nonstatistical dynamics in large polyatomic molecules. These factors are:

(1) The internal energy is close to the dissociation threshold. This case takes place for polyatomic molecules where the ergodic threshold is significantly above the dissociation limit.

(2) Motion along the reaction coordinate does not produce large energetic changes in one or more bonds in the remainder of the molecule. For the systems where such energetic changes takes place, there is an increased coupling between the reaction coordinate and the remainder of the molecule. This leads to increased intramolecular vibrational rates and a corresponding decrease in the reaction rates, which diminish the nonstatistical effects.

(3) There exists a formation coordinate for the activated reactant that is strongly coupled to the dissociation coordinate, but only weakly coupled to the other internal coordinates of the molecule. This principle has been initially introduced by Newmann-Evans *et al.*⁶³ to explain the nonstatistical behavior of the branching ratio of the products obtained in thermal rearrangement of 1- and 2-phenylbicyclo[2.1.1]hex-2-enes-5-d and trans-2-methyl-1-(trans-2-phenyl ethenyl)cyclopropane. It was argued⁶³ that, if the reaction coordinate for formation of the intermediate were weakly coupled to all of the exit channels, it would be expected that statistical selection of the channels took place, as predicted by the RRKM theory.

Detailed analysis of the factors above presented for different experimental and theoretical studies of nonstatistical reactions can be found in Ref. 62.

Mode Energies

A problem of prime interest in classical dynamical studies is related to determination of the temporal variation of mode energies and calculation of the intramolecular energy transfer rates.^{46,47,59,64-67} In the bond or local-mode energy formulation,^{59,64-67} the main difficulty is related to the arbitrary definition of the bond energy, which generally assumes a mode separability which does not exist. In other words, many of the potential coupling terms involving the mode coordinates are eliminated. In particular cases when the potential or kinetic energy includes large coupling terms, the temporal variation of the mode energy may not accurately represent the actual intramolecular energy transfer that takes place.

An alternative procedure, which eliminates the necessity of arbitrarily defining a bond or mode energy was introduced by Raff.^{46,47} The idea of the method is to use the kinetic energy, represented in the normal mode velocity system, instead of the total energy. This eliminates the influence of the potential-energy function coupling terms. The representation of kinetic energy in normal mode velocity coordinates can be done using the previously described projection method. In this case, the kinetic energy is diagonal and consequently, there are no coupling terms. The intramolecular energy transfer can be analyzed as a function of the time variation of the projected normal mode velocities. The total average energy in a given mode is then determined using the virial theorem, which states that the average total energy is equipartitioned between the kinetic and potential energy. From relation (II.18), the average total energy in a mode i is calculated as

$$\langle E_i \rangle_{t=t^*} = 2[\Delta t]^{-1} \int_{t_0}^{t_0+\Delta t} T_i(t) dt = 2[\Delta t]^{-1} \int_{t_0}^{t_0+\Delta t} a_i \dot{Q}_i^2(t) dt, \quad (II.37)$$

where t^* represents a time in the interval $t_0 < t < t_0 + \Delta t$.

We used this method to follow the intramolecular energy flow in bicyclo(2.1.0)pentane after the initial excitation of the flap mode. At given time intervals during trajectory calculations (generally 10 time units (t.u.), where 1 t.u. = 1.018×10^{-14} sec.), the trajectory is halted and the normal mode velocities $\dot{Q}(t)$ and individual mode kinetic energies are computed based on Eqs. (II.17) and (II.18). The time dependence of the mode kinetic energies makes it possible to follow the pathways of intramolecular flow and estimate the flow rates.

Power Spectra

A convenient way to obtain a more realistic description of the vibrational frequencies of a given molecule is the use of power spectra. In contradistinction to normal-mode analysis which provides a correct description of vibrations only at small energies, the use of power spectra is adequate independent of energy. This makes power spectra a useful tool in dynamical studies.

Noid *et al.*⁶⁸ used the vibrational classical trajectories of anharmonic molecules to obtain the power spectrum of the dynamical variables. It was shown that in the vibrational quasiperiodic regime, the spectrum consists of sharp lines at the frequencies of the underlying molecular motions, while in the ergodic regime the spectral lines are broad, with intensity spread over a wide band of frequencies. Based on these characteristics, it results that power spectra can be used to qualitatively investigate the phase space structure of

molecules.

Sewell *et al.*⁶⁹ have shown that for the polyatomic molecules C₂H₄, SiH₄ and CH₃ONO, the spectral mode identity is retained even well above the threshold for dissociation, such that the dynamics of these systems is not fully ergodic. Chang *et al.*⁷⁰ have used power spectra as a diagnostic tool to identify the presence of nonstatistical dynamics. For the 2-chloroethyl radical, known to exhibit statistical dynamics,⁶² the spectrum appears diffuse with a nearly complete loss of isolated structures at energies near or above the threshold. These characteristics were attributed to a very high level of mode-to-mode coupling and large intramolecular vibrational redistribution rates. On the other side, for 1,2-difluoroethane which exhibits a nonstatistical dynamics,⁴⁷ the power spectrum maintains its discrete, isolated character of spectral bands.

Two different methods can be used to calculate the power spectrum of a given dynamical variable $q(t)$.^{62,68} The first procedure is to evaluate the Fourier transform of the autocorrelation function

$$I_c(\omega) = \left[\int_{-\infty}^{\infty} C(\tau) \exp(-i\omega\tau) d\tau \right], \quad (11.38)$$

where $C(\tau)$ is the ensemble averaged autocorrelation function

$$C(\tau) = \langle x(0) x(\tau) \rangle . \quad (11.39)$$

The second procedure is based on the use of finite Fourier transform of the variable $q(t)$

$$I_q(\omega) = \lim_{T \rightarrow \infty} \frac{1}{T} \left[\int_{-T}^T q(t) \exp(-i\omega t) dt \right]^2 . \quad (11.40)$$

For a quasiperiodic system, it can be shown that in the limit $T \rightarrow \infty$ the quantities (II.38) and (II.40) are identical.⁶⁸ Specific algorithms to evaluate either (II.38) or (II.40) can be found in Ref. 71.

We have calculated the power spectra from classical trajectories by recording the time history of the internal coordinates from single trajectories and by Fourier transforming the set of reduced coordinates. The composite spectrum was then determined as a superposition of the power spectrum of individual spectra. The detailed aspects of this method are given in Chapter IV.

Variational Phase-Space Theory Methods

A systematic method to estimate the reaction rates for classical systems is represented by the variational theory of reaction rates.⁷² The basic idea of this theory is that a reacting system can be described by the motion of a representative point in the phase space of the system. For this purpose, the phase space is divided by a trial surface into regions which correspond approximately to reactants and products. Evaluation of the flux at which representative points pass through this surface in one direction will give a measure of the reaction rate. Since a necessary condition for a reaction to take place corresponds to crossing the trial surface at least once, it results that this method gives an upper limit to the true classical rate. In practical calculations, a set of different dividing surfaces dependent on a set of parameters is chosen. The minimum flux obtained from this set of surfaces represents the best approximation of the true reaction rate for the given range of parameters variations.

In the case of an ensemble of systems, each containing n classical particles, the variation of the number of systems, $N(i)$, which are in a given chemical state i is given by

$$\frac{\partial N}{\partial t} = - \int_{\Omega(i)} \text{div}(\rho \mathbf{v}) d\Omega = - \int_{S(i)} \rho(\mathbf{v} \cdot \mathbf{n}) dS \quad (\text{II.41})$$

where $\Omega(i)$ is the phase space corresponding to state i , $S(i)$ is the surface bounding $\Omega(i)$, $\rho = \rho(\mathbf{p}, \mathbf{q})$ is the density of representative points in the 6n-dimensional phase space, and \mathbf{n} is the unit outward normal to dS . Here the number of systems $N(i)$ is determined by

$$N(i) = \int_{\Omega(i)} \rho d\Omega . \quad (\text{II.42})$$

The reaction rate at which the representative points cross the boundary between state i and final states f can be written as

$$K = \frac{\int_{S(f,i)} \rho(\mathbf{v} \cdot \mathbf{n}) dS}{N(i)} = \frac{\int_{S(f,i)} \rho(\mathbf{v} \cdot \mathbf{n}) dS}{\int_{\Omega(i)} \rho d\Omega} \quad (\text{II.43})$$

where $S(f,i)$ is that part of the boundary on which $(\mathbf{v} \cdot \mathbf{n}) > 0$.

We assume that the internal degrees of freedom of the reactants are in local equilibrium and can therefore be described by a Boltzmann distribution

$$\rho = \rho_0 \exp(-H/k_B T) , \quad (\text{II.44})$$

where H is the Hamiltonian of the system.

Combining Eqs. (II.43) and (II.44), it results

$$K = \frac{\int_{S(f,i)} \exp(-H/k_B T) (\mathbf{v} \cdot \mathbf{n}) dS}{\int_{\Omega(i)} \exp(-H/k_B T) d\Omega} \quad (II.45)$$

A first requirement to evaluate the minimum flux as described by (II.45) is the choice of the dividing surface in phase-space $S(f,i)$ between the reactants and products. In the general case, this surface is expressed as a function of the $6n$ coordinates and momenta that define the phase-space of the system and the flux should be minimized with respect to this function. However, due to large computational requirements necessary to solve numerically such problems, approximate forms of the dividing surfaces have been considered.

In a study of recombination and desorption of hydrogen on Si(111) surface⁷³, the dividing surface has been determined as a linear combination of coordinates that describe the motions of adatoms relative to the Si(111) surface. Particularly, only the normal distance of the H_2 center-of-mass to the surface and the H-H separation have been considered in definition of the dividing surface. Rice *et al.*⁷⁴ have employed circular cylinder, elliptical cylinder and hyperbolic cylinder dividing surfaces to determine the jump frequencies of hydrogen atoms on the Si(111) surface. It was found⁷⁴ that the minimum flux determined using circular cylinders is approximately 50 % larger than those for elliptical and hyperbolic cylinders. Ford *et al.*⁷⁵ have employed spherical dividing surfaces in a study of oxygen atom diffusion in Ar and Xe faced-cubic-centered matrices. The examples presented above show that in practical cases, simplified types of dividing surfaces, which are adapted to the symmetry of the problem investigated, can be used.

In addition to the decision of the optimum dividing surface, the next

important step in evaluation of the rate constant is related to the calculation of the multidimensional integrals involved in Eq. (II.45). Monte Carlo methods provide a convenient procedure to approximate these multidimensional integrals. These methods are described in the next paragraph.

Monte Carlo Methods

Importance sampling

Monte Carlo procedures employ stochastic methods to estimate the values of multidimensional integrals.¹⁰ Such an integral of interest is that represented in Eq. (II.45), but equally important are the thermodynamic averages of an observable for a given ensemble. We detail the analysis for the case of a system of particles in the canonical ensemble. In this case, the expectation value of a given observable $F(\mathbf{q})$ has the form

$$\langle F \rangle = \frac{\int_{\Omega} F(\mathbf{q}) \exp(-H(\mathbf{q})/k_B T) d\mathbf{q}}{\int_{\Omega} \exp(-H(\mathbf{q})/k_B T) d\mathbf{q}} \quad (\text{II.46})$$

where $H(\mathbf{q})$ is the Hamiltonian of the system. Here \mathbf{q} denotes a representative state in the phase space Ω . The simple Monte Carlo approximant of (II.46) is calculated as

$$\langle F \rangle \approx \frac{\sum_{\mathbf{v}} F(\mathbf{q}_{\mathbf{v}}) \exp(-H(\mathbf{q}_{\mathbf{v}})/k_B T)}{\sum_{\mathbf{v}} \exp(-H(\mathbf{q}_{\mathbf{v}})/k_B T)}, \quad (\text{II.47})$$

where a set of random points in the phase-space are chosen, instead of using a regular set of points (as in common integration methods). However, this method is not useful due to the fact that the Boltzmann factor $\exp(-H(\mathbf{q}_v)/k_B T)$ has a very rapid variation with $H(\mathbf{q}_v)$. Since only configurations with low energies make a significant contribution to the average (II.47), these configurations are unlikely to be found in a reasonable calculation time.

The alternative procedure to the evaluation of integrals such as (II.46) is to concentrate the sampling in the regions of the phase space which have the most important contribution to the integrals. This can be done using the "importance sampling" procedure.^{1,10} In this case, the points in phase space are selected not totally at random, but based on a probability distribution $P(\mathbf{q}_v)$. In this case, (II.47) can be written as

$$\langle F \rangle \approx \frac{\sum_v [F(\mathbf{q}_v) / P(\mathbf{q}_v)] W(\mathbf{q}_v)}{\sum_v [1 / P(\mathbf{q}_v)] W(\mathbf{q}_v)} \quad (\text{II.48})$$

where the weight function $W(\mathbf{q}_v)$ is defined as

$$W(\mathbf{q}_v) = N_w \exp(-H(\mathbf{q}_v)/k_B T) P(\mathbf{q}_v). \quad (\text{II.49})$$

In (II.49), N_w represents a normalization constant. The specific form of the probability distribution $P(\mathbf{q}_v)$ depends on the particular system analyzed, so that two important cases are further considered.

When the equilibrium properties of the total system are of interest, the simplest choice of probability $P(\mathbf{q}_v)$ is an analytical form proportional to the equilibrium Boltzmann distribution for state \mathbf{q}_v

$$P(\mathbf{q}_v) \sim \exp(-H(\mathbf{q}_v)/k_B T). \quad (\text{II.50})$$

In this case, the points are evenly weighted and the Monte Carlo approximant (II.48) reduces to the simple arithmetical average

$$\langle F \rangle = \frac{1}{M} \sum_{v=1}^M F(\mathbf{q}_v) \equiv \bar{F}, \quad (\text{II.51})$$

where M is the number of phase space points used for average.

The general method to choose phase space points \mathbf{q}_v with probability given by (II.50) is to perform a Markov walk, for which a specified transition probability $\Gamma(\mathbf{q}_v \rightarrow \mathbf{q}_{v'})$ characterizes the passage from one phase space point \mathbf{q}_v to another $\mathbf{q}_{v'}$. It should be noted that the probability of transition in a given step ($i+1$) of a Markov chain is a function of the state at the i th step.

It can be shown⁷⁶ that a sufficient condition that the probability $P(\{\mathbf{q}_v\})$ converges toward $P_{\text{eq}}(\{\mathbf{q}_v\})$ is given by the detailed balance condition

$$\Gamma(\mathbf{q}_v \rightarrow \mathbf{q}_{v'}) \exp[-H(\mathbf{q}_v)/k_B T] = \Gamma(\mathbf{q}_{v'} \rightarrow \mathbf{q}_v) \exp[-H(\mathbf{q}_{v'})/k_B T] \quad (\text{II.52})$$

Due to the fact that this equation does not determine uniquely the transition probability,⁷⁶ a possible choice is given by

$$\Gamma(\mathbf{q}_v \rightarrow \mathbf{q}_{v'}) = \begin{cases} \exp(-\delta H/k_B T) & \text{if } \delta H > 0 \\ 1 & \text{otherwise,} \end{cases} \quad (\text{II.53})$$

where $\delta H = H(\mathbf{q}_{v'}) - H(\mathbf{q}_v)$. This sequential Markov walk procedure is known as Metropolis sampling.¹⁰

In practical calculations, a trial configuration in phase-space is generated by randomly modifying the canonical coordinates of one or more particles of the system. The change in system energy due to this trial move is evaluated. If the energy is decreased, the move is accepted. If the energy is increased by an amount δH , the move is accepted with the probability $\exp[-\delta H/k_B T]$. It is generally accepted⁷⁷ that the most rapid convergence for Metropolis walks occurs when the acceptance ratios are approximately 50% of the number of trial configurations.

Another important situation considered here is the evaluation of the total flux of a representative phase-space point across a theoretical dividing surface (see Eq. (II.45)), in the case of a process which simulates the diffusion of a particle between two adsorption sites. In this case, we assume that the potential terms are functions only of the interparticle distances and that the total Hamiltonian of the system can be separated as

$$H = H' + V_i, \tag{II.54}$$

where V_i is the interaction potential of the diffusing particle with the system (for example a lattice-gas potential interaction) and H' includes the rest of the total Hamiltonian terms.

In this case, the choice of the probability distribution $P(\mathbf{q}_v)$ in Eqs. (II.48) and (II.49) is done such that the states corresponding to the diffusion barrier, rarely accessible with unbiased sampling, become freely accessible. This can be done by selecting the probability distribution as^{74,75}

$$P(\mathbf{q}_v) \sim \exp[V_i / k_B T]. \tag{II.55}$$

In order to sample phase space points with this probability, the previously described Markov walk procedure can be used, the total Hamiltonian H in (II.53) being replaced with H' from Eq. (II.54).

Significant simplifications in the flux calculation are obtained in the case of spherical or cubic dividing surfaces, when integrals over momenta can be performed analytically and the Markov walk is considered only in the configuration space. Details of this procedure are presented in Chapter III.

Several applications of Monte Carlo sampling techniques have been reported. Doll⁷⁸ has adapted a Monte Carlo sampling technique to calculate the unimolecular rate constant. Viswanathan *et al.*⁷⁹ have applied the Metropolis Monte Carlo sampling procedure to evaluate the microcanonical rate coefficients for unimolecular dissociation of CH_4 and SiH_4 systems. A large number of recombination, desorption and surface-diffusion studies^{73,74,79-85} have employed Monte Carlo techniques in connection with variational phase-space theory methods. Extensions of Monte Carlo methods for grand-canonic or isothermal-isobaric ensembles have also been considered.^{10,76,86}

We used the Monte Carlo method with importance sampling incorporated to evaluate the classical jump frequencies of hydrogen atoms between different binding sites on $\text{Si}(111)-(7 \times 7)$ reconstructed surface. The results obtained in this case are given in Chapter III.

CHAPTER III

DIFFUSION OF HYDROGEN ATOMS ON A SI(111)-(7X7) RECONSTRUCTED SURFACE: MONTE CARLO VARIATIONAL PHASE-SPACE THEORY

Introduction

Understanding of the elementary processes involved in the chemistry occurring on silicon surfaces is a goal of great importance in modern surface science. These processes include surface chemisorption, dissociation, diffusion, chemical reaction and desorption. While molecular adsorption and desorption are related to the variation of the potential in a direction perpendicular to the surface, surface diffusion is dependent on the variation of the potential parallel to the surface, which is generally different on different crystal faces. Surface diffusion of chemisorbed atoms is particularly important in phenomena such as growth of crystals and thin films, heterogeneous catalysis, sintering and corrosion. Consequently, this subject has generated considerable interest, both for experimental and theoretical investigations.^{74,84,85,87-99}

In this chapter we present the theoretical study performed by us to investigate hydrogen-atom diffusion on a Si(111)-(7x7) reconstructed surface.¹⁰⁰ The favorable premises to perform such a study are multiple.

The first element is related to the existence since 1986, after more than 27 years of experimental and theoretical research, of a well defined model for

the Si(111)-(7x7) reconstructed surface, which today has received almost total support of surface scientists.⁹⁹ This is the dimer-atom-stacking fault (DAS) model, created by the group of Kunio Takayanagi^{101,102} based on transmission electron diffraction studies. It is important to note that essential elements of the DAS model were incorporated from other experimental and theoretical studies, i.e., the model of 12 adatoms per 7x7 unit cell introduced by Binnig *et al.*,¹⁰³ dimerization of the second layer atoms suggested by McRae *et al.*¹⁰⁴ and the stacking-sequence faults introduced by Bennet *et al.*¹⁰⁵

Because silicon is a key element in the microelectronic industry and fabrication of the microstructural circuits is largely dependent on the processes taking place at surfaces, there is also a continuous interest of the scientific community in the investigation of the elementary chemical-reaction processes on silicon surfaces. A recent review of chemical processes of atoms and molecules on silicon surfaces can be found in Ref. 106. Of particular importance to our investigations is the experimental study performed by Reider *et al.*,¹⁰⁷ in which the essential data related to hydrogen-atom diffusion on Si(111)-(7x7) reconstructed surface have been reported.

In Chapter II, it was noted that accurate dynamics studies require the development of an accurate potential-energy surface for the system. Bolding and Andersen¹⁰⁸ have developed such a potential for silicon systems. This potential represents a generalization of the Tersoff form,¹⁰⁹ with the interaction between a pair of atoms depending on the environment of the pair. This potential is equally useful for small clusters of 2-10 atoms, crystal phases and the 2 x 1 and 7x7 reconstructions of Si(111) surfaces.

Based on these considerations, we proceeded to investigate theoretically the interaction potential for the H atom-Si(111)-(7x7) reconstructed surface and to analyze the diffusion process on this surface.

Before presentation of the potential-energy surface, computational methods and results of this study, we review in the next section the essential experimental and theoretical data on which our study was based. These data make reference to the DAS surface model, to energetic and spectroscopic data related to H-lattice interactions, to experimental diffusion studies reported by Reider *et al.*¹⁰⁷ and to other theoretical investigations of chemical processes of hydrogen on Si(111) surface.⁷⁴

DAS Lattice Model

It is well known that in order to minimize the surface free energy, the semiconductor surfaces reconstruct, leading to structures significantly different from the corresponding bulk terminated surface. In the case of silicon, after cleaning in ultrahigh vacuum and cleavage, the Si(111) surface shows a (2x1) reconstruction pattern which transforms irreversibly into the (7x7) structure upon annealing above 390°C.⁸⁹ Heating the surface above 890°C produces a reversible phase transition from Si(111)-(7x7) to a Si(111)-(1x1) structure. The Si(111)-(7x7) is the most stable phase of the Si(111) surface¹¹⁰ and has a unit cell 49 times larger than the ideal unreconstructed 1x1 surface. Since the discovery of the (7x7) reconstruction of the Si(111) surface by low-energy electron diffraction (LEED) in 1959,¹¹¹ dozens of theoretical and experimental studies have been reported to explain the properties of this surface.^{101,102,110-116} Here, we describe only the generally accepted model for the Si(111)-(7x7) surface, i.e., the DAS model proposed by Takayanagi *et al.*^{101,102}

In this model, schematically shown in Figs. 1-3, there are 12 adatoms, 6 rest atoms, 9 dimers, and one corner hole per surface unit cell. In one half of the unit cell delimited by the short diagonal, there is a stacking fault. The DAS model contains only 19 dangling bonds in the (7x7) unit cell, instead of 49 in the

unreconstructed surface. The number of dangling bonds is the smallest among various proposed models.¹¹⁶ Of these bonds, 12 are in the top layer (adatom layer), 6 are in the second layer (stacking fault layer) on atoms which are not bonded to the adatoms, and one is in the fourth layer, corresponding to the atom below the vacancy at the corner.

Using the terminology adopted in Ref. 102, the adatoms in the first reconstructed layer (see Figs. 1 and 2) have a 2 x 2 structure at A sites. The atoms of the first reconstructed layer (Figs. 1 and 2) are located at C sites in the left subcell and at B sites in the right subcell. The third layer of the structure (see Figs. 1 and 3) is also a reconstructed layer. It contains two groups of 15 atoms at A sites and 9 dimers on the sides of the triangular subcells. The next layers of the structure are unreconstructed, with the normal sequence as in the bulk Si(111) structure. Atoms in the first unreconstructed layer (small dark circles in Figs 1 and 3) occupy A sites, while those in the next unreconstructed layer (small dots in Fig. 1) sit on "c" sites. The atoms in the right subcell are stacked with normal sequence, cAaB+adatoms, while the atoms in the left subcell are stacked with a faulted sequence, cAa/C+adatoms, where the slant indicates the stacking fault. For a more detailed description, a side view of this model can be found in Ref. 101 and 102.

Since the DAS model was proposed by Takayanagi *et al.*^{101,102}, several different experiments have illustrated its basic correctness. For example, the model was confirmed by scanning tunneling microscopy (STM) studies¹⁰³ which revealed 12 protrusions inside the surface unit cell and deep holes in the corners, corresponding to the adatoms and corner vacancies. The presence of stacking fault islands, of the 12 adatoms and one corner vacancy were also supported by the X-ray diffraction measurements of Robinson *et al.*¹¹³ Qian and Chadi¹¹⁵ have used the Keating model¹¹⁷ to calculate the total energies

for the class of $(2n+1) \times (2n+1)$ reconstructed (111) surfaces. They have found that inside this class of surfaces, the DAS model has the lowest surface energy. The existence of a minimum surface energy for 7x7 structure relative to other types of reconstructed surfaces, such as 5x5 and 3x3, has been recently confirmed by massive parallel *ab initio* calculations with supercells approaching 1000 atoms.^{116,118}

Selected Data on Elementary Chemical Processes of Hydrogen on Si(111)-(7x7) Surfaces.

The high interest in understanding of the interactions of hydrogen atoms with silicon surfaces is motivated by several factors. A first reason is due to the fact that understanding of hydrogen behavior on these surfaces can give a deeper insight into many of the gas-semiconductor interactions. As the smallest adsorbate, hydrogen can be found in various surface reactions. For example, species like H₂O, NH₃, PH₃, C₃H₆ and SiH₄ are known to chemisorb dissociatively on silicon surfaces and form silicon-hydrogen bonds.^{93,119} Below the hydrogen desorption temperature, these reactions are often rate determined by hydrogen desorption.

An additional factor of interest is related to the possibility of significant modification of the properties of the silicon surface by hydrogen atoms. For example, the density of defect states in the band gap of amorphous silicon can be reduced by saturating the silicon dangling bonds with hydrogen.¹²⁰ Processes like growth kinetics, or the stability of amorphous silicon are greatly influenced by the hydrogen content.⁹³

Another reason for studying the H-Si lattice interactions is based on the fact that the nature of binding sites on silicon surfaces can be inferred from the chemistry of H on Si(111)-(7x7). Due to the fact that the reconstruction of silicon

surfaces results in formation of strained bonds which are weaker than those in bulk, these bonds are most easily attacked by adsorbates. Consequently, the reactivity of surfaces can be directly related to the relaxation of the strained bonds formed by reconstruction.⁹²

The nature of the hydride species on the hydrogenated Si(111)-(7x7) surfaces has been investigated in a large number of studies.^{92,119-124} It is now accepted that, depending on temperature and hydrogen exposure level, mono-, di- and trihydride species may be present on the surface.⁹² In the low coverage regime, H atoms are adsorbed on the adatoms sites and passivate the dangling bonds, with formation of adatom monohydrides as the dominant species.¹²⁴ At higher coverage, the relaxation of adatoms takes place, either by insertion of H atoms into the backbonds of these atoms or by formation of adatom islands.^{92,124} At low temperatures and high exposures, the insertion process takes place with the formation of adatom dihydride and ultimately, of unstrained trihydride species. At higher temperatures, the adatoms may diffuse over the surface and new Si-Si bonds between atoms can be formed. This process can further lead to formation of adatom islands.^{92,124} A further increase in temperature determines relaxation of the rest-atom layer, with formation of a structure similar to that of the unrelaxed bulk (which is covered only by monohydride species).

Additional fundamental data regarding the kinetics of H atoms on Si(111)-(7x7) surfaces can be gathered by desorption studies.^{92,93,119,126-129} Two different desorption states have been identified: β_2 , which has a maximum desorption rate at about 680 K and β_1 with a maximum at 810 K.¹²⁷ The desorption peak corresponding to the β_2 state was attributed to the decomposition of the di- and trihydride species,^{122,124} while the β_1 state is related to the decomposition of the monohydride species. These studies reveal

that at high coverage, H₂ desorption (β_1 state) from the Si(111)-(7x7) surface follows second-order kinetics, with an activation barrier in the range 59 to 62 kcal/mol.^{93,119,127} For the case of low coverage ($\theta < 0.3$ ML) an intermediate desorption order of $n=1.56$ has been reported, together with an activation barrier of 55 kcal/mol.¹²⁸ Based on the similarities of rovibrational-states distributions of H₂ desorbed from both Si(100)-(2x1) and Si(111)-(7x7), Zare *et al.*¹²⁹ suggested that desorption of hydrogen can be described as a recombinative process localized over a single atom.

Knowledge of the experimental activation barrier for desorption of H₂ from the Si(111)-(7x7) surface can be further used to determine an upper limit for the silicon-hydrogen bond strength. Indeed, the binding energy can be approximated as $E_{\text{Si-H}}=(E_d+E_{\text{H-H}})/2$, where E_d is the activation barrier of desorption (assumed to be equal with the heat of adsorption) and $E_{\text{H-H}}$ is the experimental dissociation energy of H₂ (=4.477 eV).¹²⁶ In this calculation, it is assumed that there is no barrier to H₂ adsorption. However, theoretical calculations by Raff *et al.*⁸⁵ predicted an activation barrier of 4.2 kcal/mol for H₂ adsorption on Si(111). Without considering this activation barrier, the binding energies determined using the above relation are overestimated. A list of binding energies for the Si-H bonds determined in different experimental studies is given in Table I.

Direct identification of the types of hydride species existent on Si(111)-(7x7) surfaces can be obtained using infrared spectroscopy, high resolution electron loss spectroscopy and monochromatic low-energy electron diffraction techniques.^{107,121-123,132-134} The results of these studies show that the scissoring and stretching modes of the SiH₂ species are placed in the range 880-900 cm⁻¹ and 2064-2110 cm⁻¹, respectively, while for SiH₃ species, the deformation modes are identified around the 872 cm⁻¹ spectral line. For the

silicon monohydride, the bending and stretching vibrations are found in the range 630-637 cm^{-1} and 2057-2100 cm^{-1} , respectively. Selected values of the vibrational modes of Si-H, determined using different experimental and theoretical methods, are presented in Table I.

Observation of the vibrational stretching modes of silicon monohydride by infrared spectroscopy^{122,133,134} has provided evidence of the existence of different features as function of hydrogen coverage. At low coverages (0.05 ML), a sharp absorption doublet in the region 2076 cm^{-1} (see also Table I) was found to belong to Si-H species, which have the dipole moment perpendicular to the surface. The presence of the doublet was attributed to the existence of different binding states on the Si(111)-(7x7) surface. However, there is not yet a clear identification of these binding states.¹³⁴ Upon increasing the hydrogen exposure, the presence of the doublet is maintained, but in this case, the dipole moment has a component parallel to the surface. Correspondingly, the monohydride species have been identified as tilted species (t-SiH) (see Table I). This fact was considered a consequence of the modification of the orientation in the average Si-H bond axis due to the increasing number of broken Si-Si bonds with increasing hydrogen coverage.¹³⁴ However, it is not clear if some of the tilted monohydrides are not formed as a result of defect sites or of the surface preparation method.¹²⁴

The observation of thermal recombinative desorption of H_2 from Si(111)-(7x7) surface is an indication that hydrogen diffusion on this surface can take place.

A direct quantitative characterization of this process was done by Reider *et al.*⁹⁴ They have investigated the diffusion of H atoms on the Si(111)-(7x7) surface through optical second-harmonic diffraction from a submonolayer grating of adsorbed hydrogen. The hydrogen adsorbate grating was formed

through laser-induced thermal desorption in the field of two interfering laser beams ($\lambda=532$ nm). In this technique, the laterally averaged hydrogen coverage can be monitored from the diffracted second-harmonic signal.⁹⁴ It was found that the thermally activated diffusion process had a barrier of $E_a=1.5\pm 0.2$ eV and a preexponential factor D_0 of 10^{-3} cm²/s.

The large value of the activation energy found in this study gives a measure of highly localized bonds as compared with the case of metal surfaces. However, the activation energy of H diffusion is significantly lower than that for desorption (~ 2.48 eV). On the other hand, the measured prefactor D_0 is comparable to that found for hydrogen on metal surfaces such as W(111), W(110) and Pt(111).¹³⁵

In contradistinction to metallic surfaces, the diffusion of H on the Si(111)-(7x7) surface exhibits negligible quantum effects. Indeed, Reider *et al.*⁹⁴ have shown that tunneling processes are not expected to give a contribution to diffusivity larger than 10^{-15} cm²/s at 690 K, due to the existence of a large potential barrier.

The theoretical investigation of the recombination and desorption of hydrogen from an ideal Si(111) surface was performed by Raff, NoorBatcha and Thompson,⁷³ based on Monte Carlo variational transition-state theory. From analysis of the potential surface, a barrier of 2.52 eV for H₂ recombination/desorption and a 0.182 eV barrier to the back reaction were found. In addition, the activation parameters, determined from an Arrhenius plot of the minimized flux, were determined as 2.41 eV for the activation energy and 0.202 cm²/s for the frequency factor.

The dynamics of scattering and dissociative chemisorption of atomic hydrogen from fully and partially covered Si(111) surfaces have been investigated by Rice, Raff and Thompson¹³⁶ by the classical trajectory method.

The energy and spatial distribution of hydrogen atoms scattered from the surface, the sticking probabilities and the mechanism of adsorption were studied as functions of initial azimuthal angle and surface coverage. The energy transfer from highly excited chemisorbed hydrogen atom to the surface was found to be a first-order process with a rate coefficient of $1.74 \times 10^{12} \text{ s}^{-1}$.

The thermal diffusion of H atoms on a Si(111) surface with partial hydrogen coverage was done by Rice, Raff and Thompson.⁷⁴ The potential-energy surface used describes two kinds of binding sites, a covalent Si-H bond (top site) and an interstitial threefold bonding site (open site). Based on Monte Carlo variational phase-space theory, the calculated diffusional barriers between the two binding sites were found equal to 2.72 and 0.59 eV for top-to-open site and open-to-top site jumps, respectively. Due to the small width of the potential barrier, tunneling effects were found to give a significant contribution to the total diffusion rates at low temperatures (300 K). However, these contributions are sharply diminished with increasing the surface temperature.

General Computational Model

We have extended the previously described theoretical studies to the theoretical investigation of H-atom diffusion on Si(111)-(7x7) reconstructed surface by the aid of variational phase-space theory methods. For this purpose, we have employed the general methods presented in Chapter II to construct a semiempirical potential-energy surface for hydrogen-lattice interaction. Canonical Markov walks with importance sampling were used to evaluate the flux across a set of dividing surfaces separating different adsorption sites. The minimum jump frequencies were then used as input to a set of coupled phenomenological kinetics equations that describe the diffusion rates of

adatoms between adjacent adsorption sites. The activation energy and the diffusion coefficients at 300, 500 and 800 K were determined and compared to experimental data. Calculated upper limits for the tunneling rates at 300, 500, and 800 K show that tunneling processes make only a small contribution to the total diffusion rate.

Together with other similar studies,^{73,74,83-85,95-98} this work was designed to provide a deeper understanding of the elementary processes involved in the interaction of H, H₂, SiH, and SiH₂ molecules with Si surfaces.

In our calculations, we have used a 292-atom lattice model for the Si(111)-(7x7) surface containing all the atoms inside the (7x7) unit cell and the first ring of atoms outside the (7x7) unit cell, positioned in four layers. Of these atoms, 24 are in the first layer, 76 in the second layer, 94 in the third layer, and 98 in the fourth layer. The 54 atoms inside the (7x7) unit cell in the first two layers are allowed to move. All other silicon atoms remain fixed in their equilibrium positions.

For the purpose of future reference, the configuration of the 162 atoms with dangling bonds in the first two layers contained in 9 adjacent unit cells on the (7x7) DAS surface is presented in Fig. 4.

Potential-Energy Surface

We assume that the potential-energy surface that describes the H-Si(111)-(7x7) system can be written in the separable form

$$V = V_L + V_{gL}, \tag{III.1}$$

where V_L is the interaction between the lattice atoms and V_{gL} is the hydrogen-lattice atoms interaction potential. The functional form of V_L was developed by

Bolding and Andersen (BA)¹⁰⁸ as a generalization of Tersoff's potential¹⁰⁹ to describe silicon clusters, crystals, and surfaces.¹⁰⁸ In particular, it was shown¹⁰⁸ that the BA potential successfully modeled the (7x7) reconstructed Si(111) surface. The parametrization of the potential was done by fitting a variety of data on silicon, including the equilibrium geometries and energies of silicon clusters with 2-10 atoms and the static properties of the crystal structures, including the cohesive energy, elastic constants of the diamond-lattice phase and lattice parameters. In addition, the condition that the point defects energies of the diamond-lattice interstitials and vacancies were positive relative to the perfect diamond-lattice energy was imposed. This last requirement assures that the diamond crystal structure is the most stable phase at low temperatures. Other characteristics of the potential and the fitting procedure are discussed in Ref.108.

The BA potential energy is represented by a sum of two-body potentials, each of which is dependent on the environment of the pair:

$$V_L = \sum_{i < j} V_{ij} \quad (\text{III.2})$$

with

$$V_{ij} = f_c(r_{ij}) [V_R(r_{ij}) + I_{ij}^\pi V_\pi(r_{ij}) + I_{ij}^\sigma V_\sigma(r_{ij})] , \quad (\text{III.3})$$

where r_{ij} is the distance between atoms i and j , V_R , V_π , and V_σ are the repulsive, pi bonding and sigma bonding potentials for an isolated silicon dimer, respectively, I_{ij}^π and I_{ij}^σ are pi and sigma interference functions, respectively, and f_c is a cutoff function that ranges from 1 to 0 as r_{ij} varies from 3.45 to 3.75 Å. The presence of f_c attenuates the potential smoothly over this range, which is

equal to the second nearest neighbor distance in a tetrahedral diamond lattice. Both the p- and s- bonding interference functions are independently influenced by the environment. The sigma interference function contains three- and four-body terms, while the pi interference function contains three-, four-, and five-body terms. The explicit forms of these terms are given in Ref. 108.

The interaction of the hydrogen atom with the lattice is described by a pairwise sum of Morse functions between the hydrogen atom and the lattice atoms in the first two layers

$$V_{gL} = V_{gL}^{(1)} + V_{gL}^{(2)} . \quad (III.4)$$

Here, $V_{gL}^{(1)}$ and $V_{gL}^{(2)}$ denote the interaction between the hydrogen atom and the reconstructed lattice atoms with and without dangling bonds, respectively, in the first and second layers. We have omitted in our calculations the silicon atom with the dangling bond in the fourth layer.

The functional form of $V_{gL}^{(1)}$ is given by

$$V_{gL}^{(1)} = \sum_{i=1}^{18} (D \{ \exp[-2\beta(r_{iH} - r_e)] - 2 \exp[-\beta(r_{iH} - r_e)] \} + \frac{1}{2} k_{\theta} \theta_i^2 \exp[-\gamma(r_{iH} - r_e)^2]) . \quad (III.5)$$

In Eq. (III.5), θ_i is the angle between the surface normal and the vector from the i th lattice atom with dangling bonds in the first or second layer to the hydrogen atom. The modulus of this vector is denoted by r_{iH} .

The interaction of the hydrogen atom with silicon atoms without dangling bonds in the second layer is given by

$$V_{gL}^{(2)} = \sum_{i=19}^{54} D' \{ \exp[-2\beta'(r_{iH} - r'_e)] - 2 \exp[-\beta'(r_{iH} - r'_e)] \} . \quad (III.6)$$

In adjusting the parameters of the hydrogen-lattice interaction term, we have made use of the available experimental and theoretical data related to the equilibrium length and binding energies of the Si-H bond and the fundamental vibrational frequencies for SiH species on the Si(111)-(7x7) surface (see Table I). The values for the potential parameters are given in Table II. Using this set of parameter values, we have evaluated the Si-H equilibrium distance, the binding energy and the fundamental Si-H stretching and H-Si-Si bending frequencies. It can be seen in Table I that the results obtained using the present form of V_{gL} are in close agreement with other theoretical and experimental data.

Figure 5 shows the variation of the hydrogen atom-lattice interaction as a function of the distance in the direction of the surface normal, with the hydrogen atom positioned directly above atom A of the first silicon layer in Figure 4.

Figures 6 and 7 illustrate the potential-energy surface experienced by a hydrogen atom as it is moved across the relaxed (7x7) lattice at a distance of 3.0 a.u. above the surface plane. The contour plot given in Figure 7 shows the potential wells corresponding to the atoms with dangling bonds in the first layer.

Computational Methods

A. Monte Carlo Variational Phase-Space Theory

In order to calculate the diffusion rate of a hydrogen atom on the DAS surface, we first evaluate the rate at which a hydrogen atom chemisorbed at the lattice site denoted by "A" in Figure 4 diffuses to other adsorption sites on the

surface. This process can be represented by



where '*' and '*'' denote two sites with dangling bonds.

Using variational phase-space theory methods, the flux or jump frequency $K(T)$ across a theoretical dividing surface, S_c , separating two binding sites is given by

$$K(T) = \frac{\int d\mathbf{p} \int d\mathbf{q} \delta(S_c) |v_{\perp}| \exp(-\beta E)}{\int d\mathbf{p} \int d\mathbf{q} \exp(-\beta E)} \quad (III.8)$$

where v_{\perp} is the velocity normal to the dividing surface S_c , $\beta=1/kT$, $\delta(S_c)$ is the Dirac delta function, and E is the system energy

$$E = \sum_{i=1}^N (P_{x_i}^2 + P_{y_i}^2 + P_{z_i}^2) / 2 m_i + (P_{x_h}^2 + P_{y_h}^2 + P_{z_h}^2) / 2 m_h + V_L + V_{gL}. \quad (III.9)$$

Here, P_{qi} ($q=x, y, z$) are the components of the momentum of lattice atom i in the q direction. The subscript "i" runs over the moving lattice atoms and "h" denotes the hydrogen atom.

The flux $K(T)$, Eq. (III.8), depends on the form of the dividing surface S_c in phase space. In order to obtain the minimum flux, the dividing surface must be expressed as a general function of the 330 coordinates and momenta of the phase space and the flux minimized with respect to this function. However, in practice this is too computationally expensive. Therefore, we assume that the quantities in Eq. (III.8) are functions of the hydrogen-atom coordinates only. In

the case of cubic dividing surfaces and for the total energy given by Eq. (III.9), the integration over momenta in Eq. (III.8) can be done analytically. This yields

$$K(T) = \langle v \rangle^q \frac{\int \exp[-V/(kT)] \delta(q - q_c) \prod_{i=1}^{3N} dq_i}{\int_q \exp[-V/(kT)] \prod_{i=1}^{3N} dq_i}, \quad (\text{III.10})$$

where $\langle v \rangle$ represents the average velocity of the hydrogen atom in the direction perpendicular to S_c . The delta function is unity when on the dividing surface and zero otherwise.

Since the potential V is separable into a lattice potential plus a hydrogen-lattice interaction, Eq. (III.10) may be written in the form

$$K(T) = \langle v \rangle^q \frac{\int \exp[-V_L/(kT)] \exp[-V_{gL}/(kT)] \delta(q - q_c) \prod_{i=1}^{3N} dq_i}{\int_q \exp[-V_L/(kT)] \exp[-V_{gL}/(kT)] \prod_{i=1}^{3N} dq_i} \quad (\text{III.11})$$

The integrals in Eq. (III.11) are evaluated using standard Monte Carlo procedures with importance sampling as described in Ref. 73. This procedure requires a Markov walk in configuration space that is weighted by the canonical distribution function for the lattice, $\exp[-V_L/kT]$. By replacing the dividing surface with a dividing "slab" of sufficiently small width Δw , the Monte Carlo approximant for $K(T)$ is

$$K(T) \approx 0.5 \frac{\sqrt{\frac{2kT}{\pi m_h}} \sum_{j=1}^M \{ \exp[-V_{gL}/(kT)] I(S_c, \Delta w) \}_j}{\sum_{j=1}^M \{ \exp[-V_{gL}/(kT)] I(\Omega_c) \}_j}, \quad (\text{III.12})$$

where the sums are over the accepted moves in the Markov walk. $I(S_c, \Delta w)$ is an operator that has a value of +1 if, by the j th move, the hydrogen atom is within the volume bounded by surfaces S_c and S_c' , where S_c' is a surface very close and parallel to S_c at a distance of Δw from S_c ; otherwise $I(S_c, \Delta w)$ is equal to zero. The operator $I(\Omega_c)$ is equal to +1 if the j th move leads to a state such that the hydrogen atom is inside the volume Ω_c enclosed by the surface S_c . The factor of 0.5 is included to evaluate the flux in only one direction from the total flux in both outgoing and incoming directions.

The procedure presented above allows the diffusing atom to move in a potential-free configuration space. The configuration-space points corresponding to the diffusion barrier, which are rarely accessible by unbiased sampling, become freely accessible under the stated conditions.

The Markov walk is executed by moving the hydrogen atom and a lattice atom according to

$$q'_i = q_i + (0.5 - \xi_1) \Delta q, \quad (\text{III.13})$$

where q'_i and q_i are the old and new x , y , and z -coordinates, Δq is the step-size parameter and ξ_1 is a random number selected from a uniform distribution on the interval $[0,1]$. The choice of the lattice atom to be moved is cycled systematically over all 54 movable lattice atoms. The lattice step-size parameter was taken equal to 0.1 a.u. The width of the dividing slab, Δw

(=0.17 a.u.), is chosen to be slightly larger than the maximum step size of the hydrogen atom ($\Delta q_h = 0.15$ a.u.), to ensure that the hydrogen atom cannot traverse the dividing slab without entering its volume at least once. A trial move is accepted if it lowers the energy. If a trial move results in a higher energy ΔV_L , it is accepted with the probability $\exp(-\Delta V_L/kT)$, that is, the move is accepted if $\xi_2 < \exp(-\Delta V_L/kT)$, where ξ_2 is a random number. If the move is rejected, the procedure is repeated from the original configuration. For each step of the Markov walk, a move of the hydrogen atom is accepted if its position is inside a reflecting surface located within distance Δw outside of S_c' .

B. Thermal Diffusion Equations

The thermal diffusion coefficient can be computed from the jump frequencies of the hydrogen atom between different adsorption sites. This can be done using the method described by NoorBatcha, Raff, and Thompson⁹⁶ in a study of silicon diffusion on a Si(111) surface. The method involves the integration of a set of coupled, first-order differential equations which describe the time dependence of the concentration of diffusing atoms. Considering the i th site at a distance r_i from the reference site A (see Fig. 4), the variation of the diffusing atoms concentration at time t is given by:

$$\dot{C}_i(t) = \sum_{\substack{j=1 \\ j \neq i}}^N [-K_{ij} C_i(t) + K_{ji} C_j(t)] \quad (i = 1, 2, 3, \dots, N), \quad (\text{III.14})$$

where K_{ij} is the jump frequency from site i to site j and N is the total number of such sites considered. It is assumed that diffusion occurs only by single jumps between adjacent adsorption sites and that the barrier to diffusion is sufficiently large that each jump is uncorrelated with previous jumps. Since the actual

diffusion can involve both correlated motion and possibly multiple jumps, a diffusion coefficient calculated with these assumptions will be a lower bound of the real diffusion coefficient. However, we have verified using a limited number of trajectory calculations that the hypothesis of uncorrelated jumps from a given site, for example A in Figure 4, is justified.

The solutions of Eqs. (III.14) are used to calculate the root-mean-square displacement

$$\langle r^2(t) \rangle = \frac{\sum_{i=1}^N [C_i(t) r_i^2(t)]}{\sum_{i=1}^N [C_i(t)]} . \quad (\text{III.15})$$

The thermal diffusion coefficient D , is then calculated by using Einstein's relation¹³⁷

$$\langle r^2(t) \rangle = 2\alpha Dt , \quad (\text{III.16})$$

where α is the dimensionality of diffusion.

Results

A. Classical Jump Frequencies

Equation (III.12) was used to compute the jump frequency K_{AB} of the hydrogen atom between sites "A" and "B" in Fig. 4 at temperatures of 300, 500, and 800 K.

The region of interest for A→B diffusion is illustrated in Fig. 8. In this figure only lattice atoms with dangling bonds in the first two layers are shown. A section of the dividing surface used to evaluate the flux between the two sites is

also shown (see rectangle DFGH). Some characteristic dimensions are $FD=16$ a.u. and $AE=3.6$ a.u., where E is the midpoint of the DF distance. The dividing surface is similar to that employed by Agrawal *et al.*⁸⁵ in a study of Si diffusion on a Si(111)-(7x7) reconstructed surface; the only difference is represented by the portion DEF which, in the Si-atom diffusion study⁸⁵, was part of an ellipse with the major axis along FD and semiminor axis along AE. It was found⁸⁵ that the calculated jump frequency is an insensitive function of the shape of the DEF boundary for side lengths $3.6 \leq AE \leq 4.0$ a.u. This result was attributed to the fact that the density of reactant phase space is small for this range of lengths.

In order to determine the minimum flux, we have used a set of 14 dividing surfaces that span the important regions of the configuration space of the system. A typical dividing surface section is illustrated in Fig. 8. The position of each of the 14 dividing surfaces is determined by the length FG which is varied over the range $1.6 \leq FG \leq 10.16$ a.u. Reflecting barriers to hydrogen were placed in the planes $z=-2.4$ a.u. below and $z=4.0$ a.u., above and parallel to the surface plane. These restrictions produce a faster convergence of the calculated jump frequencies while still averaging over the important regions of the configuration space of the system.

Figure 9 shows the minimum energy along the diffusion path A→B obtained using the method introduced by Raff *et al.*⁷³ The abscissa values of the points in Fig. 9 correspond to the specific distances FG of the dividing surfaces. The barrier height for the A→B jump is 1.52 eV. We found that the minimum value of the flux was obtained for the dividing surface centered at the barrier maximum. The (z,x) coordinates of the points corresponding to the minimum energy pathway are shown in Fig. 10. These results illustrate that A→B diffusion involves lattice penetration by the hydrogen atom.

The calculated jump frequencies $K_{A \rightarrow B}$ at 300, 500, and 800 K are

given in Table III and an Arrhenius plot of the values is shown in Fig. 11. A least-squares fit yields an activation energy of 1.548 ± 0.004 eV and a frequency factor of $(3.88 \pm 0.33) \times 10^{12} \text{ s}^{-1}$. The small difference of 0.02 eV relative to the results of the minimum-energy path calculation may be due to statistical errors.

B. Diffusion Coefficients

Starting from a chemisorbed atom at the lattice site denoted by A in Fig. 4, we consider the diffusion to the other lattice sites with dangling bonds. Previous studies of silicon-atom diffusion on a DAS Si(111)-(7x7) reconstructed surface,⁸⁵ showed that the rate-controlling diffusion coefficient was determined by the jump frequencies between the triangular areas as shown in Fig. 4 and that these frequencies were insensitive to the equilibration rate within each of the triangular areas. Consequently, the jump frequencies between different pairs of atoms with dangling bonds in Fig. 4 can be classified into three groups:

(1) Jumps from sites such as A to sites such as B, which are separated by about 12.6 a.u. Symmetry considerations indicate that $K_{AB} = K_{BA}$. Since it has been shown that $K_{A \rightarrow B}$ is not affected by the nature of the DEF boundary,⁸⁵ it is reasonable to assume that the presence of the R site has no significant influence on this jump frequency. We thus assume that the A \rightarrow B jump frequencies given in Table III correspond to all types of jumps of distances 12.6 a.u. In addition, we assume, as in the above mentioned study,⁸⁵ that this jump frequency is rate-controlling for diffusion between the triangular areas shown in Fig. 4.

(2) Jumps from site A to sites such as R, which are separated by a distance of about 8.5 a.u. For this process, we assume that the jump frequencies K_{ij} are large relative to the K_{AB} values ensuring quick equilibration over the sites within one of the large triangular areas shown in Fig. 4.

(3) We assume that the K_{ij} jumps for distances greater than 12.6 a.u. are zero. It can be seen in Fig. 4 that the diffusion *via* site R from site A to A', separated by 14.5 a.u., would be very fast compared to the direct jump rate. Consequently, neglecting the direct, long-distance jumps is not expected to significantly affect the results for the overall diffusion coefficients.

Under the assumption of instantaneous equilibration of the concentration of hydrogen atoms over all lattice sites within the triangular areas shown in Fig. 4, the diffusion model can be simplified by considering each nine-atom triangular unit as a single "lattice site". Thus, each (7x7) unit cell would have two such sites. Consequently, the diffusion process is considered to take place from a half-unit cell to a neighboring half-unit cell. This simplified diffusion model for 49 unit cells is illustrated in Fig. 12; note that there are three symmetrical sites, situated at 120° angles, about a given site.

The diffusion coefficient for the two-site model shown in Fig. 12 was obtained by using Eqs. (III.14)-(III.16) with the concentrations $C_i(t)$ replaced with $C_i(t)/9$ and the jump frequencies K_{ij} by $3K_{ij}$; the first change in the equations takes into account the fact that the total concentration in the triangular areas of Fig. 4 is nine times that at each lattice site at equilibrium, and the latter because there are three possible A→B jumps that result in diffusion between triangular areas. The initial conditions are $C_i(t=0)=0$ for $i \neq A$ and $C_A(t=0)=1$.

In the study of Si atom diffusion on the Si(111)-(7x7) reconstructed surface,⁸⁵ it was shown that the temporal variation of the root-mean-square displacement contained two different slopes when finite jump frequencies over distances of 8.5 a.u. were considered. The first slope corresponds to short periods of time and characterizes the diffusion process inside the triangular areas shown in Fig. 4. The second region, at larger times, has a smaller slope of the $\langle r^2(t) \rangle$ vs t and essentially measures the rate of diffusion from one

triangular area to another. This long-time behavior of $\langle r^2(t) \rangle$ determines the rate-controlling diffusion coefficient, which was shown to be very insensitive to the equilibration rate within one of the triangular areas.⁸⁵

In our calculations, by assuming the instantaneous equilibration of the concentration of hydrogen atoms over all lattice sites within the triangular areas shown in Fig. 4, the temporal variation of $\langle r^2(t) \rangle$ is expected to be characterized by a single slope. A typical result of the time variation of the root-mean-square displacement at 800 K is plotted in Fig. 13. Diffusion coefficients obtained from the slopes of $\langle r^2(t) \rangle$ plots at 300, 500 and 800 K are given in Table III. An Arrhenius plot of these results is shown in Fig. 14. The slope of the linear least-squares fit gives an activation energy of 1.548 ± 0.004 eV. The pre-exponential factor obtained from the intercept is 0.023 ± 0.002 cm²/s.

The activation energy obtained for hydrogen-atom diffusion on the Si(111)-(7x7) surface is in very good agreement with the experimental value 1.5 ± 0.2 eV obtained by Reider *et al.*⁹⁴ by an optical second-harmonic diffraction technique. This barrier to lateral motion corresponds to roughly half of the binding energy of 3.1 eV for atomic hydrogen on the silicon surface (see Table I). This result is consistent with the presence of highly localized bonds on the silicon reconstructed surface.

The computed activation energy for the present system is significantly lower than the value of 2.6 eV calculated by Rice *et al.*⁷⁴ for H diffusion on an unreconstructed Si(111) surface. This difference is primarily the result of the different nature of the adsorption sites involved in the two studies. Rice *et al.*⁷⁴ computed the hydrogen-atom diffusion coefficient between an atop site and an "open site" on the Si(111) surface whereas the present study considers diffusion between two atop sites on the Si(111)-(7x7) reconstructed surface. As expected, the diffusion coefficient is highly sensitive to the site involved and

surface topology.

C. Tunneling Contributions

In a study of H atoms diffusion on Si(111) surface Rice, Raff and Thompson⁷⁴ have determined the tunneling rate by selecting the tunneling probability with the largest value among tunneling probabilities calculated from nine different paths. The nine possible paths were along lines parallel to the surface plane and selected such as to connect the diffusing particle in its random position to nine evenly-spaced points along the diameter of an attractive open-site well. A biased Markov walk was used to average over the reactant phase space. The results suggest that at 300 K and 600 K the rates calculated using the Monte Carlo random walk are lower than those calculated using the minimum energy path. At larger temperatures the results of the two methods coincide.

In the present study we employ the minimum-energy diffusion path for A→B jumps in order to evaluate an upper limit for the tunneling rates. We have assumed that the tunneling process may be treated as one-dimensional and that we may extrapolate symmetrically, in the -x direction, the minimum energy diffusion path given in Fig. 9. Thus, the tunneling jump frequency between adsorption sites A and B at temperature T can be approximated as

$$K_t(T) = \frac{\int_{E=0}^{E_a} v(E) T_p(E) e^{-E/kT} dE + \int_{E=E_a}^{E_b} v(E) T_p^2(E) e^{-E/kT} dE}{\int_{E=0}^{E_b} e^{-E/kT} dE} \quad (\text{III.17})$$

where E_b is the potential barrier height, E_a is the value of potential which

corresponds to the bottom of the well centered on the potential profile given in Fig. 9, $\nu(E)$ is the hydrogen-atom vibrational frequency in the adsorption site at energy E , and $T_p(E)$ is the tunneling probability at energy E .

The second term in Eq. (17) arises because of the minimum in the transition-state region (see Fig. 9).

The vibration frequency $\nu(E)$ can be calculated directly using

$$\nu^{-1}(E) = \sqrt{8 m_h} \int_{r=0}^{r=r_1} \frac{dr}{\sqrt{E - V(r)}} \quad (\text{III.18})$$

where m_h is the hydrogen-atom mass and $V(r)$ is the one-dimensional potential. The integral limit r_1 is the turning point which corresponds to the condition $V(r_1)=E$. Figure 15 shows a plot of these frequencies as a function of energy. The frequencies range from $2.7 \times 10^{13} \text{ s}^{-1}$ to $2.5 \times 10^{12} \text{ s}^{-1}$. Using the WKB (Wentzel-Kramers-Brillouin) semiclassical approximation¹³⁸, the tunneling probability at energy E is given by

$$T_p(E) = \exp\left(-\frac{4\pi}{h} \int_{r=r_1}^{r=r_2} \sqrt{2 m_h [V(r) - E]} dr\right) \quad (\text{III.19})$$

with r_1 and r_2 being the two points for which $V(r_1)=V(r_2)=E$.

The computed tunneling jump frequencies and the corresponding tunneling diffusion coefficients are given in Table IV. An Arrhenius plot of the diffusion coefficients gives an activation energy of 1.48 eV and a pre-exponential factor of $4.9 \times 10^{-4} \text{ cm}^2/\text{s}$. As can be seen by comparing the classical and quantal diffusion rates, the tunneling contribution is small for the temperature range considered and decreases with increasing temperature.

The ratio of tunneling to classical diffusion rates varies from 0.5 at 300 K to 0.06 at 800 K.

Reider *et al.*⁹⁴ concluded that for the temperature range 660-730 K used in their experiments, the contribution of quantum diffusion of hydrogen atoms on Si(111)-(7x7) surface to the diffusivity does not exceed 10^{-15} cm²/s. Our results give contributions between 2.23×10^{-15} cm²/s at 660 K and 2.73×10^{-14} cm²/s at 730 K. The slightly larger values obtained in the present study may be due to the one-dimensional approximation, which tends to overestimate the tunneling contribution; the values reported in Table IV represent upper limits to the experimental tunneling rates.

Conclusions

We have developed a potential for the interaction of hydrogen atoms with a reconstructed Si(111)-(7x7) surface.¹⁰⁰ The surface diffusion of hydrogen on the DAS reconstructed Si(111)-(7x7) surface has been investigated using Monte Carlo variational phase-space theory methods.⁷³ The potential-energy surface of the system, which comprises a 292-atom lattice and the hydrogen atom, is expressed as a pairwise sum of a lattice potential and a hydrogen-lattice atom interaction potential.

Monte Carlo variational phase-space calculations with importance sampling incorporated were performed by computing the minimum flux through planar dividing surfaces separating the two binding sites. Classical jump frequencies were computed at 300, 500, and 800 K. An Arrhenius fit to these jump frequencies yields an activation energy of 1.548 ± 0.004 eV and a pre-exponential factor of $(3.88 \pm 0.33) \times 10^{12}$ s⁻¹.

The minimum-energy diffusion path for sites separated by a 12.6 a.u. distance is obtained by using a Monte Carlo random walk procedure with

importance sampling.⁷⁵ The barrier height for the A→B jump obtained from these studies is 1.52 eV.

The classical diffusion coefficients at 300, 500 and 800 K are computed by using a simplified diffusion model for 49 unit cells on the DAS surface and integrating the phenomenological rate equations describing diffusion of hydrogen on this surface. An Arrhenius fit to these values gives an activation energy of 1.548 ± 0.004 eV and a pre-exponential factor of 0.023 ± 0.002 cm²/s. The computed activation energy for thermal diffusion is in good agreement with the experimental value⁹⁴ of 1.5 ± 0.2 eV determined by an optical second-harmonic diffraction technique.

Using the WKB semiclassical approximation, the upper limits of the tunneling diffusion rates between atop sites were estimated at 300, 500 and 800 K. Our results show small tunneling contributions to the total diffusion rates.

Table I

The equilibrium length and binding energies of the Si-H bond and the fundamental vibrational frequencies for SiH species on the Si(111)-(7x7) surface. The corresponding results obtained in our calculations are also indicated.

| Ref. | Method | r_e (a.u.) | Binding energies (eV) | Frequency (cm ⁻¹) | | |
|-------|------------------------------------|-----------------|--------------------------|-------------------------------|---|------|
| | | | | Species | Stretch | Bend |
| [130] | Self-consistent pseudopotential | 2.93 | | | | |
| [131] | Self-consistent pseudopotential | 2.73 | | | | |
| [126] | HF LCAO calc. TDS ^a | 2.808 | 3.02 3.1 - 3.2 | SiH | 2274 | 630 |
| [127] | TDS ^a | | 3.5 | | | |
| [97] | LITD ^b | | 3.49 | | | |
| [119] | LITD ^b | | 3.59 | | | |
| [128] | ID-SHG ^c | | 3.45 | | | |
| [122] | EELS ^d | | | SiH | 2100 | 630 |
| [123] | EELS ^d | | | n-SiH t- SiH | 2057 2080 | 637 |
| [121] | IR ^e | | | SiH | 2073 and 2077 shifts to 2082 and 2088 | |

Table I (continued)

| Ref. | Method | r_e (a.u.) | Binding energies (eV) | Frequency (cm ⁻¹) | | |
|------------------------|---------------------|-----------------|--------------------------|----------------------------------|---------|------|
| | | | | Species | Stretch | Bend |
| [132] | EELS ^d | | | SiH | 2089 | 637 |
| [133] | EELS ^d | | | n-SiH ^h | 2057 | 632 |
| | | | | t-SiH ^g | 2064 | |
| [134] | MIR-IR ^f | | | n-SiH ^h | 2076 | |
| | | | | t ₁ -SiH ^g | 2086 | |
| | | | | t ₂ -SiH ^g | 2095 | |
| Present calc. [100] | | 2.81 | 3.26 | SiH | 2086 | 635 |

^aTDS-thermal desorption spectroscopy;

^bLITD-laser induced thermal desorption;

^cID-SHG-isothermal desorption second harmonic generation;

^dEELS-electron energy loss spectroscopy;

^eIR-infrared spectroscopy;

^fMIR-IR-multiple internal reflection infrared spectroscopy;

^gt-tilted ~70° from the surface normal;

^hn-surface normal.

Table II

Hydrogen-lattice potential parameters.

| Parameter | Value |
|-------------------------------------|----------|
| D (eV) | 2.82 |
| β (a.u. ⁻¹) | 0.82209 |
| r_{eq} (a.u.) | 2.873212 |
| D' (eV) | 0.82 |
| β' (a.u. ⁻¹) | 0.75 |
| r'_{eq} (a.u.) | 3.50 |
| k_{θ} (eV/rad ²) | 3.9728 |
| γ (a.u. ⁻²) | 0.3521 |

Table III

Classical jump frequencies K_{AB} and diffusion coefficients D as a function of the surface temperature.

| T (K) | K_{AB} (s ⁻¹) | D (cm ² /s) |
|-------|-----------------------------------|-----------------------------------|
| 300 | $(1.57 \pm 0.15) \times 10^{-14}$ | $(9.46 \pm 0.90) \times 10^{-29}$ |
| 500 | $(1.96 \pm 0.10) \times 10^{-3}$ | $(1.18 \pm 0.06) \times 10^{-17}$ |
| 800 | $(5.17 \pm 0.21) \times 10^{+2}$ | $(3.11 \pm 0.12) \times 10^{-12}$ |

Table IV

Tunneling jump frequencies K_t and diffusion coefficients D as a function of the surface temperature.

| T (K) | K_t (s^{-1}) | D (cm^2/s) |
|-------|-------------------------|-------------------------|
| 300 | 0.905×10^{-14} | 0.544×10^{-28} |
| 500 | 0.872×10^{-4} | 0.525×10^{-18} |
| 800 | $0.360 \times 10^{+2}$ | 0.216×10^{-12} |

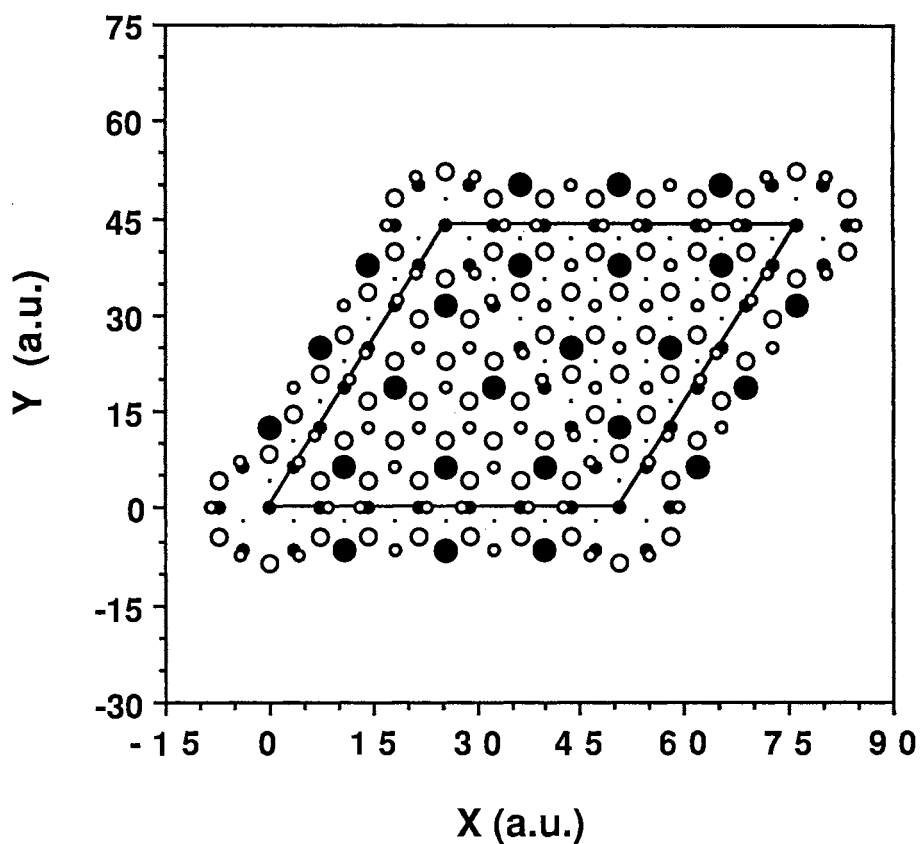


Figure 1. The top view of the atomic structure of the DAS model of the Si(111)-(7x7) reconstruction. Atoms at increasing depth are represented by circles of decreasing diameters. The larger black and open circles represent the adatoms and the atoms in the stacking fault layer, respectively. Smaller open circles represent the atoms in the dimer layer. Solid dark circles and dots represent atoms in the unreconstructed layers beneath the reconstructed surface. The left half of the unit cell contains the stacking fault. The parallelogram defines the unit cell.

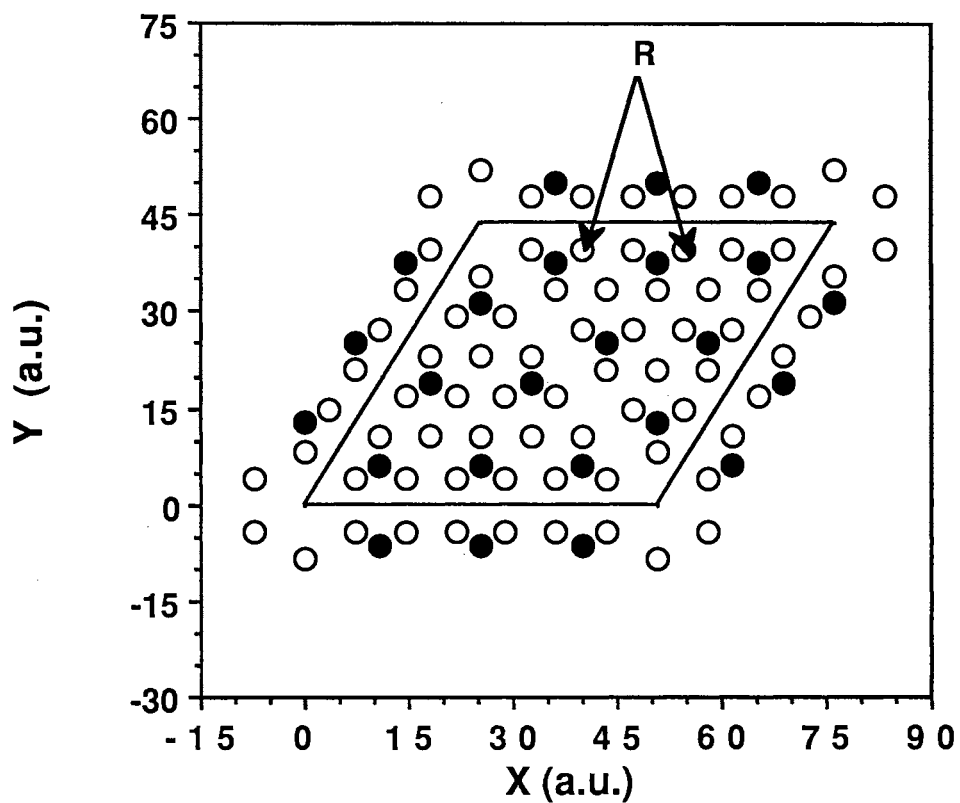


Figure 2. Detail of the DAS surface containing the stacking fault layer (open circles) and the 12 adatoms (dark circles) at A sites with local 2×2 structure. Two of the 6 rest atoms of the stacking fault layer are also indicated.

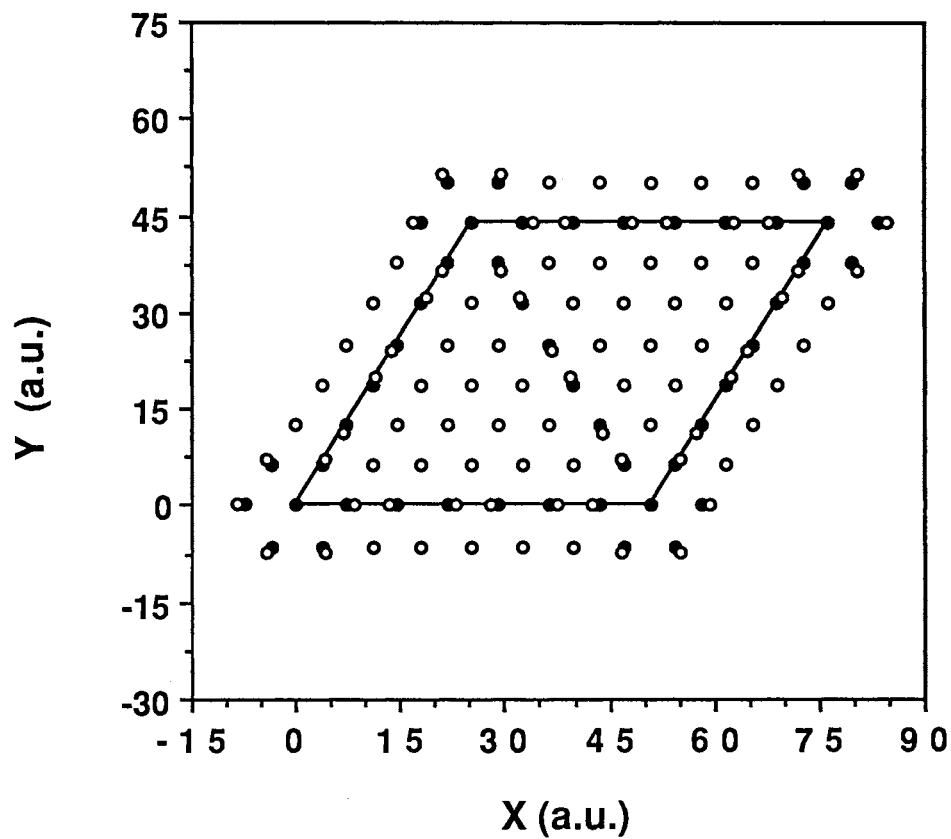


Figure 3. Detail of the DAS surface containing the layer with dimers along the sides of the triangular subunits (open circles) and the atoms in the next unreconstructed layer (solid circles). Most of the atoms in the unreconstructed layer are directly beneath second-layer atoms and are hidden from view.

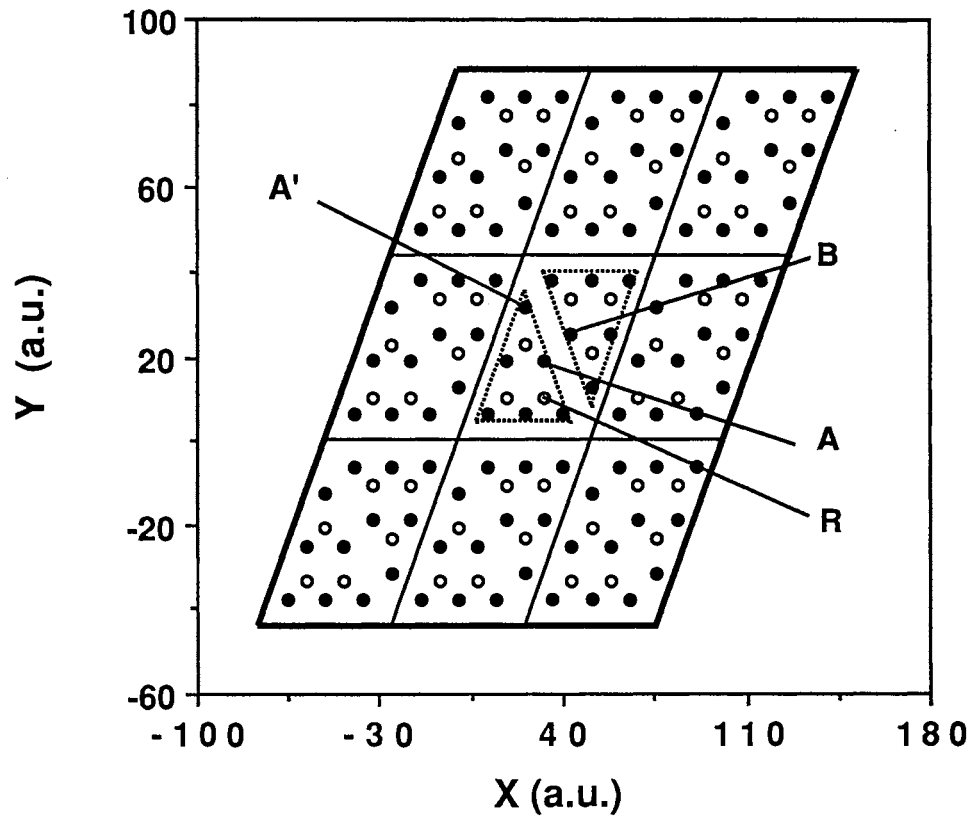


Figure 4. The relative positions of the atoms with dangling bonds in the first (dark circles) and in the second (open circles) layers for nine adjacent unit cells on the (7x7) DAS surface.

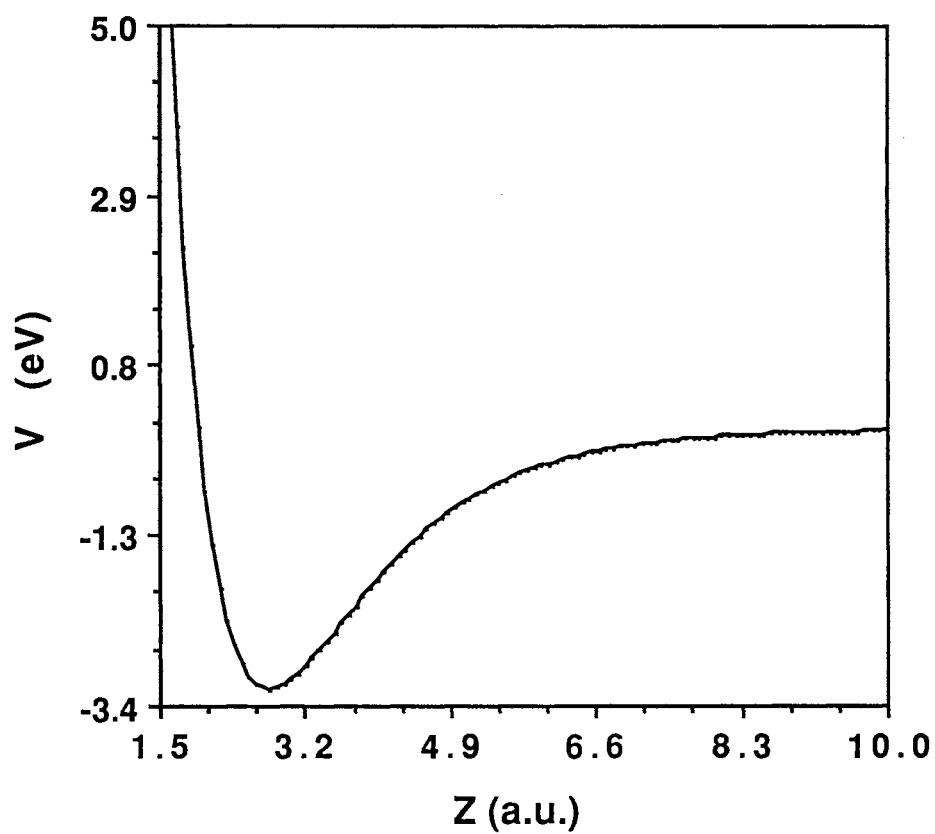


Figure 5. Potential energy variation for the symmetric stretch of the Si-H bond with the H atom positioned directly above the adatom A in Fig. 4.

Figure 6. A perspective plot of the interaction potential V_{gL} between the H atom and the relaxed (7x7) lattice as function of x and y coordinates in a plane parallel to, and 3.0 a.u. above atom A, of the top layer of the Si(111)-(7x7) lattice as shown in Fig. 4.

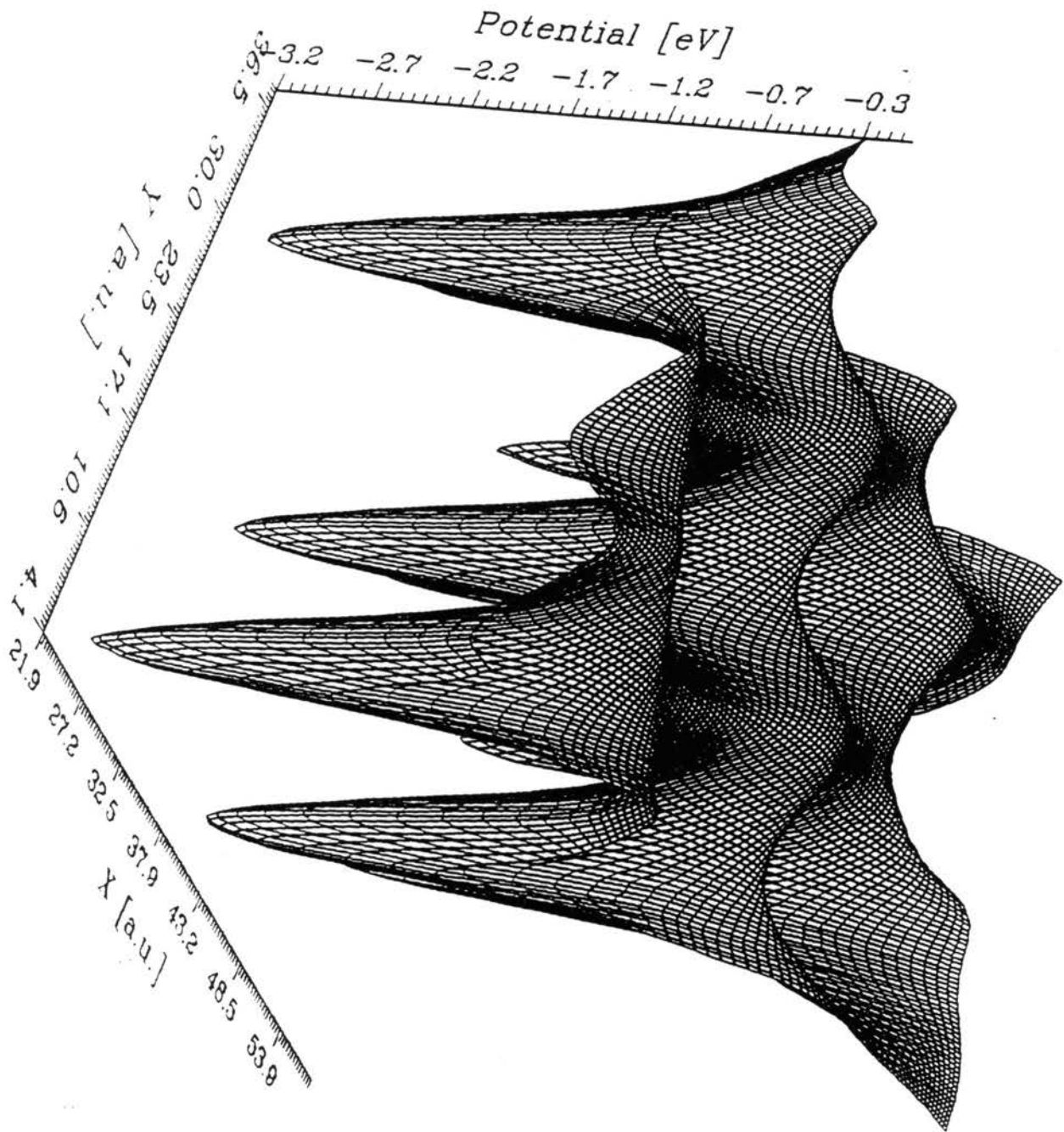


Figure 7. Contour plot for the interaction potential V_{gL} between the H atom and the relaxed (7x7) lattice as a function of x and y coordinates in atomic units in a plane parallel to, and 3.0 a.u. above atom A, of the top layer of the Si(111)-(7x7) lattice. Contour levels are given in electron volts relative to the hydrogen atom at infinity.

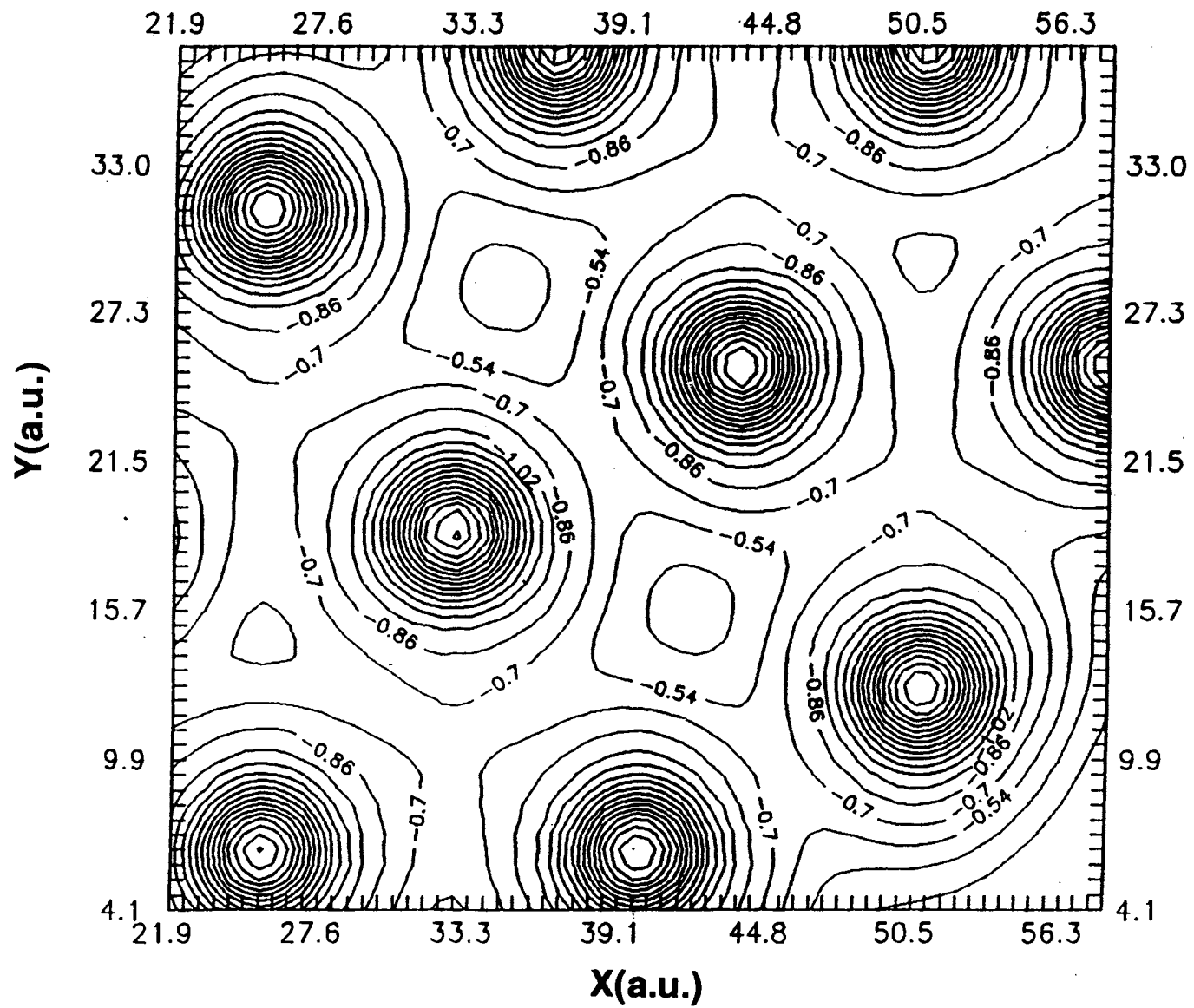
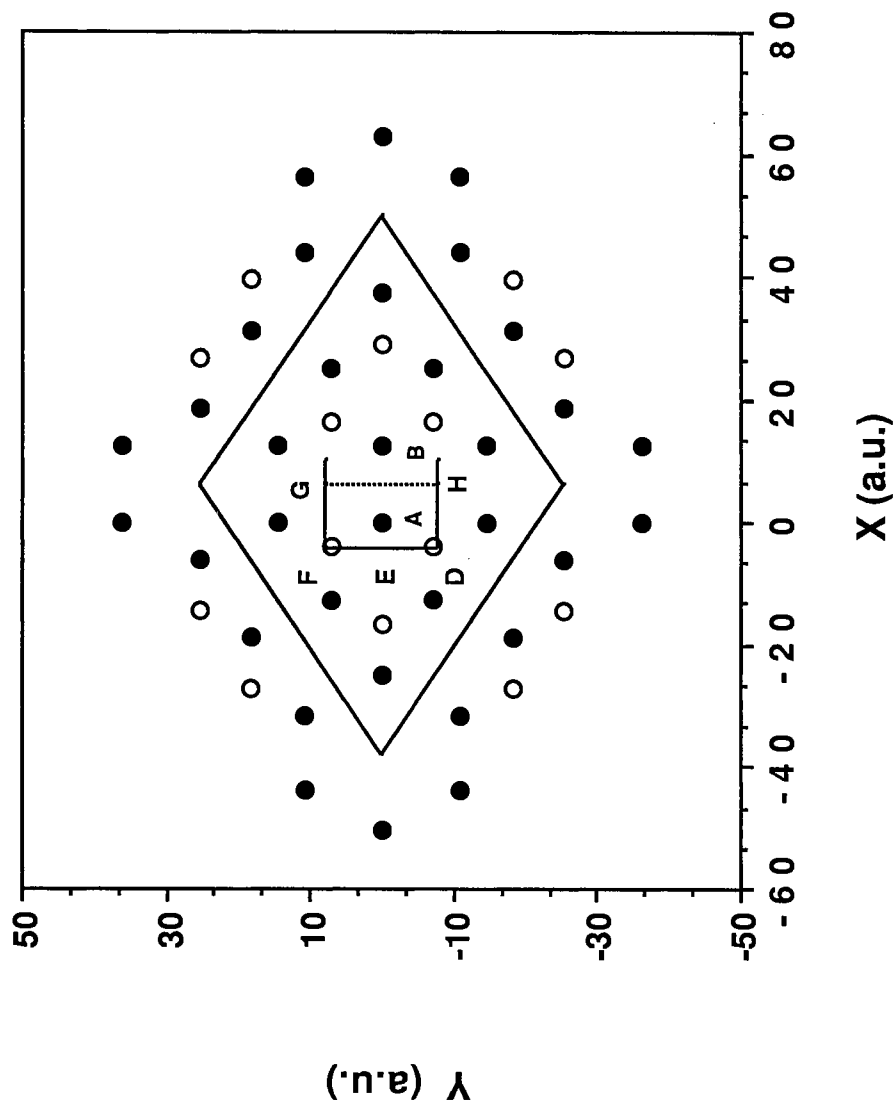


Figure 8. Details of the cross section of the dividing surfaces used in the variational calculation. Dark and open circles represent the atoms with dangling bonds in the first and second layers, respectively.



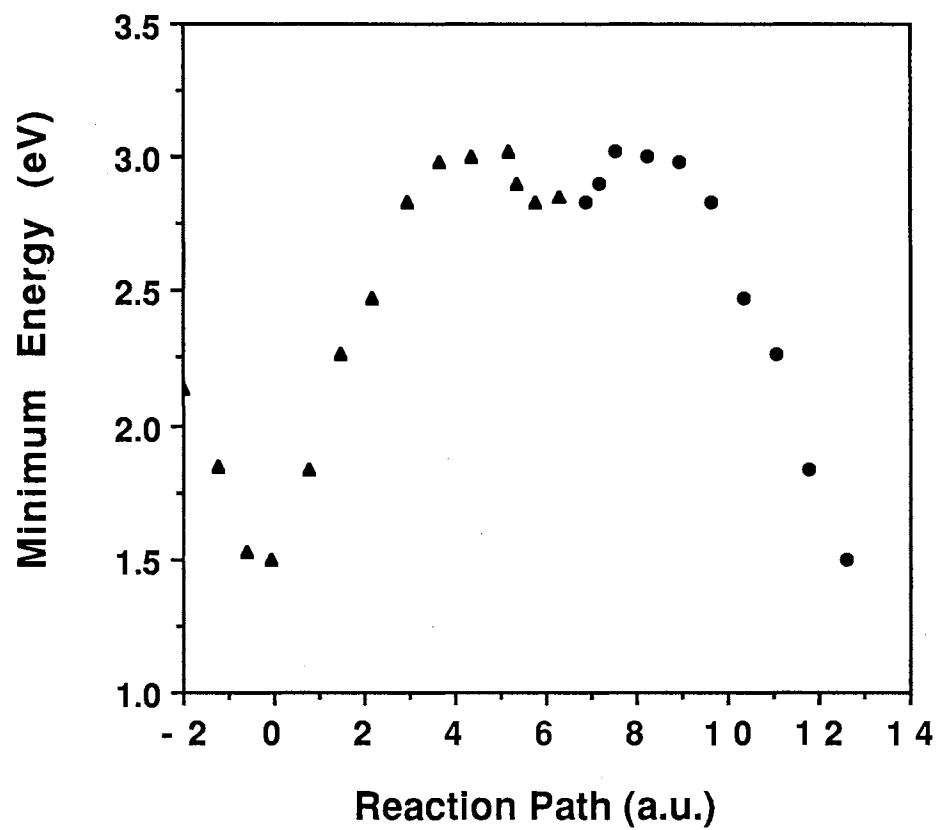


Figure 9. Minimum-energy diffusion path for A→B jumps. The triangles denote the values obtained in the variational calculations. The circles represented extrapolated results based on symmetry considerations.

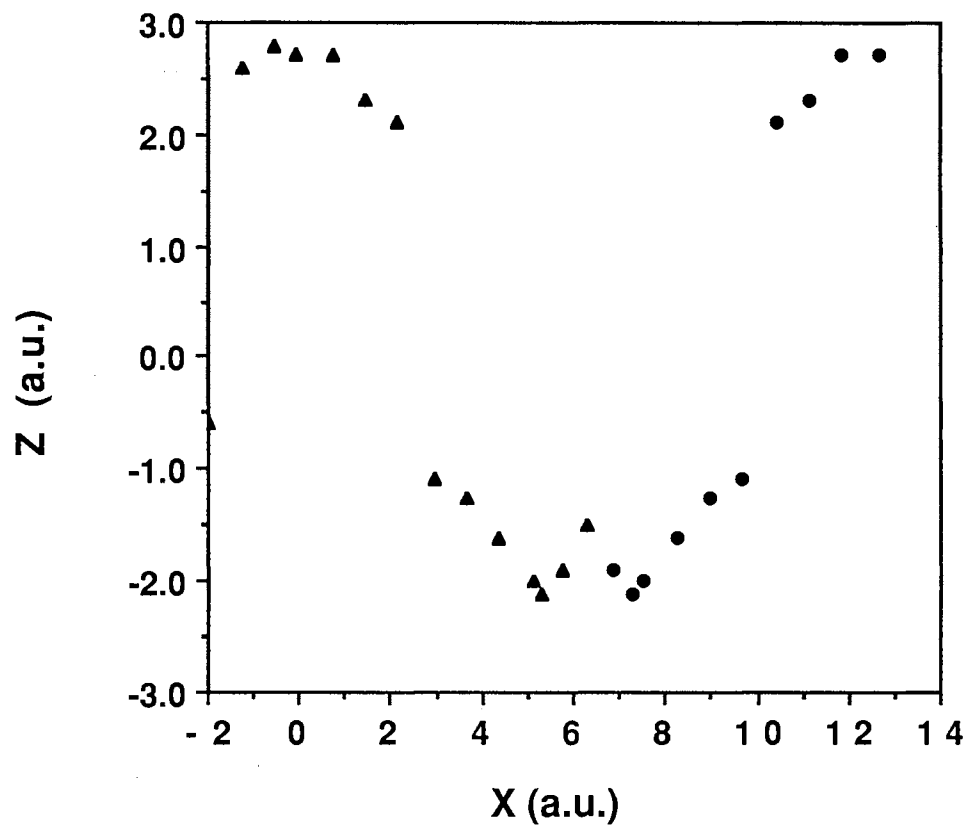


Figure10. (x,z) coordinates of the points corresponding to the minimum-energy diffusion path given in Fig. 9. The triangles denote the values obtained in the variational calculations. The circles represent extrapolated results based on symmetry considerations.

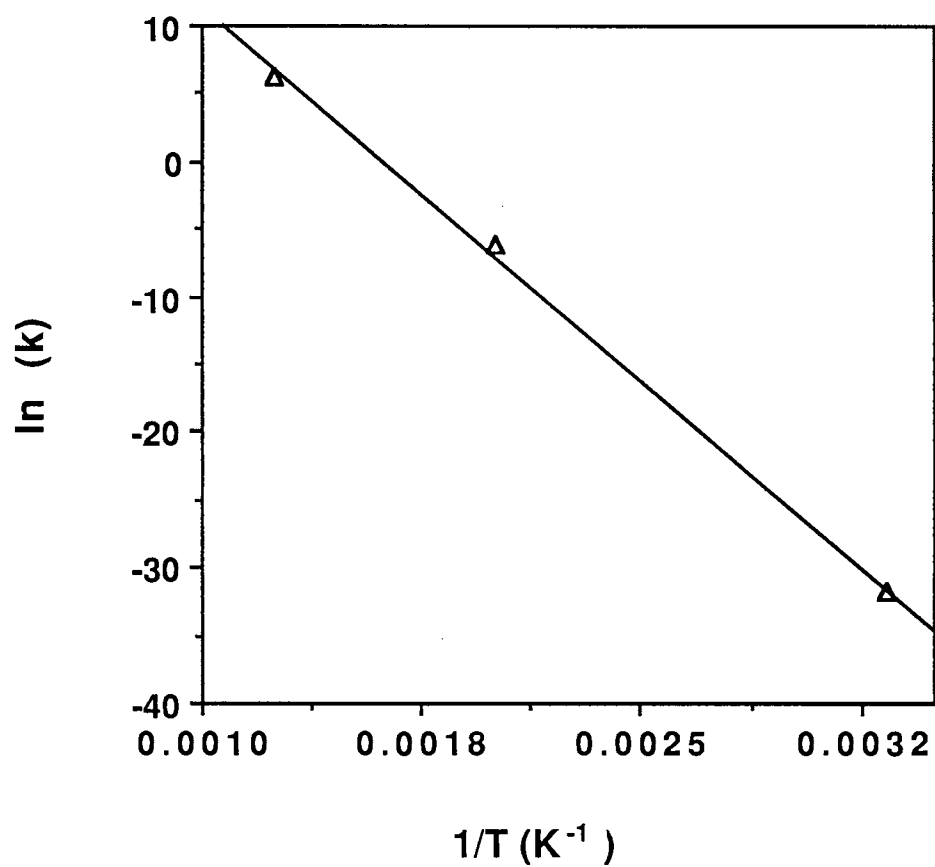


Figure 11. Arrhenius plot of the A→B jump frequencies given in Table III.

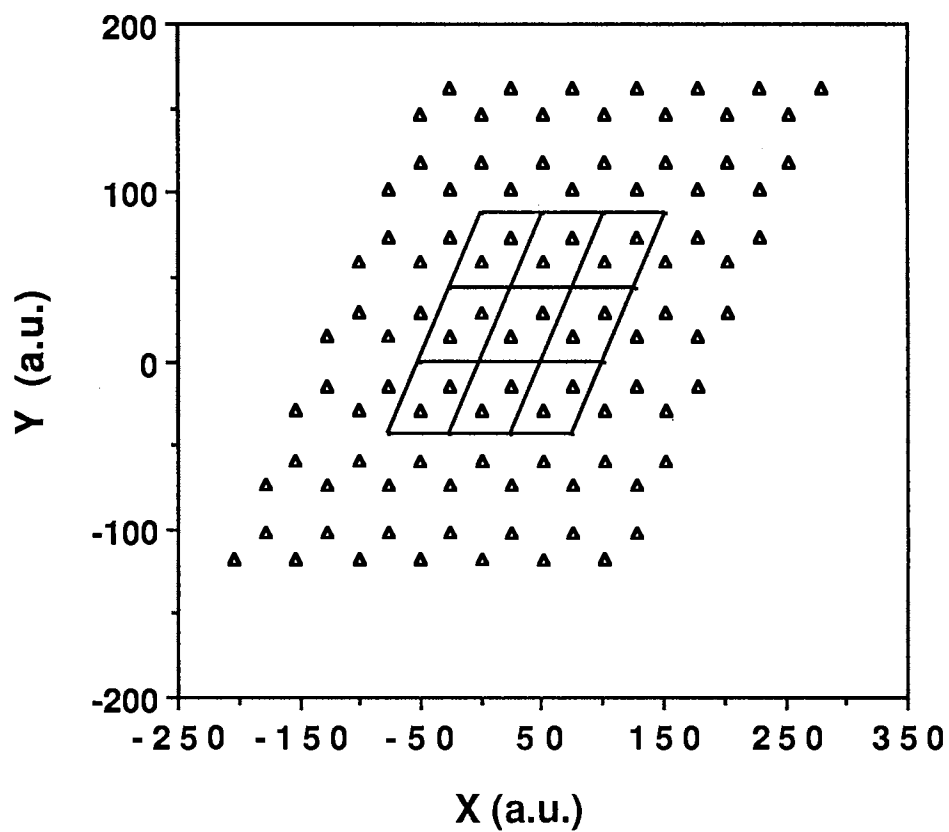


Figure 12. The simplified diffusion model for 49 unit cells on the DAS surface. Each triangle corresponds to the triangular region shown in Fig. 4 and contains nine atoms with dangling bonds.

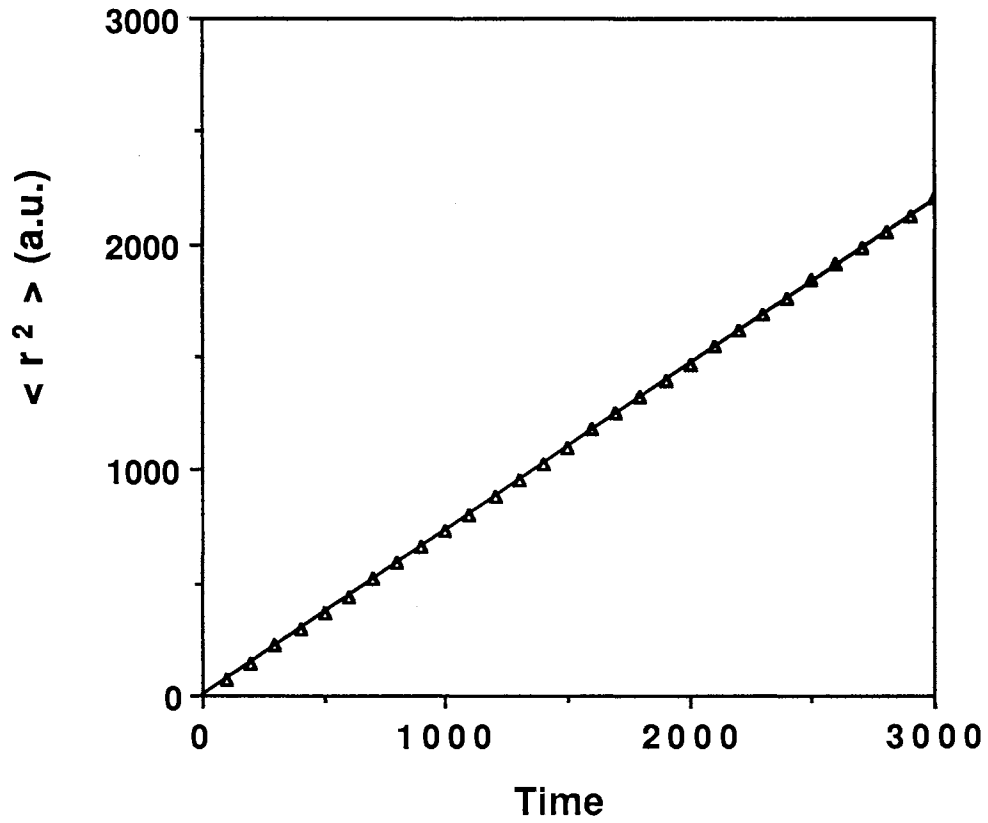


Figure 13. A plot of the mean-square displacement $\langle r^2(t) \rangle$ as a function of time in units of 1.0×10^{-6} s. The triangles are the computed points and the straight line is the least-squares fit.

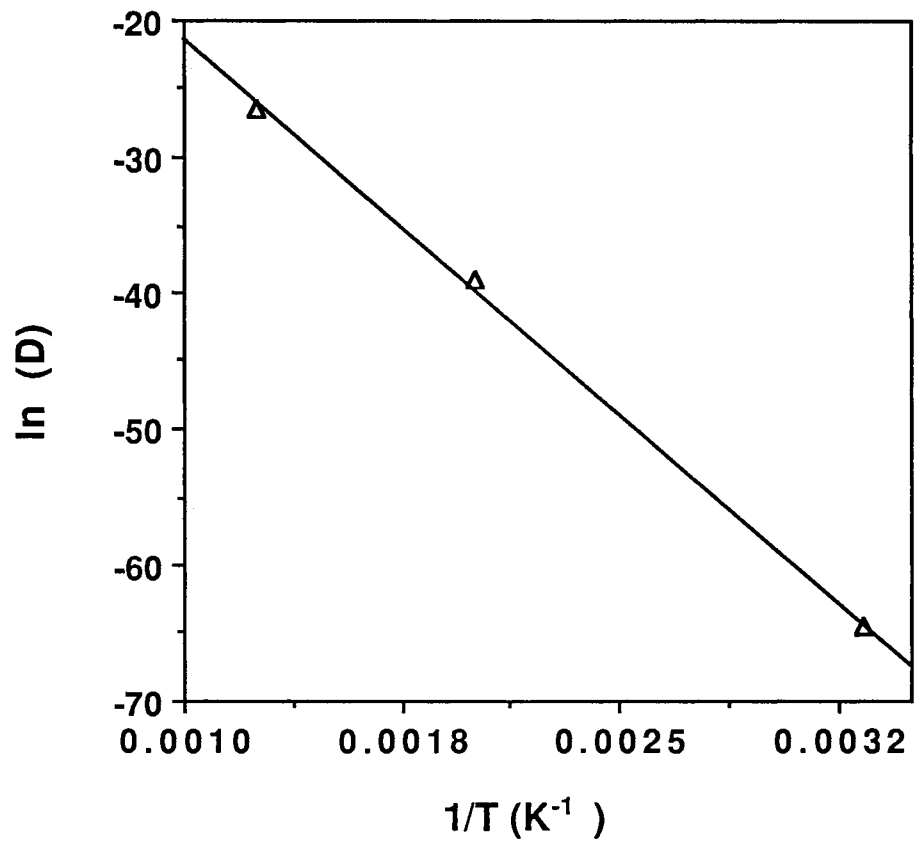


Figure 14. Arrhenius plot of the diffusion coefficients given in Table III.

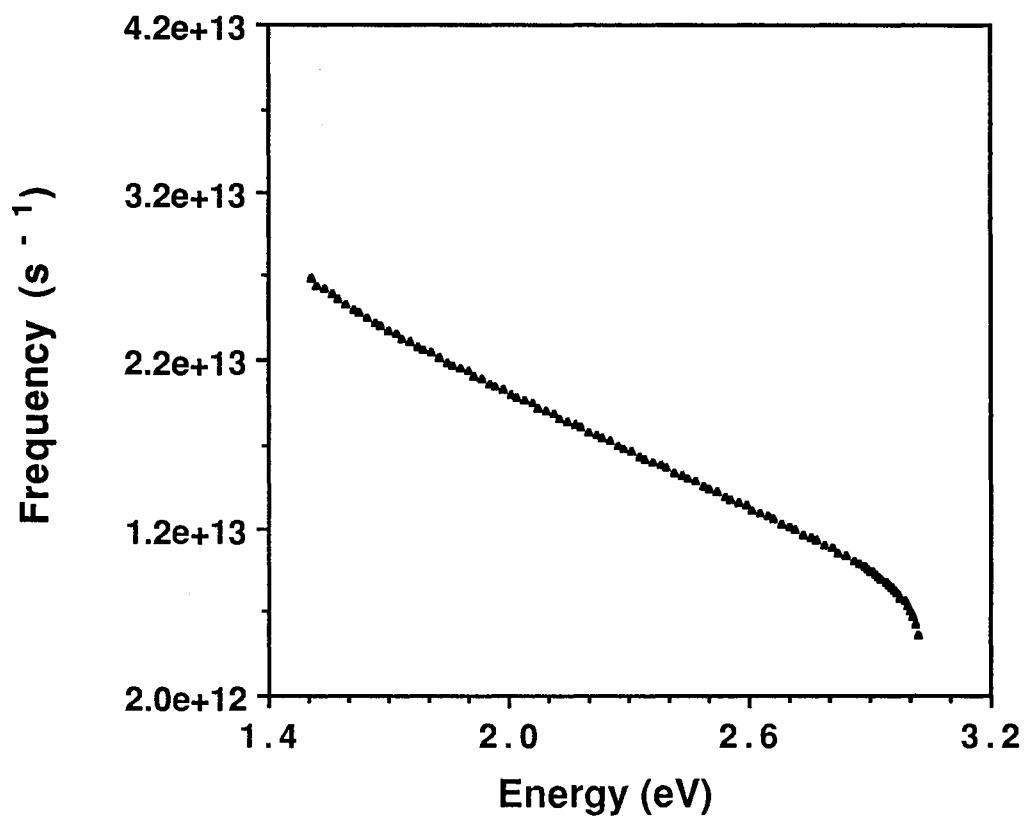


Figure 15. The frequency of surface-plane vibration of the hydrogen atom in the well of the minimum-energy diffusion potential given in Fig. 7 as a function of energy.

CHAPTER IV
STATISTICAL EFFECTS IN THE SKELETAL INVERSION OF
BICYCLO(2.1.0)PENTANE

Introduction

The unimolecular decomposition of energized molecules is commonly treated using some form of statistical rate theory. These theories assume a complete randomization of the internal molecular energy prior to reaction. That is, the energetically accessible phase space of the system must be fully explored on a time scale that is short relative to the reaction time. It has generally been assumed that this requirement will be fulfilled if the intramolecular energy transfer rate out of a given excited mode is large relative to the unimolecular reaction rate. It has likewise been assumed that under such conditions mode-specific chemical effects will not be observed.

It is clear that mode-specific chemistry will be observed whenever the reaction rate is fast relative to the intramolecular energy transfer rate. However, it is now known that the inverse of this statement is not always true. That is, the existence of a very fast intramolecular energy transfer rate out of a given set of modes is not a sufficient condition to ensure the absence of mode-specific dynamical effects. It is possible to have a molecular system in which the IVR rate out of a given set of modes is fast relative to the unimolecular reaction rate but is such that the energy tends to remain confined within a small subset of modes rather than become completely randomized over all internal degrees of

freedom. Under such conditions, pronounced mode-specific and other nonstatistical effects will often be observed.

By comparing the results of classical trajectory calculations with results obtained using classical variational transition-state theory methods, it has been found that the unimolecular reactions of many polyatomic molecules do not obey the fundamental assumption inherent in statistical theories of reaction rates that all phase-space points of energy E are equally weighted in the reaction.^{47,54,58-60,62,139} For example, Raff, Thompson and co-workers have found that bond fission rate coefficients for disilane and 1,2-difluoroethane computed by variational transition-state theory methods at energies substantially in excess of threshold are not rigorous upper bounds to the true classical rate coefficient computed by trajectory methods on the same potential-energy surface.^{47,54,58,59,139} It was further shown that this result occurs because of an incomplete global energy randomization on the time scale of the reaction even though the total intramolecular vibrational relaxation (IVR) rate out of a given mode is large compared to the reaction rate.

Several examples of thermal unimolecular reactions for larger polyatomic molecules whose dynamics could not be explained using statistical theories have been recently review by B. K. Carpenter.¹⁴⁰

An interesting reaction of this type is represented by the thermal decomposition of 2,3 diazabicyclo(2.2.1)hept-2-ene-exo, exo-5,6-d₂ (DBHD) (**1**) to bicyclo(2.1.0)pentane-exo,exo-2,3-d₂ (**2x**), -endo, endo-2,3-d₂ (**2n**), and molecular nitrogen (see Fig. 16). The intriguing aspect of this reaction is that the reaction products (**2x**) and (**2n**) are not formed in equal amounts as expected based on statistical theories of reaction rates and the symmetry of the reaction path described in Fig. 16.¹⁴⁰⁻¹⁴² Consequently, there is considerable theoretical and experimental interest in this reaction. In particular, it is important

to determine if the preference for inversion of configuration is determined by the existence of nonstatistical effects in the reaction mechanism.

We used the methods of molecular dynamics simulations to investigate the reaction mechanism of thermal decomposition of DBHD. The corresponding results are presented in Chapter V. In this chapter, we address the problem of the ring inversion dynamics of BCP, which corresponds to the product channel for the thermal decomposition of DBH. Before describing the calculation method and our results, we present in the next section a review of the available experimental and theoretical data related to the thermal skeletal inversion of BCP, which were used in the construction of the potential-energy surface for this system.

Selected Data Related to Thermal Skeletal Inversion of Bicyclo(2.1.0) pentane

The first study of thermal *cis-trans* isomerization reaction of 2-methyl(2.1.0)bicyclopentane was reported by Chesick.¹⁴³ The reaction was assumed to take place with an incomplete rupture of the bridgehead-bridgehead bond in the transition state and a partial release of the bicyclic strain. In addition, an activation energy of 38.9 ± 0.8 kcal/mol has been determined from the analysis of reaction kinetics in the range 203.3 to 231.7° C. Later, using a microwave spectrometry technique, Mathur and Harmony¹⁴⁴ have obtained an activation energy of 38.5 ± 1.4 kcal/mol for interconverting *cis-exo-* and *cis-endo-2,3-dideuteriobicyclo(2.1.0)pentane*. The similarity of the activation energy values obtained in these two studies reveals that the methyl group in 2-methyl(2.1.0)bicyclopentane has a small influence upon the activation process, which is primarily determined by partial breaking of the bridgehead-bridgehead bond.

A more precise determination of the activation parameters for skeletal inversion of *cis*-exo-2,3,-dideuteriobicyclo(2.1.0)pentane has been reported by Baldwin and Ollerenshaw based on NMR spectroscopy.¹⁴⁵ They have determined that for BCP the skeletal inversion equilibrium constant is 1, with an identical activation energy of 37.8 ± 0.1 kcal/mol for interconversion of *cis*-exo \longleftrightarrow *cis*-endo systems.

A great deal of interest in the thermal skeletal inversion of BCP was related to the characterization of the reaction transition state leading to 1,3-cyclopentadiyl diradical.

The direct experimental observation of the 1,3-cyclopentadiyl radical was first reported in 1975¹⁴⁶ in an electron spin study under matrix-isolated conditions. Based on the temperature dependence of the electron spin resonance spectra and the technique of chemically-induced dynamic nuclear polarization (CIDNP), it was concluded that the cyclopentadiyl radical has a triplet ground state, while the lowest singlet represents a transition state between the *cis* and *trans* bicyclopentanes.¹⁴⁶ A barrier height of 2.3 ± 0.2 kcal/mol for formation of BCP from 1,3-cyclopentadiyl has been determined. However, it was noted¹⁴⁶ that the experimental data were inconsistent with the predictions of Benson-type thermochemical calculations, which suggest the existence of a minimum on the singlet surface with a well-depth of 9 kcal/mol. This controversy between experimental data and thermochemical estimates was also emphasized in the study of Hermann and Goodman.¹⁴⁷ Their experimental data, obtained using time-resolved photoacoustic calorimetry, also suggest that the singlet diradical is a transition state or a local minimum with a barrier for ring closure significantly smaller than that predicted from thermochemical estimates.

A more quantitative characterization of the geometry of 1,3-cyclopenta-

diyl radical has been obtained using *ab initio* electronic structure theory at the self-consistent-field (SCF) and configuration interaction, singles and doubles (CISD), levels of theory.^{148,149} The theoretical studies of Conrad *et al.*¹⁴⁸ represent the first theoretical prediction of the structure of a cyclic diradical. Based on two-configuration SCF calculations, they found that under the constraint of C_{2v} symmetry, the triplet ground state is 0.9 kcal/mol below the singlet state, in good agreement with the work of Buchwalter and Closs.¹⁴⁶ For the planar configuration of the diradical, a bridgehead C-C bond distance of 2.37 Å has been determined. A similar difference value of about 1 kcal/mol between the ground-state triplet and the singlet diradical has been found by Sherrill *et al.*¹⁴⁹ at the CISD level, together with additional evidence for the existence of a shallow local diradical minimum on the singlet potential-energy surface. In addition, a transition state of C_s symmetry which connects the ground state of BCP molecules with the singlet state of 1,3-cyclopentadiyl radical has been identified.

General Calculation Method

In the next sections of the present chapter, we describe the development of a potential-energy surface for BCP.¹⁵⁰ This surface can be used to test different aspects of the molecular dynamics, but in the present work we focus on the skeletal inversion process. The general methodology used in this study is similar to that employed for analysis of other systems such as Si_2H_6 ⁵⁴, $C_2H_4F_2$ ^{41,42} and hexahydro-1,3,5-trinitro-1,3,5-triazine (RDX).¹⁵¹ The total potential is essentially expressed as a sum of bond stretching interactions, plus bending potentials along with torsional terms. Different asymptotic limits of the interaction terms are incorporated through multiplication by appropriate switching functions. Adopting a semiempirical methodology in the construction

of the potential-energy surface, we seek a parametrization of the potential terms which allows us to reproduce the maximum number of known physical-chemical features. The quantities used in the parameter adjustment include the equilibrium bond lengths, bond angles, and the experimental fundamental vibrational frequencies for the reactants and products, the exo- and endothermicities for each of the reaction channels, and the reaction profiles and barrier heights. The main difficulties of the above procedure are related to the lack of measured or calculated data in the critical regions of the potential. This is particularly true for various transition states for which the geometry, fundamental frequencies and barrier heights are not generally known. In these cases, the errors may be large, especially when the dynamical processes analyzed are sensitive to the topographical features that are not properly described. Another difficulty involves the fact that the mathematical functions and type of parametrization used to describe different features of the energy surface are often highly coupled. This makes parameter adjustment difficult and tedious. On the positive side, experience has shown that when structures, vibrational frequencies, reaction energetics, and potential barriers for all important reaction channels have been accurately fitted, the computed dynamics usually accurately reproduces the measured experimental results.

The bond dissociation energies for BCP have been estimated using the available thermochemical data and results of *ab initio* molecular orbital calculations performed at the fourth order Möller Plesset (MP4) perturbation theory level using a 6-31G** basis set. The potential parameters have been adjusted to reproduce the equilibrium geometry of BCP and of the 1,3-cyclopentadiyl radical, the barrier for the ring inversion, and the fundamental frequencies of BCP. For random energization of the vibrational modes in the range 100-250 kcal/mol, trajectory calculations have been performed to

determine the character of the reaction mechanism and to extract the microcanonical reaction rates. Using a projection method of the instantaneous Cartesian velocities onto the normal mode vectors and classical trajectory calculations, the skeletal inversion and the intramolecular energy flow in BCP are studied for different types of excitation. The character of the reaction dynamics has been also investigated using the results of power spectra calculated at different energization levels. The total intramolecular vibrational relaxation rates for the energy flow from the flap mode have been extracted from the time dependence of the average total normal-mode energy in this mode and compared with the microcanonical ring inversion rates. The totality of the results has been found to support the statistical character of the ring inversion of BCP.

Potential-Energy Surface

A. Evaluation of Bond-Dissociation Energies in BCP

A major impediment in the development of a realistic, global potential-energy surface for BCP is the lack of data on bond dissociation energies. In this section, we present an approximate method for estimating these energies from thermochemical experimental data and *ab initio* quantum calculations. The atom designation and numbering used throughout this paper are given in Fig. 17.

The method utilized to determine the bond dissociation energies for BCP contains the following assumptions and computational steps:

(1) We assume that the values of the C-C bond dissociation energies in cyclobutane and cyclopropane, which may be calculated using the available thermochemical data and the experimental C-H bond dissociation energies,

can be transferred to the corresponding C-C bonds in the cyclobutyl and cyclopropyl rings of BCP, excepting the bridgehead C-C bond. Since the BCP molecule possesses C_s symmetry, equal values of the bond dissociation energies for the equivalent C-H bonds in the cyclopropyl and cyclobutyl rings have been assumed. Similarly, the energies of the two C-H bonds at the bridgehead carbon atoms have been taken to be equal.

(2) The C-H bond dissociation energies in cyclopropane, cyclobutane and BCP are calculated using *ab initio* molecular orbital methods at the MP4/6-31G** level. However, due to the fact that accurate quantitative calculations of the bond dissociation energies require both larger basis sets and a higher level of correction for electron correlation, we expect the computed values to be close, but not identical to, the experimental data. Consequently, for the case of cyclopropane and cyclobutane, where the experimental C-H bond dissociation energies data are available, we have determined the ratio of theoretical (calculated) to experimental data. The resulting values of this ratio are assumed to be transferable to the case of the corresponding C-H bond dissociation energies in BCP, for which new estimated values were calculated. For the bridgehead C-H bonds, we assume that the average of the cyclopropane and cyclobutane ratios may be employed.

(3) The bridgehead C-C bond dissociation energy in BCP was evaluated using the available thermochemical data for BCP and the C-C and C-H bond dissociation energies computed using the procedures described above.

The *ab initio* molecular orbital calculations were carried out using the Gaussian 92 systems of programs.¹² The structure of BCP was first optimized under C_s symmetry at the restricted Hartree-Fock (RHF) level using analytical gradients and the internal 6-31G*^{20,21} basis set, and then refined within the Möller-Plesset¹⁵² perturbation theory approximation using both 6-31G* and

6-31G**^{20,21} basis sets. A parallel set of calculations was performed for cyclopropane (D_{3h} symmetry) and cyclobutane (D_{2d} symmetry). Harmonic frequency analyses using analytical second derivatives were carried out at the HF/6-31G**/6-31G* level of theory. The optimized geometries for all three molecular systems are compared with the available experimental data in Table V.

In the case of BCP at the MP2/6-31G* level, the root-mean-square deviation of the calculated data from the experimental values is 0.0052 Å for bond lengths and 0.95° for bond angles; at the MP2/6-31G** level, the same quantities are 0.0058 Å and 0.85°, respectively. As can be seen, the agreement of calculated structural parameters with experimental values is very good.

The effect of higher level corrections for electron correlation was obtained by single-point calculations at the MP4/6-31G** level using the optimized geometries obtained at the MP2/6-31G** level. Total energies of the previous optimized structures are given in Table VI.

The energies of cyclopropyl, cyclobutyl and the corresponding radicals in BCP (see Table II) were calculated at the UMP4/6-31G** level using the optimized MP2/6-31G** geometries. In the case of the BCP molecule, the radicals obtained by removal of the hydrogen atoms H₆, H₉ and H₁₃ were also considered. The total energy of these radicals was calculated at a fixed MP2/6-31G** geometry to assure minimum changes in the strain energy. Zero-point energies of the radical structures have been evaluated using the HF/6-31G* geometries.

The final values of the calculated bond dissociation energies are given in Table VII. These values include zero-point energy corrections scaled by a factor of 0.91 as recommended by Grev *et al.*¹⁵⁷ to take into account the fact that this level of theory generally yields vibrational frequencies that are too

large. As can be seen, there is fair agreement between the experimental and calculated C-H bond energies for cyclopropane and cyclobutane. The estimated values of C-H bond dissociation energies for BCP (column 3 in Table VII) have been evaluated using the scaling method previously described.

The C-C bond dissociation energies in cyclopropane and cyclobutane have been calculated using the thermochemical data given in Table VIII and the experimental values of C-H bond energies presented in Table VII. The results obtained were transferred identically to the corresponding C-C bonds in the cyclobutyl and cyclopropyl rings of BCP. Finally, the bridgehead C-C bond dissociation energy in BCP (see Table VII) was determined using the thermochemical data given in Table VIII and the estimated C-H and C-C bond dissociation energies.

B. General Requirements on the Potential-Energy Surface

The first requirement imposed in the development of an empirical global potential is that its stationary points reproduce the equilibrium configuration for the system of interest. In the case of BCP, the molecular structure has been determined by both electron diffraction¹⁶³ and microwave spectroscopy.^{155,156} The results of these two studies contain significant discrepancies, particularly for the case of the C-C single bonds. In this study, we use the parameters reported in the microwave studies which are supported by several *ab initio* self-consistent field (SCF) calculations,¹⁶⁴⁻¹⁶⁶ as well as our results (see Table V). We note that in the equilibrium configuration, the angle between the planes of the three- and four-member rings, α , is 67.26° (see also Fig. 17).

A second requirement used in the construction of the potential surface is related to the accurate prediction of the main features of the BCP geometry in the planar configuration corresponding to the 1,3-cyclopentadiyl radical.

A detailed investigation of the stationary points on the singlet surface of the diradical has been reported by Sherrill *et al.*¹⁴⁹ It has been found that the transition state, denoted C_s' , which connects the ground state of the BCP molecule to the singlet diradical, has C_s symmetry and corresponds to an angle $\alpha_{tr}=24.96^\circ$. The theoretical investigations of the singlet surface at the TCSCF (two-configuration self-consistent field) level have revealed a complex structure around the singlet C_{2v} structure ($\alpha=0^\circ$). Particularly, two equivalent C_2 local minima and two equivalent transition states are found to be connected with a C_{2v} state characterized as a saddle point. The C_2 local minima are also connected *via* C_s transition states. However, the energetic differences between these local minima and transition states are small, i.e., less than 0.55 kcal/mol, which indicates that the diradical potential-energy surface is quite flat. For the total depth of the singlet diradical region relative to the C_s' transition state, a value of 1.28 kcal/mol was found at the CISD level.¹⁴⁹

For the purpose of the present study, we have chosen to adjust the parameters of the surface so as to reproduce the main features of the singlet diradical under C_{2v} geometry. Relative to the equilibrium configuration of the BCP molecule, the most significant geometrical changes occur for the bridgehead C-C bond distance, for the $H_6-C_5-H_6$ bond angle and for the angles formed by the bonds of hydrogen atoms 6 and 7 with the cyclopropyl ring. These changes have been incorporated into the potential by specific modifications of the equilibrium bond distances and bond angles using switching functions which smoothly make connections between the limiting values of the geometrical parameters corresponding to the equilibrium and planar configurations.

A key topographical feature of the potential-energy surface is the accurate prediction of the barrier height for skeletal inversion of BCP, for which

a value of 37.8 ± 0.1 kcal/mol has been found experimentally.¹⁴⁶ This barrier height was taken to correspond to the transition-state geometry (C_s') characterized by the angle α_{tr} between the cyclopropyl and cyclobutyl planes.

Finally, we require that the global potential predicts the BCP fundamental vibrational frequencies with acceptable accuracy. The experimental gas-phase vibrational spectra of BCP, together with assignments for all 33 fundamental frequencies, has been reported by Bragin and Guthais.¹⁶² However, to the best of our knowledge, a normal-coordinate analysis for BCP was not carried out and consequently, a complete set of force constants is still not available. Thus, we have iteratively adjusted the force constants in our potential to obtain the best fit possible.

C. Technical Aspects of the Potential-Energy Surface

We assume that the potential-energy surface of the BCP molecule can be described as a superposition of analytical functions of interatomic distances and bond angles. For the structure illustrated in Fig. 17, we have used the bond and angle assignments given in Table IX. The total potential-energy surface is constructed as follows:

$$V_{\text{total}} = V_{\text{stretch}} + V_{\text{bend}} + V_{\text{dih}} + V_{\text{flap}} . \quad (\text{IV.1})$$

The potential V_{stretch} represents a sum of bond stretching potentials which are taken to be Morse-type functions

$$V_{\text{stretch}} = \sum_{\substack{i=1 \\ i \neq 4}}^{14} D_i \{ \exp [- 2\beta_i (r_i - r_i^0)] - 2 \exp [- \beta_i (r_i - r_i^0)] \} \\ + D_4 \{ \exp [- 2\beta_4 g(r_4, \alpha)] - 2 \exp [- \beta_4 g(r_4, \alpha)] \} , \quad (\text{IV.2})$$

where

$$g(r_4, \alpha) = r_4 - r_4^0 - (r_4^f - r_4^0) f_{sw}(\alpha) \quad (IV.3)$$

and

$$f_{sw}(\alpha) = \tanh^2[b_{sw}(\alpha^2 - \alpha_{eq}^2)] \quad (IV.4)$$

In Equation (IV.2), D_i represents the potential well-depth, β_i is the curvature parameter and r_i^0 is the equilibrium bond distance for the bond with index i . The special form of the term $i=4$ in equation (IV.2) takes into account the increase of the bridgehead C-C bond distance as function of the decrease to zero of the flap angle α .

The bending potential V_{bend} is taken to be a superposition of quadratic forms

$$\begin{aligned} V_{bend} = & \sum_{i=1}^8 0.5 k_i (\theta_i - \theta_i^0)^2 + \sum_{i=23}^{29} 0.5 k_i (\theta_i - \theta_i^0)^2 \\ & + \sum_{i=9}^{22} 0.5 k_i [\theta_i - \theta_i^0 - (\theta_i^f - \theta_i^0) \cos(\frac{\pi \alpha}{2 \alpha_0})]^2, \end{aligned} \quad (IV.5)$$

where k_i represents the bending force constant associated with the angle θ_i , which takes the value θ_i^0 in the equilibrium configuration. The analytical form used for the angles 9-22 models the change of the equilibrium angles from the value θ_i^0 to θ_i^f ($i=9-22$), corresponding to a variation of the flap angle from $\alpha=\alpha_0$ in the equilibrium state to $\alpha=0$ in the planar configuration.

The dihedral potential V_{dih} in Eq. (IV.1) is given by

$$V_{dih} = 0.5 k_d \Phi^2, \quad (IV.6)$$

where k_d is the dihedral force constant and Φ is the C₁-C₂-C₃-C₄ dihedral angle with $\Phi = 0$ in the equilibrium configuration.

The flap potential, V_{flap} , is represented by a truncated cosine series

$$V_{\text{flap}} = \sum_{j=0}^6 a_j \cos(j\alpha) \quad (\text{IV.7})$$

This form of the flap potential, together with the rest of the terms in Eq. (IV.1), assures a symmetric reaction profile for positive and negative flap angles, with a maximum fitted to the experimental value of the barrier height. The flap angle corresponding to the barrier maximum was taken equal to α_{tr} . In addition, the analytical expression used in Eq. (IV.7) reproduces the small well, whose depth is $\Delta E_{\text{gap}} \approx 1 \text{ kcal/mol}$, along the reaction profile between the angles $-\alpha_{\text{tr}}$ and α_{tr} . The flap angles $\alpha_0 = \pm 67.26^\circ$ characterize the two equivalent equilibrium configurations for the ring inversion.

The parameters r_i^0 and θ_i^0 in Eqs. (IV.2), (IV.3) and (IV.5) are adjusted to reproduce the equilibrium experimental geometry of BCP given in Table V. The values for r_4^f and θ_i^f have been fitted to the corresponding parameters evaluated by *ab initio* calculations¹⁴⁹ for the planar configuration. The preexponential Morse factors in Equation (IV.2) are set equal to the estimated bond dissociation energies given in Table VII. The parameters a_0 - a_6 in the flap potential, together with the other terms in the potential, have been adjusted to the computed reaction profile and the measured flap fundamental frequency. The remaining parameters of the potential, i.e. β_i , k_i , k_d , have been adjusted to yield reasonable values for the remaining fundamental experimental frequencies. The numerical values of all parameters used in construction of the potential-energy surface are given in Tables X, XI, and XII.

D. Properties of the Potential Surface

The equilibrium structures for the system have been determined by running damped trajectories. This method consists of computing a trajectory with all initial momenta set to zero. Each time the kinetic energy attains a maximum, all momenta are again set to zero. This procedure is repeated until the system converges to a local minimum. The predicted structure for BCP in the equilibrium configuration is in excellent agreement with reported experimental data (see Table V). The predicted structure for the planar configuration is given in Table XIII, together with the corresponding C_{2v} structure determined by *ab initio* calculations.¹⁴⁹ The small differences which appear for bond lengths are due to the fact that the other equilibrium bond lengths were not adjusted to the values specific for the planar configuration, with the exception of the r_{14} bond distance.

The reaction profile and barrier height given by our potential for skeletal inversion in BCP are shown in Fig. 18. This figure shows the calculated values of the total potential as a function of the flap angle with all the other internal variables being relaxed to their most stable configuration. The barrier height is 37.799 kcal/mol. The barrier crest occurs at $\alpha_{tr} = \pm 25.2^\circ$. This barrier height value is in very good agreement with the experimental value of 37.8 kcal/mol.¹⁴⁴ The depth of the potential well at top of the potential profile is 1.6 kcal/mol, which is in good agreement with calculated data¹⁴⁹ and experimental results,^{145,146} which suggest a value in the range 1-3 kcal/mol.

The experimental and calculated normal mode frequencies are compared in Table XIV. The calculated values were obtained using analytical second-derivatives of the potential. For the flap mode, the calculated frequency

$\nu_2=475\text{ cm}^{-1}$ differs by 59 cm^{-1} from the experimental value. The average root-mean-square deviation between the experimental and the calculated frequencies is 47 cm^{-1} .

Computational Procedures

A. Trajectory Calculations

In this section, trajectory methods are utilized to investigate the statistical/nonstatistical character of the ring inversion in BCP. In addition, the rate of energy transfer from the flap mode into all the other modes to which the flap mode is effectively coupled is calculated. The overall objective is to determine the statistical or nonstatistical character of the dynamics followed in the ring skeletal inversion of BCP.

In order to obtain qualitative information on intramolecular energy-transfer dynamics in BCP, two types of initial excitations have been used. Both procedures employ a projection method^{46,47} to insert energy either randomly or into a specified normal mode of the molecule. This method, described in Chapter II, is based on the calculation of the normal-mode velocities by projection of the Cartesian velocities onto the normal-mode vectors. The advantage of working with the normal-mode kinetic energy instead of the total energy comes from the fact that the kinetic energy matrix is diagonal when expressed in terms of the normal-mode velocities. Since there are no kinetic coupling terms and since the potential energy is not involved in this analysis, the procedure gives a classically exact description of the intramolecular energy flow in the molecule.

With the molecule initially placed in the equilibrium configuration predicted by the semiempirical surface, zero-point vibrational energy is inserted

into the normal modes, while the normal mode velocities for rotation and translation are set to zero. The equations of motion in a space-fixed Cartesian coordinate system are integrated for a random period of time

$$t_r = \xi T_m \quad (IV.8)$$

using a fourth-order Runge Kutta routine¹ with a fixed step size of 0.01 time units (1 t.u.=1.018 10⁻¹⁴ s). Four significant digits of energy conservation are generally achieved. In Eq. (IV.8), ξ is a random number chosen uniformly on the interval [0,1] and T_m is the vibrational period for the lowest frequency mode in the molecule. At this point, the desired excitation energy is then inserted either randomly or into a given normal mode. The time t_r is taken to be zero for the purpose of rate calculations. The random choice of t_r for an ensemble of trajectories assures a properly weighted average over the vibrational phases.

In the case of a random distribution of the excitation energy, ensembles of 500-800 trajectories were calculated. Each trajectory was followed for maximum 500 t.u.

The investigation of energy flow from the flap mode has been executed by exciting this mode only subsequently to zero-point energy partitioning as described above. The instantaneous normal-mode velocities or equivalently the mode kinetic energies are computed after every tenth integration step. The average total energy in mode i ($i=1, 33$) can then be calculated from

$$\langle E_i(t) \rangle = 2(\Delta t)^{-1} \int_{t_0}^{t_0+\Delta t} K_i(\tau) d\tau, \quad (IV.9)$$

where $K_i(t)$ represents the normal-mode-kinetic energy of mode i and t is a time in the interval $t_0 \leq t \leq t_0 + \Delta t$. The time interval Δt is chosen to average out most

of the fluctuations in $K_i(t)$ due to the interconversion of potential and kinetic energy within the same mode. If the initial excitation energy is placed into mode i , the temporal variation of $\langle E_i(t) \rangle$ is directly related to the rate of energy flow from the mode i . For a first order relaxation process, the intramolecular vibration rate λ_i can be deduced from equation⁵⁹

$$\langle E_i(t) \rangle = [\langle E_i(0) \rangle - \langle E_i(\infty) \rangle] e^{-\lambda_i t} + \langle E_i(\infty) \rangle \quad (\text{IV.10})$$

provided that there is only one time scale for energy relaxation from mode i . In Eq. (IV.10), $\langle E_i(\infty) \rangle$ is the statistical equilibrium value. This expression has been used to evaluate the total intramolecular vibrational rate (IVR) coefficient λ_2 from the flap mode.

B. Power Spectra

It was shown in Chapter II that the autospectral density function can provide useful information on the intramolecular dynamics of polyatomic molecules. Whenever quasiperiodic dynamics exist, sharp peaks corresponding to fundamentals and overtones will be present in the autospectral density function.⁶⁸ In contrast, ergodic dynamics determine a relaxation of the autospectral density function with a corresponding broadening of spectra over a wide band of frequencies.

The utilization of the power spectra obtained from classical trajectories has been proven to be a useful diagnostic tool for identifying the presence of statistical/nonstatistical dynamics in unimolecular reactions of large, complex molecules.^{69,70} Consequently, we have used this methodology in the present study to gain insight into the dynamics of ring skeletal inversion of BCP.

For positive frequencies $0 \leq f < \infty$, the autospectral density function of a

quantity $x(t)$ is defined by⁷¹

$$G_{xx}(f) = 2 \lim_{T \rightarrow \infty} \frac{1}{T} \langle |X_T(f)|^2 \rangle, \quad (\text{IV.11})$$

where $X_T(f)$ is the finite Fourier transform of $x(t)$ of length T , given by

$$X_T(f) = X(f, T) = \int_0^T x(t) e^{-i2\pi ft} dt \quad (\text{IV.12})$$

and $\langle \dots \rangle$ represents an ensemble average, for fixed f , over n_d sample records.

In the case of stationary random data, it can be shown⁷¹ that the autospectral density function $\hat{G}_{xx}(f)$ is twice the Fourier transform of the autocorrelation function and can be estimated as

$$\hat{G}_{xx}(f) = \frac{2}{n_d N \Delta t} \sum_{j=1}^{n_d} |x_j(f_k)|^2, \quad k=0, 1, \dots, \frac{N}{2} \quad (\text{IV.13})$$

Here, each record segment of duration $T=N\Delta t$ contains N data values $\{x_{jn}\}$, $n=0, 1, \dots, N-1$, $j=1, 2, \dots, n_d$. The quantities $X_j(f_k)$ represent the Fourier components for each segment

$$X_j(f_k) = \Delta t \sum_{n=0}^{N-1} x_{jn} \exp\left(-\frac{i2\pi kn}{N}\right) \quad (\text{IV.14})$$

where Δt is the sampling interval and f_k is the k th frequency component of a set of $N/2 + 1$ discrete frequencies in the range $0 \leq f_k \leq (2\Delta t)^{-1}$. The fast Fourier transform (FFT) algorithm¹⁶⁷ provides a powerful technique for evaluation of the autospectral density function. Assuming the normalization condition of FFT coefficients (H1) is satisfied, Parseval's theorem¹⁶⁷ gives

$$\sum_{n=0}^{N-1} |x_{jn}|^2 = \frac{1}{N} \sum_{l=0}^{N-1} |H_l|^2. \quad (\text{IV.15})$$

For a given set of N data, the autospectral density function scaled to the sampling interval can be evaluated in terms of the (N/2+1) FFT coefficients as¹⁶⁸

$$\begin{aligned} \hat{G}_{xx}(0) &= \frac{1}{N} |H_0|^2, \\ \hat{G}_{xx}(f_j) &= \frac{2}{N} |H_j|^2, \quad j=1,2,\dots, \left(\frac{N}{2}-1\right) \end{aligned} \quad (\text{IV.16})$$

$$\hat{G}_{xx}(f_{N/2}) = \frac{1}{N} |H_{N/2}|^2.$$

In this case, the resolution of the spectrum is determined by the total length of the record

$$\Delta f = \frac{1}{T} = \frac{1}{N \Delta t} \quad (\text{IV.17})$$

In the present study, Eq. (IV.16) has been used to evaluate the power spectra by transforming the time histories of the internal coordinates (bond lengths, bond angles, etc.) from single trajectories. Before transforming, every data set of N sampling points was modified as follows

$$x'_{jn} = \frac{x_{jn} - \langle x_j \rangle}{|x_{jn} - \langle x_j \rangle|_{\max}}, \quad n=0,1,\dots,N-1, \quad j=1,2,\dots,n_d, \quad (\text{IV.18})$$

where $\langle x_j \rangle$ is the mean value of the N data recorded during trajectory j. The denominator in Eq. (IV.18) represents the absolute maximum deviation of the

values x_{jn} relative to the average value $\langle x_j \rangle$. This procedure provides a set of dimensionless, reduced coordinates which are stationary, with zero average and with values in the range $[-1,1]$. The above method was used to evaluate the corresponding individual power spectra for every internal coordinate. The composite power spectrum was then calculated as a superposition of these individual spectra.

Results and Discussions

The ring inversion dynamics in BCP have been investigated for internal excitation energies between 100-250 kcal/mol. In all calculations, zero point energy of 71.04 kcal/mol is partitioned into the normal modes using the projection method previously described.^{46,47} After averaging over the vibrational phases, the excitation energy is randomly distributed over the 33 vibrational modes.

Figure 19 shows the typical reaction coordinate (flap angle) as a function of time for a trajectory when ring inversion takes place. Initially, the flap angle vibrates around the equilibrium value. When the energy in the flap mode exceeds the barrier height, the ring inversion takes place. Subsequently, the flap angle vibrates around the new equilibrium position.

Decay plots are obtained from ensembles of 500 trajectories for the energy range 130-250 kcal/mol and 700 trajectories for excitation energies between 100-120 kcal/mol. A panel of selected plots at different excitation energies is presented in Fig. 20. As can be seen, these plots generally exhibit a high degree of linearity, as expected for a first-order process in a statistical system.

Microcanonical rate constants, $k(E)$, have been extracted by least-squares fitting of the decay plots, using

$$\ln (N_t/N_0) = -k(E) t , \quad (\text{IV.19})$$

where N_t is the number of unreacted trajectories at time t and N_0 is the total number of trajectories in the ensemble. The rate coefficients obtained from the slopes of the least-square fits are given in Table XV.

The rate coefficients data presented in Table XI have been fitted to the RRK equation⁵²

$$k(E) = \nu [(E - E_0) / E]^{s-1} \quad (\text{IV.20})$$

where E_0 is taken to be the barrier height for reaction ($E_0=37.8$ kcal/mol). For a 95% confidence interval,⁷¹ the resulting RRK parameters are $\nu=1.22\pm 0.26$ ps⁻¹ and $s=12.28\pm 0.72$. The least-squares regression coefficient is $r=0.994$. The RRK fit is shown as a curve in Fig. 21 together with the calculated rate coefficients. These results suggest that at internal energies between 100-250 kcal/mol, the behavior of the system is statistical. However, coupling of the modes is not complete. This fact is suggested by the value of the s parameter in Eq. (IV.20), which is about one third of the full classical limiting value of $3N-6=33$.

An additional investigation of the statistical/nonstatistical character of the ring inversion in BCP has been carried out using power spectra methods. In each case, ensembles of 20 trajectories were used in the calculations to mimic the distribution of the classical initial conditions over a specified initial region of the phase space. The internal coordinates were recorded after every 40th integration step and the trajectories were followed for a time period of 818.8 t.u. A resolution of 4.0 cm⁻¹ was obtained for all power spectra presented in this study.

The composite power spectra for BCP and for the flap angle at zero-point energy and at different excitation energies are shown in Figure 22. In the latter cases, internal excitation energies of 120 kcal/mol and 225 kcal/mol were initially distributed at random over the normal modes using projection methods.^{46,47} Analysis of the spectra for trajectories containing only zero-point energy [see Figs. 22(a) and 22(b)] shows that the spectral peaks corresponding to different modes are more distinct and well resolved. As the internal energy increases, a significant broadening of the spectral lines occurs which, at even higher energies, leads to the overlap of spectral features. This effect is directly related to the enhancement of the mode coupling, and consequently, to an increase of the intramolecular vibrational relaxation (IVR) rates, with the increase in the total excitation energy. In addition, a red shift of the spectra at higher energies is observed. The disappearance of discrete spectral bands at higher energies is even more pronounced in the spectra of the flap angle [see Figs. 22(b), 22(d) and 22(f)]. These results suggest a significant coupling of modes and correspondingly, an internal dynamics which can be well described by statistical theories. A similar interpretation was given for the case of unimolecular bond-fission reaction of 2-chloroethyl radical.⁷⁰ In this same study,⁷⁰ it was shown that the spectral bands for nonstatistical systems remain reasonably well resolved even at higher internal energies.

A quantitative characterization of the intramolecular energy transfer in ring inversion reactions of BCP can be obtained by evaluating the total IVR rate for the energy flow from the flap mode. This can be done by examining the time dependence of the normal mode energies for different excitation levels of the flap mode. Ensembles of 20 trajectories, each initially having zero-point energy in all normal modes and a given excitation energy in the flap mode have been employed.

A typical result for the time variation of the instantaneous kinetic energy of the flap mode ν_2 is represented in Fig. 23. The initial state has zero-point energy inserted in all vibrational modes and an excitation energy of 30 kcal/mol in the flap mode. The oscillations in energy reflect the transformation of kinetic into potential energy, and vice versa. As can be seen, the amplitude of these oscillations decreases to near equilibrium levels after about 20 t.u. This result indicates a very fast energy flow out of the flap mode.

The pathways of energy flow from the flap mode have been determined by examining the time variation of the kinetic energy in all the other normal modes. Figure 23 also shows the kinetic energy for the modes with the most significant increase in the energy envelope function. An examination of these plots indicates that the major transfer pathways are to the ν_{21} and ν_{24} modes which correspond to the bridgehead CH deformation and CH_2 deformation motions.

In order to determine the time variation of the average total energy of the ν_2 mode, ensembles of 20 trajectories with a duration of 500 t.u. have been computed. For every trajectory, the calculated average energy values have been obtained using Eq. (IV.9), with a time interval $\Delta t = 30$ t.u. A typical result is shown in Fig. 24 for an initial 30 kcal/mol excitation of the flap mode in excess of zero-point energy. As can be seen, after a rapid energetic transfer from the flap mode, the average mode energy is found to oscillate about the equilibrium value. The total average decay rate coefficient can be extracted using the exponential dependence given by Eq. (IV.10). The resulting total IVR rates for different excitation energies of the flap mode are presented in Table XVI. As can be seen, the total IVR rates are large compared to the ring inversion rates, which is a necessary condition for the absence of nonstatistical effects.

Summary

We have developed a global potential-energy surface that describes the ring inversion in BCP. The potential includes bond stretching and bending terms as well as torsional terms. The geometrical parameters in the expression of the potential have been adjusted to reproduce the equilibrium structure of the BCP molecule and the planar configuration corresponding to the 1,3-cyclopentadiyl radical.

Bond dissociation energies in BCP have been estimated using the available thermochemical experimental data for cyclopropane, cyclobutane and BCP, as well as results of *ab initio* calculations carried out at the MP4/6-31G** level of theory. Other potential parameters are adjusted to fit the experimental barrier height and the reaction profile. The force constant parameters in the potential are obtained by fitting the experimental fundamental vibrational frequencies.

Projection methods^{46,47} and molecular dynamics simulations are used to investigate the type of statistics obeyed by the flap motion of BCP. For random energization of the vibrational modes in the range 100-250 kcal/mol, the results of the trajectory calculations suggest statistical behavior. The RRK parameters extracted from the analysis of the microcanonical rate constants for the ring inversion are $\nu=1.22\pm 0.26 \text{ ps}^{-1}$, $s=12.28\pm 0.72$. Statistical dynamics are also indicated by the results of power spectra analyses, which show the existence of large modal couplings at high energies.

The total IVR rates for energy transfer from the flap mode have been extracted from the temporal dependence of the average mode energy. For excitation levels between 30-60 kcal/mol, the calculated IVR rates are

significantly higher than the ring inversion rates, which is a necessary condition for statistical theories to hold.

Table V

Ab initio calculated and experimental observed geometries for cyclopropane, cyclobutane and bicyclo(2.1.0)pentane.

| Compound | Bond or angle | HF/ 6-31G* | MP2/ 6-31G* | MP2/ 6-31G** | Exp.a) |
|---|--|---------------|----------------|-----------------|-------------|
| cyclopropane | R(C-C) | 1.497 | 1.503 | 1.502 | 1.514±0.002 |
| | R(C-H) | 1.076 | 1.084 | 1.080 | 1.082±0.003 |
| | θ(H-C-H) | 114.0 | 114.2 | 114.4 | 116.5 |
| cyclobutane | R(C-C) | 1.545 | 1.545 | 1.543 | 1.548±0.003 |
| | R(C-H) | 1.084 | 1.094 | 1.090 | 1.092 |
| | θ(C-C-C) | 88.53 | 87.91 | 87.78 | 87.2 |
| | θ(H-C-H) | 108.47 | 108.74 | 108.9 | |
| | θ(C-C-H _e) | 117.69 | 118.43 | 118.58 | |
| | θ(C-C-H _a) | 111.68 | 110.99 | 110.77 | |
| | τ(C ₁ -C ₂ -C ₄ -C ₃) | 154.21 | 149.25 | 148.37 | 145-160 |
| bicyclo(2.1.0) pentane | R(C ₁ -C ₂) | 1.528 | 1.527 | 1.526 | 1.528±0.002 |
| | R(C ₁ -C ₄) | 1.512 | 1.528 | 1.527 | 1.536±0.001 |
| | R(C ₁ -C ₅) | 1.493 | 1.499 | 1.498 | 1.507±0.002 |
| | R(C ₂ -C ₃) | 1.558 | 1.559 | 1.558 | 1.565±0.001 |
| | R(C ₁ -H ₈) | 1.075 | 1.086 | 1.081 | 1.082±0.001 |
| | R(C ₅ -H ₆) | 1.076 | 1.086 | 1.082 | 1.088±0.001 |
| | R(C ₅ -H ₇) | 1.079 | 1.089 | 1.085 | 1.090±0.001 |
| | R(C ₂ -H ₉) | 1.083 | 1.093 | 1.088 | 1.085±0.001 |
| | R(C ₂ -H ₁₀) | 1.085 | 1.096 | 1.091 | 1.097±0.001 |
| | θ(H ₆ -C ₅ -H ₇) | 114.0 | 114.3 | 114.6 | 116.7±0.1 |
| | θ(H ₈ -C ₁ -H ₅) | 121.6 | 121.6 | 121.5 | 121.2±0.1 |
| | θ(H ₈ -C ₁ -H ₄) | 129.0 | 128.8 | 128.9 | 128.6±0.1 |
| | θ(C ₁ -C ₂ -H ₉) | 113.1 | 113.1 | 113.1 | 113.3±0.1 |
| θ(C ₁ -C ₂ -H ₁₀) | 115.9 | 115.7 | 115.7 | 115.2±0.1 | |

Table V (continued)

| Compound | Bond or angle | HF/ 6-31G* | MP2/ 6-31G* | MP2/ 6-31G** | Exp. ^{a)} |
|----------|---|---------------|----------------|-----------------|--------------------|
| | $\theta(\text{C}_3\text{-C}_2\text{-H}_9)$ | 112.1 | 111.9 | 111.8 | 111.9±0.1 |
| | $\theta(\text{C}_3\text{-C}_2\text{-H}_{10})$ | 116.9 | 117.0 | 117.0 | 116.6±0.1 |
| | $\theta(\text{H}_1\text{-C}_5\text{-H}_6)$ | 115.5 | 115.4 | 115.3 | 114.7±0.1 |
| | $\theta(\text{H}_1\text{-C}_5\text{-H}_7)$ | 120.4 | 120.1 | 119.9 | 119.0±0.1 |
| | α | 67.1 | 67.2 | 67.3 | 67.26±0.18 |

^aC₃H₆ (Ref. 153); C₄H₈ (Ref. 154); C₅H₈ (Refs. 155,156).

Table VI

Total energies (Hartrees) for bicyclo(2.1.0)pentane, cyclopropane, cyclobutane and related radicals. Radicals (6), (9) and (13) correspond to elimination of hydrogen atoms H₆, H₉ and H₁₃ from BCP.

| Species | HF/6-31G* //HF/6-31G* | MP2/6-31G* //MP2/6-31G* | MP2/6-31G** //MP2/6-31G** | MP4/6-31G** MP2/6-31G** |
|---------------------------|--------------------------|----------------------------|------------------------------|----------------------------|
| bicyclo(2.1.0) pentane | -193.92696 | -194.574485 | -194.639051 | -194.712707 |
| -radical (6) | | | | -194.027294 |
| -radical (9) | | | | -194.037981 |
| -radical (13) | | | | -194.030442 |
| cyclopropane | -117.05886 | -117.44857 | -117.49714 | -117.54594 |
| -radical | | | | -116.86230 |
| cyclobutane | -156.09720 | -156.617990 | -156.68278 | -156.74879 |
| -radical | | | | -156.07468 |

Table VII

Calculated and experimental bond dissociation energies (kcal/mol)

| Compound/ bond type | MP4/6-31G** | Estimated values |
|--|-------------|--------------------|
| cyclopropyl-H | 108.06 | 106.3 ^a |
| cyclopropane: C-C | | 71.35 |
| cyclobutyl-H | 102.16 | 96.5 ^a |
| cyclobutane: C-C | | 93.86 |
| bicyclo(2.1.0)propyl-H | 109.26 | 107.33 |
| bicyclo(2.1.0)butyl-H | 102.47 | 96.79 |
| bridgehead H | 107.72 | 103.40 |
| bicyclo(2.1.0)pentane: bridgehead C-C | | 57.84 |

^a Experimental values from Ref. 158.

Table VIII

Thermodynamic data for cyclopropane, cyclobutane and bicyclo(2.1.0)pentane.

| Molecule | ΔH_f° (kcal/mol) | ZPE (kcal/mol) |
|-----------------------|----------------------------------|--------------------|
| cyclopropane | 12.74 ^a | 49.1 ^c |
| cyclobutane | 6.38 ^a | 67.3 ^c |
| bicyclo(2.1.0)pentane | 37.3 ^b | 71.58 ^d |

^a From Ref. 159.

^b From Ref. 160.

^c From Ref. 161.

^d Estimated using the fundamental frequencies given in Ref. 162.

Table IX

Bond and angle assignments for bicyclo(2.1.0)pentane.

| Distance between atoms | Label | Angle between atoms | Label |
|------------------------|-----------------|---------------------|-----------------|
| 1-2 | r ₁ | 4-1-2 | θ ₁ |
| 1-4 | r ₂ | 1-2-3 | θ ₂ |
| 1-5 | r ₃ | 2-3-4 | θ ₃ |
| 1-8 | r ₄ | 3-4-1 | θ ₄ |
| 2-3 | r ₅ | 4-5-1 | θ ₅ |
| 2-9 | r ₆ | 5-1-4 | θ ₆ |
| 2-10 | r ₇ | 1-4-5 | θ ₇ |
| 3-4 | r ₈ | 6-5-7 | θ ₈ |
| 3-11 | r ₉ | 9-2-10 | θ ₉ |
| 3-12 | r ₁₀ | 11-3-12 | θ ₁₀ |
| 4-5 | r ₁₁ | 8-1-2 | θ ₁₁ |
| 4-13 | r ₁₂ | 8-1-5 | θ ₁₂ |
| 5-6 | r ₁₃ | 9-2-1 | θ ₁₃ |
| 5-7 | r ₁₄ | 9-2-3 | θ ₁₄ |
| | | 10-2-1 | θ ₁₅ |
| | | 10-2-3 | θ ₁₆ |
| | | 11-3-2 | θ ₁₇ |
| | | 11-3-4 | θ ₁₈ |
| | | 12-3-2 | θ ₁₉ |
| | | 12-3-4 | θ ₂₀ |
| | | 13-4-3 | θ ₂₁ |
| | | 13-4-5 | θ ₂₂ |
| | | 6-5-4 | θ ₂₃ |
| | | 6-5-1 | θ ₂₄ |
| | | 7-5-4 | θ ₂₅ |
| | | 7-5-1 | θ ₂₆ |
| | | 8-1-4 | θ ₂₇ |
| | | 13-4-1 | θ ₂₈ |

Table X

Equilibrium Morse parameters.

| Diatomic pair | D (eV) | β (\AA^{-1}) | R_0 (\AA) | R_f (\AA) |
|---------------------------------|-----------|-------------------------------|------------------------|------------------------|
| C ₁ -C ₂ | 4.0701638 | 1.7512728 | 1.528 | |
| C ₁ -C ₄ | 2.5081853 | 2.1456101 | 1.536 | 2.417 |
| C ₁ -C ₅ | 3.0940356 | 2.0086168 | 1.507 | |
| C ₂ -C ₃ | 4.0701638 | 1.7512728 | 1.565 | |
| C ₁ -H ₈ | 4.4838582 | 1.8448380 | 1.082 | |
| C ₂ -H ₉ | 4.1972209 | 1.8693807 | 1.085 | |
| C ₂ -H ₁₀ | 4.1972209 | 1.8693807 | 1.097 | |
| C ₅ -H ₆ | 4.6542795 | 1.8273350 | 1.080 | |
| C ₅ -H ₇ | 4.6542795 | 1.8273350 | 1.090 | |

| Attenuation factor | Value (\AA^{-1}) |
|--------------------|-----------------------------|
| bsw | 1.55 |

Table XI

Bending potential parameters.

| Angle α - β - γ | $k_{\alpha\beta\gamma}$ (eV/rad ²) | θ_0 (rad) | θ_f (rad) |
|---|--|------------------|------------------|
| C ₂ -C ₁ -C ₄ | 8.7381 | 90.54 | 74.72 |
| C ₁ -C ₂ -C ₃ | 10.6105 | 89.45 | 105.27 |
| C ₄ -C ₅ -C ₁ | 8.1139 | 61.27 | 103.68 |
| C ₅ -C ₁ -C ₄ | 9.3622 | 59.36 | 38.15 |
| H ₈ -C ₁ -C ₂ | 2.6838 | 126.31 | 123.3 |
| H ₈ -C ₁ -C ₅ | 2.6214 | 121.2 | 123.6 |
| H ₈ -C ₁ -C ₄ | 3.1207 | 128.6 | 162.15 |
| H ₆ -C ₅ -C ₁ | 3.7449 | 114.65 | 112.0 |
| H ₇ -C ₅ -C ₁ | 3.7449 | 119.0 | 112.0 |
| H ₆ -C ₅ -H ₇ | 1.5603 | 116.7 | 106.3 |
| H ₉ -C ₂ -H ₁₀ | 1.8724 | 109.32 | ... |
| H ₉ -C ₂ -C ₁ | 3.8697 | 113.3 | ... |
| H ₉ -C ₂ -C ₃ | 3.6824 | 111.9 | ... |
| H ₁₀ -C ₂ -C ₁ | 3.8697 | 115.2 | ... |
| H ₁₀ -C ₂ -C ₃ | 3.6824 | 116.6 | ... |

Table XII

Flap and dihedral potential parameters.

| Parameter (eV) | Value |
|-------------------------------------|-----------------|
| a ₀ | 649.032257691 |
| a ₁ | -1161.253421253 |
| a ₂ | 830.132209470 |
| a ₃ | -462.038532829 |
| a ₄ | 192.012760921 |
| a ₅ | -54.120663551 |
| a ₆ | 7.757472971 |
| Parameter (eV/rad ²) | Value |
| K _d | 4.4 |

Table XIII

Predicted and *ab initio* calculated geometries for planar configuration. The distances are given in Å and the angles in degrees.

| Parameter | Predicted Geometry | <i>Ab Initio</i> Geometry (C_{2v}) ¹⁴⁹ |
|---|--------------------|---|
| R (C ₁ -C ₂) | 1.528 | 1.506 |
| R (C ₁ -C ₄) | 2.367 | 2.359 |
| R (C ₁ -C ₅) | 1.507 | 1.506 |
| R (C ₂ -C ₃) | 1.566 | 1.550 |
| R (C ₁ -H ₈) | 1.082 | 1.083 |
| R (C ₅ -H ₆) | 1.088 | 1.098 |
| R (C ₅ -H ₇) | 1.090 | 1.098 |
| R (C ₂ -H ₉) | 1.084 | 1.096 |
| R (C ₂ -H ₁₀) | 1.096 | 1.096 |
| θ (H ₆ -C ₅ -H ₇) | 106.0 | 106.3 |
| θ (H ₈ -C ₁ -H ₅) | 122.0 | 123.6 |
| θ (H ₈ -C ₁ -H ₂) | 124.9 | 123.3 |
| θ (C ₁ -C ₂ -H ₉) | 111.0 | 111.3 |
| θ (C ₁ -C ₂ -H ₁₀) | 112.7 | 111.3 |
| θ (C ₃ -C ₂ -H ₉) | 109.5 | 111.3 |
| θ (C ₃ -C ₂ -H ₁₀) | 114.0 | 111.3 |
| θ (C ₁ -C ₅ -H ₆) | 111.8 | 112.0 |
| θ (C ₁ -C ₅ -H ₇) | 111.8 | 112.0 |
| τ (C ₄ -C ₃ -C ₂ -C ₁) | 0.0 | 0.0 |
| τ (C ₃ -C ₂ -C ₁ -C ₅) | 0.0 | 0.0 |
| τ (C ₁ -C ₅ -C ₄ -C ₃) | 0.0 | 0.0 |

Table XIV

Experimental and calculated frequencies for bicyclo(2.1.0)pentane.

| Mode | Calculated (cm ⁻¹) | Experimental (cm ⁻¹) |
|-----------------|-----------------------------------|-------------------------------------|
| v ₁ | 265 | 280 |
| v ₂ | 475 | 416 |
| v ₃ | 700 | 755 |
| v ₄ | 717 | 774 |
| v ₅ | 752 | 787 |
| v ₆ | 842 | 883 |
| v ₇ | 854 | 914 |
| v ₈ | 859 | 922 |
| v ₉ | 913 | 968 |
| v ₁₀ | 917 | 978 |
| v ₁₁ | 943 | 1012 |
| v ₁₂ | 1019 | 1030 |
| v ₁₃ | 1029 | 1053 |
| v ₁₄ | 1088 | 1106 |
| v ₁₅ | 1090 | 1195 |
| v ₁₆ | 1121 | 1198 |
| v ₁₇ | 1194 | 1218 |
| v ₁₈ | 1243 | 1238 |
| v ₁₉ | 1246 | 1279 |
| v ₂₀ | 1312 | 1280 |
| v ₂₁ | 1337 | 1325 |
| v ₂₂ | 1421 | 1332 |
| v ₂₃ | 1479 | 1446 |
| v ₂₄ | 1507 | 1465 |
| v ₂₅ | 1548 | 1470 |
| v ₂₆ | 2899 | 2875 |
| v ₂₇ | 2901 | 2922 |
| v ₂₈ | 2968 | 2936 |
| v ₂₉ | 2971 | 2945 |

Table XIV (continued)

| Mode | Calculated (cm ⁻¹) | Experimental (cm ⁻¹) |
|------|-----------------------------------|-------------------------------------|
| v30 | 2976 | 2965 |
| v31 | 2999 | 2982 |
| v32 | 3008 | 3058 |
| v33 | 3082 | 3070 |

^aFrom Ref. 162

Table XV

Microcanonical rate constants for flap motion in bicyclo(2.1.0)pentane for initial random energization. The correlation coefficients for the fitting are also indicated.

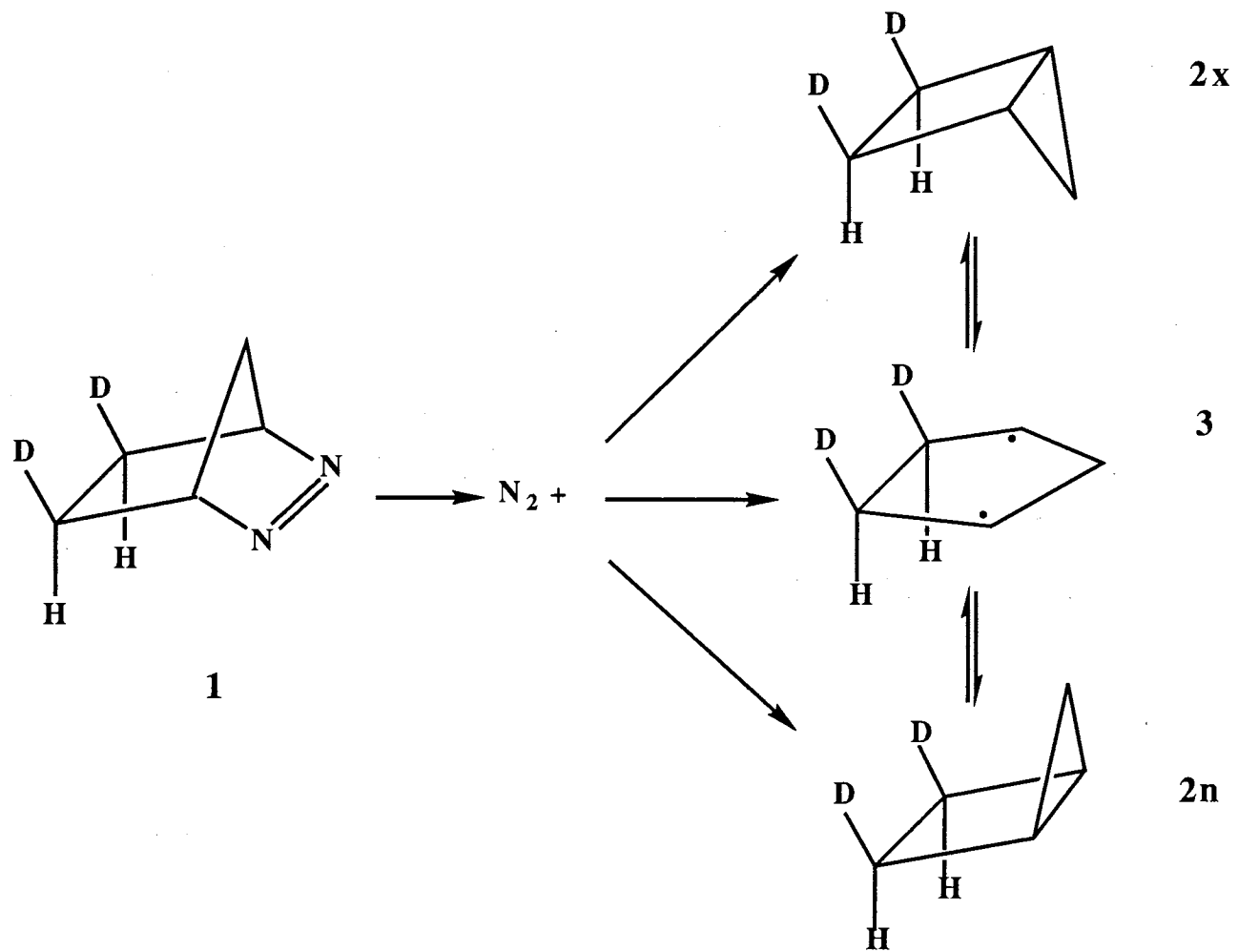
| Energy (kcal/mol) | k(E) (ps ⁻¹) | r |
|-------------------|--------------------------|-------|
| 100 | 0.0064 ± 0.0012 | 0.960 |
| 110 | 0.0118 ± 0.0015 | 0.985 |
| 120 | 0.0159 ± 0.0023 | 0.992 |
| 130 | 0.0026 ± 0.0034 | 0.993 |
| 140 | 0.0034 ± 0.0036 | 0.994 |
| 150 | 0.0421 ± 0.0038 | 0.994 |
| 160 | 0.0485 ± 0.0041 | 0.992 |
| 170 | 0.0625 ± 0.0045 | 0.995 |
| 180 | 0.0849 ± 0.0050 | 0.996 |
| 190 | 0.1021 ± 0.0057 | 0.993 |
| 200 | 0.1181 ± 0.0059 | 0.997 |
| 210 | 0.1323 ± 0.0062 | 0.997 |
| 225 | 0.1732 ± 0.0067 | 0.996 |
| 250 | 0.2253 ± 0.0073 | 0.998 |

Table XVI

Total IVR rates and other parameters for relaxation out of the flap mode. The parameters were obtained from least-squares fits of the average normal-mode decay.

| Energy (eV) | λ_2 (ps^{-1}) | $\langle E(0) \rangle$ (eV) | $\langle E(\infty) \rangle$ (eV) |
|-------------|----------------------------------|-----------------------------|----------------------------------|
| 1.30 | 13.806 | 1.30370 | 0.11162 |
| 1.95 | 14.160 | 1.97011 | 0.15248 |
| 2.60 | 15.329 | 2.62057 | 0.17219 |

Figure 16. The general reaction scheme for skeletal inversion of bicyclo(2.1.0)pentane obtained in thermal decomposition of 2,3 diazabicyclo(2.2.1)hept-2-ene-exo-,exo-5,6-d₂ (**1**). (**2x**) and (**2n**) represent the exo- and endo-deuterium labeled bicyclo(2.1.0)pentane and (**3**) is the 1,3 cyclopentadiyl radical.



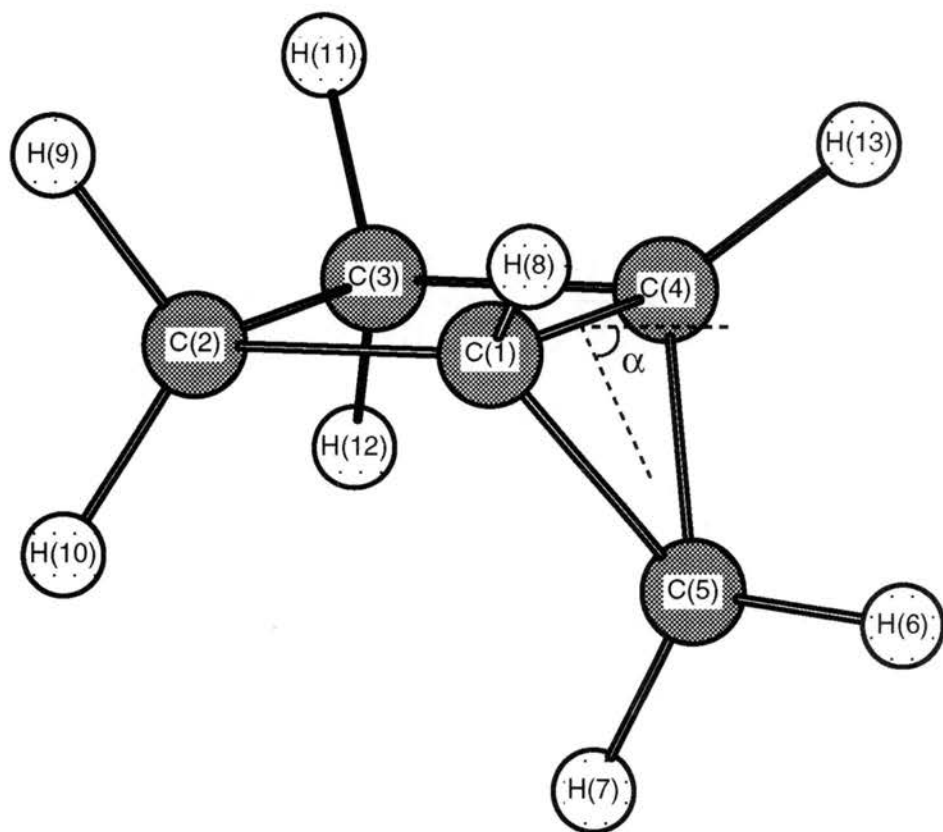


Figure 17. Atom designation and numbering for bicyclo(2.1.0) pentane.

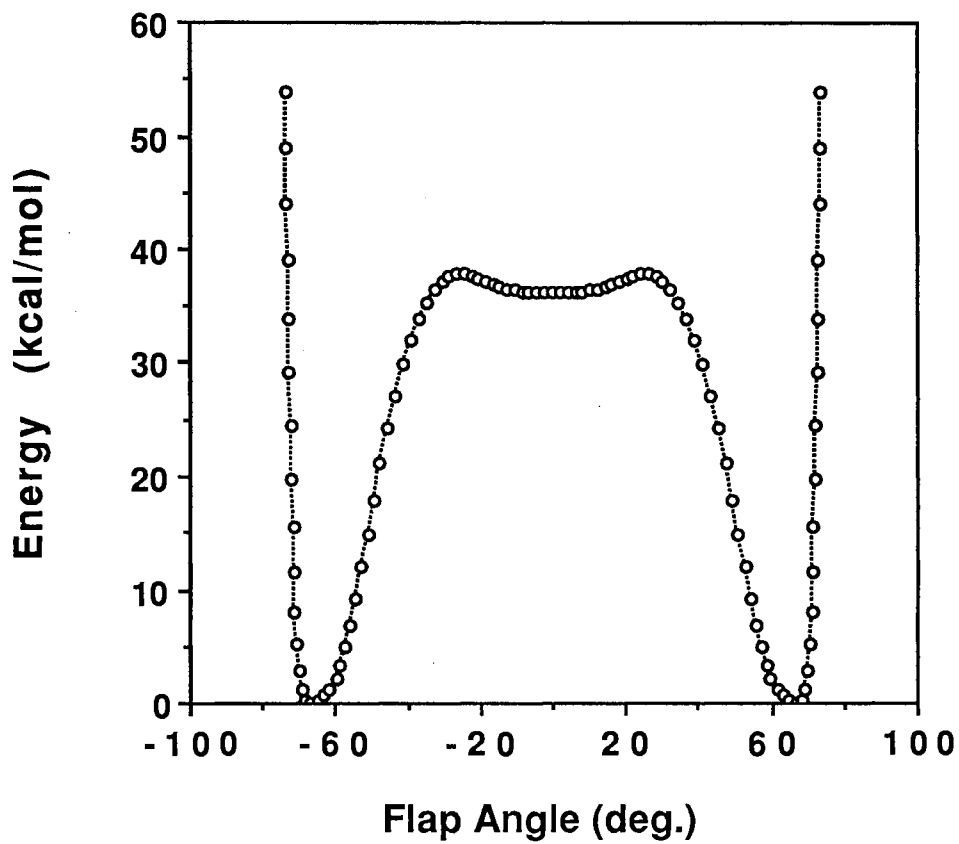


Figure 18. The variation of the total potential as function of the flap angle. The dashed line is a guide for the eye.

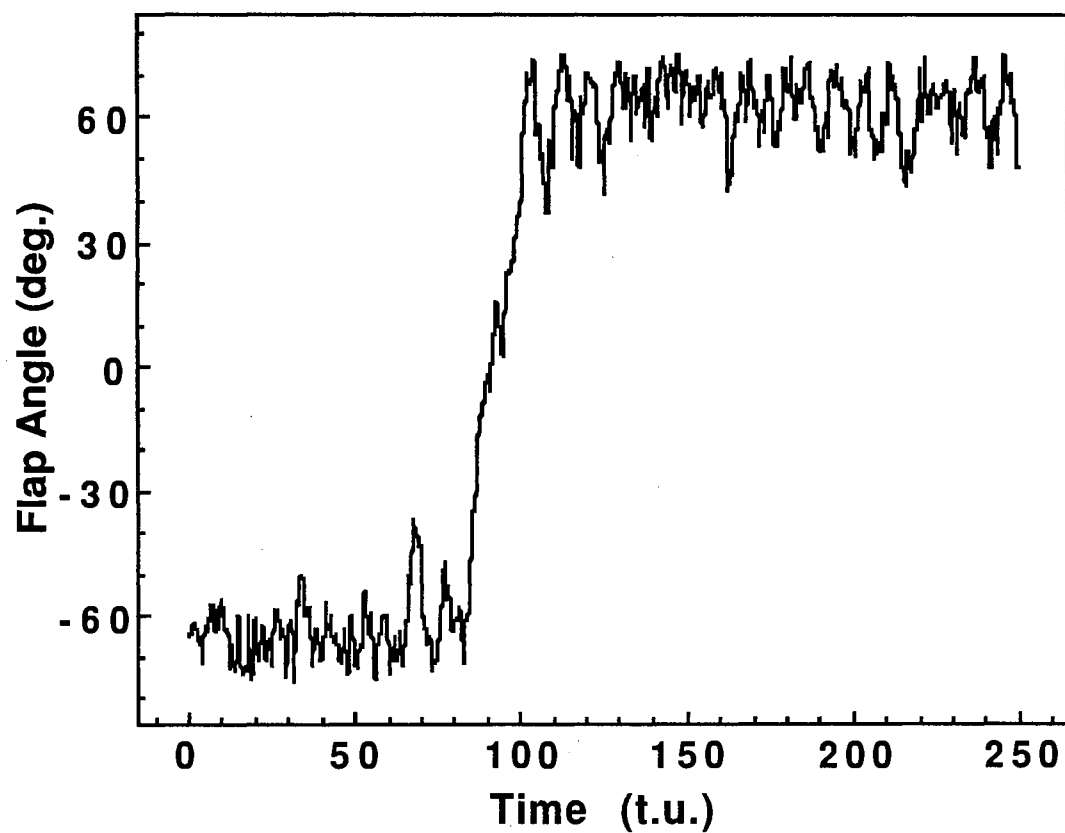
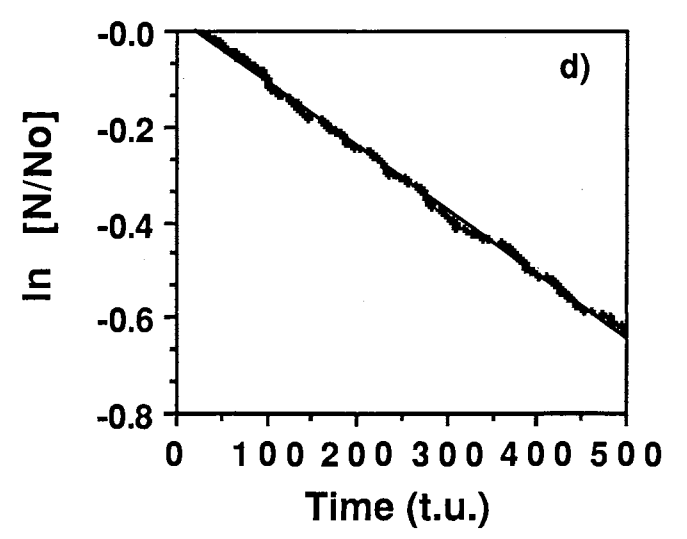
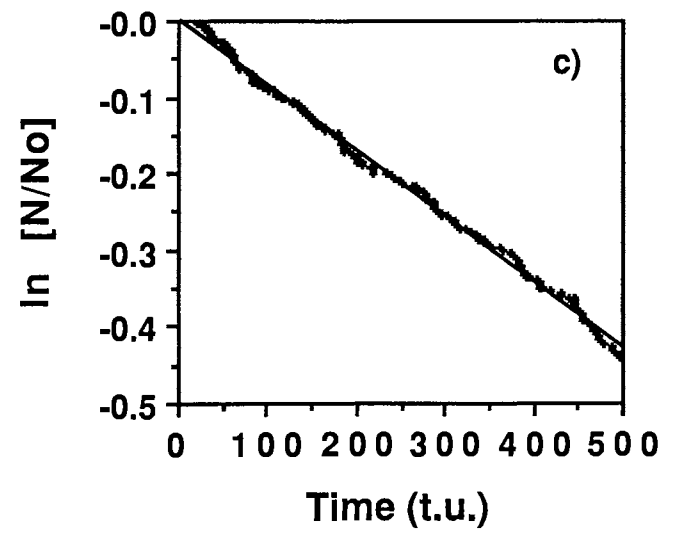
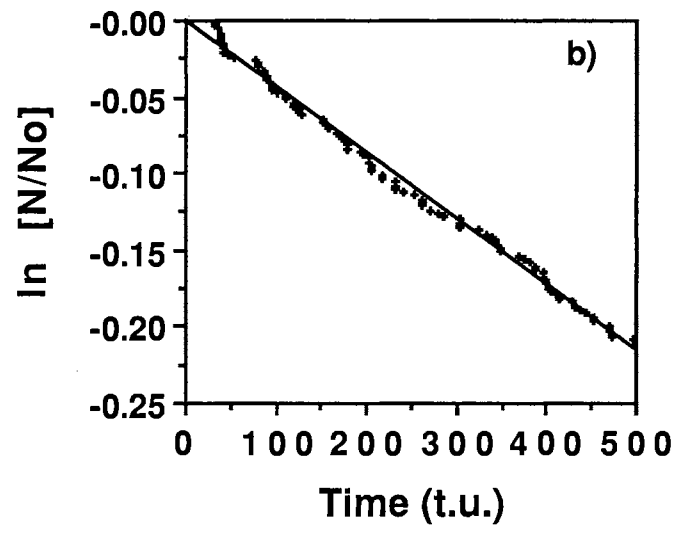
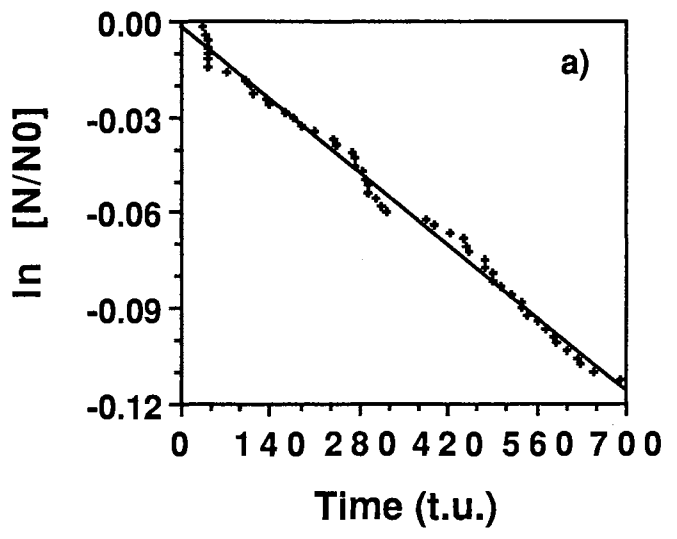


Figure 19. Temporal variation of the flap angle extracted from a trajectory for which ring inversion takes place. The abscissa unit is 1 t.u. = 1.018×10^{-14} s.

Figure 20. Decay plots for random excitation of the vibrational modes at the energies (a) $E=120$ kcal/mol, (b) 150 kcal/mol, (c) 180 kcal/mol and (d) 210 kcal/mol in excess to zero-point energy. In each case, the line is a linear least-squares fit to the calculated points.



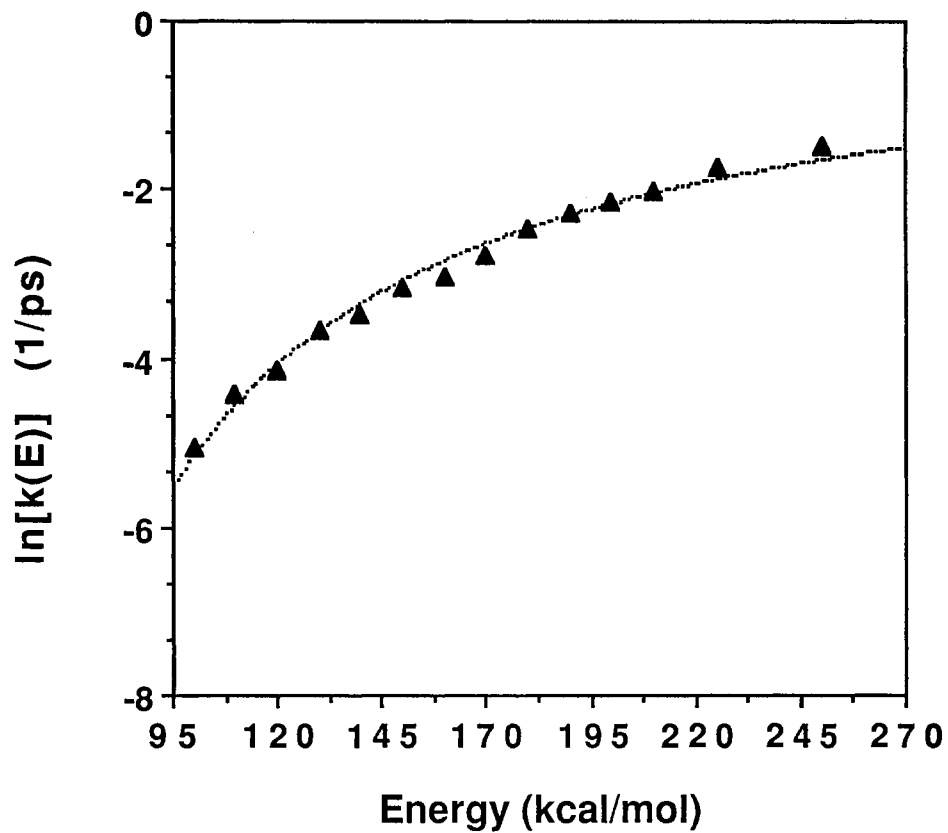


Figure 21. Total microcanonical rate constants for the ring inversion of BCP as function of the excitation energy in excess to zero-point energy. Calculated points are denoted by symbols and the corresponding RRK fit by smooth curve.

Figure 22. Power spectra for BCP in arbitrary units (a.u.) at: (a, b) zero-point energy, (c, d) 120 kcal/mol, (e, f) 225 kcal/mol. The excitation energies are initially distributed at random over the normal-modes in excess to zero-point energy. Plots (a), (c) and (e) represent the composite spectrum. The power spectrum of the flap angle is given in plots (b), (d) and (f).

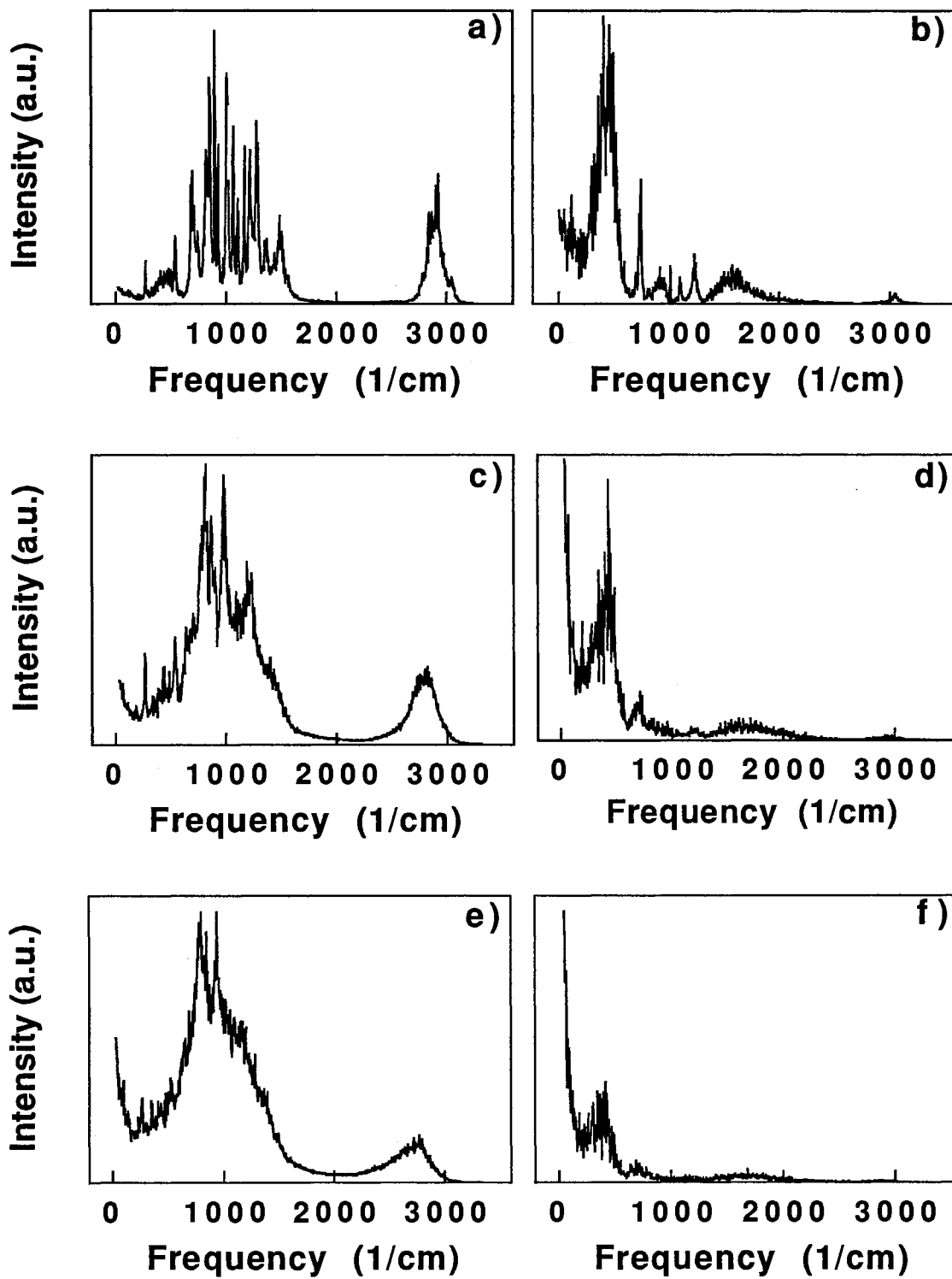
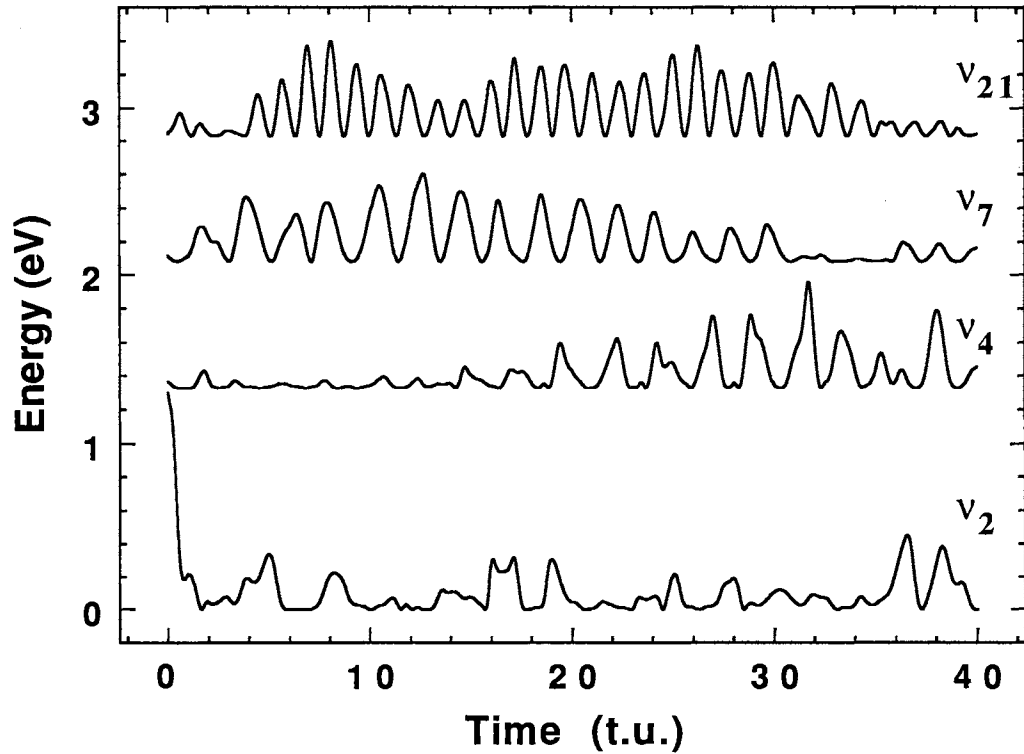
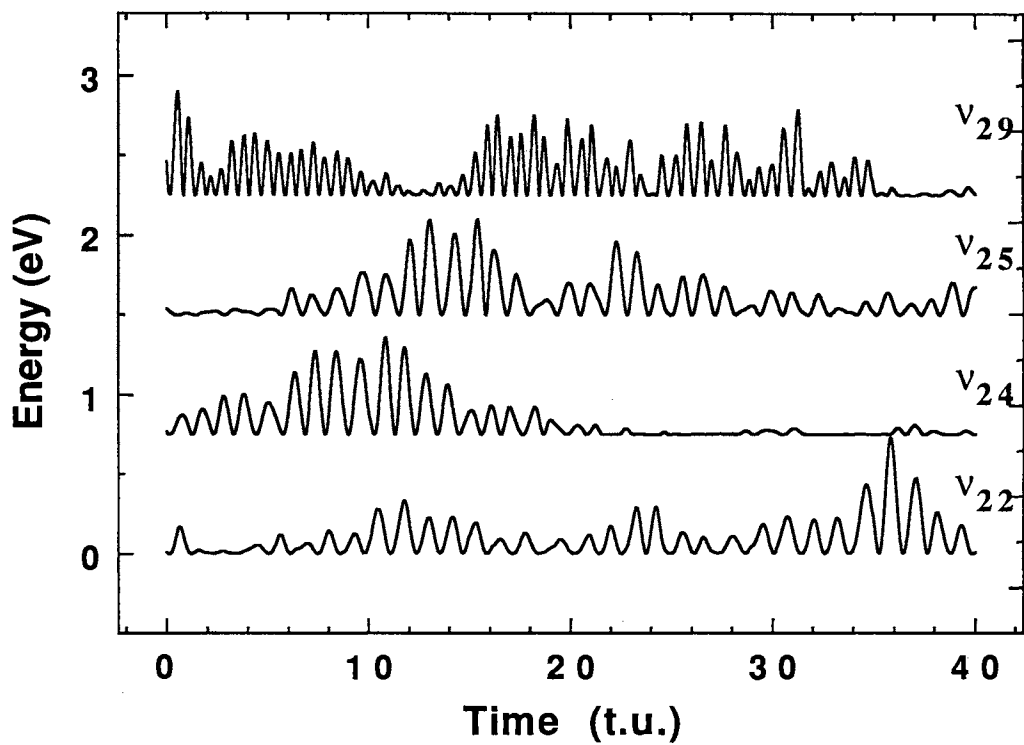


Figure 23. Instantaneous mode kinetic energies for the modes with the highest increase in energy subsequent to the initial excitation of the flap mode ν_2 . Initial state corresponds to excitation of the flap mode with 30 kcal/mol above zero-point energy. Each successive curve is displaced upward by 0.75 eV to provide clarity. The abscissa unit is 1 t.u. = 1.018×10^{-14} s.



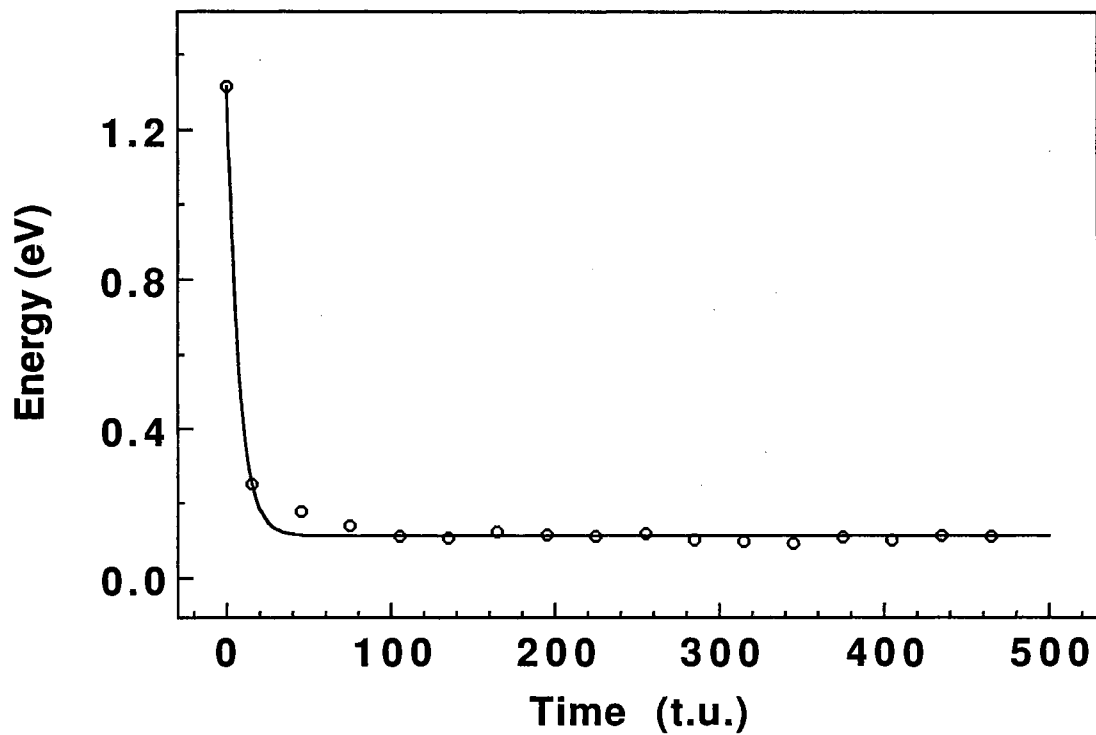


Figure 24. Decay curve for the average mode energy of the flap mode initially excited with 30 kcal/mol in excess of zero-point energy. The solid curve is a nonlinear least-squares fit of the points with the equation (IV.10).

CHAPTER V

MOLECULAR DYNAMICS STUDIES OF THE THERMAL DECOMPOSITION OF 2,3-DIAZABICYCLO(2.2.1)HEPT-2-ENE

Introduction

As described in Chapter IV, we have developed¹⁵⁰ a semiempirical potential-energy surface for bicyclo(2.1.0)pentane (BCP) and for 1,3-cyclopentadiyl radical (see structures 5 and 6 in Fig. 25 for the corresponding deuterated compounds), which is fitted to the available experimental data and to the results of *ab initio* calculations for equilibrium structures,^{149,155,156,164-166} fundamental vibrational frequencies,¹⁶² and the barrier for the ring inversion.^{145,149} One of the main findings of our study (see Chapter IV) is that the results of classical trajectory calculations agree well with the predictions of statistical unimolecular theory, for random energization of the vibrational normal modes of BCP. This implies a fast energy flow relative to the reaction time. Indeed, we have found¹⁵⁰ that the total intramolecular vibrational relaxation rates of the flap mode are significantly larger than the microcanonical ring inversion rates. These results do not indicate any nonstatistical effects in the channel corresponding to thermal BCP ring inversion.

The availability of the potential-energy surface for BCP makes it possible to extend the study to a much more complex reaction, i.e., the thermal decomposition of 2,3-diazabicyclo(2.2.1)hept-2-ene-exo, exo-5,6-d₂ (DBHD) (**1**) to bicyclo(2.1.0)pentane-exo,exo-2,3-d₂ (**5x**), endo,endo-2,3-d₂ (**5n**) and

molecular nitrogen (see Fig.25). For this purpose, in the next section we analyze the experimental and theoretical data related to thermal decomposition of 2,3-diazabicyclo(2.2.1)hept-2-ene (DBH).

Selected Experimental and Theoretical Data

Related to Thermal Decomposition of

2,3-diazabicyclo(2.2.1)hept-2-ene

Despite the fact that studies of this reaction were first reported several decades ago,^{141,169,170} the reaction mechanism still continues to be a source of intriguing interpretation. In 1961, Cohen *et al.*¹⁶⁹ reported the kinetics of decomposition of DBH in the gas phase at temperatures between 131.5°-180.8°C. They found that the reaction is characterized by first-order kinetics with an activation energy of 37.3±0.3 kcal/mol. The reaction mechanism was interpreted as a simultaneous rupture of two C-N bonds of the DBH molecule. Similar results have been obtained later by Crawford and Mishra.¹⁷⁰ Their results show that in the temperature range 171.0°-202.4°C, DBH undergoes a first-order unimolecular decomposition with an activation energy of 36.9±0.2 kcal/mol. In their early study, Roth and Martin^{141a} reported that thermolysis of DBHD at 180° C in the gas-phase (100-200 Torr) gives a 75:25 mixture of (**5x**) and (**5n**). These results were initially interpreted as a concerted elimination of nitrogen with simultaneous back-lobe overlap of carbon-centered orbitals. Later, they proposed^{141b} a new mechanism involving a stepwise cleavage of the two C-N bonds and formation of the diazenyl biradical (DB) with back-side displacement of nitrogen by the carbon radical site.

An alternative explanation of the reaction mechanism has been advanced by Allred and Smith.¹⁴² In their study of thermal decomposition of the exo and endo epimers of 5-methoxy-2,3-diazabicyclo(2.2.1)hept-2-ene, the

inversion of stereochemistry was explained on the basis of interconversion of pyramidal diradical-like intermediates, which are formed as a consequence of a "recoil effect" accompanying nitrogen departure, with closure of the ring before planarization.

In the last few years, the controversial problem of concerted C-N bond cleavage of azoalkanes leading directly to the 1,3-cyclopentadiyl diradical vs. the one-bond cleavage involving DB appears to have been resolved, by both theoretical¹⁷¹ and experimental studies,¹⁷²⁻¹⁷⁷ in favor of the latter mechanism.

Using time-resolved coherent anti-Stokes Raman spectroscopy (CARS), Adams *et al.*¹⁷² have shown that the measured N₂ vibrational distribution of nascent N₂ in photodissociation of 2,3-diazabicyclo(2.2.1)hept-2-ene (DBH) can be explained by involving DB as an intermediate and correspondingly, a stepwise mechanism of cleavage of the two C-N bonds. A similar two-step mechanism was found in ultraviolet-induced dissociation of nonsymmetrical azoalkane 3-(methylazo)-3-methyl-1-butene.¹⁷³

Direct insight into the dynamics of the thermal decomposition of DBH was obtained by Simpson *et al.*¹⁷⁴ using shock-tube methods. The vibrational energy content of the N₂ reaction product was analyzed over the temperature range 900-1400 K. It was found that N₂ is formed with low amounts of vibrational energy, while BCP contains vibrational energy in excess of the equilibrium distribution. Since a concerted C-N bond cleavage with the N-N axis perpendicular to the reaction coordinate would be expected to give highly vibrational excited nitrogen,¹⁷⁵ these results clearly support a stepwise dissociation mechanism.

A comprehensive discussion of the question of one-bond vs. two-bond cleavage during decomposition of DBH has been given by Adam *et al.*^{176,177} for different types of activation modes. It has been shown that the thermal and

long wavelength ($\lambda > 300$ nm) photolyses lead exclusively to BCP, while photo-induced electron transfer, laser-jet and 185 nm-photolyses yield BCP and different cyclopentane derivatives. It has been suggested that a diazenyl diradical ($1D'_{\sigma,\sigma}$) resulting in a stepwise one-bond cleavage mechanism serves as a common intermediate in both pyrolyses and in 350-nm photolyses of DBHD, while a two-bond cleavage leading directly to the 1,3-cyclopentadiyl biradical is involved in 185-nm photolyses. A ratio of 2.94 ± 0.02 for the exo/endo bicyclopentanes (**5x**) and (**5n**) has been reported for thermolysis of DBHD at 180°C .¹⁷⁶

For theoretical investigations of the thermal deazetization of DBH (see Figure 25), a point of significant interest is the development of a consistent model able to predict the observed preference for inversion of configuration to give the exo- labeled bicyclo(2.1.0)pentane (**5x**) as the major product.

In this direction, important steps have recently been taken by the group of B. K. Carpenter.^{140,178-179} In their kinetic studies on DBHD, a ratio of 4.74 for the rate constants leading to (**5x**) and to (**5n**) was reported,¹⁷⁹ with no statistically significant temperature dependence over the range 129.8 - 180.5°C . However, it should be noted that the errors propagated into this ratio were relatively large.^{140,179} Using trajectory calculations on a dimensionally-limited potential-energy surface containing the C-N bond distance and the angle between the planes of the three- and four-membered rings in BCP as independent variables, they confirmed the preference for inversion of stereochemistry. Despite the disagreement between the experimental and calculated magnitude of the rate constant ratio leading to formation of the products (**5x**) and (**5n**), it was found that the computed product ratio is nearly independent of temperature. These results were directly related to the potential-energy surface used in the calculations, which had a single transition

state that could lead to different products.¹⁷⁹ However, concerns about the use of a two-dimensional model for the potential-energy surface instead of one with proper dimensionality (39) have been expressed.¹⁴⁰

General Calculation Method

In the present chapter, we present a more realistic characterization of the overall mechanism of the thermal decomposition of DBH.¹⁸⁰ The study involves the development of an accurate potential-energy surface for this reaction and classical trajectories computed on that surface. Since it has been suggested^{140,176-178} that the deazetization reaction shown in Fig.25 is not properly described by statistical theory, it is important to investigate the possibility of nonstatistical effects. As in similar studies,^{54,41,42,151} we seek a parametrization of the potential terms that reproduces the most critical topographical features of the reaction: the geometrical structures, the potential curvatures at the local potential minima, and the relative energies of the reactants, products and transition states. In the present case, a major impediment to the construction of an empirical potential-energy surface is the lack of experimental or high-accuracy calculated data corresponding to the energy and geometry of DB, the critical transition states, and to the fundamental frequencies of DBH and DB. The geometries of DBH, the DB and of the transition state corresponding to breaking of the remaining C-N bond of diazenyl biradical have been determined at the second order Möller-Plesset perturbation theory (MP2/6-31G*) and at Hartree-Fock (HF/6-31G*) levels, respectively. The fundamental frequencies for both DBH and DB have been obtained based on *ab initio* calculations at MP2/6-31G* level using the optimized geometries at the same level. The relative energy of the DB to DBH is determined by a combination of experimental heats of formation, barrier

heights and *ab initio* results. Finally, the bond-dissociation energies for DBH and DB were determined from experimental enthalpies of reaction and reported data for bond dissociation energies of BCP.¹⁵⁰ Using a projection method of the instantaneous Cartesian velocities onto the normal mode vectors and classical trajectory calculations, the dissociation dynamics of 2,3-diazabicyclo(2.2.1)hept-2-ene-exo, exo-5,6-d₂ (DBHD) are investigated at several excitation energies in the range 60-175 kcal/mol. Qualitative investigation of the phase space structure and of the statistical character of the reaction has been done by calculating the power spectra of the internal coordinates. In addition, the distribution of energy among the reaction products is analyzed and compared to experimental data.

Potential-Energy Surface

A. Determination of the Equilibrium Geometries

The first problem to be solved in the development of a realistic, global potential-energy surface for DBH and DB is the determination of equilibrium geometries. The atom designations and numbering used throughout this paper for these two compounds are given in Figure 26.

The molecular structure of DBH has been determined by both electron diffraction¹⁸¹ and microwave spectroscopy.¹⁸² The overall structure of the molecule exhibits C_s symmetry, with the plane of symmetry passing through the bisector of the C₂-C₃, N₁₄=N₁₅ bonds and C₅ (see Fig. 26a). However, a comparison of the internal coordinates reported in these studies shows significant discrepancies, except for certain bond lengths. This made it necessary to perform further theoretical investigations in order to obtain a more precise description of the DBH geometry and to clarify which of these results are

more accurate.

The first theoretical determination of the DBH structure was reported by Boyd *et al.*¹⁸³ using CNDO (complete neglect of differential overlap) calculations. Despite only a fair-to-moderate agreement for bond distances, the calculated bond angles accurately reproduced the microwave results.¹⁸²

Additional support for the structure determined using microwave spectroscopy was obtained by the molecular mechanics studies of Kao and Huang.¹⁸⁴ Based on a parametrized force field for azoalkanes, they predicted a geometrical structure of DBH which was found to be in good agreement with the results of the microwave study¹⁸²; the main discrepancies occurred for the bridgehead H₈C₁C₅ angle and the angles between the planes C₁N₁₄N₁₅ and C₁C₅C₄, and C₁N₁₄N₁₅ and C₁C₂C₃, respectively.

In this study, we have investigated the structure of DBH molecule by performing *ab initio* molecular orbital studies. The calculations were carried out using the Gaussian-92 system of programs.¹² The structure of DBH was first optimized under C_s symmetry at the restricted Hartree-Fock (RHF) level using analytical gradients and the internal 6-31G*^{20,21} basis set, and then refined within the Möller-Plesset (MP)¹⁵² perturbation theory approximation. Both optimized geometries and corresponding experimental data from microwave study¹⁸¹ are presented in Table XVII.

At HF/6-31G* level, the root-mean-square deviation of the calculated values from the experimental data¹⁸² is 0.013 Å for bond lengths and 0.93° for bond angles; at the MP2/6-31G* level, the same quantities are 0.037Å and 0.32°, respectively. It can be seen that the agreement between the calculated structural parameters and experimental values is very good. Consequently, the data set of internal coordinates reported in Ref. 182 was chosen in the construction of our semiempirical potential-energy surface.

In the case of DB, a limited set of geometrical parameters obtained using semiempirical AM1 and unrestricted Hartree-Fock (UHF/6-31G*) calculations was reported by Carpenter and co-workers.¹⁷⁹ Their results show very similar structures for the singlet and triplet states of DB. This result is a consequence of the large distance between the unpaired spins of DB.

In the present study, we have assumed very similar structures and energies for the triplet and singlet states of DB. In order to obtain a complete description of the biradical geometrical parameters, we have carried out a series of *ab initio* calculations. The equilibrium structure of the triplet state of DB was determined at both the unrestricted UHF/6-31G* and UMP2/6-31G* levels. Its structure is illustrated in Fig. 26, and the values of the geometrical parameters are given in Table XVIII. An inspection of the data in Table XVIII shows that the main effect introduced by the electron correlation within second-order Möller Plesset perturbation theory is a decrease of the C-N distance (from 1.843 Å to 1.508 Å) and of the bond angles H₁₃C₄C₃ and H₁₃C₄C₅. In addition, all dihedral angles of the carbon ring, and dihedral angles N₁₄C₄C₃C₂ and N₁₅N₁₄C₄C₃ suffer significant modifications.

For the transition-state corresponding to cleavage of the remaining C-N bond of DB, the geometrical parameters have been calculated at UHF/6-31G* and UMP2/6-31G* levels. The results are given in Table XVIII.

B. Vibrational Spectra

To the best of our knowledge, experimental values for the fundamental vibrational frequencies of DBH have not been reported. Consequently, a normal-mode analysis and a complete set of force constants for DBH are still not available. We have therefore computed analytical frequencies for every case of interest in order to have a better characterization of the *ab initio*

stationary points.

Vibrational frequencies for DBH and DB have been obtained at both the HF/6-31G* and MP2/6-31G* levels. These data are presented in Table XIX. The HF/6-31G* and MP2/6-31G* values have been scaled by 0.8929 and 0.94, respectively^{185,186} to take into account the overestimation of vibrational frequencies at these levels of theory. The corresponding zero-point vibrational energies are given in Table XIX.

In order to assist the future spectroscopic analysis of DBH, we present the corresponding calculated infrared intensities in Fig. 27.

We have verified the existence of a single imaginary frequency at the stationary point corresponding to the transition states given in Table XVIII.

C. Bond Dissociation Energies

An additional difficulty in the development of a global potential-energy surface for DBH and DB is the lack of data on bond dissociation energies. We used an approximate method for estimating these energies from thermochemical experimental data and *ab initio* quantum calculations.

The method used to determine the bond dissociation energies for DBH involves the following assumptions and computational steps:

- (1) We assume that the previously reported¹⁵⁰ values of the C-C and C-H bond dissociation energies in BCP can be transferred to the corresponding bonds in DBH.
- (2) Following Benson¹⁸⁷, we assume that the value of the C-N bond dissociation energy in DBH is equal to the value of the activation energy for azoisopropane (~47.5 kcal/mol).
- (3) The remaining unknown bond dissociation energy (N=N) is calculated to be 135.4 kcal/mol by using the enthalpy of formation and zero-point energy for

DBH (see Table XX), and the set of estimated C-H, C-C and C-N bond dissociation energies.

To obtain a measure of the accuracy of the N=N bond dissociation energy value, we have made an independent estimation of this bond energy in a similar environment. For this purpose, we have considered the hydrogenation reaction of dimethylenediazene (diazetene) (see also Fig. 28) leading to ethylenediamine



Based on the assumption of approximately equal values of the C-C, C-N and C-H bond dissociation energies in dimethylenediazene and ethylenediamine, the N=N bond dissociation energy can be determined using the enthalpies of formation and zero-point energies of these compounds (see Table XX), the strain energy of dimethylenediazene, and the values of N-H (~100.0 kcal/mol¹⁹⁰) and H-H (~104.204 kcal/mol¹⁹⁰) bond strengths. Except for the thermochemical data already published,^{32,185,188,189} all the other quantities in Table XX were determined as follows:

The strain energy in dimethylenediazene of 18.3 kcal/mol was estimated using group contributions taken from a compilation of Benson and O'Neal.¹⁸⁷

For ethylenediamine, Radom *et al.*¹⁹¹ have found based on *ab initio* calculations at the 4-31G level that the most stable conformations are tGg' and gGg' (see structures b and c in Fig. 28). Here, the symbols T and G refer to *trans* and *gauche* arrangements of nitrogen atoms about the central C-C bond, while symbols t, g and g' refer to the N-C-C-N dihedral angle with appropriate values 180°, 60° and -60°, respectively. Later, Alsenov *et al.*¹⁹² have determined that the sequence of conformations with the most stable energies is

gGg', tGg' and tTt at 4-21G level (structures (b), (c) and (d) in Fig. 28). We have reoptimized these structures at the HF/6-31G* level and in two cases at the MP2/6-31G* level. The corresponding geometrical parameters are given in Table XXII together with their total and zero-point energies. Our results support the sequence of conformational energies given by Alsenov et al.¹⁹² The zero-point energy for ethylenediamine in Table XX was calculated for the most stable conformation found at HF/6-31G* level, i.e. gGg'.

As a result of this analysis, a N=N bond dissociation energy of 136.48 kcal/mol is obtained, which is in close agreement with the value found using the first method presented.

The enthalpy of formation of dimethylenediazene given in Table IV was determined using the methodology proposed by Sana and Leroy,³² with molecular energies predicted at the G1 level.¹⁸⁵

At the G1 level, the total energy is calculated as a superposition of corrections to the MP4/6-311G** energy, carried out at MP(full)/6-31G* geometry¹⁸⁵

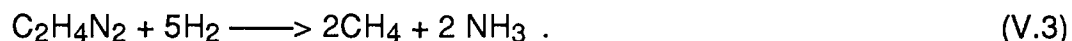
$$E^{G1} = E[\text{MP4/6-311G}^{**}] + \Delta E(+) + \Delta E(2df) + \Delta E(\text{QCI}) \\ + \Delta E(\text{HCL}) + \Delta E(\text{ZPE}) \quad (\text{V.2})$$

Here, $\Delta E(+)$ represents the correction for inclusion of diffuse sp basis functions, $\Delta E(2df)$ gives extra d- and f- contributions for non-hydrogen atoms, $\Delta E(\text{QCI})$ is a quadratic configuration interaction correction for residual correlation effects, $\Delta E(\text{HCL}) = -0.19n_{\alpha} - 5.95n_{\beta}$ gives an empirical higher level correlation correction as function of the number of n_{α} and n_{β} valence electrons, and $\Delta E(\text{ZPE})$ represents the 0.8929 scaled zero-point vibrational HF/6-31G* energy.

The MP2(FU)/6-31G* optimized C_{2v} geometry of dimethylenediazene is

given in Table XXII and the absolute energies and corrections involved in relation (V.2) are presented in Table XXIII.

As a working reaction we have considered the isogiric reaction



The corresponding enthalpy of formation for dimethylenediazene can be calculated using the individual enthalpies of formation, the total G1 energies and the temperature corrections given in Table XX.

As described in Section A of this chapter, we evaluated the structures of DB and transition state determined by the cleavage of the remaining C-N bond of the biradical. The corresponding energy difference is ~ 6.32 kcal/mol at the UHF/6-31G* level. In addition, if we assume that the energy difference between this transition state and the equilibrium state of DBH is equal to the measured activation energy of 37.3 ± 0.3 kcal/mol,¹⁶⁹ then it follows that the DB energy is 31.0 kcal/mol above the DBH energy.

For DB, we have assumed that the bond dissociation energies are given by the corresponding values in DBH, except for the N=N bond. The dissociation energy of this bond was found by imposing the condition that the energy difference between the DB and DBH molecule is 31.0 kcal/mol.

The complete lists of all bond dissociation energies in DBH and DB are given in the next section.

In order to estimate the value of the barrier crest in the case of a symmetric stretch of both C-N bonds in DBH, we used *ab initio* calculations at the HF/6-31G* level on the singlet surface. The results show that the transition state corresponding to concerted breaking of both C-N bonds lies 75.02 kcal/mol above the state of DBH.

D. Technical Aspects of the Potential-Energy Surface

It is most convenient to express the potential-energy surface in terms of analytical functions of the internal coordinates. For the structures illustrated in Fig. 26, we have used the bond and angle assignments given in Table XXIV. This notation is consistent with that previously used for describing the BCP potential-energy surface.¹⁵⁰

The total potential-energy surface for DBH and DB is constructed as follows:

$$V_{\text{tot}} = \frac{V_1 e^{-AV_1} + V_2 e^{-AV_2}}{e^{-AV_1} + e^{-AV_2}} S_1 + (V_3 + V_4) S_2 . \quad (\text{V.4})$$

Here, V_1 and V_2 describe the potential terms which connect the DBH configuration (1) with DB (2) and (3) (see Fig. 25), respectively. The V_3 term is the potential for the BCP molecule (see Ref. 100 and Chapter IV). The V_4 term represents the N-N interaction in the N_2 molecule. In the limit of infinite values of the coupling parameter A , the exponentially weighted average of V_1 and V_2 potentials assures the selection of the minimum value between the V_1 and V_2 terms.

For the sake of brevity, we describe the formulation of V_1 term only, which gives the mathematical dependence between the DBH potential terms and DB (2). The description of potential V_2 , which gives the DBH-DB (3) dependence is straightforward considering the symmetry of the problem observable in Fig. 25.

We represent the V_1 potential as a sum of bond stretching interactions, bending potentials, and torsional terms:

$$V_1 = V_{1 \text{ stretch}} + V_{1 \text{ bend}} + V_{1 \text{ dih}} \quad (\text{V.5})$$

The potential $V_{1 \text{ stretch}}$ represents a superposition of bond stretching potentials, taken to be Morse functions:

$$V_{1 \text{ stretch}} = \sum_{i=1}^{16} D_i \{ \exp[-2\beta_i(r_i - r_i^0)] - 2 \exp[-\beta_i(r_i - r_i^0)] \}, \quad (\text{V.6})$$

where the parameters vary with the interatomic C-N bond distance r_5

$$\begin{aligned} D_i &= D_i^{(1)} + (D_i^{(2)} - D_i^{(1)}) S_3(r_5) \\ \beta_i &= \beta_i^{(1)} + (\beta_i^{(2)} - \beta_i^{(1)}) S_3(r_5) \\ r_i^0 &= r_i^{0(1)} + (r_i^{0(2)} - r_i^{0(1)}) S_3(r_5) \end{aligned} \quad (\text{V.7})$$

in the case $D_i^{(2)} \neq 0$, and

$$\begin{aligned} D_i &= D_i^{(1)} \\ \beta_i &= \beta_i^{(1)} \\ r_i^0 &= r_i^{0(1)} \end{aligned} \quad (\text{V.8})$$

for $D_i^{(2)} = 0$. In Eqs. (V.5-V.8), D_i represents the potential well depth, β_i is the curvature parameter, and r_i^0 is the equilibrium bond distance for the bond with index i . The indices (1) and (2) in the same equations refer to the parameters corresponding to DBH (1) and the DB (2). The switching function S_3 in Eq. (V.7) assures a smooth change in the potential well depths, force constants and

equilibrium distances from the values specific to the DBH molecule [index (1)] to those characteristic of the DB [index(2)]. The switching function $S_3(r_5)$ has the form

$$S_3(r_5) = \tanh[w_3 (r_5 - r_5^{0(1)})^2] \quad (V.9)$$

The bending potential $V_{1 \text{ bend}}$ is taken to be a superposition of quadratic terms:

$$V_{1 \text{ bend}} = \sum_{i=1}^{32} 0.5 k_i (\theta_i - \theta_i^0)^2, \quad (V.10)$$

where

$$\begin{aligned} k_i &= k_i^{(1)} + (k_i^{(2)} - k_i^{(1)}) S_3(r_5) \\ \theta_i &= \theta_i^{(1)} + (\theta_i^{(2)} - \theta_i^{(1)}) S_3(r_5) \end{aligned} \quad (V.11)$$

if $k_i^{(2)} \neq 0$, and

$$\begin{aligned} k_i &= k_i^{(1)} S_4(r_5) \\ \theta_i &= \theta_i^{(1)} \end{aligned} \quad (V.12)$$

if $k_i^{(2)} = 0$. Here, the indices (1) and (2) correspond to DBH and the DB, and k represents the bending force constant associated with the angle θ_i , which takes the value θ_i^0 in the equilibrium configuration. The switching function $S_4(r_5)$ in

Eq. (V.12) attenuates the bending force constants when the C-N bond distance r_5 becomes large. Its functional form is

$$S_4(r_5) = \exp[-w_4 (r_5 - r_5^{0(1)})^2]. \quad (\text{V.13})$$

In addition, we attenuated the bending force constants corresponding to the C-C-N, H-C-N and C-N-N bond angles of DB as function of the remaining C-N bond distance. In these cases, the force constants $k_i^{(2)}$ in Eq. (V.11) are multiplied by the switching function $S_5(r_6)$

$$S_5(r_6) = 1 - \tanh[w_5 (r_6 - r_6^{0(1)})^2]. \quad (\text{V.14})$$

The dihedral potential $V_{1\text{dih}}$ in Eq. (5) is given by

$$\begin{aligned} V_{1\text{dih}} = & \left\{ \sum_{i=1}^2 k_{d,i}^{(1)} \sin^3(\theta_{i,1}) \sin^3(\theta_{i,2}) \sin^2\tau_i \right. \\ & + \sum_{i=3}^8 k_{d,i}^{(1)} \sin^3(\theta_{i,1}) \sin^3(\theta_{i,2}) [\cos\tau_i - \cos\tau_i^{(1)}]^2 \left. \right\} S_6(r_5, r_6) \\ & + \left\{ \sum_{i=3}^8 k_{d,i}^{(2)} \sin^3(\theta_{i,1}) \sin^3(\theta_{i,2}) [\cos\tau_i - \cos\tau_i^{(2)}]^2 \right\} S_7(r_5), \quad (\text{V.15}) \end{aligned}$$

where

$$S_6(r_5, r_6) = \exp\{-w_6 [(r_5 - r_5^{0(1)})^2 + (r_6 - r_6^{0(1)})^2]\} \quad (\text{V.16})$$

and

$$S_7(r_5) = \exp[-w_7(r_5 - r_5^{0(2)})^2] . \quad (\text{V.17})$$

In Eq. (V.15), k_d is the dihedral force constant for DBH (1) and DB (2) and τ is the dihedral angle. The definitions of these angles are given in Table XXIV for both DBH and the DB. For every set of four atoms which define a dihedral angle, i.e., α - β - γ - δ , the angles $\theta_{i,1}$ and $\theta_{i,2}$ in Eq. (V.15) represent the corresponding bond angles α - β - γ and β - γ - δ , respectively. The form of Eq. (V.15) assures that the dihedral interactions vanish when either of the two angles $\theta_{i,1}$ and $\theta_{i,2}$ is equal to 180° and the dihedral angle is no longer defined. The use of switching functions $S_6(r_5, r_6)$ and $S_7(r_5)$ determines the attenuation of the dihedral interactions for large C-N distances relative to the corresponding equilibrium values in DBH and DB.

The analytical expression of V_3 term in Eq. (V.4) is that previously described for the BCP molecule (see Chapter IV and Ref. 150).

A Morse function was used for the N-N interaction in the N_2 molecule:

$$V_4 = D_{NN} \{ \exp[-2\beta_{NN}(r - r_{NN}^0)] - 2 \exp[-\beta_{NN}(r - r_{NN}^0)] \} \quad (\text{V.18})$$

The connection between the potential terms representing the reactants and products is achieved by using the parametrized switching functions $S_1(r_5, r_6)$ and $S_2(r_5, r_6)$:

$$S_1(r_5, r_6) = \{ 1 - \tanh[w_1(r_5 - r_5^{0(1)})^2] \tanh[w_1(r_6 - r_6^{0(1)})^2] \} \{ 1 - B(r_5 - r_5^{0(1)})^2 (r_6 - r_6^{0(1)})^2 \exp\{-C[(r_5 - r_5^{0(1)})^2 + (r_6 - r_6^{0(1)})^2]\} \} \quad (\text{V.19})$$

and

$$S_2(r_5, r_6) = \tanh[w_2 (r_5 - r_5^{0(1)})^2] \tanh[w_2 (r_6 - r_6^{0(1)})^2]. \quad (\text{V.20})$$

The values of the equilibrium parameters $r_1^{0(1)}$, $\theta_1^{0(1)}$ and $\tau_1^{0(1)}$ in Eqs.(V.6)-(V.8),(V.10)-(V.12), (V.15) are adjusted to reproduce the experimental equilibrium geometry of DBH given in Table XVII. The values of the corresponding parameters for the DB (2), $r_1^{0(2)}$, $\theta_1^{0(2)}$ and $\tau_1^{0(2)}$ are determined from the *ab initio* optimized geometry of DB at the UMP2/6-31G* level (see Table XVIII). The preexponential Morse factors in Eqs. (V.6)-(V.8) are set equal to the estimated bond dissociation energies as described in paragraph C. The values of the switching parameters B, C, w_1 - w_6 have been determined so as to reproduce the experimental value of the barrier height for the case of stepwise dissociation of DBH and the *ab initio* calculated barrier for the case of symmetric stretch of both C-N bonds in DBH. The remaining parameters of the potential, i.e., the curvature parameters $\beta_i^{(1)}$, $\beta_i^{(2)}$, $k_i^{(1)}$, $k_i^{(2)}$ and $k_{d,i}^{(1)}$, $k_{d,i}^{(2)}$ were adjusted to the scaled values of fundamental vibrational frequencies for DBH and DB, respectively, which were determined by *ab initio* calculations at the MP2/6-31G* level (see Table XIX). The values of the Morse parameters in the N₂ potential term were taken from Refs. 190 and 193. The numerical values of all parameters used in construction of the potential, except for those specific to BCP, are given in Tables XXV-XXVII.

E. Properties of the Potential-Energy Surface

The equilibrium structures for the reactants and products were determined by using a damped trajectory method.⁴⁵ In this procedure, the atoms are initially placed in a configuration near the local minimum being sought, with all initial momenta set to zero. The Hamiltonian equations of

motion are then integrated until the total kinetic energy attains a maximum value, at which point the integration is halted and the momenta of all atoms are again set to zero. This procedure is repeated until the system converges to a local potential minimum.

The equilibrium energies obtained from the global potential are given in Table XXIX relative to separated atoms. The predicted heat of reaction for DBH decomposition is -13.17 kcal/mol, which is in good agreement with the experimental value of -12.26 kcal/mol calculated using the standard enthalpies of formation of DBH¹⁸⁸ and BCP.¹⁶⁰ The predicted structures for DBH, the DB, BCP and N₂ are in excellent agreement with experimental and *ab initio* calculated data (see Tables XVII and XVIII).

The fundamental vibrational frequencies for DBH and the DB (2) obtained using numerical second derivatives of the global potential surface are given in Table XXIX. The average root-mean-square deviation between the frequencies obtained from the global surface and the *ab initio* calculated values is 24.0 cm⁻¹ for DBH and 26.8 cm⁻¹ for DB (2). The corresponding normal mode frequencies for BCP have been previously reported.¹⁵⁰

The reaction profiles for the case of stepwise and concerted breaking of the C-N bonds have been obtained using a combination of grid search and constrained damped trajectory methods.¹ The execution of a constrained trajectory involves the integration of Hamilton equations of motion modified to include the effect of the virtual forces, which are determined by the constraint conditions and incorporated using the Lagrangian multipliers method (see Chapter II and Ref. 1).

In the case of a stepwise mechanism, we have assumed that the reaction coordinate between DBH and DB can be described with a function of the C-N bond subject to the greatest elongation. Proceeding from the diradical state, we

have characterized the complete deazetization reaction profile as a function of the length of the other C-N bond. In the case of practical calculations, after a given displacement of one of the C-N bonds, a constrained damped trajectory is calculated to relax the system to the most stable configuration consistent with the respective constraint. The process is then repeated starting from the relaxed structure obtained in the previous step.

The reaction profile obtained from the analytical surface for the case of stepwise mechanism is shown in Fig. 29. In the first region, the variation of the potential was recorded as a function of the C₁-N₁₄ bond distance, with zero energy assigned to the DBH equilibrium state. The DB state corresponds to the final part of this variation, for $r_5=4.45$ Å. The depth of the potential well at the diradical site is about 1.31 kcal/mol. Starting from the diradical state, we have calculated the potential profile as a function of C₄-N₁₅ bond distance. The barrier height is 37.3 kcal/mol and the crest occurs at $r_6=1.73$ Å. In Fig. 30 we show the variation of the flap angle, determined by the plane of the atoms C₁-C₅-C₄ and C₁-C₄-M, where M is the middle of the C₂-C₃ bond distance, corresponding to the potential variation given in Fig. 29. It can be seen from Fig. 30 that for the minimum energy path followed in this succession of bond distances, the variation of the flap angle seems to favor *exo* BCP as the final product, because the equilibrium flap angle for the diradical is -23.0°. A pictorial description of the molecular configurations for different points along this minimum energy path is shown in Fig. 31.

In the case of a concerted increase of both C-N bond distances, the variation of the total potential is presented in Fig. 32. In this case, the calculation was performed using the double constraint $r_5=r_6=\text{constant}$, while all atoms were relaxed to the minimum potential energy consistent with these constraints. The barrier crest occurs for $r_5=r_6=2.73$ Å and lies 66.8 kcal/mol

above the equilibrium DBH state. The position of the barrier crest is similar to that obtained in the *ab initio* calculations, but the calculated barrier is about 8 kcal/mol lower than the corresponding value found at the HF/6-31G* level.

Computational Procedures

In order to investigate the dissociation dynamics of the DBHD molecule on the analytical potential surface, we have used classical trajectory calculations¹ at several internal energies. The overall objectives are to determine the ratio of bicyclo(2.1.0)pentane-exo,exo-2,3-d₂ (**5x**) and -endo,endo-2,3-d₂ (**5n**) predicted by the semiempirical potential and to investigate the statistical/nonstatistical character of the unimolecular decomposition reaction.

The initial states of trajectories are prepared by first inserting zero-point energy into each of the DBHD vibrational normal modes using a projection method,^{46,47} while the normal mode velocities for rotation and translation are set to zero. Hamilton's equations of motion in a space-fixed Cartesian coordinate system are then integrated for a random period of time

$$t_r = \xi T_m \tag{V.21}$$

using a fourth-order Runge-Kutta procedure, with a fixed step size of 0.01 time units (1 t.u.= 1.018x10⁻¹⁴ s). Four significant digits of energy conservation were obtained. In Eq. (V.21), ξ is a pseudo random number chosen from a distribution that is uniform over the interval [0,1] and T_m is the characteristic period of the lowest frequency vibrational mode in DBHD. The purpose of this step is to average over the vibrational phases of the molecule. Subsequent to the above integration, the desired excitation energy is then inserted randomly into DBHD using projection techniques.^{46,47} The time t_r is taken to be zero for

the purpose of rate calculations. From these initial conditions, trajectories are integrated until reaction occurs or until an upper limit of time, t_{\max} , is reached.

We used power spectra of classical trajectories as an additional tool to investigate the DBHD dynamics. Power spectra were obtained by transforming the time histories of internal coordinates (bond lengths, bond angles, etc.) from single trajectories using the method described in Chapter IV (see also Ref.150). The composite power spectrum was calculated as a superposition of the individual power spectra of the scaled internal variables.

Results of Trajectory Calculations and Discussions

The decomposition dynamics of DBHD were investigated for internal energies between 60-175 kcal/mol, initially distributed at random over the 39 vibrational modes.

Figures 33 and 34 show details of the typical temporal variation of the two C-N bonds and of the corresponding flap angle for reactions leading to the **(5x)** and **(5n)** products, respectively. In the case of bond lengths plots, the $r(\text{C}_4\text{-N}_{15})$ curve is displaced upward by 2.5 Å for clarity. Time is given in molecular units (1 t.u. = 1.018×10^{-14} s). It can be seen that the breaking of the C-N bonds occurs successively. Before reaching the product state, the BCP molecule oscillates momentarily in the well corresponding to 1,3-cyclopentadiyl radical. It has been previously shown¹⁵⁰ that this well is characterized by a flap angle ranging between $\pm 25.2^\circ$. Although the statistical accuracy of our data is limited, the results suggest that those trajectories which pass through the cyclopentane-1,3-diyl radical well lead to a near unit ratio of **(5x)** and **(5n)** products as statistical theory would expect. However, not all trajectories leading to products are seen to pass through this well. Figure 35 illustrates such a case, in which there is no oscillation of the flap angle around the null value.

Trajectories of this type lead predominately to the (5x) BCP product thereby producing an overall (5x) : (5n) ratio that is greater than unity.

Decay plots are obtained from ensembles of 250 trajectories for the energy range 100-175 kcal/mol and 500 trajectories for excitation energies between 60-80 kcal/mol. A panel of selected plots at different excitation energies is presented in Fig. 36. It can be seen that these plots generally exhibit a high degree of linearity, which is a necessary condition for statistical behavior.

Microcanonical rate constants $k(E)$ have been extracted by least-squares fitting of the decay plots using

$$\ln(N_t/N_0) = -k(E) t , \quad (\text{V.22})$$

where N_t is the number of unreacted trajectories at time t and N_0 is the total number of trajectories in the ensemble. The rate obtained from the slopes of the least-square fits are given in Table XXXI.

The dependence of rate coefficients given in Table XXXI upon the internal excitation energy may be fitted with an acceptable degree of accuracy to a Rice-Ramsperger-Kassel (RRK) equation⁵²

$$k(E) = v_1(1 - E_{0,1}/E)^{s_1-1} + v_2(1 - E_{0,2}/E)^{s_2-1} \quad (\text{V.23})$$

where $E_{0,1} = 37.3$ kcal/mol and $E_{0,2} = 66.8$ kcal/mol are the minimum energies required for DBHD decomposition via the DB path or the symmetric stretch of both C-N bonds, and s_1 and s_2 are the corresponding numbers of effective degrees of vibrational freedom. The resulting RRK fitted parameters are $s_1 = 4.75$, $s_2 = 17.5$, $v_1 = 6.25$ ps⁻¹ and $v_2 = 8$ ps⁻¹. The RRK fit is shown in Fig. 37.

For every excitation energy, we also present in Table XIV the calculated branching ratios giving the exo (**5x**) and endo (**5n**) bicyclopentanes. These results clearly show a preference for inversion of stereochemistry and are in qualitative agreement with the experimental results.^{141a,176,177} Nevertheless, the large error bars make it difficult to assess the energy dependence of the exo/endo ratio, particularly for low vibrational energies. However, the relatively weak dependence of the ratio upon E clearly suggests that over the narrow temperature range that has been investigated experimentally, no significant temperature dependence of the rate should be observed. This result is in agreement with the data reported by Carpenter *et al.*¹⁷⁹

Simpson *et al.*¹⁷⁴ have investigated the vibrational energy content of the fragments formed in thermal decomposition of DBH over the range 900-1400 K. Their results show that N₂ is not formed with large amounts of vibrational energy, a result which further supports a stepwise dissociation mechanism. Indeed, the synchronous cleavage of the two C-N bonds is expected to yield N₂ in highly excited vibrational states, since the N-N axis would be orthogonal to the reaction coordinate and the variation of the N-N bond length from DBH to free nitrogen is large (ca. 0.148 Å).¹⁷⁵ In addition, it has been found¹⁷⁴ that BCP is generally formed with an excess of vibrational energy over the equilibrium distribution. This result proves that the most significant energy release in the reaction takes place after the elimination of the N₂ molecule.

Based on the results of classical trajectories, we have computed the analogous energy distributions for the fragments of DBHD decomposition. Table XXXII gives the translational, rotational, and vibrational energy distributions of N₂ and BCP at internal energies of 60-175 kcal/mol. In each case $\langle F_T \rangle$, $\langle F_R \rangle$ and $\langle F_V \rangle$ denote the average fractions of energy partitioned into translational, rotational, and vibrational motion of the products, respectively.

The translational energies of the fragments were calculated with respect to the space-fixed origin (which coincides with the mass center of the system). The rotational energy of the fragments was determined using

$$E_{\text{rot}} = \omega \cdot I \cdot \omega / 2 , \quad (\text{V.24})$$

where ω is the angular velocity vector (calculated relative to the mass center of the fragment) and I is the moment-of-inertia tensor, also calculated relative to the mass center of the fragment. The vibrational energy was approximated as the difference between the total internal energy and the rotational energy.

The values given in Table XXXII show that most of the available energy is partitioned into the vibrational modes of BCP. The ratio of BCP to N_2 translational energy is, as it should be, determined by the fragment masses. Since there are 36 internal degrees of freedom in BCP and only three in N_2 , a completely statistical distribution would yield $[\langle F_R \rangle + \langle F_V \rangle]_{\text{BCP}} / [\langle F_R \rangle + \langle F_V \rangle]_{\text{N}_2} = 12$. The trajectory results give values ranging between 12.8 and 13.6.

Further insight into the dissociation process can be gained by examining the internal energy distributions of the products resulting from DBHD deazetization. Figure 38 shows the total translational energy distributions for trajectories computed at 60 kcal/mol and 175 kcal/mol. The bandwidth for each histogram was determined using the method of Gislason and Goldfield,¹⁹⁴ such that it varies with the total energy. It can be seen in Fig. 13 that the fragments emerge with small amounts of kinetic energy, which slowly increases when the total energy is increased.

The normalized rotational and vibrational energy distributions of N_2 molecules formed in the deazetization reaction at total energies of 60 and 175 kcal/mol are presented in Figs. 39 and 40. The average rotational energy

increases from 2.6 to 5.1 kcal/mol as the total energy is increased from 60 to 175 kcal/mol. This small variation of the average rotational energy is expected since the bending force constants for C-N=N, H-C-N and C-C-N angles of DB approach zero as the C-N bond length is increased. However, the existence of some products with relatively high rotational energies (10-25 kcal/mol) indicates that a considerable torque may occur. At 60 kcal/mol, the average vibrational energy of N₂ is 7.0 kcal/mol, which is about twice the zero-point energy (3.37 kcal/mol). This value increases to 13.1 kcal/mol at 175 kcal/mol. Although our calculations are performed at a much higher excitation energy than the experimental conditions employed by Simpson *et al.*¹⁷⁴, it appears that they are in agreement with the experimental data, since at 60 kcal/mol the majority of N₂ molecules are formed with small amounts of excess vibrational energy.

The vibrational energy distributions of BCP at 60 and 175 kcal/mol are given in Figure 41. As can be seen, there is a significant increase in the average vibrational energy with the total excitation energy. This result demonstrates that most of the available reaction energy is confined to vibrational modes of BCP, again in agreement with the data reported by Simpson *et al.*¹⁷⁴

In order to obtain a more accurate description of the vibrational energy distribution in the BCP product, we have also calculated the average normal-mode velocities in this molecule at the end of reactive trajectories. This was done by taking the average of the normal-mode-kinetic energies, calculated using the projection method previously introduced by Raff.^{46,47} For a given mode *i*, the average total energy can be expressed as

$$\langle E_i(t) \rangle = 2(\Delta t)^{-1} \int_{t_0}^{t_0+\Delta t} K_i(\tau) d\tau \quad (\text{V.25})$$

where $K_i(t)$ represents the normal-mode kinetic energy of mode i , and t is a time in the interval $t_0 \leq t \leq t_0 + \Delta t$. The time interval Δt is chosen to average out most of the fluctuations in $K_i(t)$ due to the interconversion of potential and kinetic energies within the same mode. In our calculations $\Delta t=30$ t.u. Ensembles of 20 reactive trajectories, each initially having zero-point energy in all normal modes and a given excitation energy distributed at random over all modes have been considered in these calculations. At the end of trajectories, the normal-mode energies were determined for additional 300 t.u. In Fig. 42 we present the time variation of the root-mean-square deviations of the average normal mode energies, for the case of trajectories performed at 60 kcal/mol initial excitation energy. As can be seen, there is a small temporal variation of these deviations, which correspond to limited variations of the mode energies around the average value. The small spread of the normal mode energies around the average value adds further support to the view that the reaction mechanism is well described by statistical theories.

An additional means of investigation of the reaction mechanism is by the computation of power spectra for internal coordinates. In each case, ensembles of 20 trajectories were used in the calculations to represent the distribution of the classical initial conditions over a specified initial region of phase space. The internal coordinates were recorded after every 40th integration step (1 integration step=0.01 t.u.) and the trajectories were followed for a maximum period of 818.8 t.u. or until dissociation took place. A resolution of 4.0 cm^{-1} was obtained for all power spectra presented in this study. The composite power spectra at zero-point energy and at 40, 70 and 100 kcal/mol excitation energies are shown in Fig. 43. The excitation energies were initially distributed at random among the vibrational modes. As the internal energy increases, significant broadening of the spectral lines occurs, which, at higher energies,

leads to overlapping of the spectral features. This effect is directly related to the enhancement of the mode coupling, and consequently, to the increase of the intramolecular vibrational rates with the total energy.⁷⁰ These results suggest a rapid redistribution of the available internal energy over the internal modes and correspondingly large intramolecular vibrational rates compared to the reaction rates. This is a necessary condition for the absence of nonstatistical effects.

The totality of the above results suggests that the reaction mechanism is statistical. Indeed, the high degree of linearity of the decay plots, the microcanonical energy distribution in BCP, as well as the statistical energy partitioning between the reaction products support these conclusions. In addition, the significant broadening in power spectra with the overlapping of the vibrational bands further supports the statistical character of the reaction.

Summary

By extension of previously reported results for BCP,¹⁵⁰ we have constructed a global potential-energy surface that describes the thermal deazetization of the DBH molecule. The potential is written as a superposition of channel potentials connected by parametrized switching functions.

The geometrical parameters in the expression of the potential were adjusted to reproduce the experimental equilibrium structure of the DBH molecule and the *ab initio* calculated configuration corresponding to DB. The bond dissociation energies in DBH and DB were estimated based on the reported values in BCP¹⁵⁰ and the thermochemical experimental data available. The force constant parameters in the potential were determined by fitting the *ab initio* calculated values for DBH and DB. Other potential parameters were adjusted to fit the experimental and *ab initio* calculated barrier heights. The absolute difference between the experimental and predicted heat

of reaction for the thermal decomposition of DBH is 0.91 kcal/mol.

Classical trajectory calculations on the analytical potential surface are used to investigate the dissociation dynamics of DBHD at several internal energies in the range 60-175 kcal/mol in excess of zero-point energy. The results show the following:

(1) The total decomposition rate of DBHD is well described by a first-order rate law. The calculated microcanonical rate coefficients vary from 0.06 ps^{-1} at 60 kcal/mol internal excitation to 1.96 ps^{-1} at 175 kcal/mol.

(2) The preference for inversion of configuration takes place, with calculated branching ratios of (5x) to (5n) between 1.8 and 2.2. However, the large errors of these ratios, particularly at low energies, make it difficult to estimate the dependence or independence of the branching ratios on the excitation energy. An investigation of the dynamics suggests that this ratio is the result of competition between two modes of reaction that involve post-transition-state effects. The first mode involves the formation of the symmetric, planar 1,3-cyclopentadiyl radical which decays with near equal probability to both endo and exo BCP. The second mode involves the direct formation of BCP by-passing the shallow well for the 1,3-cyclopentadiyl radical. This mode favors the exo product since the equilibrium flap angle for the DB is -23° .

(3) At 60 kcal/mol, the N_2 molecules are formed with relatively small amounts of vibrational and rotational energies. These quantities increase with increasing the total excitation energy. The most significant amount of excitation energy remains concentrated in the vibrational modes of BCP molecule.

(4) Computed power spectra indicate large modal couplings and overall statistical dynamics. Similar conclusions are suggested by the linear decay plots and the statistical partitioning of product energy.

Hence, we expect RRKM theory calculations to yield results for the total

DBHD decomposition rate in good accord with the trajectory results. However, such statistical calculations will be unable to predict the exo/endo BCP ratio, since the underlying factors which produce this ratio are associated with post-transition state effects not addressed by statistical theories of reaction dynamics. This expectation is in good accord with criteria which we have previously suggested to favor statistical dynamics.⁶² We have noted that whenever a unimolecular reaction produces significant bonding changes in the products relative to the original molecule, intermodal coupling and IVR rates are expected to be large. Hence, the dynamics will be statistical. In the present case, the bonding in BCP is significantly altered from that in DBHD. The observed statistical behavior of the reaction is therefore the expected result.

Table XVII

Ab initio calculated and experimentally observed geometry for DBH.

| Parameter | Exp. ^{a)} | HF/6-31G* | MP2/6-31G* |
|---|--------------------|-----------|------------|
| C ₁ -C ₂ | 1.542±0.004 | 1.547 | 1.549 |
| C ₁ -C ₅ | 1.534±0.001 | 1.526 | 1.525 |
| C ₂ -C ₃ | 1.552±0.001 | 1.553 | 1.549 |
| C ₁ -N ₁₄ | 1.503±0.004 | 1.480 | 1.494 |
| C ₁ -H ₈ | 1.087±0.002 | 1.078 | 1.090 |
| C ₂ -H ₉ | 1.085±0.008 | 1.083 | 1.093 |
| C ₂ -H ₁₀ | 1.093±0.001 | 1.082 | 1.092 |
| C ₅ -H ₆ | 1.102±0.008 | 1.083 | 1.094 |
| C ₅ -H ₇ | 1.088±0.008 | 1.083 | 1.094 |
| N ₁₄ -N ₁₅ | 1.246±0.004 | 1.220 | 1.275 |
| δ ^{b)} | 108.9±0.2 | 109.83 | 108.38 |
| β ^{b)} | 128.3±0.8 | 128.88 | 129.06 |
| γ ^{b)} | 122.8±0.8 | 121.28 | 122.55 |
| C ₁ -C ₅ -C ₄ | 91.3±0.1 | 90.94 | 91.80 |
| N ₁₄ -C ₁ -H ₈ | 110.0±0.3 | 111.43 | 111.18 |
| C ₅ -C ₁ -H ₈ | 119.7±0.1 | 119.59 | 119.84 |
| C ₂ -C ₁ -H ₈ | 116.8±0.3 | 116.22 | 116.30 |
| H ₉ -C ₂ -H ₁₀ | 108.2±0.2 | 108.04 | 108.18 |
| H ₆ -C ₅ -H ₇ | 111.4±0.1 | 110.04 | 110.28 |

a) Ref. 182.

b) These angles are defined in Fig. 26.

Table XVIII

Calculated geometries of the diazenyl biradical and its transition state for nitrogen loss.

| Parameter | UHF/6-31G* | | UMP2/6-31G* | |
|--|------------|--------|-------------|--------|
| | biradical | TS | biradical | TS |
| C ₁ -C ₅ | 1.503 | 1.506 | 1.496 | 1.499 |
| C ₄ -C ₅ | 1.535 | 1.524 | 1.533 | 1.522 |
| C ₂ -C ₃ | 1.507 | 1.506 | 1.500 | 1.497 |
| C ₃ -C ₄ | 1.532 | 1.521 | 1.527 | 1.512 |
| C ₂ -C ₃ | 1.539 | 1.542 | 1.537 | 1.541 |
| C ₅ -H ₆ | 1.085 | 1.086 | 1.095 | 1.097 |
| C ₅ -H ₇ | 1.090 | 1.090 | 1.101 | 1.102 |
| C ₁ -H ₈ | 1.073 | 1.074 | 1.083 | 1.083 |
| C ₄ -H ₁₃ | 1.084 | 1.078 | 1.094 | 1.088 |
| C ₂ -H ₉ | 1.090 | 1.090 | 1.101 | 1.101 |
| C ₂ -H ₁₀ | 1.086 | 1.086 | 1.097 | 1.097 |
| C ₃ -H ₁₁ | 1.083 | 1.083 | 1.093 | 1.093 |
| C ₃ -H ₁₂ | 1.085 | 1.085 | 1.095 | 1.098 |
| C ₄ -H ₁₅ | 1.491 | 1.792 | 1.508 | 1.787 |
| N ₁₄ -N ₁₅ | 1.173 | 1.133 | 1.151 | 1.126 |
| C ₁ -C ₅ -C ₄ | 102.46 | 102.87 | 102.08 | 103.11 |
| C ₂ -C ₁ -C ₅ | 111.50 | 111.71 | 111.70 | 111.90 |
| C ₃ -C ₄ -C ₅ | 104.93 | 107.22 | 104.90 | 107.83 |
| C ₁ -C ₅ -H ₆ | 113.78 | 113.33 | 114.05 | 113.43 |
| C ₄ -C ₅ -H ₆ | 112.34 | 112.33 | 112.71 | 112.14 |
| C ₁ -C ₅ -H ₇ | 111.64 | 111.42 | 112.06 | 111.70 |
| C ₄ -C ₅ -H ₇ | 109.77 | 110.45 | 109.19 | 110.56 |
| C ₂ -C ₁ -H ₈ | 124.39 | 124.35 | 124.39 | 124.31 |
| C ₅ -C ₁ -H ₈ | 124.01 | 123.93 | 123.90 | 123.62 |
| C ₁ -C ₂ -C ₉ | 111.10 | 111.05 | 111.35 | 111.34 |
| C ₃ -C ₂ -C ₉ | 110.78 | 110.67 | 110.66 | 110.42 |

Table XVIII (continued)

| Parameter | UHF/6-31G* | | UMP2/6-31G* | |
|--|------------|--------|-------------|--------|
| | biradical | TS | biradical | TS |
| C ₁ -C ₂ -H ₁₀ | 112.95 | 112.94 | 113.06 | 113.04 |
| C ₃ -C ₂ -H ₁₀ | 112.14 | 112.14 | 112.30 | 112.34 |
| C ₄ -C ₃ -H ₁₁ | 112.84 | 112.90 | 112.70 | 112.79 |
| C ₂ -C ₃ -H ₁₁ | 113.58 | 113.40 | 114.15 | 113.70 |
| C ₄ -C ₃ -H ₁₂ | 109.23 | 109.44 | 108.38 | 108.54 |
| C ₂ -C ₃ -H ₁₂ | 110.02 | 109.76 | 110.67 | 110.15 |
| C ₃ -C ₄ -H ₁₃ | 110.31 | 114.82 | 111.50 | 116.50 |
| C ₅ -C ₄ -H ₁₃ | 109.34 | 114.37 | 110.34 | 115.72 |
| C ₃ -C ₄ -N ₁₅ | 117.03 | 113.42 | 114.65 | 109.40 |
| C ₄ -N ₁₅ -N ₁₄ | 120.31 | 116.34 | 127.02 | 122.46 |
| C ₂ -C ₁ -C ₅ -C ₄ | 12.80 | 6.55 | 13.39 | 2.29 |
| C ₃ -C ₄ -C ₅ -C ₁ | -31.38 | -24.98 | -32.32 | -21.06 |
| N ₁₅ -C ₄ -C ₃ -C ₂ | 161.84 | 152.29 | 160.95 | 147.09 |
| N ₁₄ -N ₁₅ -C ₄ -C ₃ | 11.11 | 12.59 | 0.93 | -12.10 |

Table XIX

The *ab initio* scaled vibrational frequencies for DBH and diazenyl biradical. The scaling factors are 0.8929 for HF/6-31G* values and 0.94 for MP2/6-31G* data. Zero-point energies (ZPE) are given in kcal/mol.

| Mode | DBH | | | | Diazenyl biradical | |
|------|-----------|-------|------------|-------|--------------------|-------------|
| | HF/6-31G* | sym | MP2/6-31G* | sym | UHF/6-31G* | UMP2/6-31G* |
| 1 | 252.66 | (A'') | 236.09 | (A'') | 73.09 | 71.28 |
| 2 | 392.35 | (A') | 380.21 | (A') | 138.38 | 141.35 |
| 3 | 449.26 | (A') | 436.08 | (A') | 158.78 | 163.87 |
| 4 | 506.85 | (A'') | 492.82 | (A'') | 209.29 | 237.44 |
| 5 | 689.35 | (A'') | 664.26 | (A'') | 234.39 | 80.04 |
| 6 | 759.72 | (A') | 751.52 | (A') | 389.93 | 380.66 |
| 7 | 802.64 | (A'') | 790.39 | (A'') | 463.03 | 474.83 |
| 8 | 804.33 | (A') | 803.53 | (A') | 555.70 | 528.43 |
| 9 | 825.08 | (A'') | 819.04 | (A'') | 630.43 | 631.08 |
| 10 | 852.24 | (A') | 838.28 | (A') | 783.19 | 782.02 |
| 11 | 868.95 | (A') | 872.50 | (A') | 819.30 | 815.87 |
| 12 | 918.15 | (A'') | 897.57 | (A'') | 858.51 | 879.39 |
| 13 | 926.47 | (A') | 936.80 | (A') | 889.51 | 888.19 |
| 14 | 958.91 | (A') | 950.27 | (A'') | 911.31 | 905.34 |
| 15 | 963.72 | (A'') | 954.62 | (A') | 920.27 | 937.35 |
| 16 | 1006.60 | (A') | 996.42 | (A') | 974.23 | 969.92 |
| 17 | 1037.25 | (A'') | 1014.91 | (A'') | 1003.11 | 1025.98 |
| 18 | 1117.66 | (A'') | 1096.61 | (A') | 1053.94 | 1049.72 |
| 19 | 1122.17 | (A') | 1099.45 | (A'') | 1097.93 | 1094.50 |
| 20 | 1200.38 | (A') | 1156.05 | (A') | 1154.14 | 1142.69 |
| 21 | 1210.33 | (A'') | 1178.66 | (A'') | 1210.63 | 1195.58 |
| 22 | 1237.82 | (A'') | 1198.75 | (A'') | 1250.32 | 1228.00 |
| 23 | 1267.39 | (A'') | 1233.64 | (A') | 1271.38 | 1243.87 |
| 24 | 1295.35 | (A') | 1237.06 | (A'') | 1289.91 | 1269.84 |
| 25 | 1297.02 | (A'') | 1252.44 | (A'') | 1313.91 | 1286.88 |

Table XIX (continued)

| Mode | DBH | | | | Diazenyl biradical | |
|------|-----------|-------|------------|-------|--------------------|-------------|
| | HF/6-31G* | sym | MP2/6-31G* | sym | UHF/6-31G* | UMP2/6-31G* |
| 26 | 1304.96 | (A'') | 1263.38 | (A'') | 1325.26 | 1312.24 |
| 27 | 1322.13 | (A') | 1294.26 | (A') | 1349.09 | 1322.75 |
| 28 | 1458.33 | (A'') | 1379.59 | (A') | 1453.78 | 1444.30 |
| 29 | 1464.80 | (A') | 1446.29 | (A') | 1457.51 | 1448.94 |
| 30 | 1484.05 | (A') | 1450.56 | (A'') | 1474.12 | 1465.04 |
| 31 | 1668.81 | (A') | 1473.35 | (A') | 1522.35 | 2779.48 |
| 32 | 2891.12 | (A'') | 2942.74 | (A'') | 2825.08 | 2870.87 |
| 33 | 2900.10 | (A') | 2945.99 | (A') | 2828.28 | 2872.20 |
| 34 | 2905.24 | (A') | 2949.82 | (A') | 2877.27 | 2933.22 |
| 35 | 2930.91 | (A'') | 2996.43 | (A'') | 2888.09 | 2943.25 |
| 36 | 2945.05 | (A') | 3007.91 | (A') | 2891.22 | 2947.90 |
| 37 | 2949.77 | (A') | 3010.30 | (A'') | 2903.25 | 2962.16 |
| 38 | 2973.19 | (A'') | 3011.00 | (A') | 2932.76 | 3002.18 |
| 39 | 2977.55 | (A') | 3013.44 | (A') | 3020.41 | 3090.62 |
| ZPE | 78.53 | | 77.87 | | 73.48 | 75.79 |

Table XX

Thermochemical and *ab initio* calculated data for the compounds of interest. The enthalpies of formation and the thermal corrections (TC) are given in kcal/mol. The total G1 energies and zero-point energies are in hartrees and milihartrees respectively.

| Compound | ΔH_f | TC | ZPE | G1 energy |
|--|---------------------------|---------------------|----------------------|-----------------------------|
| C ₂ H ₄ N ₂ | 64.0 ^{a)} | 41.42 ^{a)} | 61.45 ^{b)} | -187.71074896 ^{a)} |
| H ₂ | 0.0 | 8.32 ^{c)} | 9.45 ^{d)} | -1.16501 ^{d)} |
| CH ₄ | -17.90±0.08 ^{c)} | 29.50 ^{c)} | 42.66 ^{d)} | -40.40772 ^{d)} |
| NH ₃ | -10.97±0.1 ^{c)} | 23.94 ^{c)} | 33.04 ^{d)} | -56.45477 ^{d)} |
| C ₂ H ₈ N ₂ | -4.20±1.14 ^{e)} | | 106.88 ^{b)} | |
| C ₅ H ₈ N ₂ | 49.56±0.64 ^{f)} | | | |

a) Obtained using the procedure described in the text.

b) *Ab initio* calculated at the HF/6-31G* level and scaled by 0.8929.

c) Ref. 32.

d) Ref. 185

e) Ref. 189.

f) Ref. 188.

Table XXI

Ab initio calculated geometries (C_{2v} symmetry) and energies (in hartrees) of dimethylenediazene (diazetene).

| Parameter | HF/6-31G* | MP2/6-31G* | MP2(FU)/6-31G* |
|------------------|------------|------------|----------------|
| r(N-N) | 1.229 | 1.290 | 1.289 |
| r(N-C) | 1.470 | 1.489 | 1.487 |
| r(C-H) | 1.082 | 1.093 | 1.093 |
| θ (N-N-C) | 96.01 | 94.76 | 94.75 |
| θ (N-C-H) | 112.98 | 112.50 | 112.49 |
| θ (H-C-H) | 109.75 | 109.70 | 109.72 |
| Energy | -186.86780 | -187.44469 | -187.46086 |

Table XXII

Optimized parameters (bond distances in Å, angles in degrees), total energies (in hartrees) and zero-point energies (ZPE) (in kcal/mol) for conformations gGg' (1), tGg' (2) and tTt (3) of ethylenediamine.

| Parameter | HF/6-31G* | | | MP2/6-31G* | |
|--|-----------|--------|---------|------------|---------|
| | (1) | (2) | (3) | (1) | (3) |
| C ₂ -C ₁ | 1.5216 | 1.5284 | 1.5328 | 1.5202 | 1.5324 |
| N ₃ -C ₂ | 1.4509 | 1.4508 | 1.4526 | 1.4614 | 1.4645 |
| N ₄ -C ₁ | 1.4582 | 1.4570 | 1.4525 | 1.4698 | 1.4645 |
| H ₅ -C ₂ | 1.0945 | 1.0875 | 1.0870 | 1.1054 | 1.0970 |
| H ₆ -C ₂ | 1.0858 | 1.0858 | 1.0870 | 1.0960 | 1.0970 |
| H ₇ -C ₁ | 1.0912 | 1.0924 | 1.0870 | 1.1015 | 1.0970 |
| H ₈ -C ₁ | 1.0835 | 1.0864 | 1.0870 | 1.0937 | 1.0970 |
| H ₉ -N ₃ | 1.0013 | 1.0023 | 1.0023 | 1.0183 | 1.0195 |
| H ₁₀ -N ₃ | 1.0016 | 1.0027 | 1.0023 | 1.0194 | 1.0195 |
| H ₁₁ -N ₄ | 1.0011 | 1.0014 | 1.0023 | 1.0181 | 1.0195 |
| H ₁₂ -N ₄ | 1.0023 | 1.0026 | 1.0023 | 1.0193 | 1.0195 |
| N ₃ -C ₂ -C ₁ | 109.99 | 115.27 | 115.41 | 108.77 | 115.76 |
| N ₄ -C ₁ -C ₂ | 110.17 | 110.23 | 115.41 | 109.13 | 115.76 |
| H ₅ -C ₂ -C ₁ | 108.67 | 108.91 | 109.35 | 108.40 | 109.20 |
| H ₆ -C ₂ -C ₁ | 109.01 | 109.29 | 109.36 | 109.33 | 109.20 |
| H ₇ -C ₁ -C ₂ | 109.34 | 109.30 | 109.36 | 109.75 | 109.20 |
| H ₈ -C ₁ -C ₂ | 108.41 | 109.17 | 109.36 | 108.11 | 109.20 |
| H ₉ -N ₃ -C ₂ | 111.04 | 109.11 | 110.96 | 110.24 | 109.38 |
| H ₁₀ -N ₃ -C ₂ | 109.28 | 110.17 | 110.95 | 107.09 | 109.38 |
| H ₁₁ -N ₄ -C ₁ | 111.05 | 111.13 | 110.95 | 110.13 | 109.38 |
| H ₁₂ -N ₄ -C ₁ | 110.65 | 110.54 | 110.96 | 109.34 | 109.38 |
| N ₄ -C ₁ -C ₂ -N ₃ | -64.76 | -60.17 | -179.95 | -63.42 | -179.84 |
| H ₅ -C ₂ -C ₁ -N ₄ | 60.05 | 61.38 | -57.99 | 61.42 | -57.90 |
| H ₆ -C ₂ -C ₁ -N ₄ | 176.07 | 177.20 | 58.07 | 177.60 | 58.19 |
| H ₆ -C ₂ -C ₁ -H ₇ | 52.19 | 52.09 | -179.96 | 52.19 | -179.86 |

Table XXII (continued)

| Parameter | HF/6-31G* | | | MP2/6-31G* | |
|---|------------|------------|------------|------------|------------|
| | (1) | (2) | (3) | (1) | (3) |
| H ₇ -C ₁ -C ₂ -N ₃ | 170.41 | 174.72 | -57.97 | 171.15 | -57.90 |
| H ₈ -C ₁ -C ₂ -N ₃ | 53.33 | 58.06 | 58.08 | 63.70 | 58.19 |
| H ₉ -N ₃ -C ₂ -C ₁ | 173.53 | 50.54 | -59.40 | 169.76 | -57.82 |
| H ₁₀ -N ₃ -C ₂ -C ₁ | 54.72 | -66.03 | 59.51 | 53.43 | 57.83 |
| H ₁₁ -N ₄ -C ₁ -C ₂ | 166.32 | 170.04 | 59.45 | 166.63 | 57.83 |
| H ₁₂ -N ₄ -C ₁ -C ₂ | -75.02 | -71.43 | -59.45 | -77.03 | -57.82 |
| Energy | -189.26853 | -189.26847 | -189.26651 | -189.85846 | -189.85637 |
| ZPE ^{a)} | 75.11935 | 75.06179 | 74.76919 | | |

a) Unscaled values.

Table XXIII

Total energies (in hartrees) and G1 corrections (in mhartrees) for dimethylenediazene.

| Method | Energy (hartrees) | Corrections (hartrees) |
|--|-------------------|-------------------------------------|
| HF/6-31G*//HF/6-31G* | -186.8678022 | |
| MP2/6-31G*//MP2/6-31G* | -187.4446955 | |
| MP2(FU)/6-31G*// MP2(FU)/6-31G* | -187.4608610 | |
| MP4SDTQ(FC)/6-311G**// MP2(FU)/6-31G* | -187.5991155 | $\Delta E(\text{HLC}) = -0.06754$ |
| MP4/6-311+G**// MP2(FU)/6-31G* | -187.6075066 | $\Delta E(+) = -0.00839108$ |
| MP4/6-311G(2df)// MP2(FU)/6-31G* | -187.6974783 | $\Delta E(2df) = -0.09836278$ |
| QCISD(T)/6-311G**// MP2(FU)/6-31G* | -187.5979101 | $\Delta E(\text{QCI}) = 0.00120542$ |
| ZPE//HF/6-31G* | 0.0688269 | $\Delta ZPE = 0.061455$ |
| G1 | -187.71074896 | |

Table XXIV

Bond and angle assignments for DBH and the diazenyl biradical.

| Distance between atoms | | Label | Angle between atoms | | | Label | | |
|------------------------------|----|-----------------|---------------------|----------------|----|-----------------|----|-----------------|
| 1 | 2 | r ₁ | 1 | 2 | 3 | θ ₁ | | |
| 3 | 4 | r ₂ | 2 | 3 | 4 | θ ₂ | | |
| 1 | 5 | r ₃ | 2 | 1 | 14 | θ ₃ | | |
| 4 | 5 | r ₄ | 3 | 4 | 15 | θ ₄ | | |
| 1 | 14 | r ₅ | 1 | 14 | 15 | θ ₅ | | |
| 4 | 15 | r ₆ | 4 | 15 | 14 | θ ₆ | | |
| 1 | 8 | r ₇ | 2 | 1 | 5 | θ ₇ | | |
| 4 | 13 | r ₈ | 3 | 4 | 5 | θ ₈ | | |
| 2 | 3 | r ₉ | 5 | 1 | 14 | θ ₉ | | |
| 2 | 9 | r ₁₀ | 5 | 4 | 15 | θ ₁₀ | | |
| 3 | 11 | r ₁₁ | 1 | 5 | 4 | θ ₁₁ | | |
| 2 | 10 | r ₁₂ | 1 | 2 | 9 | θ ₁₂ | | |
| 3 | 12 | r ₁₃ | 4 | 3 | 11 | θ ₁₃ | | |
| 5 | 6 | r ₁₄ | 1 | 2 | 10 | θ ₁₄ | | |
| 5 | 7 | r ₁₅ | 4 | 3 | 12 | θ ₁₅ | | |
| 14 | 15 | r ₁₆ | 9 | 2 | 10 | θ ₁₆ | | |
| Dihedral angle between atoms | | Label | 11 | 3 | 12 | θ ₁₇ | | |
| 1 | 2 | 3 | 4 | τ ₁ | 2 | 3 | 11 | θ ₁₈ |
| 4 | 15 | 14 | 1 | τ ₂ | 3 | 2 | 9 | θ ₁₉ |
| 2 | 3 | 4 | 5 | τ ₃ | 2 | 3 | 12 | θ ₂₀ |
| 5 | 1 | 2 | 3 | τ ₄ | 3 | 2 | 10 | θ ₂₁ |
| 3 | 4 | 5 | 1 | τ ₅ | 1 | 5 | 6 | θ ₂₂ |
| 4 | 5 | 1 | 2 | τ ₆ | 4 | 5 | 6 | θ ₂₃ |
| 2 | 3 | 4 | 15 | τ ₇ | 1 | 5 | 7 | θ ₂₄ |
| 14 | 1 | 2 | 3 | τ ₈ | 4 | 5 | 7 | θ ₂₅ |
| 3 | 4 | 15 | 14 | τ ₉ | 6 | 5 | 7 | θ ₂₆ |
| | | | | | 2 | 1 | 8 | θ ₂₇ |
| | | | | | 3 | 4 | 13 | θ ₂₈ |

Table XXIV (continued)

| Dihedral angle between atoms | Label | Angle between atoms | Label |
|---------------------------------|-------------|------------------------|---------------|
| 15 14 1 2 | τ_{10} | 5 1 8 | θ_{29} |
| 15 14 1 5 | τ_{11} | 5 4 13 | θ_{30} |
| 5 4 15 14 | τ_{12} | 14 1 8 | θ_{31} |
| | | 15 4 13 | θ_{32} |

Table XXV

Morse parameters for: (a) DBH; (b) diazenyl biradical; and (c) nitrogen.

| Diatomic Pair | D (eV) | β (\AA^{-1}) | R^0 (1) (\AA) / R^0 (2) (\AA) |
|------------------------------------|------------|-------------------------------|--|
| C ₁ -C ₂ (a) | 4.07016381 | 1.75127282 | 1.542 |
| C ₁ -C ₅ | 4.07016381 | 1.68432026 | 1.534 |
| C ₁ -N ₁₄ | 2.05979950 | 2.52155557 | 1.503 |
| C ₁ -H ₈ | 4.48385828 | 1.85236803 | 1.087 |
| C ₂ -C ₃ | 4.07016381 | 1.75127282 | 1.552 |
| C ₂ -H ₉ | 4.19722092 | 1.88719422 | 1.085 |
| C ₂ -H ₁₀ | 4.19722092 | 1.88719422 | 1.093 |
| C ₅ -H ₆ | 4.65427959 | 1.78839197 | 1.102 |
| C ₅ -H ₇ | 4.65427959 | 1.78839197 | 1.088 |
| N ₁₄ -N ₁₅ | 5.87151268 | 1.78578998 | 1.246 |
| C ₁ -C ₂ (b) | 4.07016381 | 1.70692960 | 1.500 |
| C ₃ -C ₄ | 4.07016381 | 1.70692960 | 1.527 |
| C ₁ -C ₅ | 4.07016381 | 1.68432026 | 1.496 |
| C ₄ -C ₅ | 4.07016381 | 1.68432026 | 1.534 |
| C ₁ -N ₁₄ | 0.00000000 | ... | 4.454 |
| C ₄ -N ₁₅ | 2.05979950 | 2.52155557 | 1.508 |
| C ₁ -H ₈ | 4.48385828 | 1.90214159 | 1.083 |
| C ₄ -H ₁₃ | 4.48385828 | 1.82721090 | 1.094 |
| C ₂ -C ₃ | 4.07016381 | 1.70692960 | 1.537 |
| C ₂ -H ₉ | 4.19722092 | 1.84536203 | 1.101 |
| C ₃ -H ₁₁ | 4.19722092 | 1.88896633 | 1.093 |
| C ₂ -H ₁₀ | 4.19722092 | 1.86938077 | 1.097 |
| C ₃ -H ₁₂ | 4.19722092 | 1.88896633 | 1.095 |
| C ₅ -H ₆ | 4.65427959 | 1.76765082 | 1.096 |
| C ₅ -H ₇ | 4.65427959 | 1.75241217 | 1.101 |
| N ₁₄ -N ₁₅ | 6.58788926 | 3.85674952 | 1.151 |
| N-N(c) | 9.94388778 | 2.68503538 | 1.0977 |

Table XXVI

Bending potential parameters for: (1) DBH and (2) diazenyl biradical.

| Angle α - β - γ | $k^{(1)}_{\alpha\beta\gamma}$ (eV/rad ²) | $\theta^{(1)}$ (deg) | $k^{(2)}_{\alpha\beta\gamma}$ (eV/rad ²) | $\theta^{(2)}$ (deg) |
|--|---|-------------------------|---|-------------------------|
| C ₁ -C ₂ -C ₃ | 10.0488273 | 102.0128 | 10.1736575 | 103.4348 |
| C ₂ -C ₃ -C ₄ | 10.0488273 | 102.0128 | 10.1736575 | 102.9737 |
| N ₁₄ -C ₁ -C ₂ | 1.6334026 | 103.5934 | 0.0000000 | 74.9737 |
| C ₃ -C ₄ -N ₁₅ | 1.6334026 | 103.5934 | 2.0703081 | 114.6518 |
| N ₁₅ -N ₁₄ -C ₁ | 3.8697347 | 108.3805 | 0.0000000 | 42.3496 |
| C ₄ -N ₁₅ -N ₁₄ | 3.8697347 | 108.3805 | 3.7449046 | 127.0249 |
| C ₅ -C ₁ -C ₂ | 10.0138749 | 102.8002 | 10.2011201 | 111.6992 |
| C ₃ -C ₄ -C ₅ | 10.0138749 | 102.8002 | 10.2011201 | 104.9016 |
| N ₁₄ -C ₁ -C ₅ | 2.8086784 | 100.6997 | 0.0000000 | 39.0103 |
| C ₅ -C ₄ -N ₁₅ | 2.8086784 | 100.6997 | 2.8710935 | 110.6305 |
| C ₄ -C ₅ -C ₁ | 10.5356649 | 91.3000 | 10.2485556 | 102.0799 |
| C ₁ -C ₂ -H ₉ | 3.8697347 | 110.9012 | 4.0320139 | 111.3537 |
| C ₄ -C ₃ -H ₁₁ | 3.8697347 | 110.9012 | 4.0320139 | 112.7092 |
| C ₁ -C ₂ -H ₁₀ | 3.9071838 | 110.5533 | 4.0320139 | 113.0687 |
| C ₄ -C ₃ -H ₁₂ | 3.9071838 | 110.5533 | 4.0320139 | 108.3877 |
| H ₉ -C ₂ -H ₁₀ | 1.6852071 | 108.2000 | 2.1221126 | 106.1406 |
| H ₁₁ -C ₃ -H ₁₂ | 1.6852071 | 108.2000 | 2.1221126 | 107.8100 |
| C ₂ -C ₃ -H ₁₁ | 3.8697347 | 112.1424 | 4.0320139 | 114.1565 |
| C ₃ -C ₂ -H ₉ | 3.8697347 | 112.1424 | 4.0320139 | 110.6634 |
| C ₂ -C ₃ -H ₁₂ | 3.9071838 | 112.9742 | 4.0320139 | 110.6678 |
| C ₃ -C ₂ -H ₁₀ | 3.9071838 | 112.9742 | 4.0320139 | 112.2996 |
| C ₁ -C ₅ -H ₆ | 3.9633574 | 112.7917 | 3.9633574 | 114.0555 |
| C ₄ -C ₅ -H ₆ | 3.9633574 | 112.7917 | 3.9633574 | 112.7138 |
| C ₁ -C ₅ -H ₇ | 3.9633574 | 113.6044 | 3.9633574 | 112.0677 |
| C ₄ -C ₅ -H ₇ | 3.9633574 | 113.6044 | 3.9633574 | 109.1944 |
| H ₆ -C ₅ -H ₇ | 1.7476221 | 111.4000 | 2.1221126 | 106.7363 |
| C ₂ -C ₁ -H ₈ | 2.6838483 | 116.8000 | 3.1207538 | 124.3918 |
| C ₃ -C ₄ -H ₁₃ | 2.6838483 | 116.8000 | 3.1207538 | 111.5069 |

Table XXVI (continued)

| Angle α - β - γ | $k^{(1)}_{\alpha\beta\gamma}$ (eV/rad ²) | $\theta^{0(1)}$ (deg) | $k^{(2)}_{\alpha\beta\gamma}$ (eV/rad ²) | $\theta^{0(2)}$ (deg) |
|--|---|--------------------------|---|--------------------------|
| C ₅ -C ₁ -H ₈ | 2.6214332 | 119.7000 | 2.7462634 | 123.8990 |
| C ₅ -C ₄ -H ₁₃ | 2.6214332 | 119.7000 | 2.7462634 | 110.3412 |
| N ₁₄ -C ₁ -H ₈ | 2.7206732 | 110.9681 | 0.0000000 | 157.6100 |
| N ₁₅ -C ₄ -H ₁₃ | 2.7206732 | 110.9681 | 2.7830883 | 157.6100 |

Table XXVII

Dihedral potential parameters for: (1) DBH and (2) diazenyl biradical.

| Angle α - β - γ - δ | $k_d(1)$ (eV) | $\tau^0(1)$ (deg) | $k_d(2)$ (eV) | $\tau^0(2)$ (deg) |
|--|------------------|----------------------|------------------|----------------------|
| 1 2 3 4 | 2.5 | 0.0 | 2.7 | 30.0386 |
| 4 15 14 1 | 4.0 | 0.0 | 0.0 | 27.4086 |
| 2 3 4 5 | 2.5 | 37.0537 | 2.4 | 39.4018 |
| 5 1 2 3 | 2.5 | 37.0537 | 2.4 | 10.4277 |
| 3 4 5 1 | 0.0 | 57.4701 | 2.4 | 32.3197 |
| 4 5 1 2 | 0.0 | 57.4701 | 2.4 | 13.3957 |
| 2 3 4 15 | 3.0 | 67.4721 | 3.0 | 160.9551 |
| 14 1 2 3 | 3.0 | 67.4721 | 0.0 | 1.7288 |
| 3 4 15 14 | 0.0 | 72.1824 | 0.5 | 0.9301 |
| 15 14 1 2 | 0.0 | 72.1824 | 0.0 | 125.9480 |
| 15 14 1 5 | 3.5 | 33.9380 | 0.0 | 35.9421 |
| 5 4 15 14 | 3.5 | 33.9380 | 0.5 | 119.2971 |

Table XXVIII

Switching functions parameters used in Eqs. (V.4)-(V.20).

| Parameter | Value ^{a)} |
|----------------|---------------------|
| w ₁ | 3.8 |
| w ₂ | 3.901 |
| w ₃ | 8.0 |
| w ₄ | 3.0 |
| w ₅ | 2.0 |
| w ₆ | 2.0 |
| w ₇ | 6.0 |
| A | 28.0 |
| B | 0.98 |
| C | 1.52 |

a) The units are: \AA^{-2} for the w_i , $i=1,\dots,7$ and C, eV^{-1} for A, and \AA^{-4} for B.

Table XXIX

Equilibrium energies (not including zero-point energies) on the analytic surface.
The separated atoms are taken as the potential zero.

| Molecule | Total Potential (eV) |
|--|----------------------|
| C ₅ H ₈ N ₂ (DBH) | -65.407090 |
| C ₅ H ₈ | -55.971907 |
| N ₂ | -9.943887 |
| Diazenyl biradical | -64.065967 |

Table XXX

Calculated frequencies (cm^{-1}) for DBH and diazenyl biradical.

| Mode | DBH | Diazenyl Biradical |
|------|---------|--------------------|
| v 1 | 255.29 | 11.69 |
| v 2 | 390.75 | 110.09 |
| v 3 | 463.43 | 136.48 |
| v 4 | 517.82 | 223.38 |
| v 5 | 622.82 | 250.09 |
| v 6 | 684.74 | 331.38 |
| v 7 | 783.29 | 482.59 |
| v 8 | 796.38 | 589.32 |
| v 9 | 820.99 | 703.73 |
| v10 | 834.12 | 787.46 |
| v11 | 871.88 | 820.77 |
| v12 | 879.31 | 854.97 |
| v13 | 887.84 | 895.05 |
| v14 | 934.63 | 943.40 |
| v15 | 936.62 | 953.54 |
| v16 | 990.69 | 981.93 |
| v17 | 1012.90 | 991.09 |
| v18 | 1033.16 | 1041.00 |
| v19 | 1100.56 | 1133.97 |
| v20 | 1167.98 | 1157.68 |
| v21 | 1169.44 | 1168.49 |
| v22 | 1182.47 | 1196.06 |
| v23 | 1236.81 | 1242.94 |
| v24 | 1240.99 | 1248.70 |
| v25 | 1269.13 | 1282.17 |
| v26 | 1274.66 | 1305.88 |
| v27 | 1295.86 | 1387.66 |
| v28 | 1357.42 | 1442.85 |
| v29 | 1383.05 | 1458.35 |
| v30 | 1437.21 | 1504.27 |
| v31 | 1455.22 | 2781.25 |

Table XXX (continued)

| Mode | DBH | Diazenyl Biradical |
|------|---------|--------------------|
| V32 | 2916.49 | 2877.11 |
| V33 | 2928.52 | 2881.82 |
| V34 | 2929.34 | 2932.12 |
| V35 | 2993.75 | 2943.88 |
| V36 | 2999.56 | 2952.48 |
| V37 | 3008.08 | 2965.51 |
| V38 | 3011.59 | 3002.34 |
| V39 | 3011.69 | 3090.32 |

Table XXXI

Microcanonical rates constants for diazotization of DBHD and the corresponding branching ratios for random initial energization. The correlation coefficients r of the fitting are also indicated.

| Energy(kcal/mol) | $k(E)$ (ps^{-1}) | r | $N_{\text{exo}}/N_{\text{endo}}$ |
|------------------|-----------------------------|-------|----------------------------------|
| 60 | 0.0626 ± 0.0047 | 0.997 | 1.826 ± 0.438 |
| 80 | 0.1546 ± 0.0067 | 0.995 | 1.833 ± 0.291 |
| 100 | 0.3533 ± 0.0103 | 0.993 | 2.029 ± 0.325 |
| 125 | 0.8461 ± 0.0540 | 0.998 | 1.863 ± 0.248 |
| 150 | 1.3070 ± 0.0052 | 0.998 | 2.192 ± 0.300 |
| 175 | 1.9616 ± 0.0000 | 0.995 | 2.378 ± 0.329 |

Table XXXII

Distribution of available energy among different products of dissociation of DBHD as a function of total excitation energy, in excess to zero-point energy. $\langle F_T \rangle$, $\langle F_R \rangle$, and $\langle F_V \rangle$ denote the fractions of available energy partitioned into translation, rotation, and vibration, respectively.

| Energy (kcal/mol) | $\langle F_T \rangle$ | | $\langle F_R \rangle$ | | $\langle F_V \rangle$ | |
|----------------------|-----------------------|----------------|-----------------------|----------------|-----------------------|----------------|
| | BCP | N ₂ | BCP | N ₂ | BCP | N ₂ |
| 60 | 0.0041 | 0.0103 | 0.0036 | 0.0180 | 0.9150 | 0.0488 |
| 80 | 0.0037 | 0.0094 | 0.0034 | 0.0193 | 0.9160 | 0.0478 |
| 100 | 0.0033 | 0.0083 | 0.0035 | 0.0181 | 0.9239 | 0.0426 |
| 125 | 0.0032 | 0.0081 | 0.0035 | 0.0200 | 0.9161 | 0.0488 |
| 150 | 0.0029 | 0.0072 | 0.0039 | 0.0019 | 0.9173 | 0.0485 |
| 175 | 0.0029 | 0.0072 | 0.0034 | 0.0200 | 0.9156 | 0.0506 |

Figure 25. The general reaction scheme for thermal decomposition of 2,3-diazabicyclo(2.2.1)hept-2-ene-exo, exo-5,6-d₂.

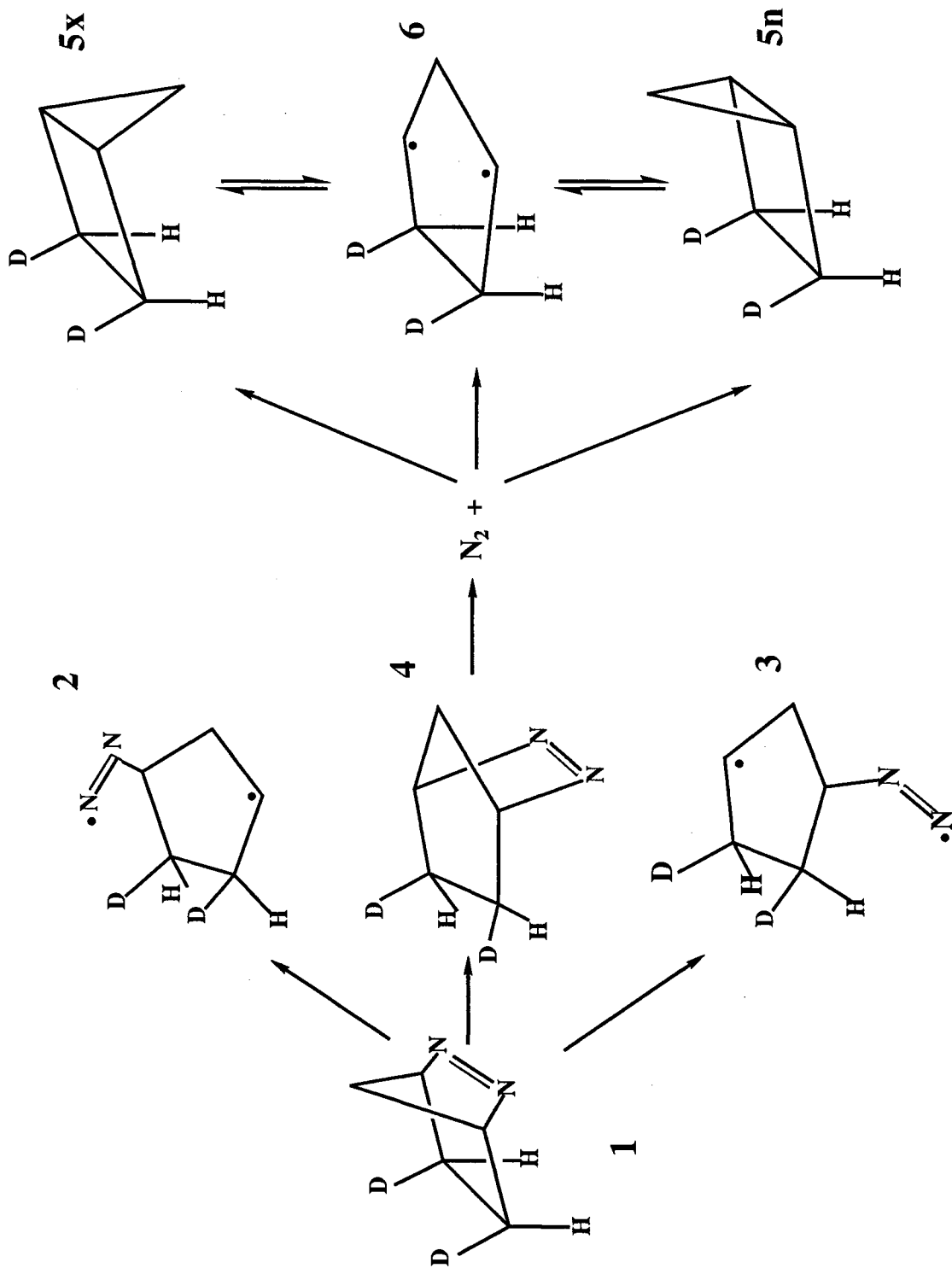
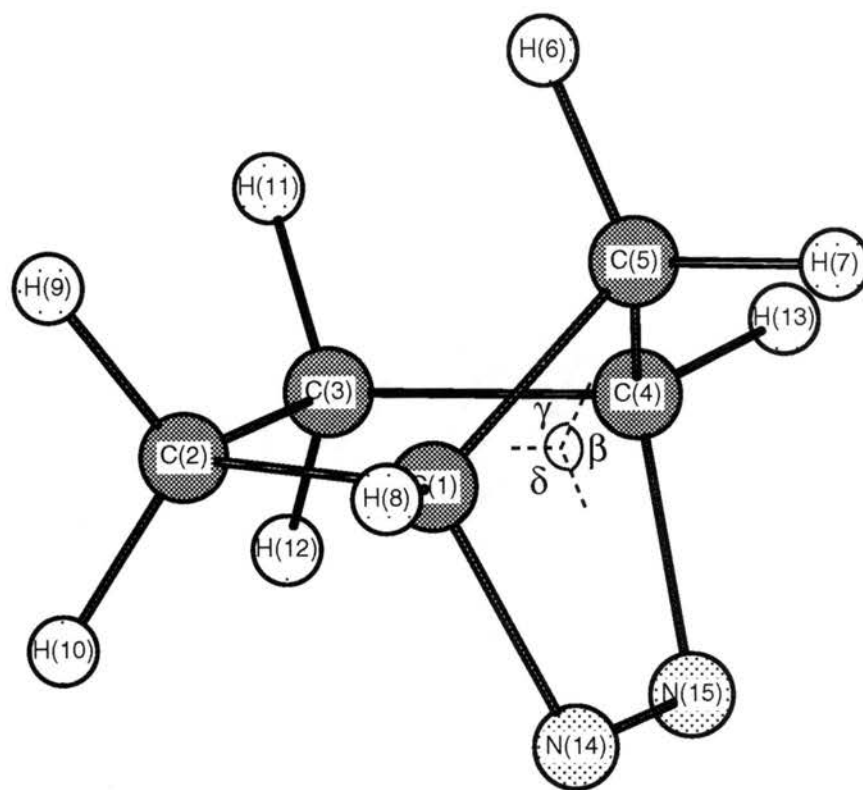
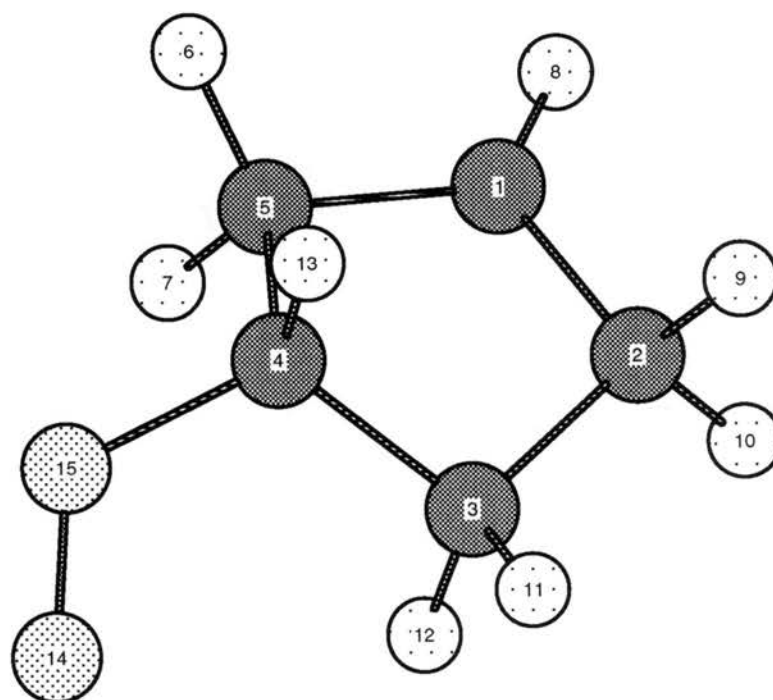


Figure 26. Atom designation and numbering for: a) 2,3-diazabicyclo(2.2.1)hept-2-ene and b) diazenyl biradical.



a)



b)

Figure 27. Calculated (MP2/6-31G*) infrared spectra of DBH.

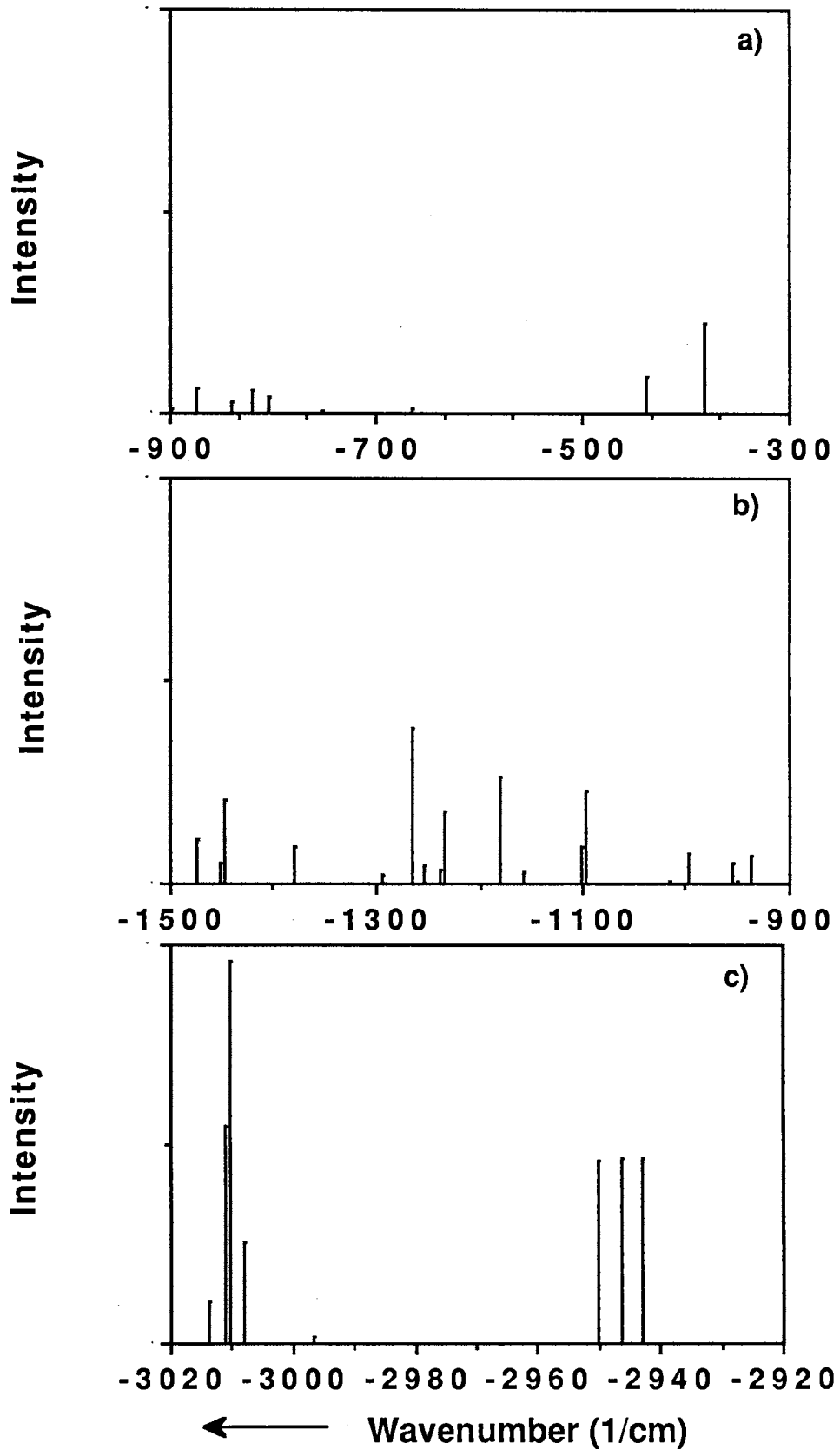
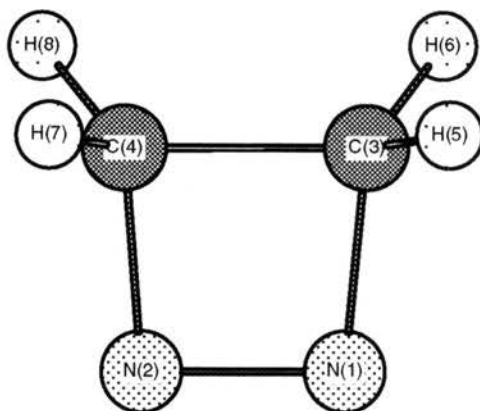
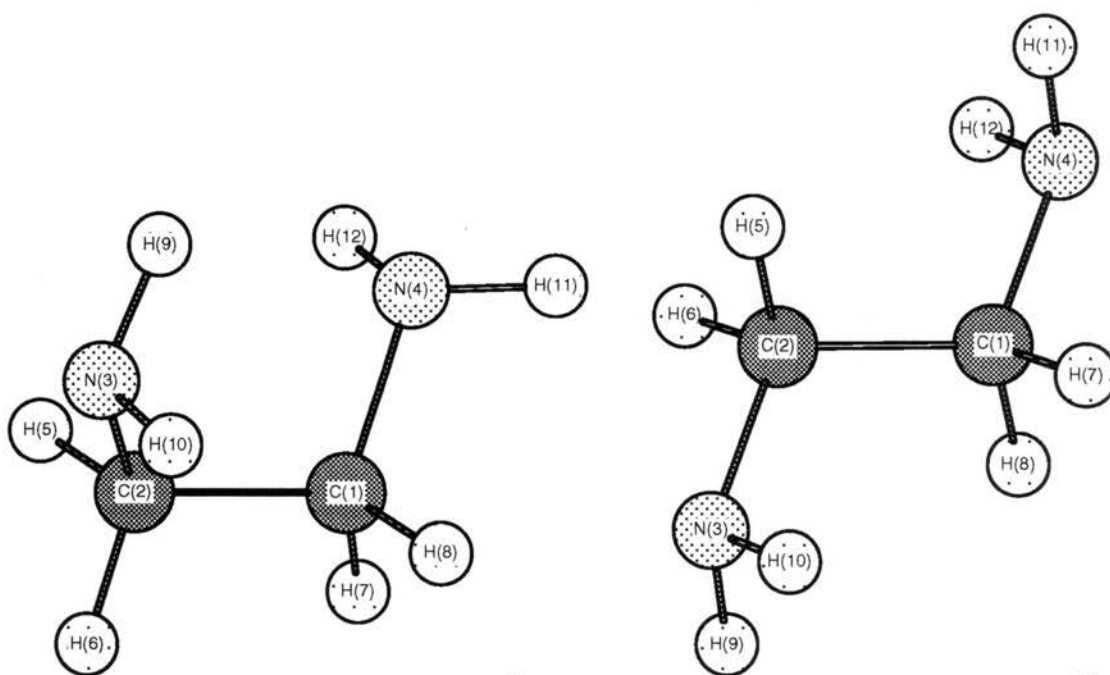
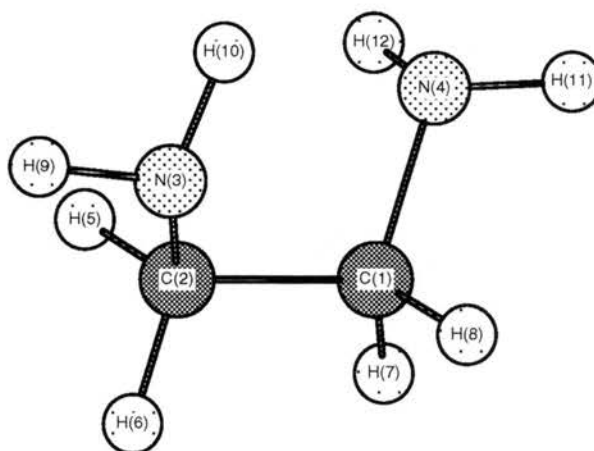


Figure 28. Pictorial view of dimethylenediazene (a) and ethylenediamine configurations: gGg' (b); tGg' (c) and tTt (d).

a)



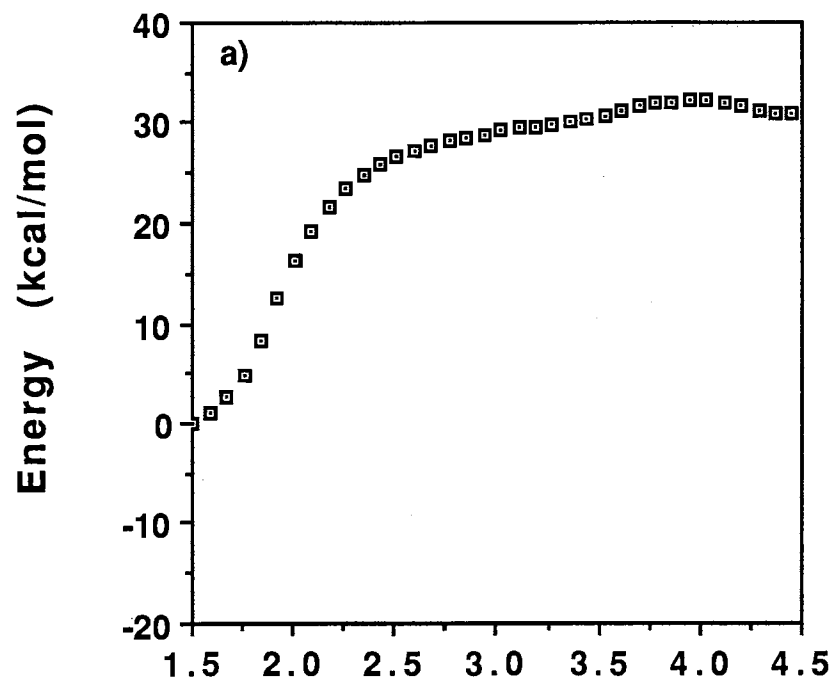
b)



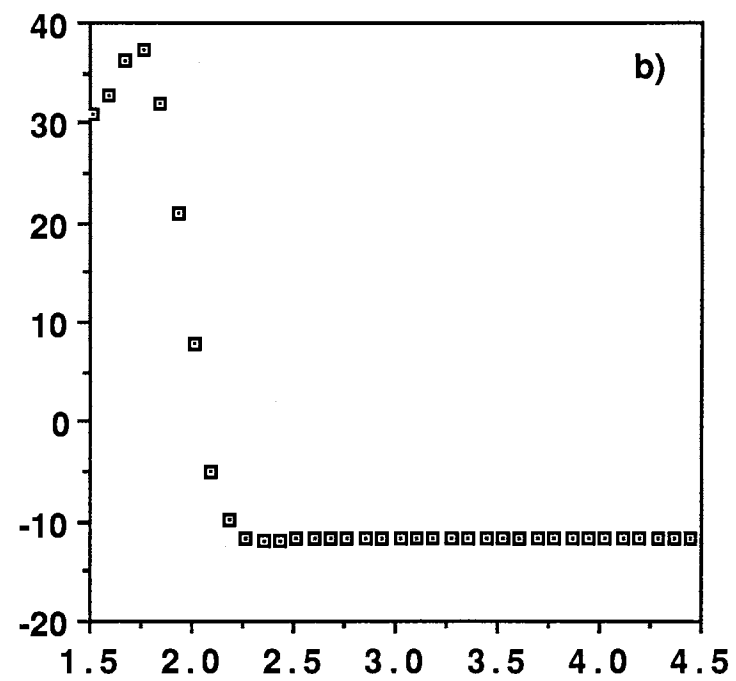
c)

d)

Figure 29. The variation of the total potential as a function of the C-N bond distances : a) $r(\text{C}_1\text{-N}_{14})$; b) $r(\text{C}_4\text{-N}_{15})$ for the successive cleavage reaction mechanism.



R(C1-N14) Å



R(C4-N15) Å

Figure 30. The variation of the flap angle as a function of the C-N bond distances: a) $r(\text{C}_1\text{-N}_{14})$; b) $r(\text{C}_4\text{-N}_{15})$ corresponding to the potential profile given in Figs. 29 a) and 29 b).

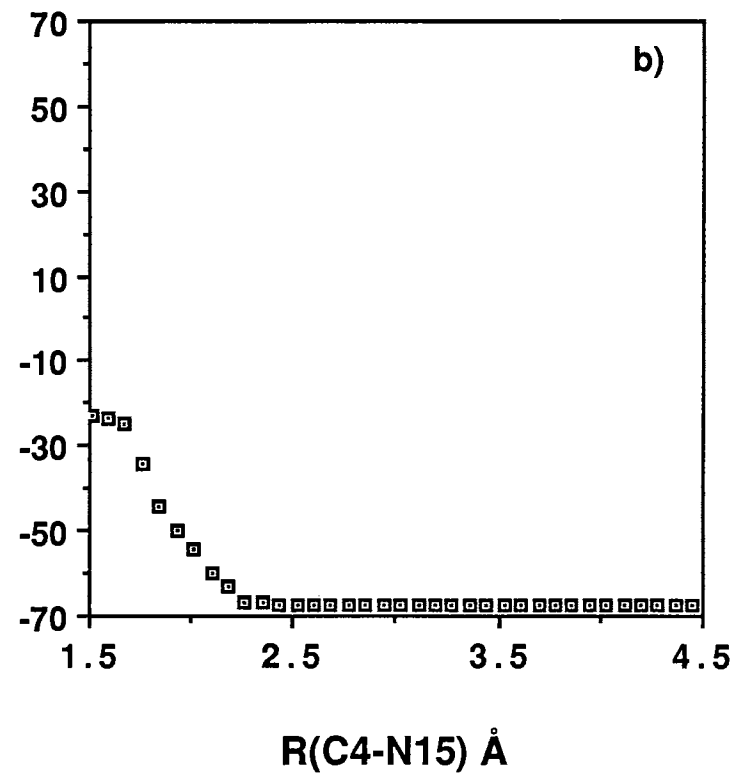
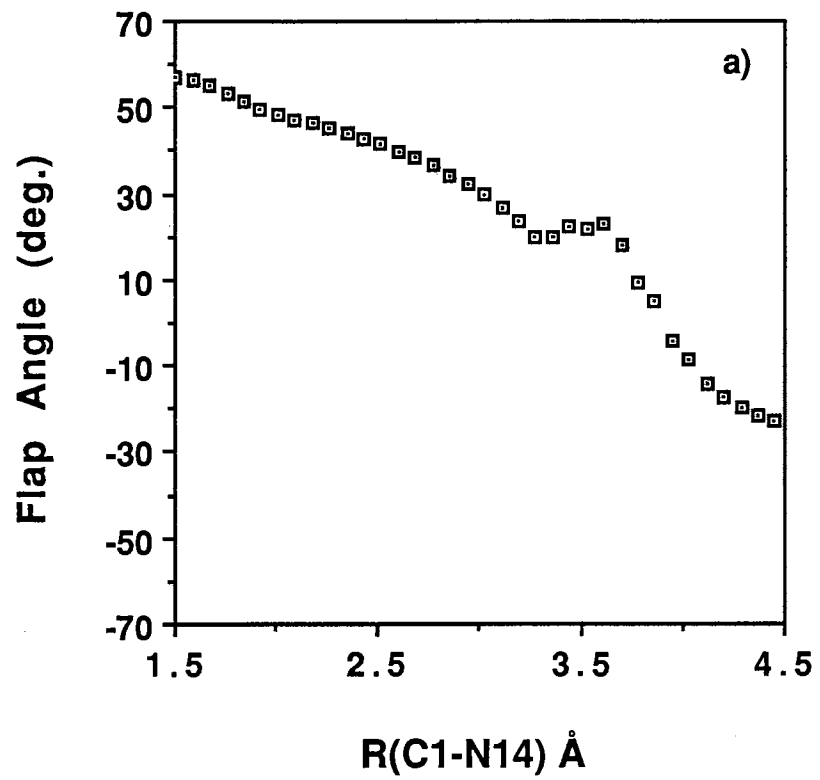
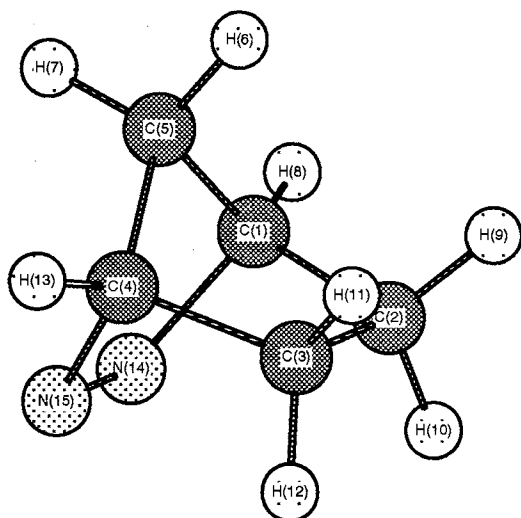
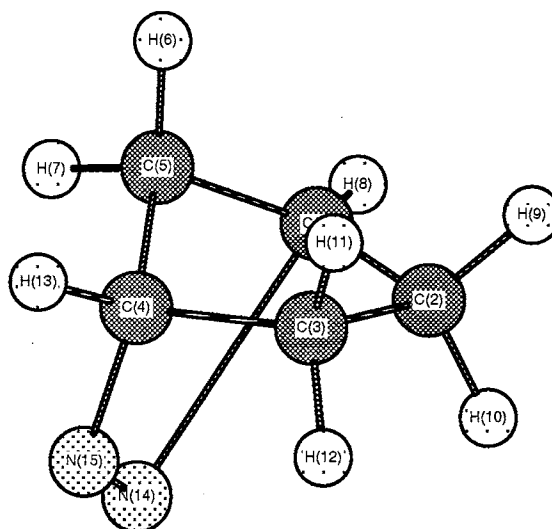


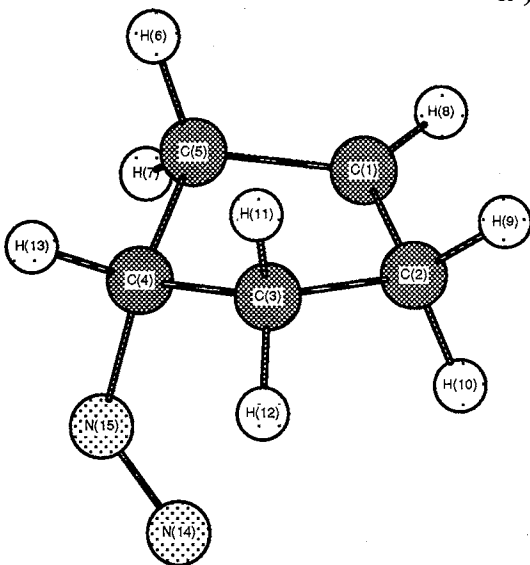
Figure 31. Panel showing different molecular structures corresponding to the potential profile given in Figs.4a and 4b. The configurations (a-d) correspond to r_5 values of 1.503 Å, 2.5 Å, 3.5 Å, and 4.45 Å. The configurations (e) and (f) correspond to r_6 values of 1.73 Å and 3.5 Å.



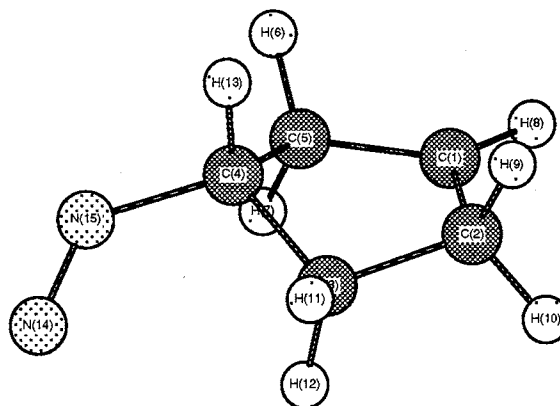
a)



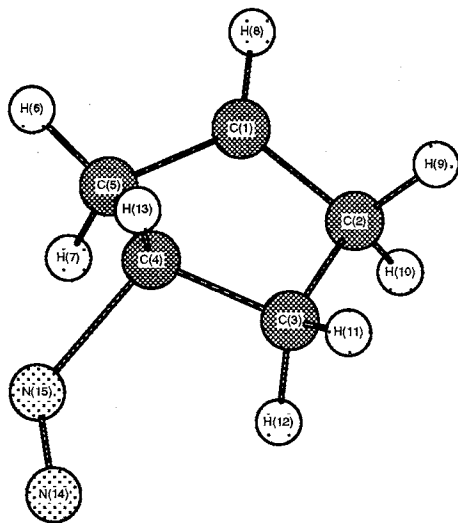
b)



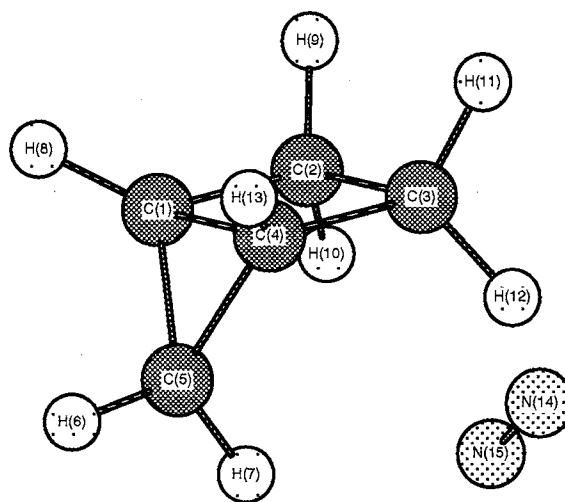
c)



d)



e)



f)

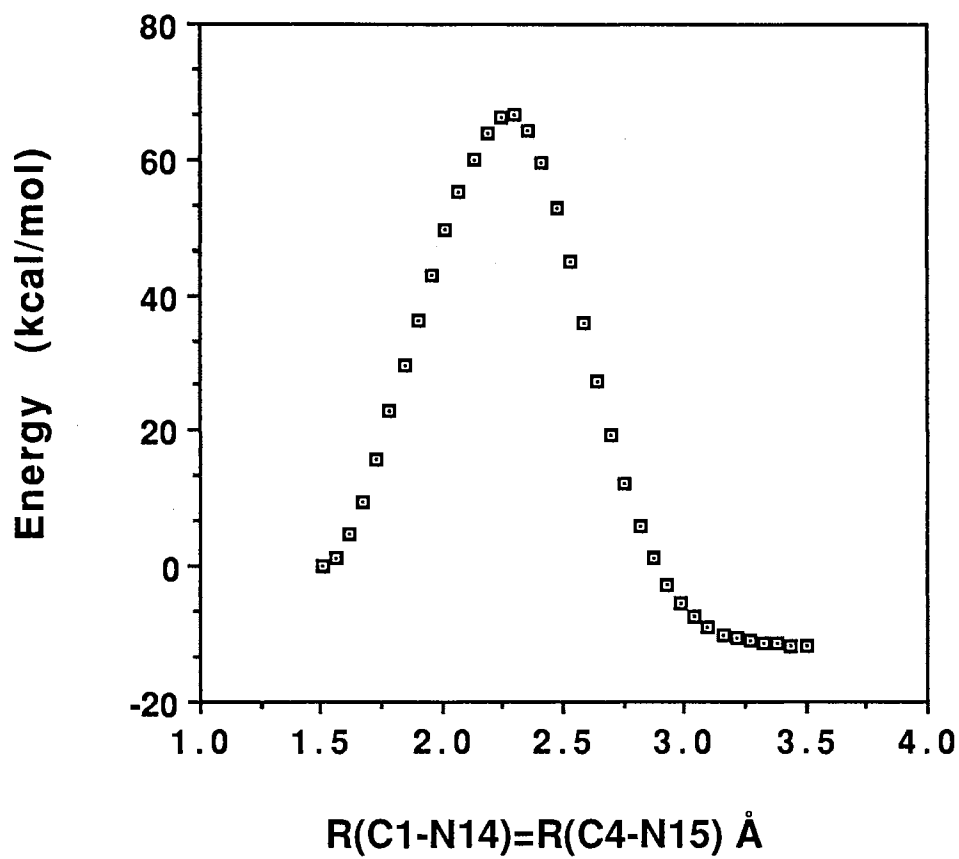


Figure 32. The variation of the total potential as a function of the C-N bond distance for simultaneous stretching of both C-N bonds.

Figure 33. Temporal variation of (a) the C-N bond lengths $r(\text{C}_1\text{-N}_{14})$ and $r(\text{C}_4\text{-N}_{15})+2.5 \text{ \AA}$ and (b) flap angle, for a trajectory leading to **(5x)**. $r(\text{C}_4\text{-N}_{15})$ has been displaced upwards by 2.5 \AA to enhance the visual clarity. Time is given in units of 1.018×10^{-14} sec.

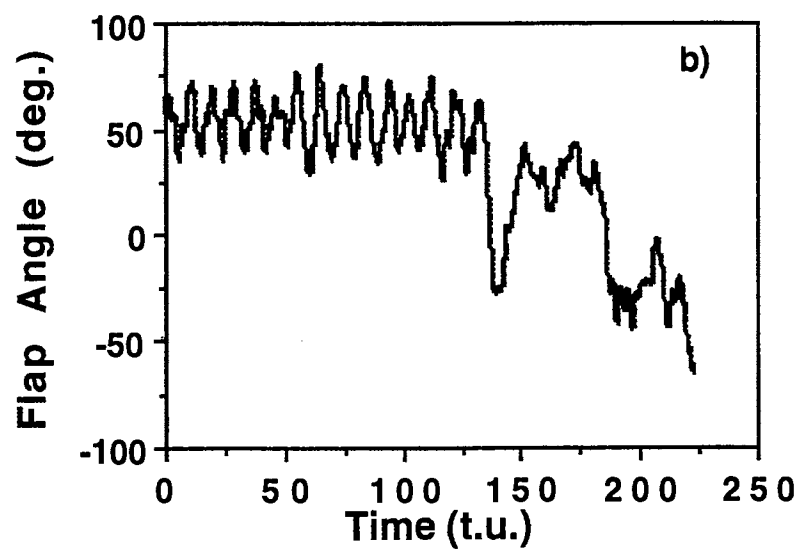
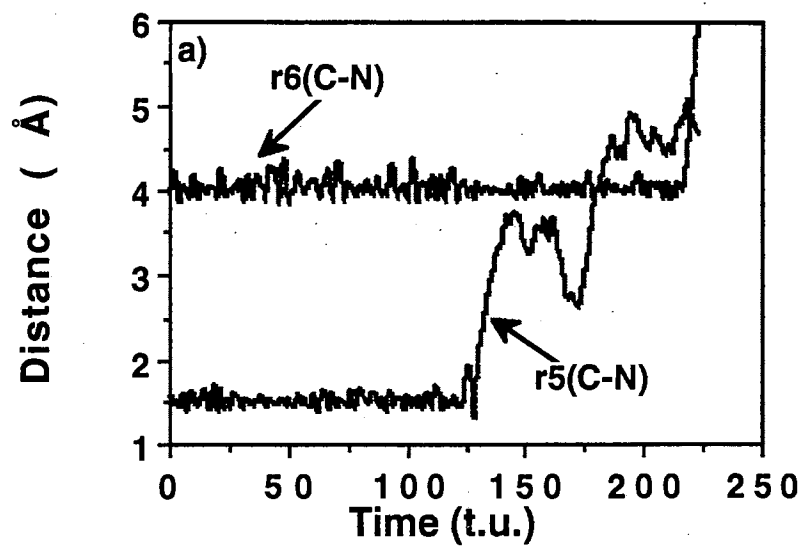
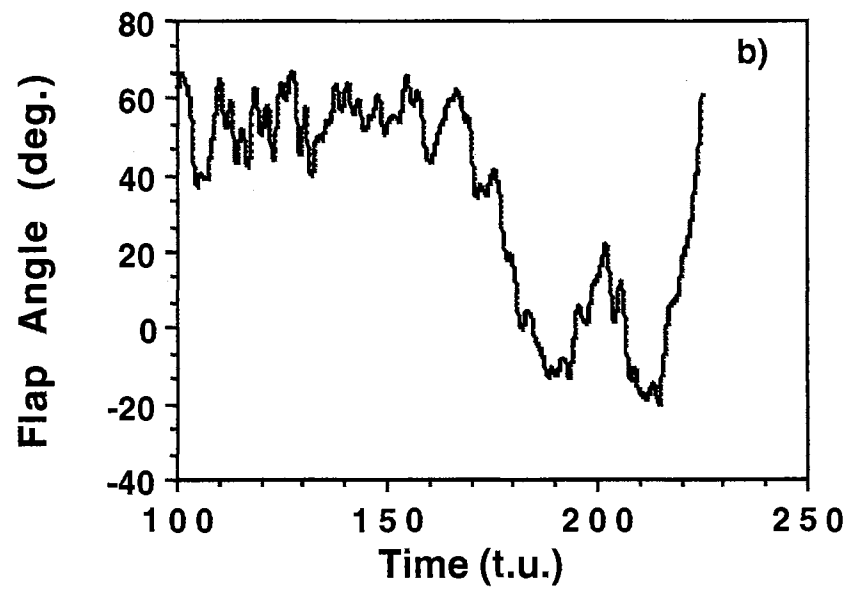
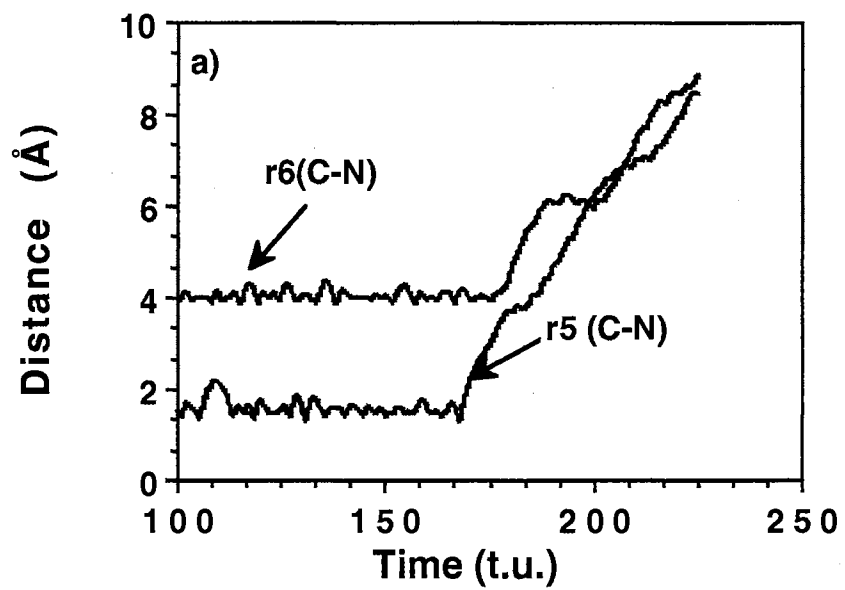


Figure 34. Temporal variation of (a) the C-N bond lengths $r(\text{C}_1\text{-N}_{14})$ and $r(\text{C}_4\text{-N}_{15})+2.5 \text{ \AA}$ and (b) flap angle, for a trajectory leading to **(5n)**. $r(\text{C}_4\text{-N}_{15})$ has been displaced upwards by 2.5 \AA to enhance the visual clarity. Time is given in units of $1.018 \times 10^{-14} \text{ sec}$.



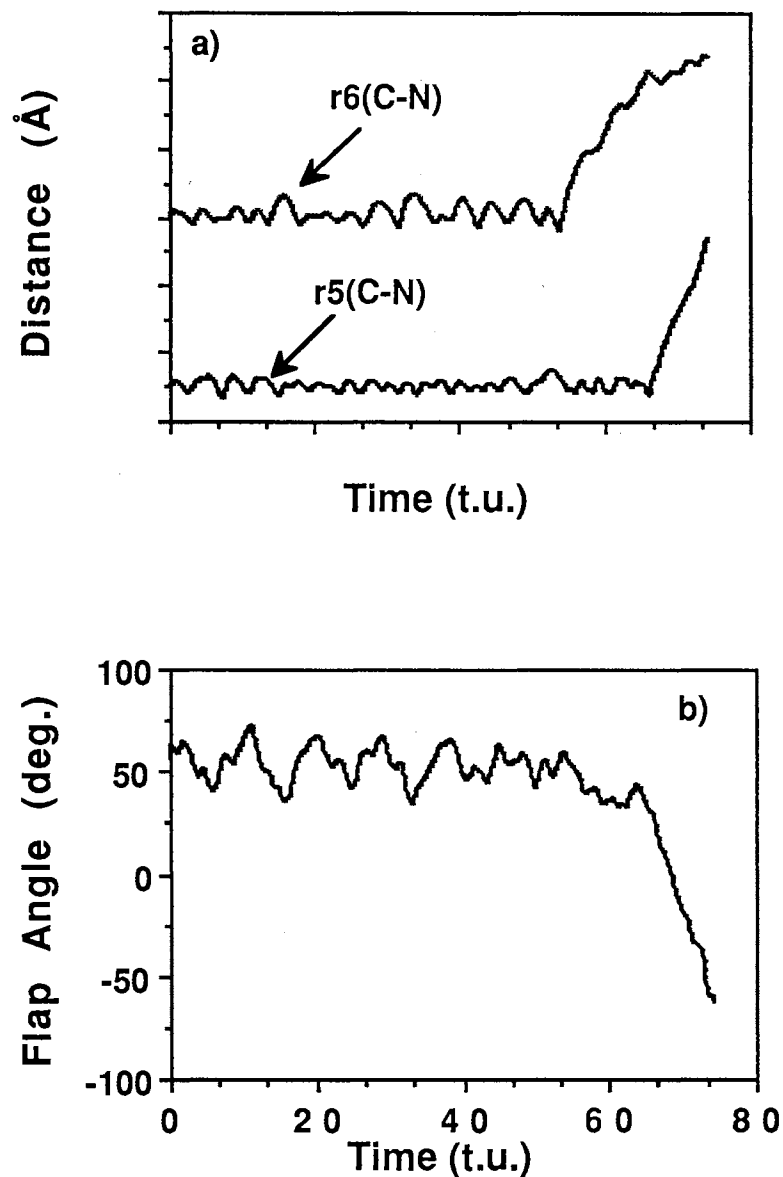
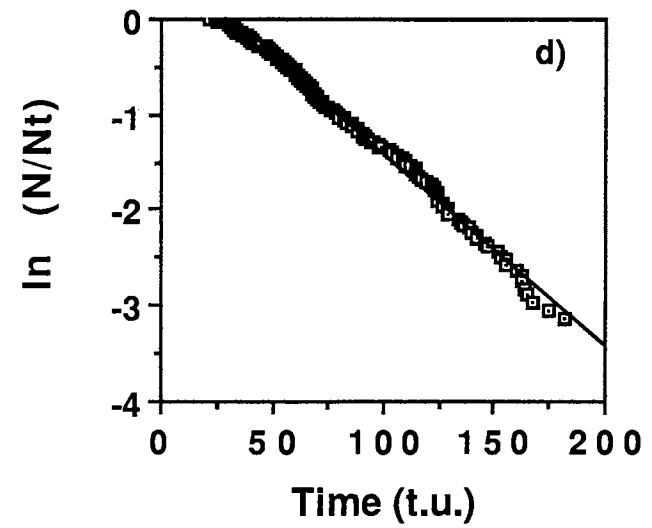
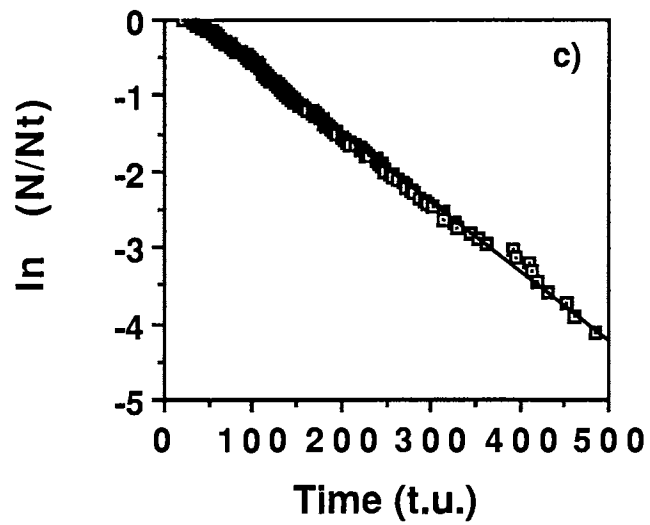
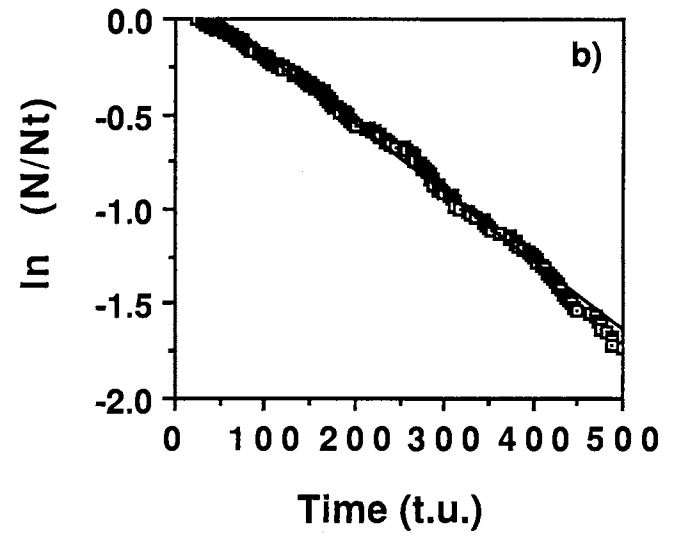
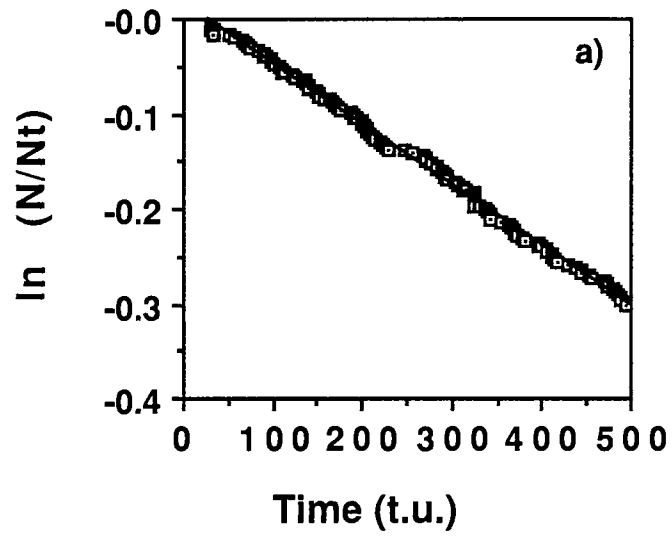


Figure 35. Temporal variation of (a) the C-N bond lengths $r(C_1-N_{14})$ and $r(C_4-N_{15})+2.5 \text{ \AA}$ and (b) flap angle, for a trajectory leading to (**5x**) without passing through the well corresponding to the 1,3-cyclopentadiyl radical. $r(C_4-N_{15})$ has been displaced upwards by 2.5 \AA to enhance the visual clarity. Time is given in units of $1.018 \times 10^{-14} \text{ sec}$.

Figure 36. Decay plots for random excitation of the vibrational modes of DBHD at the energies (a) 60 kcal/mol; (b) 100 kcal/mol; (c) 125 kcal/mol; (d) 175 kcal/mol in excess of zero-point energy. In each case, the line is the result of linear least-squares fit to the calculated points.



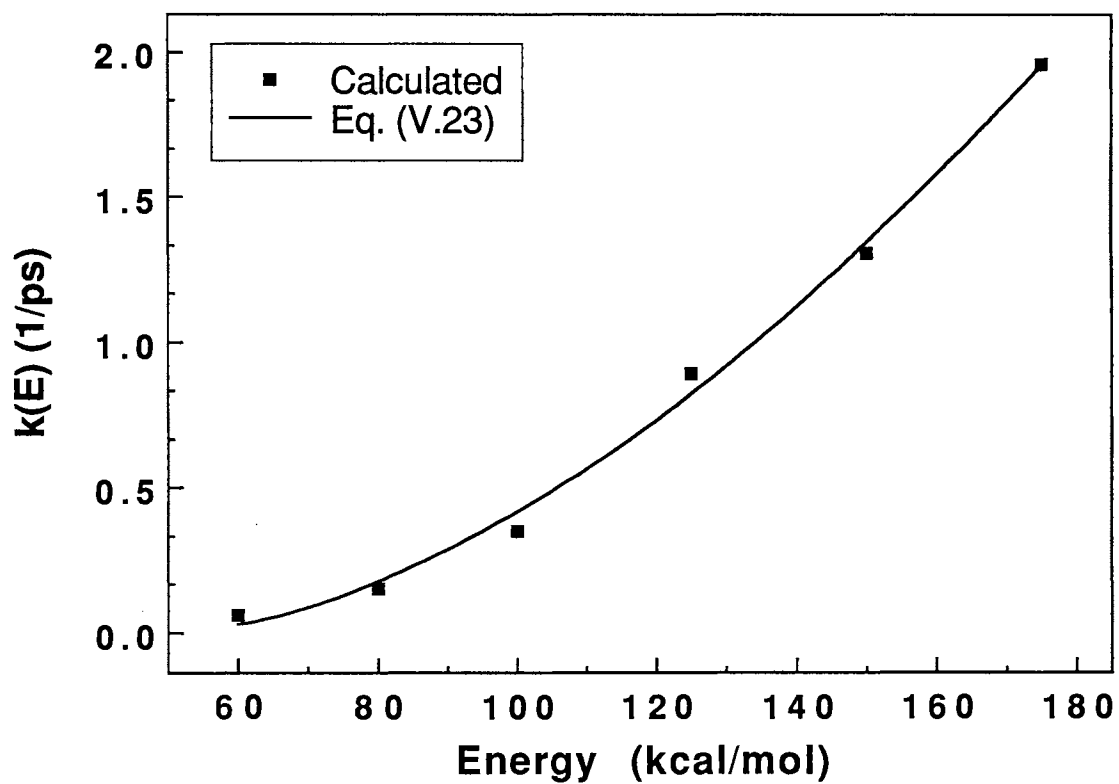


Figure 37. Microcanonical rate coefficients for the decomposition of DBHD as a function of excitation energy in excess of zero-point energy. The points are the calculated values. The line is a least-square fit of Eq. (V.23).

Figure 38. Normalized distribution of the total translational energy released in deazetization reaction of DBHD. Total energies are (a) 60 kcal/mol; (b) 175 kcal/mol.

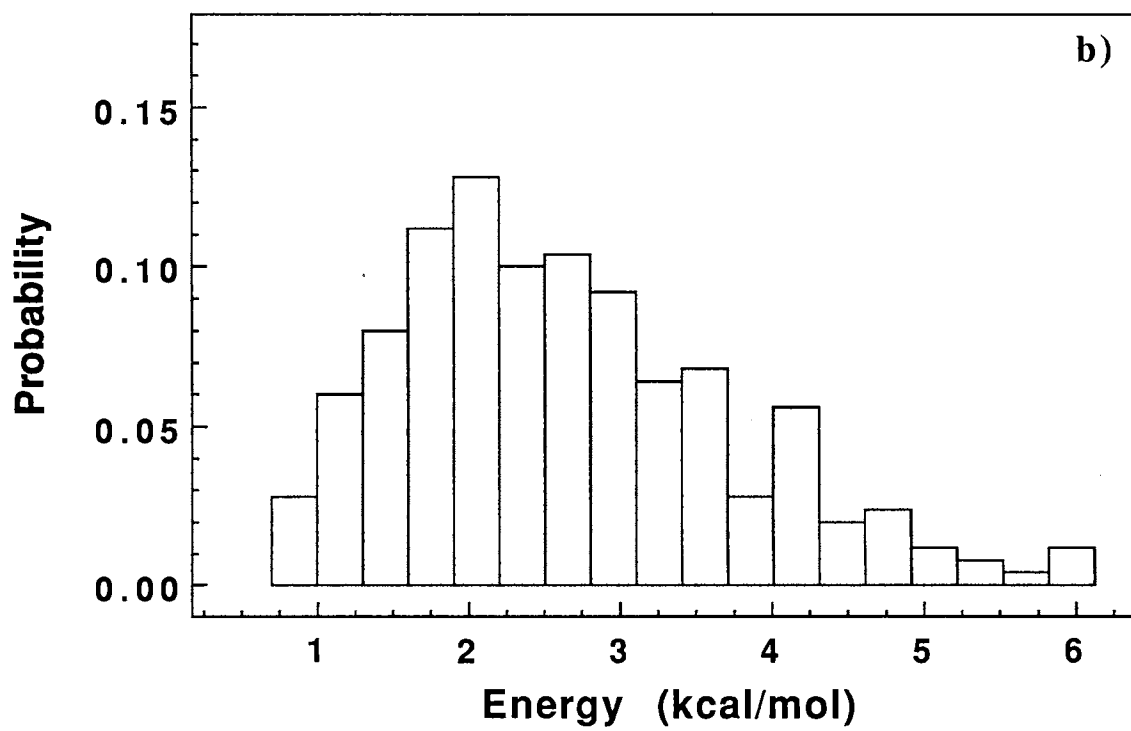
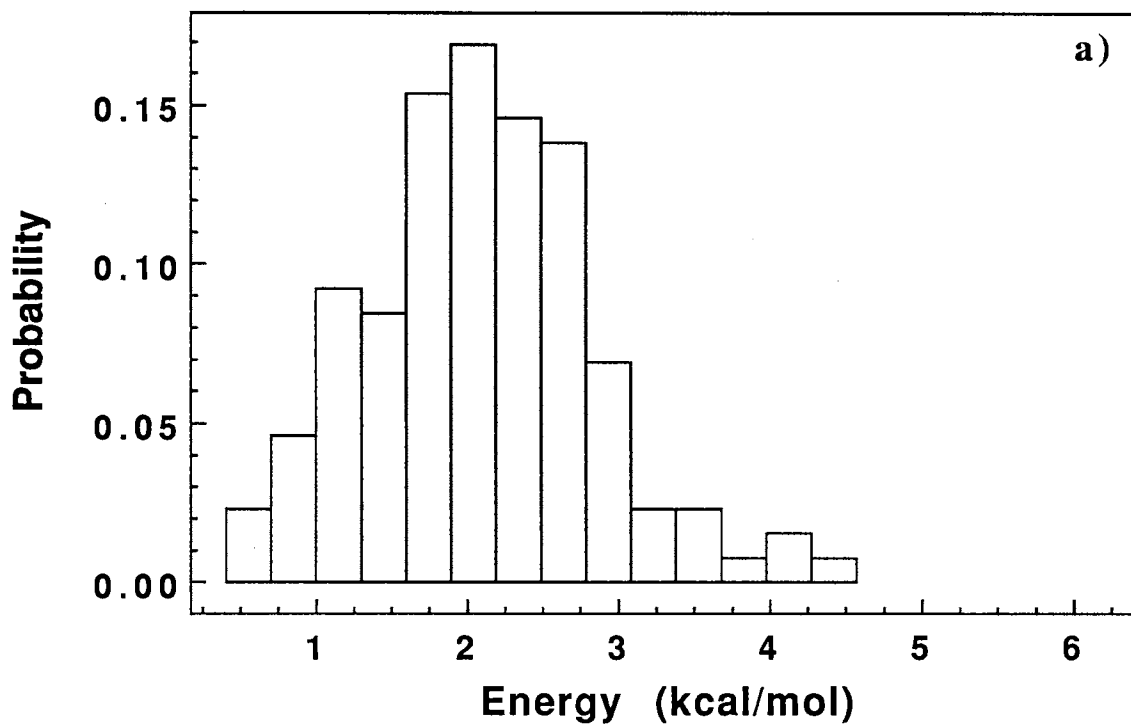


Figure 39. Normalized distribution of the rotational energy of N₂ molecules formed in deazetization reaction of DBHD. Total energies are (a) 60 kcal/mol; (b) 175 kcal/mol.

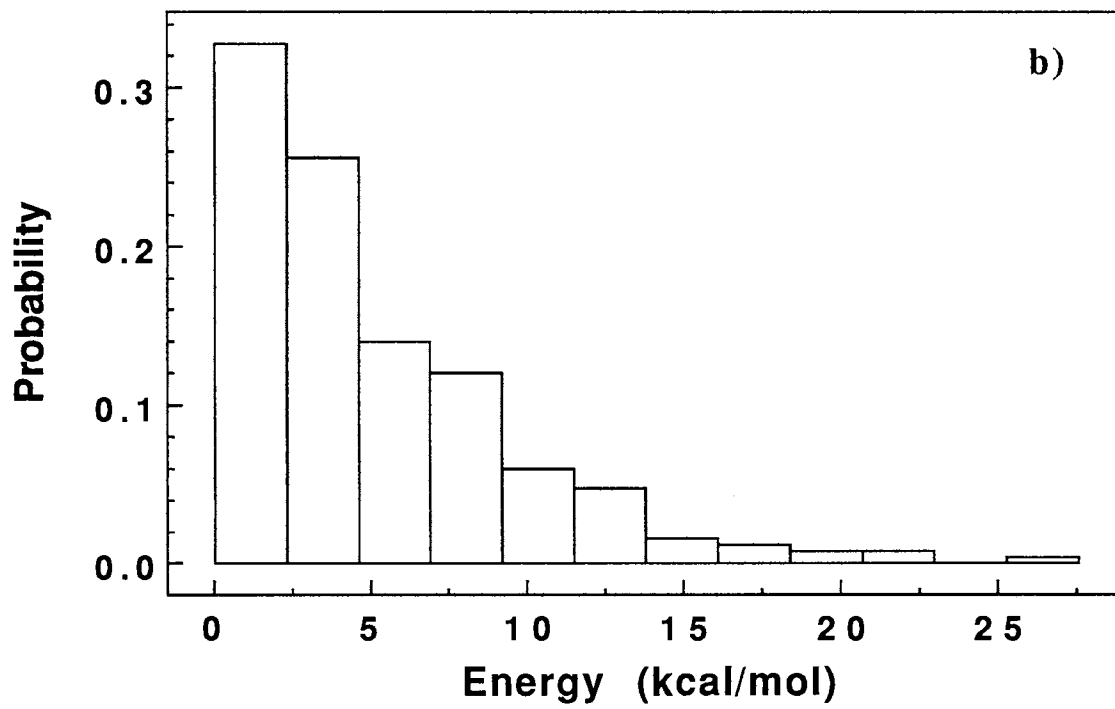
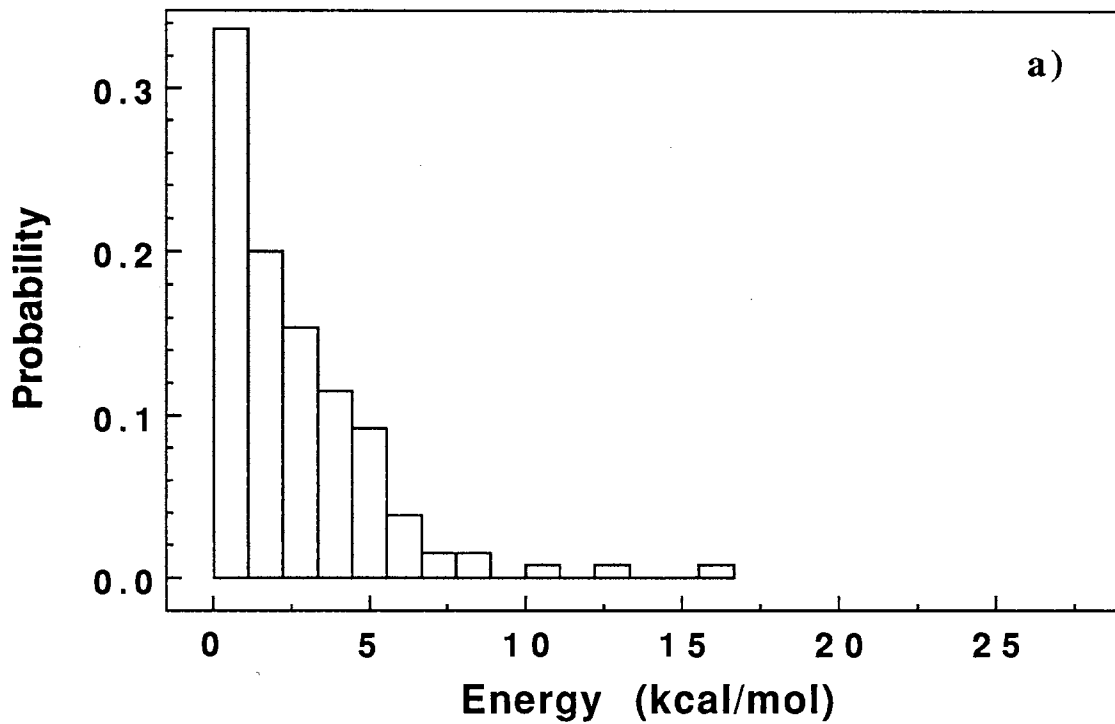


Figure 40. Normalized distribution of the vibrational energy of N₂ molecules formed in deazetization reaction of DBHD. Total energies are (a) 60 kcal/mol; (b) 175 kcal/mol.

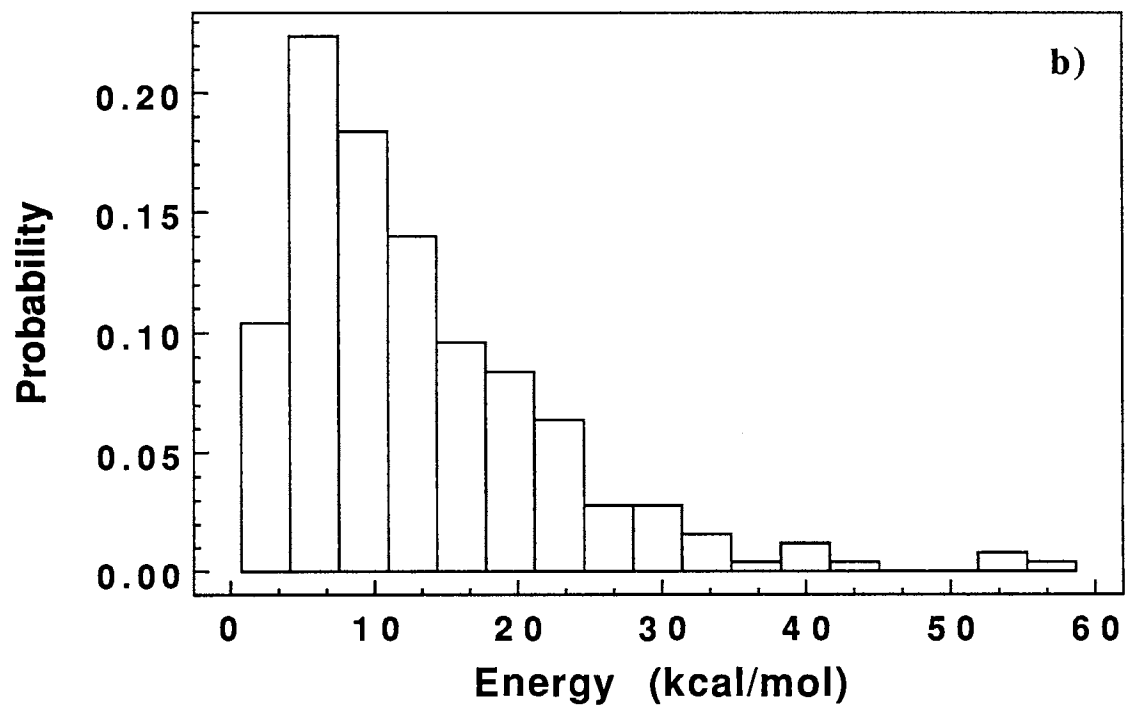
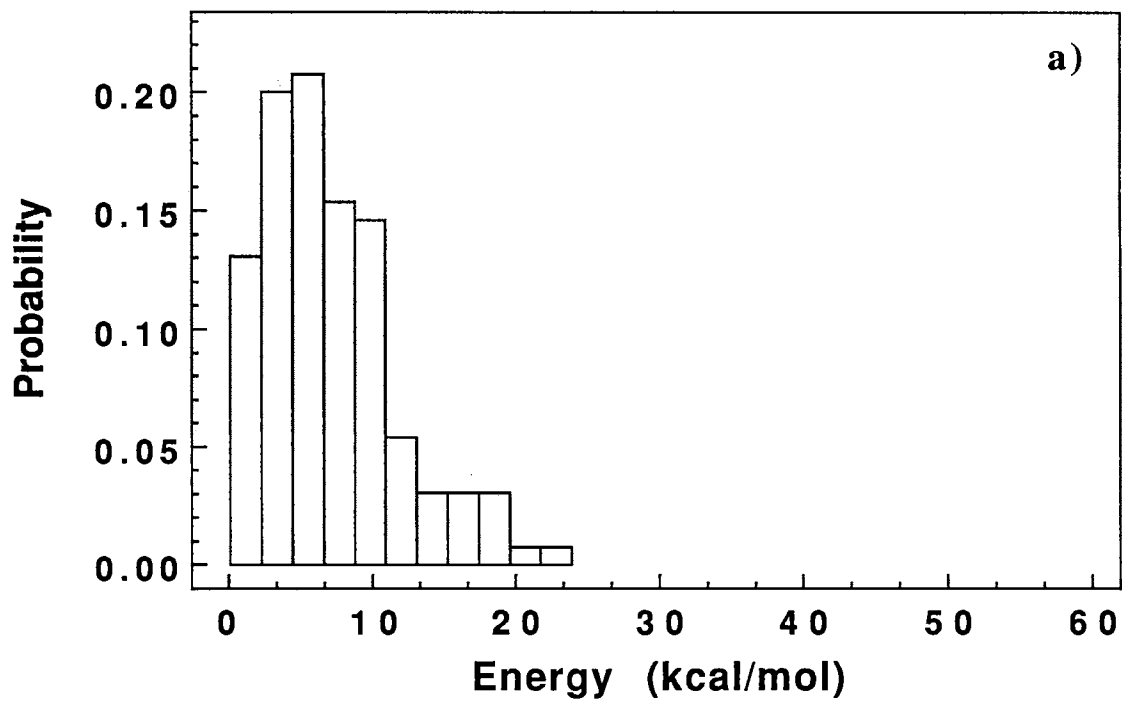


Figure 41. Normalized distribution of the vibrational energy of BCP molecules formed in deazetization reaction of DBHD. Total energies are (a) 60 kcal/mol; (b) 175 kcal/mol.

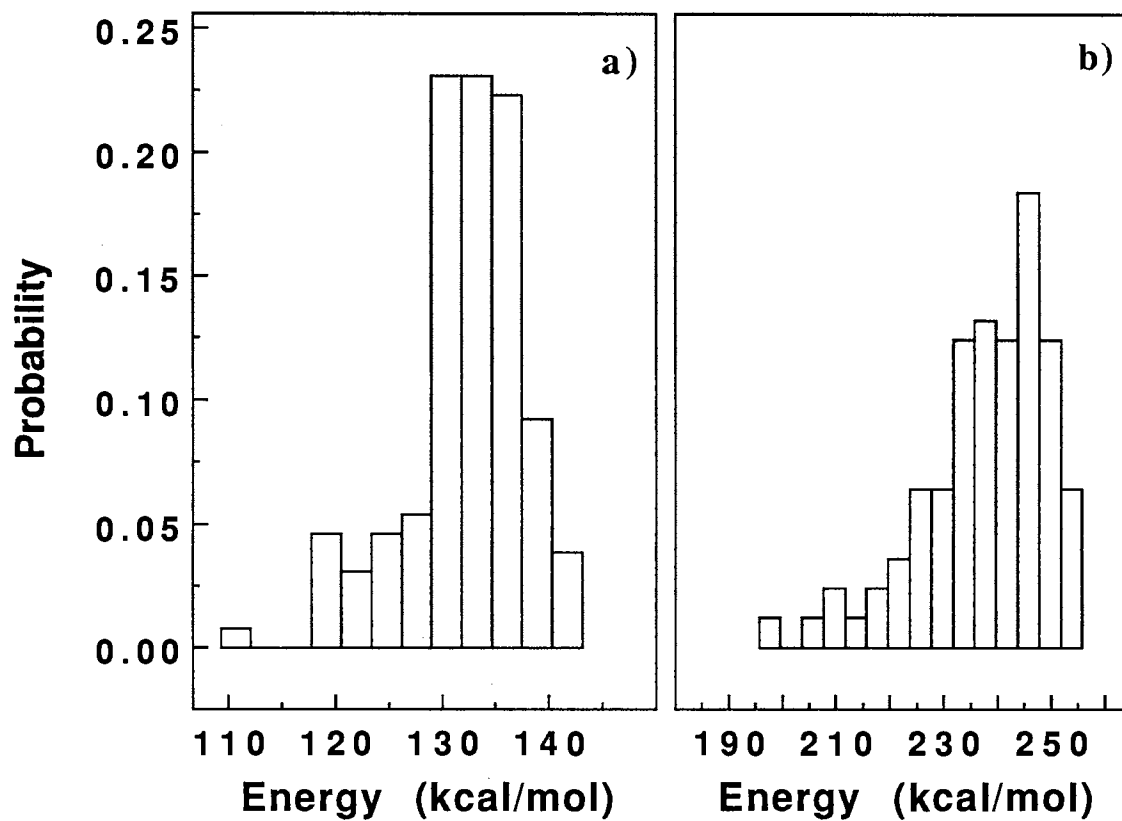


Figure 41. Normalized distribution of the vibrational energy of BCP molecules formed in deazetization reaction of DBHD. Total energies are (a) 60 kcal/mol; (b) 175 kcal/mol.

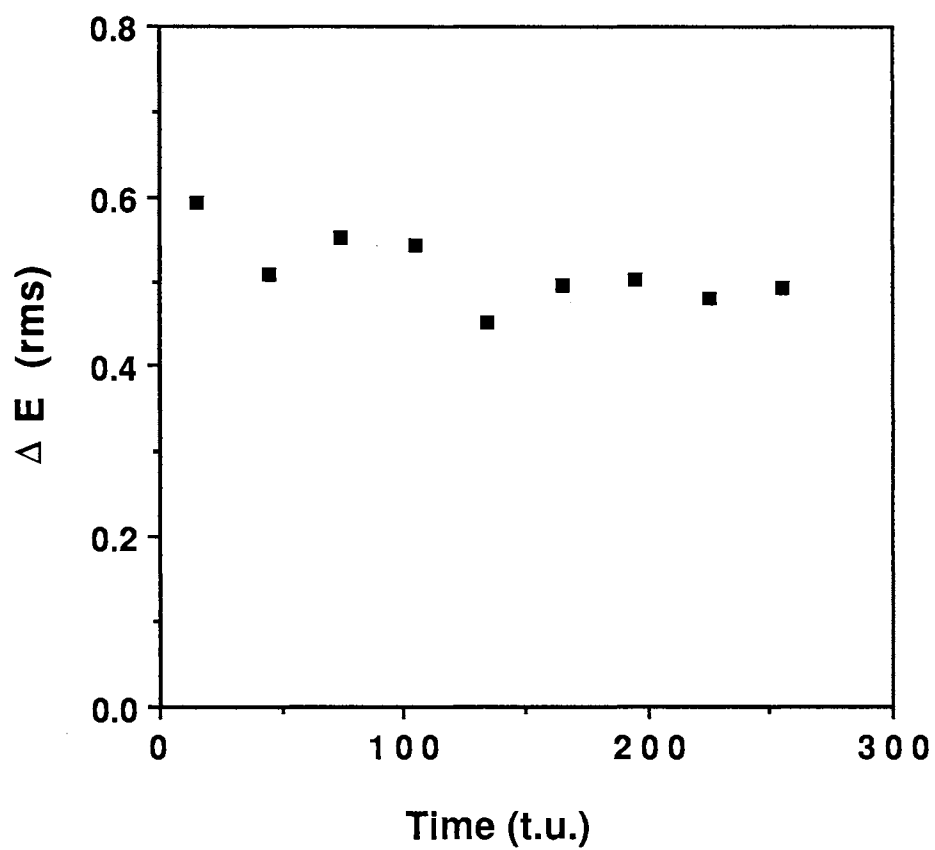
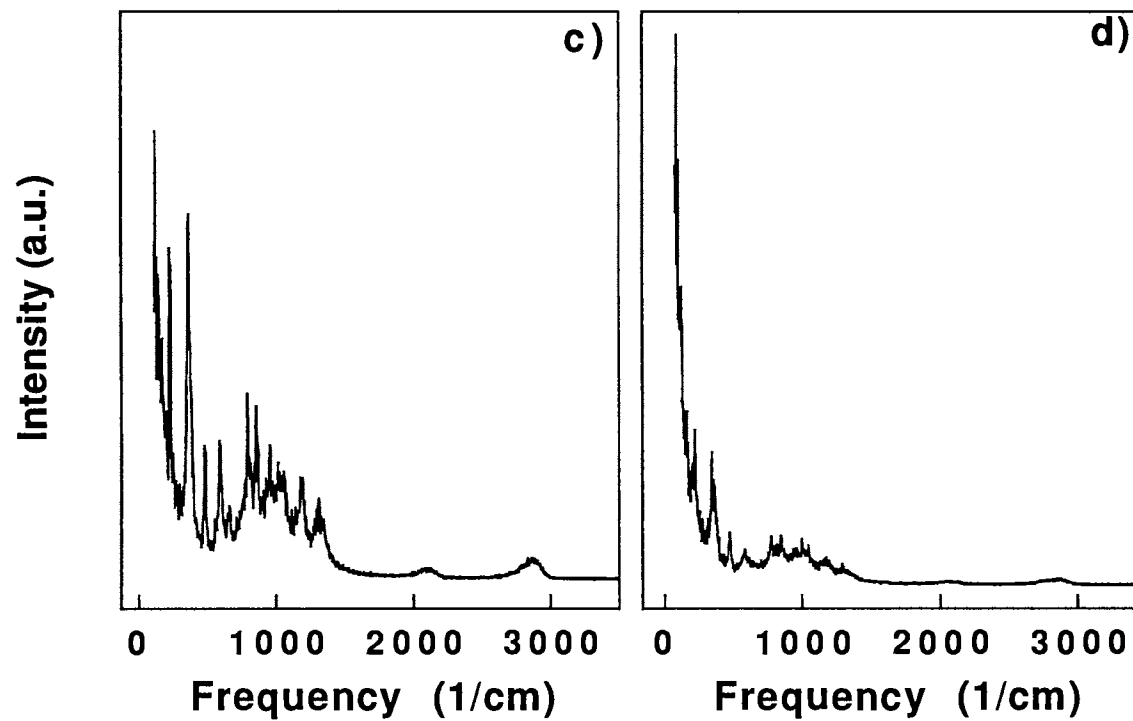
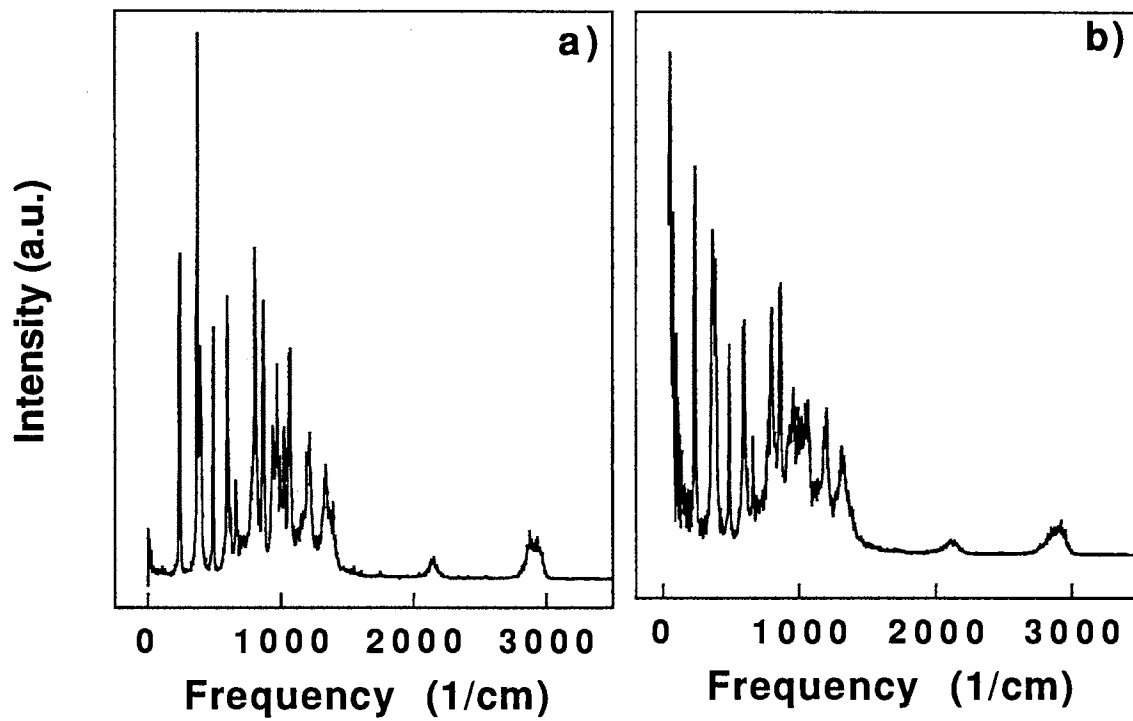


Figure 42. Time variation of the root-mean-square of the average normal-mode energies for an ensemble of trajectories initial excited with 60 kcal/mol.

Figure 43. Composite power spectra for DBHD in arbitrary units at: (a) zero-point energy; (b) 40 kcal/mol; (c) 70 kcal/mol; and (d) 100 kcal/mol. The excitation energies, in excess to zero-point energy, are initially distributed at random over the normal-modes .



CHAPTER VI

CONCLUSIONS

Following the central idea expressed in the Preface, we have developed detailed models for three molecular systems one involving solid surfaces and two for reactions in the gas-phase: H-atoms on a Si(111)-(7x7) surface, bicyclo(2.1.0)pentane, and 2,3-diazabicyclo(2.2.1)hept-2-ene. In these last two cases, the theoretical models include description of 1,3-cyclopentadiyl and diazenyl biradicals, respectively.

In all these cases, specific potential-energy surfaces have been constructed to describe either the hydrogen-lattice interaction or the reaction kinetics between different conformations, as in the case of skeletal inversion of bicyclo(2.1.0)pentane or unimolecular decomposition, as in the case of thermal deazetization of 2,3-diazabicyclo(2.2.1)hept-2-ene.

Obtaining an accurate potential-energy surface for every system analyzed was a central goal of our theoretical investigations. For this purpose, we have used the available theoretical and experimental data related to molecular conformations (geometrical parameters) of reactants, products and transition states, to thermochemical data (bond dissociation energies, enthalpies of formation or reaction), to spectroscopical data (fundamental vibrational frequencies), and to kinetic data (activation energies, reaction rate constants, branching ratios). In those cases when this type of information, essential in construction of potential-energy surfaces, was not available, we

presented alternative methods, based on *ab initio* calculations, to obtain the necessary data. In particular, we have used *ab initio* calculations to evaluate the geometries of molecular systems at equilibrium and in the transition states, their total energies and the curvature of the potential-energy surface at the position of the local minima. Based on these data, additional information related to enthalpy of formation, bond-dissociation energies and zero-point energies has been obtained.

We have also presented in detail the general procedures for construction of a potential-energy surface that reproduces the available theoretical and experimental data. For this purpose, we analyzed the essential steps related to the choice of the analytical functional forms used in description of potential interactions and in connecting the important regions on the potential-energy surface. In addition, we have described the particular fitting and testing procedures of the potential parameters to the ensemble of geometrical, thermochemical, spectroscopic and kinetic data.

Following the construction of potential-energy surfaces, we have presented the general strategy used to investigate the dynamics of molecular systems, using either trajectory methods or Monte Carlo calculations. In these cases, particular attention was paid to general methods and theories used in analysis of trajectories, intramolecular energy transfer and reaction mechanism.

For the systems analyzed, the principal results can be summarized as follows:

Diffusion of Hydrogen Atoms on a Si(111)-(7x7) Reconstructed Surface

The diffusion of hydrogen atoms on a reconstructed Si(111)-(7x7) surface has been investigated using variational phase-space theory methods. The dimer-atom-stacking fault model of the reconstructed Si(111)-(7x7) surface

proposed by Takayanagi *et al.*^{101,102} was employed to describe a four-layer lattice structure containing 292 atoms. The lattice potential is that developed by Bolding and Andersen.¹⁰⁸ We developed a potential for the interaction of hydrogen atoms with the reconstructed Si(111)-(7x7) surface which reproduces the Si-H equilibrium distance, the binding energy and the fundamental Si-H stretching and H-Si-Si bending frequencies. This gas-lattice interaction potential is described by a sum of Morse functions and bending terms between the hydrogen adatom and the Si atoms in the first and second layers.

Canonical Markov walks with importance sampling have been used to evaluate the flux across a set of planar dividing surfaces separating different adsorption sites. Classical jump frequencies were computed at 300, 500, and 800 K. An Arrhenius fit to these jump frequencies yielded an activation energy of 1.548 eV and a preexponential factor of $3.88 \times 10^{12} \text{ s}^{-1}$.

The minimum-energy diffusion path for sites separated by 12.6 a.u. distance was obtained using a Monte Carlo random walk procedure with importance sampling.⁷⁵ The barrier height for these jumps was found to be 1.52 eV.

The classical diffusion coefficients at 300, 500 and 800 K were obtained by integrating a system of phenomenological rate equations describing the diffusion of hydrogen atoms on a simplified model for 49 units cells on the DAS surface, followed by calculation of the slope in the plots giving the time variation of the root-mean-square displacement obtained from the solution of the rate equations. The computed activation energy for thermal diffusion was found to be 1.548 eV, and a pre-exponential factor of $0.023 \text{ cm}^2/\text{s}$ was determined, in good agreement with the experimental value.⁹⁴

Calculated upper limits for the tunneling rates at 300, 500 and 800 K show that tunneling processes make only small contributions to the total

diffusion rate.

Statistical Effects in the Skeletal Inversion of Bicyclo(2.1.0)pentane

We have developed a semiempirical potential-energy surface for bicyclo(2.1.0)pentane which includes bond stretching, bending and torsional terms.

The bond dissociation energies were estimated using the available thermochemical data and results of *ab initio* molecular calculations performed at the fourth order Möller-Plesset perturbation theory level using a 6-31G** basis set. The equilibrium geometry of bicyclo(2.1.0)pentane and 1,3-cyclopentadiyl radical, the barrier for ring inversion, and the fundamental frequencies of bicyclo(2.1.0)pentane obtained with our semiempirical potential-energy surface are in fair-to-good agreement with the measured and *ab initio* values.

Projection methods^{46,47} and molecular dynamics simulations were used to investigate the type of statistics obeyed by the flap motion of bicyclo(2.1.0)pentane. For random energization of the vibrational modes, the results of trajectory calculations agree with the predictions of statistical unimolecular theory. The RRK parameters extracted from the analysis of microcanonical rate constants for the ring inversion are $\nu=1.22\pm 0.26$ ps⁻¹ and $s=12.18\pm 0.72$. A global statistical behavior is also supported by the results of the power spectra calculated at different energization levels. The significant broadening and overlapping of the spectral bands, together with the disappearance of characteristic spectral features in the power spectra of the flap angle, indicate high intramolecular vibrational redistribution rates and overall statistical behavior. The total intramolecular vibrational relaxation rates for the energy flow out of the flap mode were extracted from the time dependence of the average total normal-mode energy in this mode. For initial excitation of the

flap mode in the range 30-60 kcal/mol, the calculated total intramolecular vibrational relaxation rates were found to be significantly larger than the microcanonical ring inversion rates. This result further supports the statistical character of the ring inversion in bicyclo(2.1.0)pentane.

Molecular Dynamics Studies of the Thermal Decomposition of 2,3-Diazabicyclo(2.2.1)hept-2-ene

The reaction dynamics of the thermal gas-phase decomposition of 2,3-diazabicyclo(2.2.1)hept-2-ene-*exo*, *exo*-5,6- d_2 have been investigated using classical trajectory methods on a semiempirical potential-energy surface. The global potential was written as a superposition of different reaction channel potentials containing bond stretching, bending and torsional terms, connected by parametrized switching functions. Reaction channels for stepwise and concerted cleavage of the two C-N bonds of the reactant were considered in the construction of the potential.

The geometries of 2,3-diazabicyclo(2.2.1)hept-2-ene, the diazenyl biradical and of the transition state corresponding to breaking of the remaining C-N bond of diazenyl biradical were determined at the second order Möller-Plesset perturbation theory (MP2/6-31G*) and at the Hartree-Fock (HF/6-31G*) levels, respectively.

The bond dissociation energies were estimated using the available thermochemical data and previously reported results for bicyclo(2.1.0)pentane.¹⁵⁰ The equilibrium geometries predicted by the semi-empirical potential for reactants and products, the barrier height for thermal nitrogen extrusion from 2,3-diazabicyclo(2.2.1)hept-2-ene and the fundamental vibrational frequencies are in good to excellent agreement with the measured or *ab initio* calculated values.

Using a projection method of the instantaneous Cartesian velocities onto the normal mode vectors and classical trajectory calculations, the dissociation dynamics of 2,3-diazabicyclo(2.2.1)hept-2-ene-exo, *exo*-5,6-d₂ were investigated at several excitation energies in the range 60-175 kcal/mol. The results showed the following:

- (1) The thermal reaction takes place with a preference for inversion of configuration in the reaction products, the *exo*-labeled bicyclo(2.1.0) pentane being the major product. The *exo*/*endo* ratio of bicyclo(2.1.0) pentane isomers is found to vary between 1.8-2.2 for the energy range considered.
- (2) For random energization of the vibrational modes, the energy dependence of the rate coefficients can be described by an RRK expression.
- (3) The significant broadening and overlapping of the power spectral bands, together with the disappearance of characteristic features in the power spectra of the internal coordinates calculated at different energies, indicate high intramolecular vibrational redistribution rates and global statistical behavior.
- (4) The energy partitioning among products shows that the internal energy is preferentially distributed into the vibrational degrees of freedom in BCP, while N₂ is formed with small amounts of rotational and vibrational energies.
- (5) Stepwise dissociation of the C-N bonds is the predominant mechanism which characterizes the N₂ elimination from the parent molecule.
- (6) Although statistical theories of reaction rates, such as the Rice-Ramsperger-Kassel-Marcus (RRKM) theory, are unable to predict the product *exo*/*endo* ratio, this is not a result of the breakdown of the statistical assumption inherent in these theories, but is rather due to the fact that statistical theories do not address mechanistic questions related to post transition-state events.

The results of the present investigation demonstrate that the method of molecular dynamics simulations represents a very powerful theoretical

methodology for the detailed investigation of molecular systems in both the condensed and gas phases. In addition, the incorporation of *ab initio* calculations in molecular dynamics studies represents a complementary procedure to determine the essential data necessary in the construction of potential-energy surfaces. However, following the development of computational systems and parallel processing techniques, a much larger interconnection of the *ab initio* and molecular dynamics simulations methods is expected. In the future, molecular dynamics simulations on *ab initio* calculated potential-energy surfaces will become a reference method in the investigation of medium-size and eventually large molecular systems.

BIBLIOGRAPHY

1. L. M. Raff and D. L. Thompson, *Theory of Chemical Reaction Dynamics*, (edited by M. Bare, Chemical Rubber, Boca Raton, 1985), vol. III., p. 1.
2. R. N. Porter and L. M. Raff, in *Dynamics of Molecular Collisions*, (edited by W. H. Miller, Plenum Press, New York, 1976), vol. II, p. 1.
3. M. P. Allen and D. J. Tidesley, *Computer Simulation of Liquids*, (Clarendon Press, Oxford 1987).
4. J. A. McCammon and S. C. Harvey, *Dynamics of Proteins and Nucleic Acids*, (Cambridge University Press, Cambridge, 1989).
5. M. L. Klein, *Ann. Rev. Phys. Chem.* **36**, 525 (1985).
6. A. V. Komolkin, A. Laaksonen, and A. Maliniak, *J. Chem. Phys.* **101**, 4103 (1994).
7. W. H. Miller, *Adv. Chem. Phys.* **25**, 69 (1974).
8. R. A. Marcus, *Faraday Disc. Chem. Soc.* **55**, 9 (1973).
9. G. C. Schatz, *Chem. Rev.* **87**, 81 (1987).
10. J. P. Valleau and S. G. Whittington, in *Modern Theoretical Chemistry*, (edited by B. J. Berne, Plenum Press, New York, 1977), vol. 5, p.137.
11. N. Metropolis, A. W. Metropolis, M. N. Rosenbluth, A. H. Teller, and E. Teller, *J. Chem. Phys.* **21**, 1087 (1953).
12. M. J. Frisch, G. W. Trucks, M. Head-Gordon, P. M. W. Grill, M. W. Wong, J. B. Foresman, B. G. Johnson, K. Raghavachari, J. S. Binkley, C. Gonzalez, R. L. Martin, D. J. Fox, D. J. Defrees, J. Baker, J. J. P. Stewart, and J. A. Pople, GAUSSIAN 92, (Gaussian Inc.: Pittsburgh, PA, 1992).
13. M. Born and J. R. Oppenheimer, *Ann. Physik* **84**, 457 (1927).
14. U. Burkert and N. L. Allinger, *Molecular Mechanics*, (ACS Monograph 177, Washington, D.C., 1982).

15. S. S. Shaik, H. B. Schlegel, and S. Wolfe, *Theoretical Aspects of Physical Organic Chemistry*, (John Wiley & Sons, Inc., New York, 1992).
16. N. L. Allinger, *J. Am. Chem. Soc.* **99**, 8127 (1977).
17. N. L. Allinger, Y. H. Yuh, and J.H. Lii, *J. Am. Chem. Soc.* **111**, 8551 (1989).
18. J. H. Lii and N. L. Allinger, *J. Am. Chem. Soc.* **111**, 8566 (1989).
19. W. J. Hehre, L. Radom, P. V. R. Schleyer and J. A. Pople, in *Ab Initio Molecular Orbital Theory*, (John Wiley & Sons, Inc. 1986).
20. P. C. Hariharan and J. A. Pople, *Theoret. Chim. Acta.* **28**, 213 (1973).
21. M. M. Francl, W. J. Pietro, W. J. Hehre, J. S. Binkley, M. S. Gordon, D. J. DeFrees, and J. A. Pople, *J. Chem. Phys.* **77**, 3654 (1982).
22. M. Frisch, J. Foresman, and E. Frisch, in *Gaussian 92 User Guide*, Gaussian, Inc. Pittsburgh, 1992).
23. E. B. Wilson, J. C. Decius and P. C. Cross, in *Molecular Vibrations*, (Dover Publications, Inc., New York, 1980).
24. K. B. Wiberg, S. T. Waddell, and R. E. Rosenberg, *J. Am. Chem. Soc.* **112**, 2184 (1990).
25. K. B. Wiberg, R. E. Rosenberg, and S. T. Waddell, *J. Phys. Chem.* **96** 8293 (1992).
26. N. V. Riggs, U. Zoller, M. T. Nguyen, and L. Radom, *J. Am. Chem. Soc.* **114**, 4354 (1992).
27. J. W. Gault and L. Radom, *J. Phys. Chem.* **98**, 777 (1994).
28. Y. Chen, S. J. Paddison, and E. Tschuikow-Roux, *J. Phys. Chem.* **98**, 1100 (1994).
29. L. A. Curtiss and J. A. Pople, *J. Chem. Phys.* **88**, 7405 (1988).
30. J. A. Pople, M Head-Gordon, D. J. Fox, K. Raghavachari, and L. A. Curtiss, *J. Chem. Phys.* **90**, 5622 (1989).
31. L. A. Curtiss, K. Raghavachari, G. W. Trucks, and J. A. Pople, *J. Chem. Phys.* **94**, 7221 (1991)
32. M. Sana and G. Leroy, *J. Molec. Struct. (Theochem)* **226**, 307 (1991).

33. M. Sana and M. T. Nguyen, Chem. Phys. Lett. **196**, 390 (1992).
34. L. A. Curtis, K. Raghavachari, and J. A. Pople, Chem. Phys. Lett. **214**, 183 (1993).
35. N. Sathyamurthy and L. M. Raff, J. Chem. Phys. **63**, 464 (1975).
36. N. Sathyamurthy and L. M. Raff, J. Chem. Phys. **72**, 3163 (1980).
37. C. L. Stroud and L. M. Raff, J. Chem. Phys. **72**, 5479 (1980).
38. P. G. Jasien and R. Shepard, Int. J. Quantum Chem. Quantum Chem. Symp. **22**, 183 (1988).
39. J. Ischtwan and M. A. Collins, J. Chem. Phys. **100**, 8080 (1994).
40. J. N. Murrell, S. Carter, S.C. Farantos, P. Huxley, and A. J. C. Varandas, in *Molecular Potential Energy Functions* (Wiley, Chichester, 1984).
41. L. M. Raff, J. Phys. Chem. **91**, 3266 (1987).
42. S. A. Abrash, R. W. Zehner, G. J. Mains, and L. M. Raff, J. Phys. Chem. (to be published 1994).
43. T. D. Sewell and D. L. Thompson, J. Chem. Phys. **93**, 4077 (1990).
44. H. Goldstein, *Classical Mechanics*, 2nd ed. (Addison-Wesley, Reading Massachusetts, 1980).
45. L. M. Raff, J. Chem. Phys. **93**, 3160 (1990).
46. L. M. Raff, J. Chem. Phys. **89**, 5680 (1988).
47. L. M. Raff, J. Chem. Phys. **90**, 6313 (1989).
48. C. L. Stroud and L. M. Raff, J. Chem. Phys. **72**, 5479 (1980).
49. W. L. Hase, in *Potential Energy Surfaces and Dynamics Calculations*, (edited by D. G. Truhlar, Plenum Press, New York, 1981), p.1.
50. W. L. Hase, in *Dynamics of Molecular Collisions*, (edited by W. H. Miller, Plenum Press, New York, 1976), vol. II, Part B, p. 121.
51. D. L. Bunker, *Theory of Elementary Gas Reaction Rates*, (Pergamon Press, New York 1966).
52. P. J. Robinson and K. A. Holbrook, *Unimolecular Reactions*, (Wiley: New York, 1972).

53. W. Forst, *Theory of Unimolecular Reactions*, (Academic Press, New York, 1973).
54. P. M. Agrawal, D. L. Thompson, and L. M. Raff, *J. Chem. Phys.* **92**, 1069 (1990).
55. P. Felder and Hs. H. Gunthard, *Chem. Phys.* **85** 1 (1984).
56. W. F. Hoffman, III and J. S. Shirk, *Chem. Phys.* **78**, 331 (1983).
57. D. L. Bunker and W. L. Hase, *J. Chem. Phys.* **59**, 4621 (1973); *ibid.* **69**, 4711 (1978).
58. H. W. Schranz, L. M. Raff, and D. L. Thompson, *J. Chem. Phys.* **94**, 4219 (1991).
59. H. W. Schranz, L. M. Raff, and D. L. Thompson, *J. Chem. Phys.* **95**, 106 (1991).
60. H. W. Schranz, L. M. Raff, and D. L. Thompson, *Chem. Phys. Lett.* **171**, 68 (1990).
61. H. W. Schranz, L. M. Raff, and D. L. Thompson, *Chem. Phys. Lett.* **182**, 455 (1991).
62. T. D. Sewell, H. W. Schranz, D. L. Thompson, and L. M. Raff, *J. Chem. Phys.* **95**, 8089 (1991).
63. R. H. Newman-Evans, R. J. Simon, and B. K. Carpenter, *J. Org. Chem.* **55**, 695 (1990).
64. K. L. Blintz and D. L. Thompson, *J. Chem. Phys.* **86**, 4411 (1987).
65. K. L. Blintz, D. L. Thompson, and J. W. Bradly, *J. Chem. Phys.* **85**, 1848 (1988).
66. B. G. Sumpter and D. L. Thompson, *J. Chem. Phys.* **82**, 4557 (1985); **86**, 2805 (1987); **86**, 3301 (1987).
67. Y. Guan, G. C. Lynch, and D. L. Thompson, *J. Chem. Phys.* **87**, 6957 (1987).
68. D. W. Noid, M. L. Koszykowski, and R. A. Marcus, *J. Chem. Phys.* **67**, 404 (1977).
69. T. D. Sewell, D. L. Thompson, and R. D. Levine, *J. Chem. Phys.* **96**, 8006 (1992).
70. X. Y. Chang, T. D. Sewell, L. M. Raff, and D. L. Thompson, *J. Chem. Phys.*

- 97**, 7354 (1992).
71. J. S. Bendat and A. G. Piersol, in *Random Data Analysis and Measurement Procedures*, (John Wiley & Sons, New York, 1986).
 72. J. C. Keck, in *Advances in Chemical Physics*, (edited by I. Prigogine, Interscience, New York, 1967) Vol. XIII, p. 85.
 73. L. M. Raff, I. NoorBatcha, and D. L. Thompson, *J. Chem. Phys.* **85**, 3081 (1986).
 74. B. M. Rice, L. M. Raff, and D. L. Thompson, *J. Chem. Phys.* **88**, 7221 (1988).
 75. M. B. Ford, A. D. Foxworthy, G. J. Mains, and L. M. Raff, *J. Phys. Chem.* **97**, 12134 (1993).
 76. K. Binder, in *Monte Carlo Methods in Statistical Physics*, (edited by K. Binder, Springer-Verlag, Berlin, 1986), p.1.
 77. J. A. Barker, in *Lattice Theories of the Liquid State*, (Mac Millan, New York, 1963).
 78. J. D. Doll, *J. Chem. Phys.* **74**, 1074 (1980).
 79. R. Viswanathan, L. M. Raff., and D. L. Thompson, *J. Chem. Phys.* **81**, 828 (1984).
 80. A. F. Voter and J. D. Doll, *J. Chem. Phys.* **80**, 5832 (1984).
 81. J. D. Doll, H. K. McDowell, and S. M. Valone, *J. Chem. Phys.* **78**, 5276 (1983).
 82. S. M. Valone, A. F. Voter and J. D. Doll, *Surf. Science* **155**, 687 (1985).
 83. I. NoorBatcha, L. M. Raff, and D. L. Thompson, *J. Chem. Phys.* **83**, 1382 (1985).
 84. P. M. Agrawal, D. L. Thompson, and L. M. Raff, *J. Chem. Phys.* **91**, 6463 (1989).
 85. P. M. Agrawal, D. L. Thompson, and L. M. Raff, *J. Chem. Phys.* **94**, 6243 (1991).
 86. H. C. Andersen, *J. Chem. Phys.* **72**, 2384 (1980).
 87. G. A. Somorjai, *Introduction to Surface Chemistry and Catalysis*, (John Wiley & Sons, Inc. New York 1994).

88. G. A. Somorjai, *Chemistry in Two Dimension: Surfaces* (Cornell Univ. Press, Ithaca, 1981).
89. R. H. Williams and I. T. McGovern, *The Chemical Physics of Solid Surfaces and Heterogeneous Catalysis*, edited by D. A. King and D. P. Woodruff (Elsevier, New York, 1984), vol. 3B.
90. G. Ehlich and K. Stolt, *Ann. Rev. Phys. Chem.* **31**, 603 (1980).
91. J. M. Jasinski, B. S. Meyerson, and B. A. Scott, *Ann. Rev. Phys. Chem.* **38**, 109 (1987).
92. J. J. Boland, *Surf. Sci.* **244**, 1 (1991).
93. B. G. Koehler, C. H. Mak, D. A. Arthur, P. A. Coon, and S. M. George, *J. Chem. Phys.* **89**, 1709 (1988).
94. G. A. Reider, U. Höfer, and T. F. Heinz, *Phys. Rev. Lett.* **66**, 1994 (1991).
95. NoorBatcha, L. M. Raff, and D. L. Thompson, *J. Chem. Phys.* **81**, 3715 (1984).
96. I. NoorBatcha, L. M. Raff, and D. L. Thompson, *J. Chem. Phys.* **82**, 1543 (1985).
97. I. NoorBatcha, L. M. Raff, and D. L. Thompson, *J. Chem. Phys.* **83**, 6009 (1985).
98. P. M. Agrawal, D. L. Thompson, and L. M. Raff, *Surf. Sci.* **195**, 283 (1988).
99. A. L. Robinson, *Science*, **232**, 451 (1986).
100. D. C. Sorescu, D. L. Thompson, and L. M. Raff, *J. Chem. Phys.* **101**, 1638 (1994).
101. K. Takayanagi, Y. Tanishiro, S. Takahashi and M. Takahasi, *J. Vac. Sci. & Technol.* **A 3**, 1502 (1985).
102. K. Takayanagi, Y. Tanishiro, S. Takahashi and M. Takahasi, *Surf. Sci.* **164**, 367 (1985), and references therein.
103. G. Binnig, H. Rohrer, Ch. Gerber, and E. Weibel, *Phys. Rev. Lett.* **50**, 120 (1983).
104. E. G. Mac Rae and C. W. Caldwell, *Phys. Rev. Lett* **46**, 1630 (1981); E. G. Mac Rae, *Phys. Rev.* **B 28**, 2305 (1983).
105. A. Bennett, L. C. Feldman, Y. Kuk, E. G. McRae, and J. P. Rose, *Phys. Rev.*

- B 28**, 3656 (1983).
106. J. Hoshinoby, S. I. Tanaka, and M. Nishijima, *Jpn. J. Appl. Phys.* **32**, 1171 (1993).
 107. G. A. Reider, U. Hofer and T. F. Heinz, *J. Chem. Phys.* **94**, 4080 (1991).
 108. B. C. Bolding and H. C. Andersen, *Phys. Rev.* **41**, 10568 (1990).
 109. J. Tersoff, *Phys. Rev. Lett.* **56**, 632 (1986); *Phys. Rev.* **B 37**, 6991 (1988); *Phys. Rev.* **B 38**, 9902 (1988).
 110. R. I. G. Uhrberg and G. V. Hansson, *Crit. Rev. Sol. State and Mat. Sci.* **17**, 133 (1991).
 111. R. E. Schlier and H. E. Farnsworth, *J. Chem. Phys.* **30**, 917 (1959).
 112. R. M. Tromp, E. J. VanLowen, M. Iwami, F. W. Saris, *Solid State Commun.* **44**, 971 (1982).
 113. I. K. Robinson, W. K. Waskiewicz, P. H. Fuoss, J. B. Stark, and P. A. Bennett, *Phys. Rev.* **B 33**, 7013 (1986).
 114. R. M. Tromp, R. J. Hamers, and J. E. Demuth, *Phys. Rev.* **B 34**, 1388 (1986).
 115. G. X. Qian and D. J. Chadi, *Phys. Rev.* **B 35**, 1288 (1987), and references therein.
 116. K. D. Brommer, M. Needels, B. E. Larson, and J. D. Joannopoulos, *Phys. Rev. Lett.* **68**, 1355 (1992).
 117. P. N. Keating, *Phys. Rev.* **145**, 637 (1966).
 118. I. Stich, M. C. Payne, A. De Vita, M. J. Gillan, and L. J. Clarke, in *Computations for the Nano-Scale*, (eds. P. E. Blöchl, C. Joachim, and A. J. Fisher, Kluwer Academic Publisher, The Netherlands, 1993).
 119. M. L. Wise, B. G. Koehler, P. Gupta, P. A. Coon and S. M. George, *Surf. Sci.* **258**, 166 (1991) (and references herein).
 120. H. Fritzsche, C. C. Tsai, and P. Pearson, *Solid State Technology.* **21**, 55 (1978).
 121. Y. J. Chabal, G. S. Higashi, and S. B. Christman *Phys. Rev.* **B28**, 4472 (1983).
 122. H. Wagner, R. Butz, U. Backes, D. Bruchmann, *Solid State Commun.* **38**, 1155 (1981).

123. H. Kobayashi, K. Edamoto, M. Onchi, and M. Nishijima, *J. Chem. Phys.* **78**, 7429 (1983).
124. C. M. Greenlief, S. M. Gates, and P. A. Holbert, *Chem. Phys. Lett.* **159**, 202 (1989).
125. J. J. Boland, *J. Phys. Chem.* **95**, 1521 (1991).
126. K. Hermann and P. S. Bagus, *Phys. Rev.* **B 20**, 1603 (1979).
127. G. Schulze and M. Henzler, *Surf. Sci.* **124**, 336 (1983).
128. G. A. Reider, U. Höfer, and T. F. Heinz, *J. Chem. Phys.* **94**, 4080 (1991).
129. S. F. Shane, K. W. Kolasinski, and R. N. Zare, *J. Chem. Phys.* **97**, 1520 (1992).
130. J. A. Appelbaum and D. R. Hamann, *Phys. Rev. Lett.* **34**, 8 (1975).
131. K. M. Ho, M. L. Cohen and M. Schluter, *Phys. Rev.* **B 15**, 3888 (1977).
132. H. Froitzheim, U. Kokhler, and H. Lammering, *Surf. Sci.* **149**, 537 (1985).
133. M. Nishijima, K. Edamoto, Y. Kubota, H. Kobayashi, and M. Onchi, *Surf. Sci.* **158**, 422 (1985).
134. U. Jansson and K. J. Uram, *J. Chem. Phys.* **91**, 7978 (1989).
135. R. Gomer, *Rep. Prog. Phys.* **53**, 917 (1990).
136. B. M. Rice, L. M. Raff, and D. L. Thompson, *Surf. Sci.* **198**, 360 (1988).
137. J. D. Doll and A. F. Voter, *Ann. Rev. Phys. Chem.* **38**, 413 (1987).
138. D. Rapp, *Quantum Mechanics* (Holt, Rinehart, and Winston, Dallas, (1971).
139. H. W. Schranz, L. M. Raff, and D. L. Thompson, *Chem. Phys. Lett.* **187**, 455. (1991).
140. B. K. Carpenter, *Acc. Chem. Res.* **25**, 520 (1992).
141. (a) W. R. Roth and M. Martin, *Justus Liebigs Ann. Chem.* **702**, 1 (1967);
(b) W. R. Roth and M. Martin, *Tetrahedron Lett.* **47**, 4695 (1967).
142. E. L. Allred and R. L. Smith *J. Am. Chem. Soc.* **89**, 7133 (1967); *ibid.* **91**, 6766 (1969).
143. J. P. Chesick, *J. Am. Chem. Soc.* **84**, 3250 (1962).

144. S. N. Marthur and M. D. Harmony, *Anal. Chem.* **48**, 1509 (1976).
145. J. E. Baldwin and J. Ollerenshaw, *J. Org. Chem.* **46**, 2116 (1981).
146. S. L. Buchwalter and G. L. Closs, *J. Am Chem. Soc.* **97**, 3857(1975); *ibid.* **101**, 4688 (1979).
147. M. S. Herman and J. L. Goodman, *J. Am. Chem. Soc.* **110**, 2681 (1988).
148. M. P. Conrad, R. M. Pitzer, and H. F. Schaefer III, *J. Phys. Chem.* **101**, 2245 (1979).
149. C. D. Sherill, E. T. Seidl, and H. F. Schaefer III, *J. Phys. Chem.* **96**, 3712 (1992).
150. D. C. Sorescu, D. L. Thompson, and L. M. Raff, *J. Chem. Phys.* **101**, 3729 (1994).
151. E. P. Wallis and D. L. Thompson, *J. Chem. Phys.* **99**, 2661 (1993).
152. (a) C. Möller and M. S. Plesset, *Phys. Rev.* **46**, 618 (1934); (b) J. S. Binkley and J. A. Pople, *Int. J. Quantum Chem.* **9**, 229 (1975).
153. O. Bastiansen, F. N. Fritsch, and K. Hedberg, *Acta Cryst.* **17**, 538 (1964).
154. (a) A. Almenningen, O. Bastiansen, and P. N. Skancke, *Acta Chem. Scand.* **15**, 17 (1961); (b) S. Meiboom and L. C. Snyder, *J. Chem. Phys.* **52**, 3857 (1970); (c) A comprehensive reference list for the experimental values of the puckering angle in C₄H₈ can be found in Ref. 19, p. 266. The experimental values are spread over the range 145°-160°.
155. R. D. Suenram and M. D. Harmony, *J. Chem. Phys.* **56**, 3837 (1972).
156. S. N. Marthurm, M. D. Harmony, and R. D. Suernam, *J. Chem. Phys.* **64**, 4340 (1967).
157. R. S. Grev, C. L. Janssen, and H. F. Schaefer, *J. Chem. Phys.* **95**, 5128 (1991).
158. D. F. McMillen and D. M. Golden, *Ann. Rev. Phys. Chem.* **33**, 493 (1982).
159. D. R. Stull, E. F. Westrum Jr, and G. C. Sinke, *The Chemical Thermodynamics of Organic Compounds*, (John Wiley & Sons, Inc.: New York, 1969).
160. R. B. Turner, P. Geobel, B. J. Mallon, W. v. E. Doering, J. F. Coburn, and M. Pomerantz, *J. Am. Chem. Soc.* **90**, 4315 (1968).

161. J. D. Cox and G. Pilcher, *Thermodynamics of Organic and Organometallic Compounds*, (Academic Press: London, 1970).
162. J. Bragin and D. Guthals, *J. Phys. Chem.* **79**, 2139 (1975).
163. R. K. Bohn and Tai Yuan-Heng, *J. Am. Chem. Soc.* **92**, 6447 (1970).
164. C. Van Alsenoy, J. N. Scarsdale, and L. Schafer, *J. Chem. Phys.* **74**, 6278 (1981).
165. P. N. Skancke, *J. Mol. Struct.* **86**, 255 (1982).
166. K. B. Wiberg and J. J. Wendoloski, *J. Am. Chem. Soc.* **104**, 5679 (1982).
167. W. H. Press, B. P. Flannery, S. A. Teukolsky, and W. T. Vetterling, *Numerical Recipes*, (Cambridge University: New York, 1989).
168. K. L. Bintz, D. L. Thompson, T. R. Gosnell, and P. J. Hay, *J. Chem. Phys.* **97**, 6432 (1992).
169. S. C. Cohen, R. Zand, and C. Steel, *J. Am. Chem. Soc.* **83**, 2895 (1961).
170. R. J. Crawford and A. Mishra, *J. Am. Chem. Soc.* **88**, 3963 (1966).
171. B. Bigot, A. Sevin, and A. Devaquet, *J. Am. Chem. Soc.* **100**, 2639 (1978).
172. J. S. Adams, R. B. Weisman, and P. S. Engel, *J. Am. Chem. Soc.* **112**, 9115 (1990).
173. J. S. Adams, K. A. Burton, B. K. Andrews, R. B. Weismann, and P. S. Engel, *J. Am. Chem. Soc.* **108**, 7935 (1986).
174. C. J. S. M. Simpson, G. J. Wilson, and W. Adam, *J. Am. Chem. Soc.* **113**, 4728 (1991).
175. S. H. Bauer, *J. Am. Chem. Soc.* **91**, 3688 (1969)
176. W. Adam, T. Oppenlander, and G. Zang, *J. Org. Chem.* **50**, 3303 (1985).
177. W. Adam, U. Denninger, R. Finzel, F. Kita, H. Platsch, H. Walter, and G. Zang, *J. Am. Chem. Soc.* **114**, 50027 (1992).
178. (a) B. A. Lyons, J. Pfeifer, and B. K. Carpenter, *J. Am. Chem. Soc.* **113**, 9006 (1991); (b) T. H. Peterson and B. K. Carpenter, *J. Am. Chem. Soc.* **114**, 766 (1992).
179. B. A. Lyons, J. Pfeifer, T. H. Peterson, and B. K. Carpenter, *J. Am. Chem. Soc.* **115**, 2427 (1993).

180. D. C. Sorescu, D. L. Thompson, and L. M. Raff, J. Chem. Phys. (to be published 1994).
181. J. F. Chiang, R. L. Chiang, and M. T. Kratus, J. Mol. Struct. **26**, 175 (1975).
182. R. D. Suenram, J. Mol. Struct. **33**, 1 (1976).
183. R. J. Boyd, J. C. G. Bunzli, and J. P. Snyder, J. Amer. Chem. Soc. **98**, 2398 (1976).
184. J. Kao and T. N. Huang, J. Am. Chem. Soc. **101**, 5546 (1979).
185. A. Pople, M Head-Gordon, D. J. Fox, K. Raghavachari, and L. A. Curtiss, J. Chem. Phys. **90**, 5622 (1989).
186. N. V. Riggs, U. Zoller, M. T. Nguyen, and L. Radom, J. Am. Chem. Soc. **114**, 4354 (1992).
187. S. W. Benson and H. E. O'Neal, Nat. Stand. Ref. Data Ser, Natl. Bur. Stand. **21**, 1 (1970).
188. P. S. Engel, Chem. Rev. **80**, 99 (1980).
189. J. B. Pedley, R. D. Naylor, and S. P. Kirby *Thermochemical Data of Organic Compounds*, (Chapman and Hall: London 1986).
190. CRC Handbook of Chemistry and Physics, 70th ed., (CRC.Press, Inc., Boca Raton, Florida: 1989).
191. L. Radom, W. A. Lathan, W. J. Hehre, and J. A. Pople, J. Am. Chem. Soc. **95**, 693 (1973).
192. C. V. Alsenoy, K. Siam, J. D. Ewbank, and L. Schafer, J. Mol. Struct. (Theochem), **136**, 77 (1986).
193. B. Rosen, *Spectroscopic Data Relative to Diatomic Molecules*; Pergamon: Oxford, 1970.
194. E. A. Gislason and E. M. Goldfield, J. Chem. Phys. **80**, 701 (1984).

VITA

Dan Constantin Sorescu

Candidate for the Degree of

Doctor of Philosophy

Thesis: THEORETICAL STUDIES OF MOLECULAR DYNAMICAL PROCESSES ON SOLID SURFACES AND IN THE GAS PHASE

Major Field: Physics

Biographical:

Personal Data: Born in Pitesti, Romania, December 12, 1962, the son of Dumitru and Sofia Sorescu.

Education: Graduated from College for Mathematics and Physics "Nicolae Balcescu", Pitesti, Romania, in June 1981; received Bachelor of Science degree in Physics from the University of Bucharest, Bucharest, Romania, in June 1986; received Master of Science degree in Physics from the University of Bucharest, Bucharest, Romania, in June 1987; completed requirements for Doctor of Philosophy degree at Oklahoma State University in December, 1994.

Professional Experience: Physicist, Institute for Power Nuclear Reactors, Pitesti, Romania, September 1987 to February 1990; Research Scientist, Institute of Atomic Physics/Institute of Optoelectronics, Bucharest, Romania, February 1990 to August 1992; Research Assistant, Department of Chemistry, Oklahoma State University, August 1992 to December 1994.

Professional Memberships: American Physical Society, Phi Kappa Phi (honorary society).